Stellar populations, Morphology and Kinematics of the Magellanic Clouds

Dalal El Youssoufi
Leibniz-Institut für Astrophysik Potsdam (AIP)

Kumulative dissertation

zur Erlangung des akademischen Grades
doctor rerum naturalium (Dr. rer. nat.)
in der Wissenschaftsdisziplin Physik

Eingereicht an der Mathematisch-Naturwissenschaftlichen Fakultät
Institut für Physik und Astronomie
der Universität Potsdam
und
das Leibniz-Institut für Astrophysik Potsdam (AIP)

Potsdam, den September 2023

Front Cover: VISTA image of the Small Magellanic Cloud obtained from the VMC survey. Credit: ESO/VMC.
Back cover: VISTA image of the Large Magellanic Cloud obtained from the VMC survey. Credit: ESO/VMC.

Betreuer:	Prof. Dr. Maria-Rosa L. Cioni
1. Gutachter:	Prof. Dr. Maria-Rosa L. Cioni Leibniz-Institut für Astrophysik Potsdam/Universität Potsdam
2. Gutachter:	Prof. Dr. Matthias Steinmetz Leibniz-Institut für Astrophysik Potsdam/Universität Potsdam
3. Gutachter: 3	Prof. Dr. Andrew A. Cole School of Natural Sciences, University of Tasmania

الى مراكش، بكل من فيها و ما فيها

لم نحلم بأشياء عصية
نحن أحياء وباقون ... وللحلم بقية

محمود درويش، لا أريد لهذي القصيدة أن تنتهي

Declaration

This thesis is the result of my own work and includes nothing which is the outcome of work done in collaboration except as declared below and specified in the text:

- Chapter 2 is based on the work published under the title: The VMC survey–XXXIV .Morphology of stellar populations in the Magellanic Clouds in Monthly Notices of the Royal Astronomical Society; El Youssoufi et al. (2019).
- Chapter 3 is based on the work published under the title Stellar substructures in the periphery of the Magellanic Clouds with the VISTA hemisphere survey from the red clump and other tracers in Monthly Notices of the Royal Astronomical Society; El Youssoufi et al. (2021).
- Chapter 4 is based on the work published under the title "Kinematics of Stellar Substructures in the Small Magellanic Cloud" in Monthly Notices of the Royal Astronomical Society; El Youssoufi et al. (2023).

It is not substantially the same as any that I have submitted, or, is being concurrently submitted for a degree or diploma or other qualification at the University of Potsdam or any other University or similar institution except as declared below and specified in the text. I further state that no substantial part of my thesis has already been submitted, or, is being concurrently submitted for any such degree, diploma or other qualification at the University of Potsdam or any other University or similar institution.

Berlin, September 2023

Dalal El Youssoufi

Summary

Galaxy morphology is a fossil record of how galaxies formed and evolved and can be regarded as a function of the dynamical state of a galaxy. It encodes the physical processes that dominate its evolutionary history, and is strongly aligned with physical properties like stellar mass, star formation rate and local environment. At a distance of $\sim$50 and 60 kpc, the Magellanic Clouds represent the nearest interacting pair of dwarf irregular galaxies to the Milky Way, rendering them an important test bed for galaxy morphology in the context of galaxy interactions and the effect of the local environment in which they reside. The Large Magellanic Cloud is classified as the prototype for Magellanic Spiral galaxies, with one prominent spiral arm, an offset bar and an inclined rotating disc while the Small Magellanic Cloud is classified as a dwarf Irregular galaxy and is known for its unstructured shape and large depth across the line–of–sight. Resolved stellar populations are powerful probes of a wide range of astrophysical phenomena, the proximity of the Magellanic Cloudss allows us to resolve their stellar populations to individual stars that share coherent chemical and age distributions. The coherent properties of resolved stellar populations enable us to analyse them as a function of position within the Magellanic Clouds, offering a picture of the growth of the galaxies' substructures over time and yielding a comprehensive view of their morphology. Furthermore, investigating the kinematics of the Magellanic Clouds offers valuable insights into their dynamics and evolutionary history. By studying the motions and velocities of stars within these galaxies, we can trace their past interactions, with the Milky Way or with each other and unravel the complex interplay of forces that have influenced the Magellanic Clouds' formation and evolution.

In Chapter 2, the VISTA survey of the Magellanic Clouds was employed to generate unprecedented high-resolution morphological maps of the Magellanic Clouds in the near-infrared. Utilising colour-magnitude diagrams and theoretical evolutionary models to segregate stellar populations, this approach enabled a comprehensive age tomography of the galaxies. It revealed previously uncharacterised features in their central regions at spatial resolutions of 0.13 kpc (Large Magellanic Cloud) and 0.16 kpc (Small Magellanic Cloud), the findings showcased the impact of tidal interactions on their inner regions. Notably, the study highlighted the enhanced coherent structures in the Large Magellanic Cloud, shedding light on the significant role of the recent Magellanic Clouds' interaction 200 Myr ago in shaping many of the fine structures. The Small Magellanic Cloud revealed asymmetry in younger populations and irregularities in intermediate-age ones, pointing towards the influence of past tidal interactions.

In Chapter 3, an examination of the outskirts of the Magellanic Clouds led to the identification of new substructures through the use of near-infrared photometry from the VISTA Hemisphere Survey and multi-dimensional phase-space information from *Gaia*. The distances and proper motions of these substructures were investigated. This analysis revealed the impact of past Magellanic Clouds' interactions and the influence of the Milky Way's tidal field on the morphology and kinematics of the

Magellanic Clouds. A bi-modal distance distribution was identified within the luminosity function of the red clump stars in the Small Magellanic Cloud, notably in its eastern regions, with the foreground substructure being attributed to the Magellanic Clouds' interaction around 200 Myr ago. Furthermore, associations with the Counter Bridge and Old Bridge were uncovered through the detection of background and foreground structures in various regions of the SMC.

In chapter 4, a detailed kinematic analysis of the Small Magellanic Cloud was conducted using spectra from the European Southern Observatory Science Archive Facility. The study reveals distinct kinematics in the Wing and bar regions, attributed to interactions with the Large Magellanic Cloud and variations in star formation history. Notably, velocity disparities are observed in the bar's young main sequence stars, aligning with specific star-forming episodes, and suggesting potential galactic stretching or tidal stripping, as corroborated by proper motion studies.

Zusammenfassung

Galaxienmorphologie ist ein fossiles Aufzeichnungsmaterial dafür, wie Galaxien entstanden und sich entwickelt haben und kann als Funktion des dynamischen Zustands einer Galaxie betrachtet werden. Sie kodiert die physischen Prozesse, die ihre Entwicklungsgeschichte dominieren, und ist stark mit physischen Eigenschaften wie stellare Masse, Sternentstehungsrate und lokaler Umgebung verknüpft. In einer Entfernung von $\sim$50 und 60 kpc stellen die Magellanschen Wolken das nächstgelegene interagierende Paar von Zwergirregulären Galaxien zur Milchstraße dar und sind somit ein wichtiges Testfeld für Galaxienmorphologie im Kontext von Galaxieninteraktionen und dem Einfluss der lokalen Umgebung, in der sie sich befinden. Die Große Magellansche Wolke wird als Prototyp für Magellanische Spiralgalaxien klassifiziert, mit einem prominenten Spiralarm, einem versetzten Balken und einer geneigten rotierenden Scheibe, während die Kleine Magellansche Wolke als Zwergirreguläre Galaxie klassifiziert wird und für ihre unstrukturierte Form und große Tiefe entlang der Sichtlinie bekannt ist. Aufgelöste Sternpopulationen sind mächtige Sonden für eine breite Palette von astrophysikalischen Phänomenen, die Nähe der Magellanschen Wolken ermöglicht es uns, ihre Sternpopulationen bis zu einzelnen Sternen aufzulösen, die kohärente chemische und Altersverteilungen aufweisen. Die kohärenten Eigenschaften von aufgelösten Sternpopulationen ermöglichen es uns, sie als Funktion der Position innerhalb der Magellanschen Wolken zu analysieren, und bieten ein Bild des Wachstums der Galaxienunterstrukturen über die Zeit und vermitteln eine umfassende Sicht auf ihre Morphologie. Darüber hinaus bietet die Untersuchung der Kinetik der Magellanschen Wolken wertvolle Einblicke in ihre Dynamik und Entwicklungsgeschichte. Durch das Studium der Bewegungen und Geschwindigkeiten der Sterne innerhalb dieser Galaxien können wir ihre vergangenen Interaktionen, sei es mit der Milchstraße oder untereinander, nachverfolgen und das komplexe Zusammenspiel der Kräfte, die die Formation und Evolution der Magellanschen Wolken beeinflusst haben, entwirren.

In Kapitel 2 wurde die VISTA Untersuchung der Magellanschen Wolken verwendet, um bisher beispiellose hochauflösende morphologische Karten der Magellanschen Wolken im nahen Infrarot zu erstellen. Mit Hilfe von Farb-Helligkeits-Diagrammen und theoretischen Entwicklungsmodellen zur Abgrenzung der Sternpopulationen ermöglichte dieser Ansatz eine umfassende Alters-Tomographie der Galaxien. Es wurden bisher unbekannte Merkmale in ihren Zentralregionen mit räumlichen Auflösungen von 0,13 kpc (Große Magellansche Wolke) und 0,16 kpc (Kleine Magellansche Wolke) offenbart, die Ergebnisse zeigten die Auswirkungen von Gezeitenwechselwirkungen auf ihre inneren Regionen. Bemerkenswert ist, dass die Studie die verstärkten kohärenten Strukturen in der Großen Magellanschen Wolke hervorhob und auf die bedeutende Rolle der jüngsten Interaktion der Magellanschen Wolken vor 200 Myr bei der Formung vieler Feinstrukturen hinwies. Die Kleine Magellansche Wolke zeigte Asymmetrie in jüngeren Populationen und

Unregelmäßigkeiten bei mittelalten, was auf den Einfluss vergangener Gezeitenwechselwirkungen hinweist.

In Kapitel 3 führte eine Untersuchung der Außenbereiche der Magellanschen Wolken zur Identifizierung neuer Unterstrukturen durch die Nutzung von Nahinfrarot-Photometrie aus der VISTA Hemisphere Survey und mehrdimensionalen Phasenraum-Informationen von Gaia. Die Entfernungen und Eigenbewegungen dieser Unterstrukturen wurden untersucht. Diese Analyse offenbarte die Auswirkungen vergangener Interaktionen der Magellanschen Wolken und den Einfluss des Gezeitenfeldes der Milchstraße auf die Morphologie und Kinetik der Magellanschen Wolken. Eine bimodale Entfernungsverteilung wurde innerhalb der Leuchtkraftfunktion der Red-Clump-Sterne in der Kleinen Magellanschen Wolke identifiziert, insbesondere in ihren östlichen Regionen, wobei die Vordergrundstruktur der Interaktion der Magellanschen Wolken vor etwa 200 Myr zugeschrieben wurde. Zudem wurden durch die Entdeckung von Hintergrund- und Vordergrundstrukturen in verschiedenen Regionen der SMC Assoziationen mit der Counter Bridge und Old Bridge aufgedeckt.

In Kapitel 3 wurde eine detaillierte kinematische Analyse der Kleinen Magellanschen Wolke durchgeführt, unter Verwendung von Spektren aus der European Southern Observatory Science Archive Facility. Die Studie zeigt unterschiedliche Kinetik in den Wing- und Bar-Regionen auf, die auf Interaktionen mit der Großen Magellanschen Wolke und Variationen in der Sternentstehungsgeschichte zurückgeführt werden. Bemerkenswert sind Geschwindigkeitsunterschiede, die bei den jungen Hauptreihensternen der Bar beobachtet werden, die mit spezifischen Sternentstehungs-Episoden übereinstimmen und auf potenzielle galaktische Dehnung oder Gezeitenstripping hinweisen, wie es durch Studien der Eigenbewegung bestätigt wird.

Contents

List of Figures

List of Tables

Acronyms

1001MC	The One Thousand and One Magellanic Fields survey
AAT	The Anglo-Australian Telescope
AGB	Asymptotic giant branch
APOGEE	The Apache Point Observatory Galactic Evolution Experiment
ASKAP	The Australian Square Kilometre Array Pathfinder
CASU	The Cambridge Astronomy Survey Unit
CCD	Charge-coupled device
CMD	Colour-magnitude diagram
DENIS	The Deep Near-Infrared Survey of the Southern Sky
DES	Dark Energy Survey
ESO	European Southern Observatory
FLAMES	The Fibre Large Array Multi Element Spectrograph
FOR2S	FOcal Reducer and low dispersion Spectrograph 2
FWHM	Full width at half maximum
GALEX	The Galaxy Evolution Explorer
HST	The Hubble Space Telescope
HI	Neutral atomic Hydrogen
HII	Ionised atomic Hydrogen
IMACS	The Inamori-Magellan Areal Camera and Spectrograph
LCO	Las Campanas Observatory
LMC	Large Magellanic Cloud
LSST	The Rubin Observatory Legacy Survey of Space and Time
MC	Magellanic Clouds
MCMC	Markov Chain Monte Carlo
MIKE	The Magellan Inamori Kyocera Echelle
MOONS	The Multi-Object Optical and Near-infrared spectrograph
MW	Milky Way
NIR	Near-infrared
OGLE	The Optical Gravitational Lensing Experiment
PA	Position angle
PCA	Principal Component Analysis
PM	Proper motion
PSF	Point-spread-function
RC	Red clump
RV	Radial velocity
SAF	Science Archive Facility
SDSS	The Sloan Digital Sky Survey
SMC	Small Magellanic Cloud
SNR	Signal-to-noise ratio
STFC	Science and Technology Facility Council

TGAS	The Tycho-Gaia Astrometric Solution
TOPCAT	The Tool for OPerations on Catalogues And Tables
t-SNE	t-Distributed Stochastic Neighbor Embedding
UT2	Unit Telescope 2
VDFS	The VISTA Data Flow System
VHS	The VISTA Hemisphere Survey
VIRCAM	The VISTA infrared camera
VMC	The VISTA survey of the Magellanic Clouds system
VSA	The VISTA Science archive
VSTA	Visible and Infrared Survey Telescope for Astronomy

1 Introduction

"The history of astronomy is a history of receding horizons."
– Edwin Hubble

1.1 The Magellanic Clouds in Context

The Magellanic Clouds (MCs) are a pair of interacting galaxies orbiting our Milky Way (MW). Visible in the southern hemisphere, both Clouds appear as bright nebulae in the Dorado (Large Magellanic Cloud, LMC) and Tucana (Small Magellanic Cloud, SMC) constellations, and are named after the Portuguese explorer Ferdinand Magellan, best known for his historic journey to circumnavigate the globe starting in the year 1519. Indigenous populations of South America, Australian Aborigines, the Maori people of New Zealand, and the Polynesian people of the South Pacific, among others, had a long-standing knowledge of the southern sky where the MCs served as navigational markers way before Europeans reached the southern hemisphere. For the indigenous people encountered by Magellan and his crew, the explorer's arrival foreshadowed a new age of conquest, Christianization, and colonization.

The most ancient record of a possible mention of the MCs dates back to the year 964 AD by the Persian astronomer Abd al-Rahman al-Sufi, described in his book of fixed stars, where the LMC is named as al-bakar, the white ox, by the inhabitants of Tihamat, and is described as stars below the feet of the Suhail (Canopus). During the course of history, several notable figures have contributed to our understanding of the MCs. Petrus Plancius, a Dutch astronomer, made a significant impact in the year 1598 with his celestial globe and star catalogue. Drawing from navigational data collected during Ferdinand Magellan's circumnavigation, Plancius acknowledged the MCs as "Nubecula Major" and "Nubecula Minor", representing the Large and Small Clouds, respectively. Although Plancius' work lacked detailed information, it marked the recognition of the MCs in Western astronomical tradition. In the mid-18th century, French astronomer Nicolas Louis de Lacaille made remarkable contributions through his observations at the Cape of Good Hope. His 1755 catalogue encompassed an

extensive range of southern celestial objects, including the MCs, which he referred to as "le grand & le petit nuage" (Large & Small Cloud). Lacaille's meticulous catalogue provided a more comprehensive description of the MCs and their precise positions in the sky. Continuing the pursuit of knowledge, the British astronomer John Herschel made significant contributions to MC studies in the 19th century. During his stay at the Cape of Good Hope in the 1830s, Herschel (1847) conducted extensive observations, resulting in detailed catalogues of celestial objects visible from the southern hemisphere. These catalogues included invaluable information about the content of the MCs, further advancing our understanding of these fascinating galaxies (see Figure 1.1). The MCs' nomenclature was rather widely spread among western nautical circles while the scientific community had long used the Latin names, Nubecula Minor and Major, until 1847 when Herschel first used the name MCs in a scientific publication, alongside the scientific names of Nubecula Major and Minor (Dennefeld 2020). The collective efforts of Plancius, Lacaille, Herschel, and subsequent astronomers have paved the way for a deeper understanding of the MCs. In the late 19th century, the Lick and the Harvard Observatory southern stations were established, marking the beginning of observations with modern telescopes. A significant discovery made during this time was by Leavitt (1908), who identified numerous variable stars in the MCs. This discovery led Leavitt & Pickering (1912) to establish the period-luminosity relation for Cepheids, which became the first method for measuring distances to extragalactic objects.

Since then, the MCs have remained a vital target for astronomical observations across the entire electromagnetic spectrum and continue to occupy a prominent position in our exploration of galaxy formation and evolution within the framework of the Lambda Cold Dark Matter (ΛCDM) paradigm (e.g. White & Frenk 1991; Bullock & Johnston 2005). With their unique characteristics, such as proximity, ongoing star formation, and interactions with the MW, the MCs serve as invaluable laboratories for investigating the interplay between dark matter and baryonic processes in the context of dwarf galaxies. By examining the properties of the MCs, including their stellar populations, kinematics, and structural features, we can impose significant constraints on theoretical models and simulations, thereby enhancing our understanding of galaxy formation mechanisms. Moreover, the MCs afford us a glimpse into the early stages of galaxy assembly. As satellites of the MW, their relatively modest masses and shallow potential wells render them susceptible to tidal interactions and environmental effects, thereby providing valuable insights into the role of these processes in shaping the properties of dwarf galaxies. Through in-depth investigations of the MCs, we can delve into the impacts of tidal forces, ram pressure stripping, and interactions with the MW's disc and halo on gas accretion, star formation, and the morphological transformation of galaxies. These inquiries contribute to our broader comprehension of how the environment influences the formation and evolution of galaxies across cosmic epochs. However, studying the MCs comprehensively poses a challenge due to their extensive coverage of the sky spanning hundreds of square degrees. As technology advanced in the 20th century, early investigations involved photographic plates (e.g. de Vaucouleurs 1955a,b; Irwin 1991; Gardiner & Hatzidimitriou 1992) while progress in large field–of–view, multi-charge-coupled device (CCD) detectors facilitated comprehensive mapping of

the MCs. These panoramic photometric surveys have yielded observations across multiple wavelengths, enabling a thorough view of the system and playing a crucial role in advancing our knowledge of the MCs. Significant advancements have also been made in the field of spectroscopy, including (but not limited to) the development of multi-object spectroscopy, which has revolutionised our ability to study multiple targets simultaneously. Traditionally, spectroscopy was limited to observing one object at a time, resulting in time-consuming and inefficient processes, particularly when studying large populations of celestial objects like galaxies. However, multi-object spectroscopy has overcome these limitations by allowing astronomers to obtain spectra of numerous objects within a given field of view in a single exposure. In regard to astrometry, the *Gaia* mission (Gaia Collaboration et al. 2016a) has brought remarkable advancements (Brown 2021), especially in the measurement of PMs (PMs) and parallaxes, surpassing the capabilities of its predecessor, *Hipparcos* (ESA 1997). *Gaia*'s unprecedented accuracy and sensitivity have enabled the precise determination of stellar positions, motions, and distances. By providing highly accurate PMs and parallaxes for almost two billion stars, *Gaia* has significantly improved our understanding of the kinematics, dynamics and spatial distribution of celestial objects.

Building upon these advancements, this thesis aims to use photometric data from the Visible and Infrared Survey Telescope for Astronomy (VISTA; Sutherland et al. 2015) survey of the Magellanic Clouds system (VMC; Cioni et al. 2011) and the VISTA Hemisphere Survey (VHS; McMahon et al. 2013), astrometry from the *Gaia* space mission (Gaia Collaboration et al. 2016b) and multi–object spectroscopy from the Fibre Large Array Multi Element Spectrograph (FLAMES; Pasquini et al. 2002) to provide a comprehensive view of the morphology of the MCs as well as the kinematics of some of their substructures. In the forthcoming sections, a comprehensive overview is presented, encompassing multiple facets of the MCs. Firstly, the morphology and structure of the MCs are extensively discussed, incorporating the intricate details of their stellar distributions, prominent morphological features, as well as their three-dimensional (3D) structure. The investigation extends to the outskirts of the MCs. Substructures in the outer regions of the MCs emphasise the significant value of studying their periphery to gain insights into their interaction history. Furthermore, an in-depth analysis of the MCs' kinematics and dynamics sheds light on their internal motions, rotational properties, orbits and mass estimates. Precise distance measurements of the MCs derived from standard candles are employed to refine the calibration of the extragalactic ladder. Additionally, the exploration of the star formation history (SFH) within the MCs provides insights into their evolution, including the temporal variations in star formation rates and the influence of environmental factors. Finally, by examining analogues to the MCs, such as other dwarf galaxies and satellite systems, we can gain comparative perspectives that deepen our knowledge of the MCs' distinct characteristics and contextualise their evolutionary history. Through this overview, this chapter aims to summarise our understanding of the MCs' morphology, kinematics, and stellar populations.

Figure 1.1: The two MCs as seen with the naked Eye (Herschel 1847) and VMC (Cioni et al. 2011).

1.2 Morphology and Structure

The morphology and structure of galaxies are fundamental components of modern astrophysics, as they provide critical insights into the formation and evolution of galaxies. The structure, dimensions, and distance of the MCs were not thoroughly studied until the 1950s. Notably, de Vaucouleurs conducted significant research during this time, publishing several papers (e.g. de Vaucouleurs 1954a,b, 1955a,b,c, 1957) that provided accurate descriptions of their shape and distinctive morphology. These studies marked a significant advancement in our understanding of the MCs.

1.2.1 The Large Magellanic Cloud

The LMC is classified as the prototype of Magellanic Spiral galaxies (de Vaucouleurs & Freeman 1972) and displays a well-defined morphology, featuring a prominent stellar disc, a distinct bar, and a single dominant spiral arm. Zhao & Evans (2000) argued that the bar is located in front of the LMC, they further suggested that it could either be a tidally stretched companion originating from the proto-MC or a

dynamically young feature possibly induced by tidal interactions. This finding was later confirmed by Nikolaev et al. (2004) through their study of Cepheids in the LMC, which revealed a displacement of at least 0.5 kpc between the bar and the disc. Zaritsky (2004) also obtained similar results using model fitting techniques based on data from the Magellanic Clouds Photometric Survey (MCPS; Zaritsky et al. 1997). However, Subramaniam & Subramanian (2009), in their investigation of red clump (RC) stars, did not find evidence for a bar in front of the LMC. Haschke et al. (2012) observed that the bar of the LMC appears to be approximately 5 kpc closer to us than the disc based on their analysis of RR Lyrae stars. However, they did not find any evidence of a protruding bar in their analysis of Cepheid stars. Jacyszyn-Dobrzeniecka et al. (2017) suggested that the structure observed in their analysis of RR Lyrae stars, which could be interpreted as evidence for the bar, is likely an artefact caused by blending and crowding effects. No evidence of a closer bar was found employing classical Cepheids (Jacyszyn-Dobrzeniecka et al. 2016). Interestingly, there is no corresponding presence of a bar in the distribution of neutral or ionised gas in the LMC (e.g. Kim et al. 2003). Bekki (2009) proposed that the collision of a galactic dark halo with the LMC could account for the presence of a bar located in front of the main body of the LMC. Alternatively, recent studies suggest that a dwarf-dwarf galaxy interaction is a more favoured explanation (e.g. Besla et al. 2012; Yozin & Bekki 2014; Pardy et al. 2016) particularly in the case of the LMC, involving its interaction with the SMC. Van der Swaelmen et al. (2013) explored the connection between the bar and the inner disc of the LMC, focusing on the formation of the bar. The noticeable distinctions between the chemical composition of the bar and the disc support the idea that there was a period of enhanced star formation in the central regions of the LMC a few Gyr ago. This event is believed to have played a role in the formation of the bar, which aligns with the findings of recent studies on the star formation history of the LMC (e.g. Harris & Zaritsky 2009). Determining the precise location of the stellar dynamical centre remains a topic of debate (e.g. Niederhofer et al. 2022). The photometric centre, which corresponds to the densest point on a star count map, is found to be located approximately 0.4 kpc away from the centre of the stellar disc. Furthermore, it is situated over 1 kpc away from the dynamical centre of the neutral gas disc (van der Marel 2001). Moreover, it has been observed that the dynamical centre of the stellar component appears to vary depending on the stellar population (Wan et al. 2020). Estimating the viewing angles of the LMC involves the use of diverse tracers and methodologies. Studies have revealed a wide range of values for both the inclination angle and line–of–node position angle (PA), depending on the specific region studied, sky coverage, the choice of stellar tracer, as well as the employed methodology. Determining the orientation of the LMC can be accomplished through a geometric framework, consisting of employing distance indicators to fit a flat plane to the 3D geometry of these stellar populations (e.g. Haschke et al. 2012; Subramanian & Subramaniam 2013; Inno et al. 2016; Jacyszyn-Dobrzeniecka et al. 2016, 2017; Ripepi et al. 2017; Choi et al. 2018b). Moreover, stellar dynamics can also shed light on the geometry of the galaxy by fitting a flat-rotating disc to analyse and interpret its kinematics (e.g. van der Marel et al. 2002; Olsen et al. 2011; Gaia Collaboration et al. 2021b; Wan et al. 2020; Niederhofer et al. 2022).

The LMC disc is known to be warped, as demonstrated by a variation in the PA of the line–of–nodes as the radius increases. Olsen & Salyk (2002a) detected a warp feature in the south-west, between 2 deg and 4 deg from the centre along the maximum gradient. Choi et al. (2018b) successfully replicated the observed warp in the inner LMC disc and further uncovered a notable warp in the outer disc of the LMC, specifically in its south-western region. This warp becomes evident at a distance of approximately 7 deg from the centre of the LMC and deviates from the established LMC plane by approximately 4 kpc in the direction of the SMC. These findings strongly suggest that the warp originated from a significant interaction between the LMC and the SMC. Saroon & Subramanian (2022) identified a warp in the northeastern region of the outer LMC disc. This warp exhibits a similar deviation from the disc plane as the south-western outer warp, albeit with a smaller magnitude. These findings indicate the presence of an asymmetric stellar warp in the outer LMC disc, which is likely to take the form of a U-shaped warp. The disc is also found to be flared, with the scale height rising from 0.3 to 1.6 kpc over the range of a radius from 0.5 to 5.6 kpc (Alves & Nelson 2000). Balbinot et al. (2015) determined that the thickness of the inner regions of the LMC ranges from 1.8 to 2.8 kpc, increasing by 0.5 kpc in the outer regions. Assuming an exponential profile for the disc's height, the scale height was found to range from 1.3 to 1.9 kpc, with a 0.3 kpc increase in the outer regions. This gradual increase towards the outskirts can be interpreted as the flaring of the disc. van der Marel & Cioni (2001) suggest that this behaviour is expected if the LMC disc experiences tidal perturbations from the MW's gravitational potential. Alternatively, dynamical models proposed by Besla et al. (2012) indicate that the disc's thickening can be explained solely by LMC dynamics, where the older stellar component forms a dynamically hotter component. The observation of disc thickening only at the edge of the LMC may be due to the steep truncation of the young disc, allowing for the measurement of a thickness dominated by the older population only in the outskirts of the LMC. The initial identification of a ring-like or shell-like structure within the disc of LMC was made by de Vaucouleurs (1955a). He observed a faint outer loop and interpreted it as a one-arm spiral originating from the western end of the LMC's bar, encircling its main body. Additional evidence supporting this structure was found in the distribution of star clusters (Westerlund 1964b; Irwin 1991; Bica et al. 2008) and in a ratio map of carbon-rich to oxygen-rich asymptotic giant branch (AGB) stars (Cioni & Habing 2003). Choi et al. (2018a) detected this stellar overdensity in the RC star count map at a radius of $\sim$6 deg. They argued that the formation of the overdensity surrounding the main body of the LMC can be attributed to two possible scenarios. Firstly, the overdensity could have originated from an asymmetric one-armed spiral that wrapped around the LMC due to repeated encounters with the SMC over the past Gyr. Alternatively, the overdensity may have formed more recently as a response to a direct collision with the SMC.

1.2.2 The Small Magellanic Cloud

The SMC is considered one of the nearest metal poor dwarf irregular (dIrr) galaxies to the MW. It features an eastern extension known as the Wing (Shapley 1940). Despite

having a notable absence of dense interstellar gas and dust, the Wing has been recognised for harbouring young stars and hosting ongoing, active star formation (e.g. Westerlund 1964a; Westerlund & Glaspey 1971; Hodge 1985; Pierre et al. 1986; Cioni et al. 2000a; Zaritsky et al. 2000; Rubele et al. 2018; El Youssoufi et al. 2019). The SMC contains a shell-like overdensity located 1.9 deg from the centre of the SMC in the north-east direction. Martínez-Delgado et al. (2019) found it consisting primarily of a young population estimated to be around 150 Myr old and proposed that it originated from a relatively recent occurrence of star formation. Unlike the LMC, the SMC exhibits a less prominent bar structure with several studies (e.g. Jacyszyn-Dobrzeniecka et al. 2016) consistently revealing that the north-eastern region of the bar/disc in the SMC is situated closer to us compared to its south-western counterpart. The SMC has experienced significant influences from past interactions, resulting in a highly distorted structure in its distribution of neutral atomic Hydrogen (HI) as observed by Stanimirović et al. (2004a). This distortion is particularly evident in the younger stellar populations of the SMC. In contrast, the older populations display a more symmetric and uniform distribution (e.g. Zaritsky et al. 2000; Cioni et al. 2000a; El Youssoufi et al. 2019).

Understanding the structure of the SMC poses challenges due to the significant variation in its line–of–sight (LOS) depth, spanning a few kpc to more than 20 kpc. Despite multiple investigations, the exact extent of this depth and the 3D geometry of the SMC remain uncertain (e.g Tatton et al. 2013; Jacyszyn-Dobrzeniecka et al. 2016, 2017; Ripepi et al. 2016, 2017; Tatton et al. 2020).

Nidever et al. (2013) conducted a study utilising photometry of RC stars and identified a distinct stellar structure located closer to us, at approximately 55 kpc, compared to the main body of the SMC, which was estimated to be around 67 kpc in their analysis. They observed this structure in the eastern part of the SMC, approximately 4.2 kpc away from the SMC centre and interpreted it as a component that was likely tidally stripped during the SMC's most recent interaction with the LMC approximately 200 Myr ago. Subramanian et al. (2017) detected a foreground population located approximately 11.8 ± 2.0 kpc closer to us than the main body of the SMC. This population is believed to have originated from the tidal stripping of the SMC at approximately $2 - 2.5$ kpc in the south-east from the SMC centre (where the indications of interactions become noticeable). These findings support the hypothesis that the Magellanic Bridge, a feature connecting the two MCs that is most prominent in HI gas (Hindman et al. 1963), was formed through the stripping of material from the SMC (e.g. Carrera et al. 2017; Schmidt et al. 2020). El Youssoufi et al. (2021) found the presence of a bi-modality in the structure of the SMC can still be observed in its eastern regions up to a distance of 10 deg from the galaxy's centre. Additionally, in the northern region, a background structure is identified between 7 deg and 10 deg from the centre, which is potentially associated with the Counter Bridge, a tidal counterpart of the Magellanic Bridge predicted by Diaz & Bekki (2012). In the southern region, a foreground structure is detected between 6 deg and 8 deg from the centre, which could be linked to the Old Bridge, a tail of stars offset from the gaseous Magellanic Bridge . Omkumar et al. (2021) found that the foreground population is present only up to $\sim 5 - 6$ deg from the centre of the SMC in the eastern regions. Based on the analysis of the second *Gaia* data release

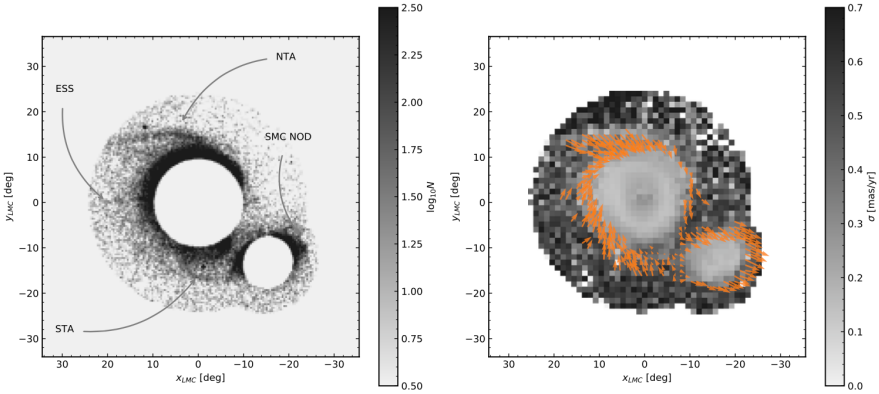

Figure 1.2: (Left) Annotated stellar density map of the outskirts regions of the LMC/SMC, with labels indicating the names of the most prominent substructures, (Right) total velocity dispersion map, accompanied by orange arrows representing the velocity vector field within the same regions. Adapted from Gaia Collaboration et al. (2021b).

(DR2; Gaia Collaboration et al. 2018a) PM measurements, it has been determined that the foreground stellar structure exhibits distinct kinematics compared to the main body population. Specifically, it displays a tangential velocity that is approximately 3 km s^{-1}) slower. This observation indicates a noticeable difference in the motion patterns between these two components. Furthermore, James et al. (2021) observed a bimodal distribution of radial velocities (RVs) among red giant branch (RGB) stars in the outer regions of the eastern and south-western areas of the SMC. The two distributions were separated by approximately $35-45$ km s^{-1}, indicating they are at similar distances to the foreground RC substructure. They estimated an approximate time of formation of this substructure as 307 ± 65 Myr ago.

1.3 Magellanic Outskirts

In-depth photometric surveys targeting the outer regions of the MCs have provided extensive evidence of numerous substructures present in their vicinity. These substructures offer valuable insights into the intricate history of interactions that the MCs have experienced with each other and with the MW. By carefully examining the stellar periphery, a wealth of information that sheds light on the complex dynamics and evolutionary paths of these extragalactic systems can be uncovered.

1.3.1 Substructures in the periphery of the Magellanic Clouds

In the LMC periphery, Muñoz et al. (2006) detected a coherent structure with a radial distance of at least $\sim$22 deg from the LMC centre. The structure lies in the foreground of the Carina dwarf spheroidal galaxy. However, it shares numerous properties such as the colour–magnitude diagram (CMD) position, metallicity, and

velocity–angular separation trend with LMC stellar populations. The structure was further investigated by Majewski et al. (2009), confirming its existence across an azimuthal range of over 180 deg and roviding evidence that the LMC might have an extended halo-like structure. Saha et al. (2010) found the oldest main sequence (MS) stars associated with the LMC out to 16 deg from its centre. Belokurov & Koposov (2016) employed Blue Horizontal Branch stars selected from the Dark Energy Survey (DES; The Dark Energy Survey Collaboration 2005) in search of the Magellanic stellar halo sub-structures and mapped out stellar streams around the MCs with some extending to distances of R$\sim$40 deg. Navarrete et al. (2019) carried out a spectroscopic study of the four new streams found by Belokurov & Koposov (2016). Only two are kinematically confirmed. The phase space distribution of Magellanic-like type stars belonging to them extend as far as 29 kpc from the centre of the LMC. Navarrete et al. (2019) provided further kinematic evidence that some of these stars might have originated from the SMC. Mackey et al. (2016) identified a stellar feature emanating from the edge of the outer LMC disc at a radius $\sim$13.5 deg. Besla et al. (2016) explored stellar substructure in the outskirts of the stellar disc of the LMC and brought to light the existence of stellar arcs and spiral arms in its northern part ($\leq$10 deg). Pieres et al. (2017) discovered a shell–like overdensity 8 deg northwest of the SMC, mainly composed of intermediate–age (6 Gyr, Z=0.001) stars and quite a similar metallicity and distance to the nearby SMC stars, the feature was probably removed from the SMC disc by tidal stripping. Deason et al. (2017) found that Mira-like stars trace the LMC as far as 20 deg from its centre. Belokurov et al. (2017) demonstrated that the distribution of RR Lyrae stars traces a bridge joining the SMC from its trailing tidal tail to the LMC known as the Old Bridge, however, the strength of this bridge is still debated (e.g. Jacyszyn-Dobrzeniecka et al. 2017; Clementini et al. 2019; Jacyszyn-Dobrzeniecka et al. 2020a). Mackey et al. (2018), El Youssoufi et al. (2019) and Deason et al. (2017) found an elongated distribution of intermediate–age stellar populations and Mira variables, respectively, pointing towards the Old Bridge. Mackey et al. (2018) found two claw–like substructures located at the south of the LMC disc, emanating at $\sim$ 10 deg from the centre of the galaxy and extending to a radius of 14 deg. Belokurov & Erkal (2019) traced the northern substructure found by Mackey et al. (2016) out to 23 deg from the centre of the LMC. El Youssoufi et al. (2021) found diffuse substructures east of the LMC disc ($\sim$16 deg) consistent with the influence of the MW deflecting the LMC disc. They detected another new substructure on the northern side of the SMC, 7 deg from its centre, lying at a similar distance to the galaxy's main body suggesting the feature belongs to the ellipsoidal structure of the galaxy. Gatto et al. (2022) reported the discovery of the North-East Structure, a diffuse tidal feature extending up to 20 deg from the LMC centre, filling the gap between the LMC disc and the features identified by Mackey et al. (2016) and El Youssoufi et al. (2021) northeast of the LMC owing to the bending of the LMC disc due to tidal forces induced by the MW. Gaia Collaboration et al. (2021b) employed the early third data release of *Gaia* (EDR3; Gaia Collaboration et al. 2021a) to trace most of the features mentioned above and confirmed the existence of the faint overdensity east of the LMC found by El Youssoufi et al. (2021), in the stellar count as well as the velocity field (see Figure 1.2).

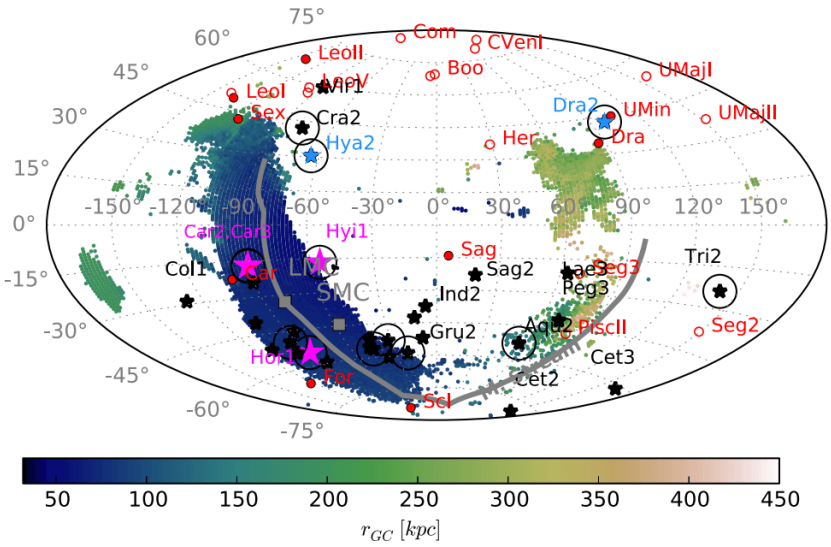

Figure 1.3: The coloured points show the location of the debris associated with the closest LMC analogue in the Aquarius simulations, chosen to match the present-day position and the measured the orbital velocity of the LMC. The debris is colour-coded by Galactocentric distance and its particles at infall outline a clear stream following the location of the Magellanic Stream represented with a thick gray line. The figure displays various satellite galaxies of the MW, represented by red circles. The "classical" dwarfs are indicated by filled-in red circles. The newly discovered dwarf galaxies are denoted by black stars, while those with successful PM measurements are marked by encircled black stars. Among them, dwarfs exhibiting kinematics consistent with an association with the LMC are highlighted in magenta (Hydrus I, Carina II, Carina III, and Horologium I). Additionally, Hydra 2 and Draco 2 are shown in light blue, requiring further analysis to determine their membership as Magellanic satellites in the future. Adapted from Kallivayalil et al. (2018).

1.3.2 Magellanic Satellites

The search for Magellanic Satellites dates back almost forty years ago. Lynden-Bell (1976) suggested that if the LMC/SMC are truly physically associated then they were part of the 'Greater Magellanic Galaxy', where observational evidence for associations between dwarf galaxies in the Local Group show that several MW classical dwarf satellites were found to reside along the Magellanic Stream (Lynden-Bell 1982). This elicited the use of high-quality, large-scale photometric surveys such as the DES (The Dark Energy Survey Collaboration 2005), the Survey of the Magellanic Stellar History (SMASH; Nidever et al. 2017), and the Panoramic Survey Telescope and Rapid Response System (Pan-STARRS1; Chambers et al. 2016, to undertake an extensive search of satellite galaxies amounting to the recent discoveries of over thirty candidate dwarf galaxies in the vicinity of the MCs (Bechtol et al. 2015; Drlica-Wagner et al. 2015; Laevens et al. 2015; Martin et al. 2015; Kim & Jerjen 2015; Kim et al. 2015; Koposov et al. 2015; Drlica-Wagner et al. 2016; Luque

et al. 2016; Homma et al. 2018; Koposov et al. 2018; Torrealba et al. 2018; Cerny et al. 2021a). Many studies have employed simulations in a bid to investigate the predicted satellite population of the MCs and found that up to a third of the satellites around the MW have entered the halo of the Galaxy with the MCs (Deason et al. 2015; Wetzel et al. 2015; Jethwa et al. 2016; Dooley et al. 2017a; Jahn et al. 2019; Nadler et al. 2020).

Prior to the *Gaia* mission, PM measurements have only been available for more massive dwarfs and have generally been limited in accuracy. The arrival of the *Gaia* DR2 (Gaia Collaboration et al. 2018a) has enabled PM measurements for these satellite galaxies allowing us to trace their 3D kinematics and reconstruct their orbital history (Fritz et al. 2018; Kallivayalil et al. 2018; Massari & Helmi 2018; Simon 2018; McConnachie & Venn 2020). Kallivayalil et al. (2018) investigated which of the satellites belonged to the LMC. They analysed the PMs of thirteen dwarf galaxy candidates with available RVs and compared their 3D kinematics to those expected for the debris of an LMC analogue in a cosmological numerical simulation. They found that four ultra-faint dwarf galaxies (Carina 2, Carina 3, Horologium 1, Hydrus 1) are likely members of the Magellanic system (see Figure 1.3). Erkal & Belokurov (2020) confirmed the LMC group infall and extended the number of satellites by identifying six dwarf galaxies as being highly likely bound to the Cloud previously (Carina 2, Carina 3, Horologium 1, Hydrus 1, Reticulum 2, Phoenix 2). They used *Gaia* DR2 PMs to integrate orbits back in time (rewind orbits) for twenty five ultra-faint dwarf satellites and the classical dwarfs in a combined MW+LMC potential. Pardy et al. (2020) revisited the possibility that the Fornax and Carina dwarf spheroidals might be associated with the MCs as their PMs place them on orbits closely aligned with the orbital plane of the MCs. Patel et al. (2020) calculated the orbital histories of thirteen ultra-faint satellites and five classical dwarf spheroidals in a combined MW+LMC+SMC potential for the first time. They identified Carina 2, Carina 3, Horologium 1, and Hydrus 1 as long-term Magellanic satellites, while Reticulum 2 and Phoenix 2 were recently captured Magellanic satellites less than 1 Gyr. *Gaia* EDR3 (Gaia Collaboration et al. 2020a) enabled more accurate PM measurements where the precision has increased by a factor of two while systematic errors decreased by a factor $\sim$2.5. Battaglia et al. (2022) determined the systemic PMs of seventy–four dwarf galaxies and dwarf galaxy candidates in the Local Group based on *Gaia* EDR3. The inclusion of the infall of a massive LMC in addition to the MW in their modelling leads to the finding of six galaxies that are highly likely to have been satellites of the LMC (Carina II, Carina III, Horologium I, Hydrus I, Phoenix II, Reticulum II), three that might have been possibly associated as satellites (Horologium II, Tucana IV, Carina) and one that has been recently captured (Grus II). These results are in general agreement with the previous orbital analysis with *Gaia* DR2 and updated EDR3 studies (Correa Magnus & Vasiliev 2022; Pace et al. 2022).

1.4 Distance

Precise distances to the MCs play a crucial role in the calibration of the extragalactic distance ladder and the determination of the Hubble constant. The LMC and SMC are two of the most extensively studied galaxies, representing ideal environments for

distance measurements as they host numerous commonly used standard candles, including Cepheids, RR Lyrae, RC stars, the tip of the RGB, and eclipsing binaries among others. The first determinations of heliocentric distances to the MCs date back to 1924 when different tracers and methodologies yielded different results. In the LMC, Wilson (1924) used O–stars and found a distance of 15 kpc. Lundmark (1924) obtained a distance of 30.7 kpc utilising O–stars and a star cluster while Shapley (1924) employed Cepheids and found a distance of 34.5 kpc. Thackeray & Wesselink (1953) followed the steps of Shapley and were the first to use variable RR Lyrae stars as distance indicators for the MCs. They found both MCs to be at the same distance of 44 kpc which they eventually revised to 55 kpc in Thackeray & Wesselink (1955). This distance value was confirmed by de Vaucouleurs (1955c). Sandage & Tammann (1968) used observations of classical Cepheids to show that the MCs have different distance moduli corresponding to a distance difference of 11 kpc.

Notable advances have been made in determining distances to the MCs with at least more than 500 distance determinations (de Grijs et al. 2014; de Grijs & Bono 2015). Discrepancies in distance measurements generally depend on the technique, the tracer, as well as the band in which the observations were carried out. Furthermore, systematic effects like extinction correction, differences in age and metallicity of various stellar populations as well as the sample size can result in further discrepancies.

The LMC has traditionally served as the primary calibrator of the extragalactic distance scale. de Grijs et al. (2014) compiled 233 separate LMC distance determinations published between 1990 and 2013. Figure 1.4 shows a comparison of distance determinations between different tracers. They suggest a canonical distance modulus of $(m - M)_0 = 18.49 \pm 0.09$ mag based on a careful, weighted combination. They recommend the use of this value for all intents and purposes for which an accuracy of only a few per cent is required in the distance scale.

Significant interest has been shown in the precise determination of the distance to the SMC, making it an important secondary calibrator of the extragalactic scale. Its low metallicity is key in quantifying the population effects of a number of distance indicators, especially in period-luminosity relations of classical Cepheids. As in de Grijs et al. (2014), de Grijs & Bono (2015) recommends the use of canonical weighted mean distance of $(m - M)_0 = 18.96 \pm 0.02$ mag based on a careful statistical analysis. However, they emphasise that systematic uncertainties possibly exceed $0.15 - 0.20$ mag.

1.5 Kinematics and Dynamics

1.5.1 Line–of–sight velocities of the Magellanic Clouds

The development of spectroscopic facilities in the last few decades enabled access to more accurate RV measurements and has led to a greater understanding of the kinematics and stellar motions of the MCs. However, our knowledge of stellar LOS kinematics in the MCs is predominantly limited to small samples belonging to different tracer populations. For the LMC, its kinematic properties have been studied

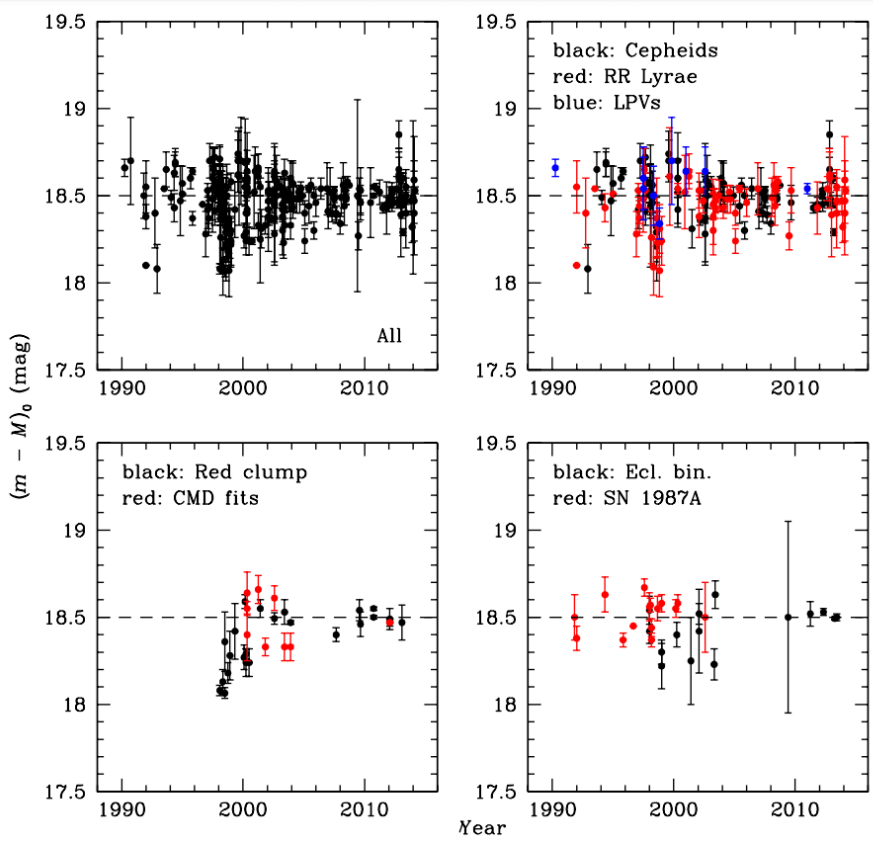

Figure 1.4: Extinction-corrected distance moduli of the LMC since 1990, plotted against the publication date (year). The horizontal dashed lines indicate the reference value for the "canonical" distance modulus, $(m - M)_0 = 18.50$ mag (Freedman et al. 2001). The top left-hand panel displays all distance determinations, regardless of the method used. The remaining panels focus on specific distance tracers, including Cepheids, RR Lyrae and long-period variables, RC stars, eclipsing binaries, and Supernova 1987A. The error bar represents the statistical uncertainties associated with each determination. Adapted from de Grijs et al. (2014).

by tracers including star clusters (e.g. Freeman et al. 1983; Schommer et al. 1992; Grocholski et al. 2006), planetary nebulae (Meatheringham et al. 1988), ionised atomic Hydrogen (HII) regions and supergiants (Feitzinger et al. 1977), red supergiants (Olsen & Massey 2007), RGB stars (Zhao et al. 2003; Cole et al. 2005), carbon stars (e.g. (van der Marel et al. 2002; Olsen & Massey 2007; Olsen et al. 2011) and RR Lyrae stars Minniti et al. (2003). These studies had rather focused on the internal rotation of the LMC. Older tracer populations such as carbon stars, RGB stars, and star clusters have been found to have higher velocity dispersions ($20 - 25$ km s^{-1}) and lower rotation velocities (due to asymmetric drift) compared to younger populations such as red supergiants (8 km s^{-1}). Additionally, within the RGB population, metal-poor stars (and older stars) have been found to have higher dispersions than metal-rich stars. Carbon stars constitute the tracer with the largest number of stars allowing for more precise measurements of the LOS velocity with a current value of 242 km s^{-1} (e.g. van der Marel et al. 2002; Olsen et al. 2011).

The kinematics of the SMC are closely related to its 3D structure and depth along the LOS. Both theoretical and observational studies indicate that old and intermediate-age stars in the SMC are distributed in a spheroidal or slightly ellipsoidal component (e.g. Zaritsky et al. 2000; Jacyszyn-Dobrzeniecka et al. 2017). This is supported by a spectroscopic study of 2000 red giant stars (Harris & Zaritsky 2006) which found that the older component of the SMC has a velocity dispersion of 27.5 km s^{-1}, comparable to those found in the outer LMC, and a maximum rotation of 17 km s^{-1}. While coherent rotation is not usually observed in the SMC's stellar kinematics, there have been some exceptions (e.g. Dobbie et al. 2014). HI observations show that the SMC has a rotation of 60 km s^{-1} and a large velocity gradient from 91 km s^{-1} in the south-west to 200 km s^{-1} in the north-east (Stanimirović et al. 2004a). Young stars (O-, B-, and A-type) are found to have a velocity gradient similar to what is seen in the HI (Evans & Howarth 2008), while the kinematics of red giants suggests a line–of–nodes that is almost orthogonal to that of the HI and the bar-like feature (Dobbie et al. 2014). Kinematic studies also suggest that the SMC is undergoing tidal disruption due to its interaction with the LMC (De Leo et al. 2020).

1.5.2 Proper motions

Our understanding of the dynamics of the Local Group and galaxies, in general, relies heavily on observations of LOS velocities. However, these measurements only provide information about one component of an object's motion, requiring various assumptions for interpretation. PMs, on the other hand, provide a more comprehensive view of the motion of an object in the plane of the sky.

Initial attempts to calculate the PMs of the MCs were made by Kroupa et al. (1994), who acquired preliminary PM measurements in relation to the Positions and PMs catalogue (Röser & Bastian 1993). Jones et al. (1994) utilised photographic plates to determine the PM of the LMC with background galaxies as a reference frame while Kroupa & Bastian (1997) utilised data from the *Hipparcos* mission (ESA 1997) to establish the PM of both the MCs.

Understanding the manner in which the MCs reached their current position is essential for deciphering how their present state aligns with the evolutionary trajectory

of a smaller galaxy interacting with a larger one. The advancement of space-based PM measurements and the usage of the *Hubble* Space Telescope (HST) has brought about a substantial advancement in refining the accuracy of PM measurements and significantly enhanced our knowledge of the MCs. Kallivayalil et al. (2006a,b) utilised HST's PM measurements to demonstrate that the MCs had not completed multiple orbits around the MW as previously believed. Their PM measurements were significantly more precise (with uncertainties ≤ 5 per cent, compared to $\geq 10-15$ per cent in earlier studies). Instead, it was proposed that they were in their initial infall into the MW (Besla et al. 2007). This new understanding, supported by (Piatek et al. 2008), has become the prevailing perspective on the evolution of the MCs. Kallivayalil et al. (2013) improved PM error estimates for 26 LMC fields by utilising a longer baseline and the new Wide Field Camera 3, allowing for more precise measurements. Consequently, van der Marel & Kallivayalil (2014) were able to directly measure the PM rotation curve of the LMC in the plane of the sky, leveraging the reduced uncertainties, while Zivick et al. (2018) revealed limited evidence of rotational motion while observing a consistent and organised radial motion away from the SMC in the outer regions of the galaxy, suggesting that the SMC is currently undergoing tidal disruption.

The VMC is currently the most comprehensive ground-based near-infrared (NIR) multi-epoch photometric survey for studying resolved stellar populations in the MCs (Cioni et al. 2011). Its CMDs enable the identification of distinct stellar populations and the differentiation between stellar sources and background galaxies. Cioni et al. (2014) conducted a preliminary study where they combined VMC observations with data from the Two Micron All Sky Survey (2MASS; Skrutskie et al. 2006) to determine the motions of stars within the LMC. In subsequent research, Cioni et al. (2016) focused on calculating PMs for various stellar populations in the outer regions of the SMC and within the Galactic globular cluster 47 Tucanae (47 Tuc). Their work shed light on the PM properties of these populations. Building upon these studies, Niederhofer et al. (2018a) presented updated results for 47 Tuc, introducing an improved technique for measuring stellar PMs. This novel approach was then applied by Niederhofer et al. (2018b) to investigate the central regions of the SMC, revealing a non-uniform velocity pattern among the stars. Additionally, Schmidt et al. (2020) conducted research on the Magellanic Bridge and determined the PMs of stars revealing a distinct flow directed from the SMC toward the LMC, while Schmidt et al. (2022) employed stellar PMs to investigate the kinematics of the outer regions of the LMC and found distinct motion in the South–East outer region which might be related to stripped SMC debris. Finally, Niederhofer et al. (2022) investigated PM measurements within the central region of the LMC. The velocity maps show that intermediate-age/old stars follow elongated orbits aligned with the bar structure's major axis. This provides direct observational evidence of x1 family orbits within the LMC, offering valuable insights into the stellar dynamics of the galaxy.

The *Gaia* mission (Gaia Collaboration et al. 2016b), launched by the European Space Agency on December 19, 2013, serves as the successor to *Hipparcos*. Its primary mission is to precisely measure the spatial distribution in three dimensions as well as the velocity distribution of stars. van der Marel & Sahlmann (2016) investigated the

dynamics of the LMC and SMC by employing the Tycho-*Gaia* Astrometric Solution (TGAS) Catalog (Lindegren et al. 2016) which combines *Gaia* Data Release 1 (*Gaia* DR1; Gaia Collaboration et al. 2016a) with the *Hipparcos* Tycho-2 Catalog (Høg et al. 2000). The obtained results exhibit comparable accuracy and are consistent, within the associated uncertainties, with previous measurements of PM using HST for both of the MCs. The LMC disc exhibits a clearly evident clockwise stellar motion while no rotation in the plane of the sky has been detected for the SMC. Gaia DR2 (Gaia Collaboration et al. 2018a) revolutionised the field of stellar kinematics within the MW and its satellite galaxies. Gaia Collaboration et al. (2018b) provided an initial analysis and revealed remarkable dynamical maps of the MCs providing a wealth of information, including the derivation of a high-quality rotation curve for the LMC based solely on tangential velocities as well as observational evidence of the influence of the LMC bar on the kinematics of the disc. Vasiliev (2018) and Wan et al. (2020) brought forth detailed analyses of internal LMC dynamics based on PMs giving insight into its rotation and mass estimate (see Sect. 1.5.4). Thanks to the accurate PM data from *Gaia* DR2 in conjecture with HST, Zivick et al. (2019) measured the tangential motions of stars in the Magellanic Bridge region revealing that they are moving away from the SMC and towards the LMC while Zivick et al. (2021) found that both rotation and tidal effects are necessary in order to explain the observed PMs and RVs in the SMC. The *Gaia* EDR3 (Gaia Collaboration et al. 2020a) has yielded several significant improvements over *Gaia* DR2. These include a remarkable reduction by a factor of 2 in the uncertainty of PM measurements, the utilisation of 33 months of data has proven instrumental in mitigating the *Gaia* scanning law effects observed in Gaia DR2, particularly when computing means and medians of parallaxes and PMs, while the new photometry has resulted in reduced systematic effects. Gaia Collaboration et al. (2021b) have generated radial and tangential velocity maps as well as global profiles for different subsamples of the LMC. Notably, this is the first instance where both planar components of ordered and random motions have been determined for various stellar evolutionary phases in a galactic disc beyond the MW. Their analysis revealed distinct variations between younger and older phases, highlighting the differences in their kinematic properties. Choi et al. (2022) explored the kinematics of RC stars of the LMC selected from the *Gaia* EDR3. Their analysis of the residual PM suggests that the most recent interaction between the LMC and SMC was a direct encounter. The estimated impact parameter for this interaction is < 10 kpc. Moreover, the timing of this encounter is estimated to have occurred within the past 250 Myr. By applying the timing constraint of approximately $140 - 160$ Myr ago, as determined in earlier investigations (e.g. Zivick et al. 2018), their findings indicate that the most recent encounter between the MCs took place with an impact parameter of ~ 5 kpc.

1.5.3 3D Kinematics of the Magellanic Clouds

Gaining knowledge of the kinematics of the MCs and obtaining complete 6D phase-space information for their stellar populations is crucial in comprehending their motion and determining their potential evolutionary history. However, there have been relatively few studies addressing this objective.

van der Marel & Kallivayalil (2014) presented a comprehensive analysis of the overall rotation of the LMC using 3D velocity measurements, which is the first of its kind. Specifically, they combined average PM measurements of stars in 22 fields obtained from HST, along with existing LOS velocity measurements of 6790 individual stars. The study provides a coherent depiction of the rotation of the LMC, leading to several novel findings. The PM data revealed that the centre of stellar dynamics aligns with the HI dynamical centre, while the amplitude of its rotation curve is consistent with previous findings from LOS velocity studies.Cullinane et al. (2020) addressed the lack of large-scale studies of 3D kinematics in the outskirts of the MCs, and presented the Magellanic Edges Survey (MagES), an ongoing spectroscopic survey targeting approximately 7000 RC and red giant stars. In conjunction with *Gaia* astrometry, it provides the full 3D kinematic information for substructures across the Magellanic periphery. One of their surveyed fields is positioned near the lower portion of an arm-like structure situated north of the LMC and is found to be kinematically perturbed from an equilibrium disc, likely through SMC/MW interactions. They extended their study of the northern arm by analysing seven additional fields in Cullinane et al. (2022a) and found that the arm structure shares similar characteristics in terms of its geometry and metallicity with the outer disc of the LMC, suggesting that it is composed of perturbed material from the LMC disc. Cullinane et al. (2022b) observed that the northeastern disc of the LMC, even at large galactocentric radii $\leq$10 deg, appears relatively undisturbed, exhibiting kinematics consistent with an inclined disc at approximately 36.5 deg and a line–of–nodes PA of around 145 deg east of north. On the other hand, fields in the southern and western parts of the disc at similar radii show significant deviations from equilibrium, characterised by non-zero radial and vertical velocities. Subsequently, Cullinane et al. (2023) studied the extreme southern outskirts of the SMC and found evidence for two stellar populations in the field, one has properties consistent with the outskirts of the main SMC body, and the other is significantly perturbed, most likely comprised of debris from the inner SMC that has been recently tidally stripped by interactions with the LMC. Cheng et al. (2022) investigated the kinematics of stellar substructures located in the vicinity of LMC, in particular its southern periphery. They reported the 3D kinematical measurements of 88 stars employing *Gaia* EDR3 (Gaia Collaboration et al. 2021a) and the Apache Point Observatory Galactic Evolution Experiment (APOGEE; Majewski et al. 2017). Their analysis revealed that a significant portion of the stars exhibits exceptionally high space velocities that are distinguishable from and do not merely extend the disc of the LMC. They explore plausible explanations by comparing them with hydrodynamical simulations of an LMC–SMC analogue pair of galaxies. They concluded that their sample can be accounted for as a combination of an LMC and SMC tidal debris, however, they could not dismiss other scenarios. In a recent study, Navarrete et al. (2023) analysed the 6D phase-space information of 27 Mira candidates in the outskirts of the LMC. The results suggest that the motions of stars in the LMC periphery have been greatly disturbed by multiple close interactions with the SMC (at $\sim$1.18 Gyr, $\sim$950 Myr, and $\sim$350 Myr) as supported by their numerical simulations.

1.5.4 Mass estimates of the Magellanic Clouds

Although the MCs are the brightest satellites of the MW, determining their total masses is a challenging task that remains largely unconstrained. Attempts to accurately determine the mass of the LMC have been made through the examination of its rotation curves. Schommer et al. (1992) endeavoured to determine the mass of the LMC directly through the dynamics of its star clusters and found an estimate of $1.5 - 2 \times 10^{10}\,\mathrm{M}_{\odot}$ out to 8 deg radius. van der Marel & Kallivayalil (2014) used HST PMs of 22 stars with known LOS velocities to determine the rotation curve of the LMC. The peak of the derived rotation curve was found to be 91.7 ± 18.8 km s^{-1} at a distance of 8.7 kpc, implying a total enclosed dynamical mass of $1.7 \times 10^{10}\,\mathrm{M}_{\odot}$ within 8.7 kpc. Vasiliev (2018) employed *Gaia* DR2 PMs and RVs and found a similar circular velocity reaching $\sim$90 km s^{-1} at 5 kpc. Wan et al. (2020) investigated the internal dynamics of the LMC using the deep, multi-epoch, multi-colour photometry of SkyMapper (Wolf et al. 2018) coupled with *Gaia* DR2. They determined the LMC's circular velocity to be 123.6 ± 1.9 km s^{-1} at 7 kpc, which is moderately higher than previous values, implying a mass of $(2.5 \pm 0.1) \times 10^{10}\,\mathrm{M}_{\odot}$. The total mass of the LMC within 30 kpc was estimated to be $(1.06 \pm 0.32) \times 10^{10}\,\mathrm{M}_{\odot}$ based on the assumption of a constant circular velocity to the tidal radius. Cullinane et al. (2020) employed MagES, a spectroscopic survey charting the kinematics of RC and red giant branch stars in the complex outer regions of the MCs, in conjunction with *Gaia* DR2. They found that the 3D kinematics of an undisturbed field in the outskirts of the LMC show a circular velocity of 87.7 ± 8.0 km s^{-1} at a distance of approximately 10.5 kpc from the centre of the LMC. This leads to an estimated enclosed mass for the LMC of $(1.8 \pm 0.3) \times 10^{10}\,\mathrm{M}_{\odot}$ (see Figure 1.5). Estimates of the LMC mass based on the modelling of its rotation curve are relatively modest ($\sim 2 \times 10^{10}\,\mathrm{M}_{\odot}$ within 10 kpc) when compared to supplementary indirect methods. Section 1.3 highlights the wealth of debris and substructures found in the outskirts of the LMC beyond 10 kpc emphasising that the mass of the LMC is most likely underestimated due to the absence of dynamical markers at extremely large distances, hence hindering the ability to determine the total mass of the LMC through kinematic methods until substantial RVs in these regions are available.

The presence of the SMC and additional dwarf galaxies associated with the LMC (see Section 1.3) also implies that the LMC must have been relatively massive at infall. Kallivayalil et al. (2013) demonstrated that in order for the SMC to be bound to the LMC for periods as large as 2 Gyr (the estimated age of the Magellanic stream), an LMC with a mass greater than $1 \times 10^{11}\,\mathrm{M}_{\odot}$ is required. Shao et al. (2018) investigated the properties of LMC-mass dwarf galaxies in the EAGLE cosmological hydrodynamics simulations of galaxy formation and predicted that LMC-like systems that have an SMC-mass satellite possess a halo mass $\sim 3.4^{+1.8}_{-1.2} \times 10^{11}\,\mathrm{M}_{\odot}$. In order to determine which satellites belong to the LMC, Erkal & Belokurov (2020) rewound their present-day position. This technique constrains the LMC mass by determining which lower limit is needed to bind each of the satellites. They placed a lower bound on the LMC's mass at $1.24 \times 10^{11}\,\mathrm{M}_{\odot}$.

Additionally, abundance matching determines the relationship between the stellar masses of galaxies and the masses of the dark matter halos in which they reside

over the entire cosmic history, and can be applied to estimate the mass of the LMC. A peak halo mass of $\sim 2 \times 10^9\,\mathrm{M}_\odot$ is found (e.g. Boylan-Kolchin et al. 2010; Moster et al. 2013; Behroozi et al. 2013; Dooley et al. 2017a,b) based on the stellar mass of the LMC ($2.7 \times 10^9\,\mathrm{M}_\odot$; van der Marel et al. 2002).

The Timing Argument can be used to estimate the masses of galaxies in the Local Group. This method was put forward by Kahn & Woltjer (1959) and refined by Lynden-Bell (1981) and Partridge et al. (2013). It compares the galaxies' currently observed positions and velocities to the solution of their equations of motion in an expanding ΛCDM Universe. Peñarrubia et al. (2016) accounted for the LMC in the timing argument between the MW and M31, as well as in the nearby Hubble flow, giving an LMC mass of $2.5 \times 10^{11}\,\mathrm{M}_\odot$.

Finally, the LMC's gravitational influence has disrupted multiple stellar streams in the MW, enabling an accurate determination of its mass: $\sim (1.3 - 1.9) \times 10^{11}\,\mathrm{M}_\odot$ (Erkal et al. 2019; Koposov et al. 2019; Shipp et al. 2019; Vasiliev et al. 2021).

Investigations of the structure and motion of the hydrogen gas in the SMC have yielded valuable insights into the distribution of mass in the galaxy. Stanimirović et al. (2004b) derived the rotation curve and mass model for the central 4.5×4.5 deg of the SMC and found that the rotation curve rapidly rises to about 60 km s^{-1} up to the turnover radius of 3 kpc, with a total dynamical mass of $2.4 \times 10^9\,\mathrm{M}_\odot$. They analysed the rotation curve using a two-part mass model that included both gas and star discs and determined that there is no requirement for a dark matter halo to explain the observed velocities. However, their model implies a high stellar mass of $1.8 \times 10^9\,\mathrm{M}_\odot$ within a radius of 3.5 kpc. Using the velocity dispersion of old stellar populations, Harris & Zaritsky (2006) constrained the dynamical mass of the SMC to range between $2.7 - 5.1 \times 10^9\,\mathrm{M}_\odot$ within 3 kpc. These estimates are greater than those derived from the hydrogen gas kinematics. They suggest that the simplified assumptions taken during the virial analysis could easily account for the differences. Bekki & Stanimirović (2009) re-examined the rotation curve from Stanimirović et al. (2004a) to determine the potential contribution of a dark matter halo within the central 3 kpc. The rotation curve was modelled using a combination of a thick disc of stars and gas and a dark matter halo with either a Navarro–Frenk–White (Navarro et al. 1997) or a Burkert (Burkert 1995) density profile. The stellar contribution to the total rotation curve was derived using V-band images. They suggest that the dark matter halo of the SMC probably had an initial total mass and core radius of at least $6.5 \times 10^9\,\mathrm{M}_\odot$ and 3.2 kpc, respectively. Di Teodoro et al. (2019) conducted a detailed analysis of the rotation curve of the SMC using new high-resolution HI data from the Australian Square Kilometre Array Pathfinder (ASKAP; Hotan et al. 2021). They employed various dynamical models to account for the 3D configuration of mass components, including gas, stars, and dark matter. They discovered that, when considering reasonable mass–to–light ratios, a significant dark matter halo with a mass of approximately $1 - 1.5 \times 10^9\,\mathrm{M}_\odot$ solar masses within a radius of 4 kpc is necessary to accurately replicate the observed rotation curve.

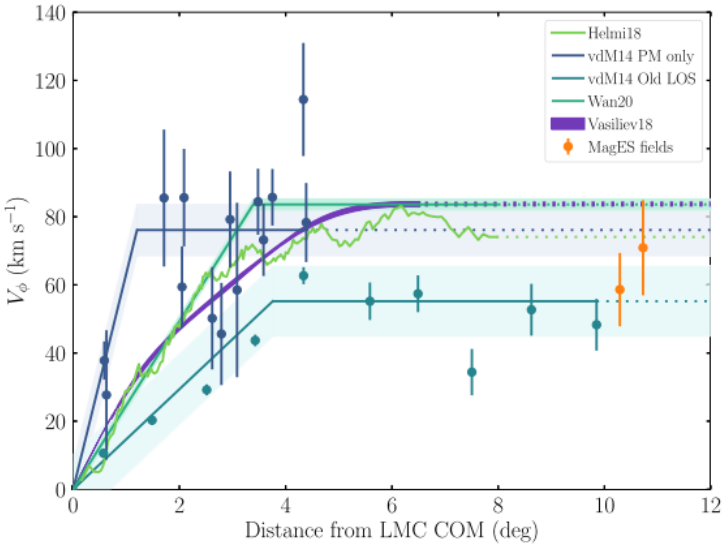

Figure 1.5: Azimuthal velocities in the disc of the LMC as a function of distance from the LMC centre of mass. Measurements for the two MagES fields in the northern LMC disc are represented by orange points, with error bars accounting for uncertainties in all parameters. Dark blue points correspond to values derived by van der Marel & Kallivayalil (2014) using HST PM measurements for a mixed population of young and old stars. Light blue/aqua points also represent van der Marel & Kallivayalil (2014) values but are derived from LOS observations specifically for the "old" stellar population. The error bars for these points only consider uncertainties in the observed motions and do not include uncertainties in disc geometry or centre of mass location, resulting in smaller error bars compared to the MagES fields. The solid lines on the figure represent the best-fitting rotation models obtained from Vasiliev (2018), Wan et al. (2020), Gaia Collaboration et al. (2018b), and van der Marel et al. (2002). The shaded regions surrounding the lines indicate the 1σ uncertainty propagated from all parameters, making them comparable to the error bars of the MagES fields. The dashed continuations of the solid lines show where these models have been extrapolated outward to facilitate comparison with the two MagES points. Adapted from Cullinane et al. (2020).

1.5.5 Orbits of the Magellanic Clouds

The trajectory of the MCs has been a topic of interest for decades, with many studies investigating its orbit and its relation to the formation history of the MW (e.g. Avner & King 1967; Hunter & Toomre 1969; Lin & Lynden-Bell 1982). Determining the orbit of the MCs is highly dependent on factors such as the masses of both the MW and MCs as well as the current position and velocity of the MCs. Any deviations in these factors can lead to different orbital trajectories. Earlier research (Gardiner & Noguchi 1996; Diaz & Bekki 2012) proposed that the MCs had orbited the MW for a sufficient duration to complete more than one revolution around it. Additionally, it was postulated that a recent encounter occurred between the LMC and the SMC, substantiated by the age of stellar populations observed within the

Magellanic Bridge area (e.g. Irwin et al. 1990). This understanding successfully replicated the primary morphological features, including the Magellanic Bridge and the Magellanic Stream. However, considerable uncertainties persisted concerning the observational constraints involved in these conclusions.

The recent measurements of PMs Kallivayalil et al. (2013) indicate that first-infall orbits are favoured if one imposes the requirement that the LMC and SMC must have been a bound pair for at least several Gyr.

Moreover, these measurements suggest a close encounter between the LMC and SMC at approximately 200 Myr and 2 Gyr. This revised model, supported by Besla et al. (2007), explains the observed morphology of the Magellanic Stream, including its leading and trailing parts, without requiring multiple passages around the MW. Besla et al. (2010) and Besla et al. (2012) used N-body hydrodynamical simulations to demonstrate how an SMC-LMC close encounter can reproduce the Magellanic Stream's morphology, addressing concerns raised by new velocity measurements. The strengths of the Besla et al. (2012) model are its capacity to accurately estimate the extent of the Magellanic Stream, predict the six-dimensional space-velocity distribution of the MCs, and identify the existence of at least one branch in the Leading Arm. However, the Besla et al. (2012) tidal model has notable limitations. Firstly, it only reproduces a small fraction (a few per cent) of the gas in the Magellanic Stream, failing to account for the prominent ionised gas component (Fox et al. 2014). Secondly, the Stream consists of two filaments, and both kinematic and chemical analyses indicate the presence of gas from both the LMC and the SMC (e.g. Nidever et al. 2008; Fox et al. 2013; Richter et al. 2013), which is not accounted for in the tidal model. Lastly, no stars have been observed in the Magellanic Stream so far, which is another limitation of the model. These limitations pose significant challenges to the viability of the tidal model in explaining the properties of the Magellanic Stream that proposes the SMC as the exclusive source, suggesting that the Magellanic Stream has a dual origin.

Hammer et al. (2015) considers the possibility of the Trailing Arm of the Magellanic Stream having a pure ram pressure origin due to the Galactic Corona. Their work suggests that other dwarf galaxies may have preceded the LMC and SMC, resulting in the formation of the Leading Arm. The "ram-pressure plus collision" model, successfully reproduces the distinctive dual filament structure observed in the Magellanic Stream. This model accounts for the presence of two ram-pressure tails attached to each of the MCs, accurately capturing the overall shape, gas mass, and RV of the Magellanic Stream. Additionally, it accounts for the velocity field of the LMC and the extensive 30 kpc long structure seen in the LOS of young stars in the SMC, both of which are attributed to the relatively recent collision between the gas-rich MCs. In fact, the model even places constraints on the mass of the LMC, indicating that it must be smaller than $2 \times 10^{10}\,\mathrm{M}_{\odot}$ in order to account for the expelled gas that contributes to the mass of the Magellanic Stream. This finding appears to contradict LMC mass estimates based on the interaction between the MW and the LMC. The study conducted by Salem et al. (2015) on the interaction between the LMC and the hot halo of the MW has indicated that ram pressure stripping is likely responsible for

only a small fraction of the mass in the Magellanic Stream. If the MW's hot halo is denser than a certain threshold, the gas in the Magellanic Stream would dissolve rapidly, and the survival time of the stream would be less than 500 Myr (Murali 2000). In such a scenario, the filament from the SMC in their model, which is older than 2 Gyr, would completely evaporate. Moreover, the presence of ram pressure can potentially explain the observed difference in gas density between the Leading Arm and the Trailing Stream, as the Leading Arm is exposed to a stronger ram pressure effect. These findings highlight the limitations of the ram pressure model in fully explaining the mass budget and density distribution within the Magellanic Stream.

Recent findings related to the Magellanic Corona and the inclusion of the MW's hot circumgalactic medium highlight the significant role of hydrodynamical effects in the orbital history of the MCs. When considering the presence of gaseous halos, the mass budget discrepancy of the Stream can be solved (Lucchini et al. 2020, 2021). It is suggested that the MCs may have experienced fewer recent interactions than previously believed in order to remain separated at present. Additionally, the existence of a Magellanic Group, which consists of loosely bound members, implies that the two largest members would have had only a few direct interactions in the past 5 to 7 Gyr (D'Onghia & Lake 2008; Nichols & Bland-Hawthorn 2011).

1.6 Star Formation History

A comprehensive understanding of how galaxies formed their stars remains one of the major goals of galaxy theory. Galaxy interactions are known to induce star formation events, and therefore, detailed, quantitative star formation histories aim not only to provide an empirical premise to galaxy formation and evolution but also to put constraints on their interaction history. The MCs are gas-rich and have active, vigorous, ongoing star formation where multiple bursts have been detected employing star clusters as well as field stars. Several photometric works have recovered the star formation rate by means of CMD analyses. Global studies deriving the SFH using wide-field photometric surveys are vital to understanding the MCs' formation history, however, they can still be complemented by works targeting smaller fields in order to obtain CMDs a few magnitudes fainter than the oldest MS turnoff. This is essential for properly characterising the intermediate-age and old population as well as breaking the age–metallicity degeneracy.

In the SMC, Harris & Zaritsky (2004a) provided the first comprehensive study of the SFH of the galaxy using MCPS, they find that the SMC has been through three major star formation history epochs: an early epoch where the galaxy has formed a significant fraction of its stars (50 per cent) 8.4 Gyr ago, followed by a long quiescent period during which it formed relatively few stars up until 3 Gyr ago, where evidence of a continuous star formation until the present epoch has been detected with star formation peaks at $2 - 3$ Gyr, 400 and 60 Myr ago. Additionally, they detect the presence of a large ring–like structure visible at the 2.5 Gyr burst. Noël & Gallart (2007) found that the SMC has an older stellar population than its single old globular

cluster. No strong population gradients are present from ~ 2.7 deg outward in the outer SMC disc. The SFH seems much more uniform while the surface brightness decreases exponentially. Noël et al. (2009) also studied the SFH across 12 fields in the SMC using the 100-inch telescope at Las Campanas Observatory. Unlike Harris & Zaritsky (2004a), which found no quiescent period at intermediate ages. The older population is distributed evenly at all radii and azimuths. Cignoni et al. (2013) studied the SFH of the SMC with HST in six fields located at projected distances of $0.5-2$ deg from the centre, probing the main body and the wing of the galaxy. They confirmed a slow star formation pace until ~ 5 Gyr ago and a strong peak at a very recent epoch (<500 Myr ago). concentrated in the bar and the area of the SMC wing. Weisz et al. (2013) also used HST to explore the SFH of the MCs and found that both galaxies exhibit a sharp increase in the SFH at 3.5 Gyr, driving gas into the centre of the SMC as indicated by the spatial variation of the SFH. Additionally, they found that the SMC has two notable peaks at ~ 4.5 and ~ 9 Gyr ago. Rubele et al. (2015, 2018) analysed the SFH of the SMC using VMC, covering a contiguous area of $\sim$24 deg^2 (30% larger than Harris & Zaritsky (2004a), they traced the formation of the wing at ages younger than 0.2 Gyr and found that the young star formation in the SMC Bar peaks at ages of about 40 Myr. Furthermore, they clearly detected periods of enhanced star formation at ages of 1.5 and 5 Gyr ago. They found that the SMC formed half of its stellar mass prior to an age of 6.3 Gyr (compared to 8.4 Gyr by Harris & Zaritsky 2004a) while also asserting that the star formation rate was moderately low at ages older than 5 Gyr.

Similar to the SMC, Harris & Zaritsky (2009) presented the first global view of the SFH of the LMC using MCPS. They found a quiescent epoch from approximately 12 to 5 Gyr ago, with enhancement peaks in the recent star formation rate at roughly 2 Gyr, 500 Myr, 100 Myr, and 12 Myr, further confirming the turbulent common history of the LMC and SMC, with almost identical peaks at $\sim$2 Gyr and ~ 500 Myr. Rubele et al. (2012) employed the VMC survey to derive the SFH of four tiles covering less than 5.6 deg^2 finding that most of the SFH occurred at ages >3 Gyr. Mazzi et al. (2021) expanded upon this study and probed the resolved SFH of the LMC, covering an area of 96 deg^2 across the main body of the galaxy, 50 per cent larger than the one obtained by Harris & Zaritsky (2009). They found a patchy SFH across all ages younger than 63 Myr and a concentration of star formation in the three spiral arms and bar up until 1.6 Gyr, older populations, however, have a wider and smoother distribution. The LMC is host to several thousands of star clusters (Bica et al. 2008) with ages ranging from a few Myr to a Hubble time. The star cluster formation in the LMC is known to have occurred through two major epochs (e.g. Bertelli et al. 1992). The first star–formation episode led to the formation of globular clusters and occurred >10 Gyr ago, followed by a long quiescent period of several Gyr known as "the age gap", until the second major formation epoch occurred $2-4$ Gyr ago. A few star clusters are found to be as old as the oldest Galactic clusters (Suntzeff et al. 1992; Olsen et al. 1998; Dutra et al. 1999). The older clusters are found to be significantly more metal-poor ($-2.2 \leq$ [Fe/H] ≤ -1.2) compared to the younger population of clusters ([Fe/H] ≥ -0.7). The so-called "age gap" in the age distribution of LMC clusters is highlighted by the existence of two intermediate–age clusters in the LMC,

ESO 121-SC03 and KMHK 1592 (Mateo et al. 1986; Olszewski et al. 1991; Piatti 2022; Gatto et al. 2022), as well as 16 cluster candidates recently discovered by Gatto et al. (2020) which have ages within the cluster–age gap.

Star formation studies further support the idea that the MCs evolved in isolation for most of their histories. Ruiz-Lara et al. (2020) and Massana et al. (2022) studied the SFH of the SMC and LMC, respectively, using optical data from SMASH. Figure 1.6 indicates the SFH of the MCs, further confirming that the galaxies have been interacting and influencing each other since at least 3.5 Gyr ago with periods of enhancements in their star formation histories at ∼3, ∼2, ∼1.1, ∼0.45 Gyr ago and at present.

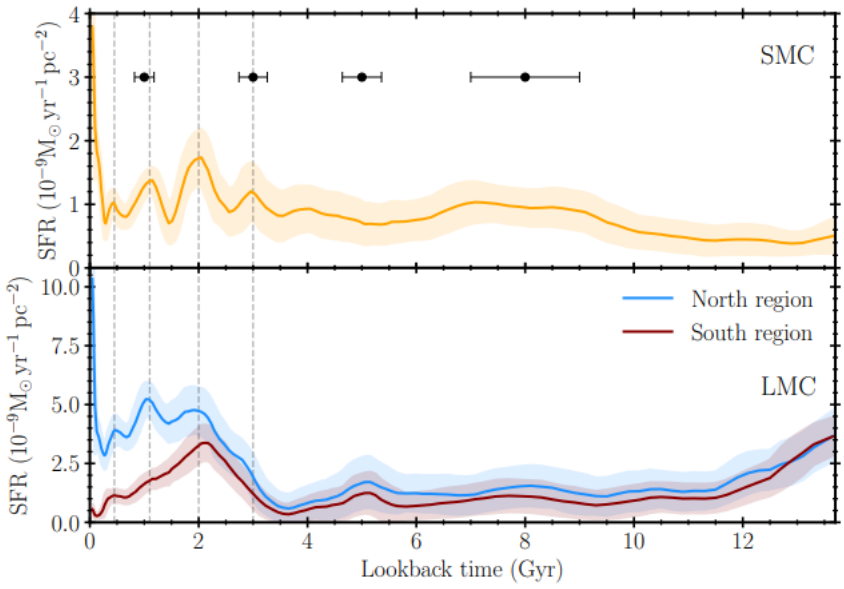

Figure 1.6: Comparison of the global star formation rates for the SMC (top; Massana et al. 2022) and the LMC (bottom; Ruiz-Lara et al. 2020). Vertical dashed lines highlight the peaks at 0.45, 1.1, 2, and 3 Gyr ago. In the top panel, horizontal bars indicate the width of the enhancement in the SFH, while the shaded regions represent the uncertainties. Adapted from Massana et al. (2022).

1.7 Magellanic Analogues

The MCs are key to understanding the dynamics and evolution of Local Group galaxies. As satellites of the MW, a growing number of studies have been investigating the influence of the MCs on our own Galaxy. It has been found that the LMC has brought its own satellites with it, some of which are now stripped and have become MW

satellites (Battaglia et al. 2022), is deflecting MW stars, satellites, and stellar streams that pass in its vicinity, in some instances dramatically changing their orbits (e.g. Boubert et al. 2020), is inducing a large-scale gravitational wake in the galactic stellar and dark matter haloes (Garavito-Camargo et al. 2019), is disturbing the Galactic disc (Laporte et al. 2018), and even perturbing the barycentre of the MW (Gómez et al. 2015).

Furthermore, the presence of the MCs as satellites of the MW is rather atypical as the occurrence of a MW-MC system is uncommon in the local universe. Observationally, Liu et al. (2011) used the Sloan Digital Sky Survey (SDSS; York et al. 2000) to obtain the frequency of LMC and SMC analogues in galaxies like the MW. Isolated MW-like galaxies were identified spectroscopically, while potential satellites were found by searching SDSS's photometric data for galaxies between two and four magnitudes fainter than these hosts. 81 per cent of galaxies like the MW were found to have no such satellites within a radius of 150 kpc, 11 per cent have one, and only 3.5 per cent of hosts have two. Empirically, observational estimates suggest that up to $\sim$40 per cent of L* galaxies [1] may host a satellite as luminous as the LMC within ~ 250 kpc and up to 10 per cent. Noteworthy examples of Magellanic Spiral Irregular galaxies include NGC 4027 (Phookun et al. 1992) and NGC 3664 (Wilcots & Prescott 2004); both possess a low mass companion to which each is connected by a bridge of gas. Figure 1.7 shows an example of an LMC-SMC-MW analogue. Paudel & Sengupta (2017) conducted a comprehensive examination of the characteristics and structures of the interacting pair UGC 4703 and UGC 4703b interconnected by a thin bridge. The two galaxies are situated near a spiral galaxy similar to our MW, known as NGC 2718.

Within the context of a ΛCDM paradigm, high-resolution N-body simulations over cosmological volumes, such as the Millennium II and Bolshoi simulations have been used to obtain the incidence of MW-MC pairs. Boylan-Kolchin et al. (2010) considered directly how common MW/LMC and MW/LMC/SMC systems showing they are potentially quite uncommon ($3-25$ per cent), depending on the assumed MW mass. Similar conclusions have been reached by (e.g. Busha et al. 2011; Rodríguez-Puebla et al. 2013; González et al. 2013).

Understanding the abundance and distribution of satellites around the MW is crucial to constraining models of galaxy formation and helps place the Local Group itself in a clearer cosmological context. In contrast, considering the large number of barred spiral galaxies with moderately tight spiral arms in the Universe (e.g. Zaritsky et al. 2013), the rarity of LMC-SMC-MW systems in both observations and simulations suggests that features of Magellanic Spirals prevail without the presence of a nearby MW-like galaxy.

[1] Galaxies within a population whose luminosity closely approximates the characteristic luminosity (L*) at which the luminosity function, typically described by the Schechter function, exhibits a peak in number density

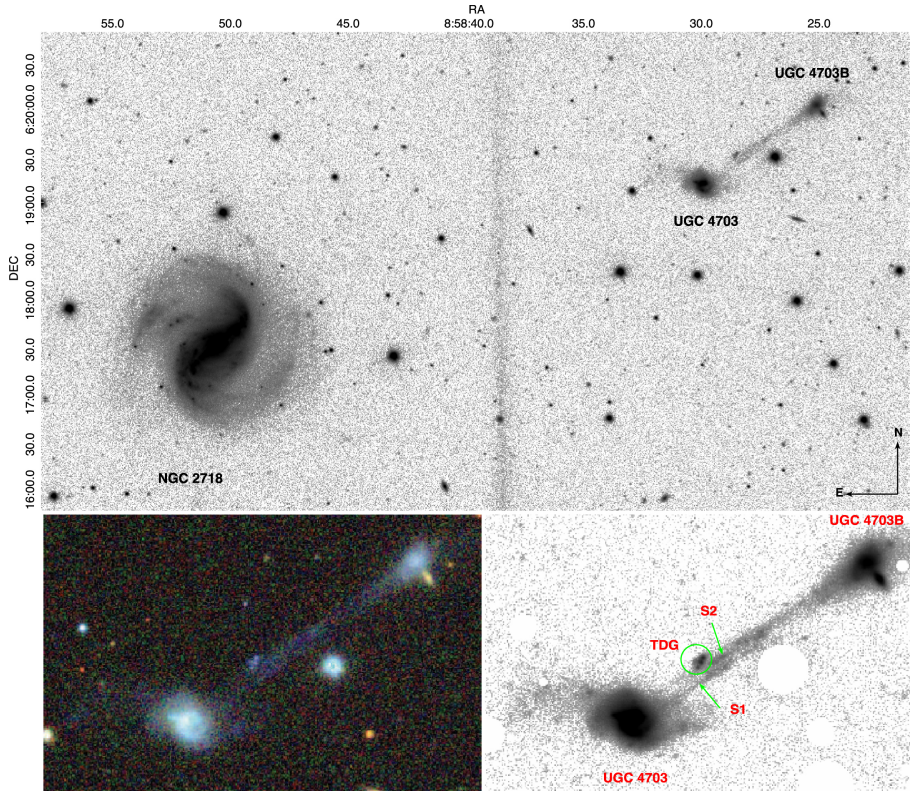

Figure 1.7: In the top panel, the SDSS r-band image of an area around NGC 2718 and its satellites (UGC 4703 and 47034B) with a field of view of 9' × 5' is shown. In the bottom panels, a zoom-in view of the interacting dwarf galaxies. The bottom left panel is a colour image cutout directly obtained from the SDSS sky-server. The bottom right panel, shows co-added g-, r-, and i-band images. Some interesting features are highlighted, such as a potential candidate of a Tidal Dwarf Galaxy (TDG), and the bifurcated stellar bridge composed of two streams (S1 and S2). Adapted from Paudel & Sengupta (2017).

1.8 Thesis structure

The remaining chapters of this thesis detail the work that was undertaken during my Ph.D., with a research focus on employing resolved stellar populations to investigate the morphology and kinematics of the MCs. They are structured as follows:

- **Chapter 2**: I investigate the morphology of the main bodies of the MCs through a comprehensive age tomography using state-of-the-art near-infrared photometry and stellar population models with a comprehensive age tomography.
- **Chapter 3**: I explore the outskirts of the MCs in search of substructures in relation to their interaction history.

- **Chapter 4**: I examine the kinematics of some of the substructures found in Chapter 2.

2 Morphology of Stellar Populations in the Magellanic Clouds

2.1 Introduction

Galaxies have diverse shapes, components, and structural properties. Their morphology is considered a fossil record of their history and carries fundamental information about galaxy formation and evolution. Located at approximately 50 kpc (e.g. de Grijs et al. 2014) and 60 kpc (e.g. de Grijs & Bono 2015), the LMC and SMC represent the nearest interacting pair of dIrr galaxies. dIrr galaxies are characterised by a gas-rich environment, low metallicity levels and an unstructured shape. The LMC is also known as a prototype of barred Magellanic spirals due to its asymmetric stellar bar with no bulge, a large star-forming region at one end of the bar, one prominent spiral arm as well as other spiral features. Its total mass is estimated at 1.7×10^{10} $M_{\odot}$ from the rotational velocities of mostly carbon stars measured to radii of 8.7 kpc (van der Marel & Kallivayalil 2014) while the total mass of the SMC is estimated at 2.4×10^{9} $M_{\odot}$ from the HI rotation curve (Stanimirović et al. 2004b). The close encounters between the two MCs and between the MCs and the MW have been corroborated by PM studies (e.g. Kallivayalil et al. 2006b, 2013; Cioni et al. 2014; van der Marel & Kallivayalil 2014; Cioni et al. 2016), SFH studies (e.g. Harris & Zaritsky 2004a; Noël & Gallart 2007; Harris & Zaritsky 2009; Rubele et al. 2012; Cignoni et al. 2013; Rubele et al. 2015; Hagen et al. 2017) and dynamical modelling (e.g. Besla et al. 2007; Diaz & Bekki 2012; Salem et al. 2015). These interactions provided the necessary forces (tidal and/or ram-pressure stripping) for the creation of the Magellanic Stream and Bridge. Due to their proximity to our own Galaxy, assuring the resolution of stellar populations into individual stars, and ongoing star formation, the MCs have

been targets of intensive research for many years, making them rather unparalleled laboratories for studying stellar evolution and galaxy interactions.

2.1.1 LMC morphology

The LMC is an almost face-on, gas-rich galaxy characterised by an inclined disc and an offset bar of which the origin is not well understood (Zhao & Evans 2000; Zaritsky 2004). The morphologies of the LMC traced by different stellar populations show different properties (e.g. de Vaucouleurs & Freeman 1972; Cioni et al. 2000a; Nikolaev & Weinberg 2000; Belcheva et al. 2011; Moretti et al. 2014). While young stars exhibit a rather irregular structure characterised by spiral arms and tidal features, older stars dominating the mass of the LMC tend to be more smoothly and regularly distributed. The bar appears to be a luminous and prominent entity in both optical and NIR images, while it is not present in the distribution of HI gas (Stanimirović et al. 2004b). The bar is also asymmetric and appears to be elliptical in the south-east while it is flat in the north-west (Zaritsky 2004). Using Cepheids, Nikolaev et al. (2004) found that the bar lies at a different distance than the disc, concluding that it is closer to us by $\sim$0.5 kpc, while in intermediate-age populations like RC stars the bar was found to be co-planar with the disc (Subramanian & Subramaniam 2009). The bar is also known for its centre being offset with respect to the disc. Recent numerical simulations of dwarf–dwarf galaxy interactions (Pardy et al. 2016) with a 1:10 mass ratio show that during the encounter of the LMC and SMC morphological structures shift in relation to the LMC's dynamical centre. The stellar disc of the LMC becomes displaced under the effect of the gravitational potential, and this can persist for up to 2 Gyr, while the bar is never actually shifted, suggesting that the dynamical centre of the LMC is always coincident with the bar centre (de Vaucouleurs & Freeman 1972) rather than with the HI centre (Stanimirović et al. 2004b) as previously assumed. Using Cepheids, Jacyszyn-Dobrzeniecka et al. (2016) redefined the classical LMC bar by including a western density, with the bar spanning the whole width of the galaxy, and found no offset from the plane of the LMC making the bar an integral part of the disc. After the redefinition of the bar, the dynamical centre is located at the bar centre.

The LMC is known for its non-planar structure (van der Marel et al. 2002; Nikolaev et al. 2004). Olsen & Salyk (2002b) found possible warps and twists in the south-east of the LMC extending up to 2.5 kpc. Choi et al. (2018b) detected a significant warp in the south-west of the disc extending up to 4 kpc in the direction of the SMC. The east and west sides of the bar are closer to us compared with its central region, indicating that the bar of the LMC is also warped (Subramaniam 2003). Extra-planar features in front as well as behind the plane were also identified in both optical (Subramanian & Subramaniam 2010) and NIR (Subramanian & Subramaniam 2013) studies of RC stars. The LMC disc is thick (van der Marel et al. 2002; Subramanian & Subramaniam 2009), flared (Alves & Nelson 2000) and intrinsically elongated (van der Marel & Cioni 2001). At large radii, the LMC disc appears strongly elliptical (van der Marel 2001). Its inner and outer parts are situated at different inclination angles making its eastern part closer to us. The orientation angles of the disc have been measured using different tracers and methods such as the RC (Olsen & Salyk 2002b; Subramanian & Subramaniam 2010, 2013), Cepheids (Nikolaev et al. 2004; Haschke et al. 2012;

Jacyszyn-Dobrzeniecka et al. 2016; Inno et al. 2016), RR Lyrae stars (Haschke et al. 2012; Jacyszyn-Dobrzeniecka et al. 2017), carbon to oxygen rich AGB stars (van der Marel & Cioni 2001; Cioni et al. 2001), outer isophotes (de Vaucouleurs & Freeman 1972), as well as HI gas. Using these different tracers, the inclination angle is found to be between 22 ± 6 deg and 37.4 ± 2.3 deg while the PA of the line–of–nodes is between 122.5 ± 8.3 deg and 170 ± 5 deg.

The prominent work of de Vaucouleurs & Freeman (1972) revealed a distinct multi-arm spiral structure in the LMC. Besla et al. (2016) followed up on this work and explored the stellar substructures in the outskirts of the LMC. They found that stellar arcs and spiral arms exist in the northern periphery with no southern counterpart. They examined numerical simulations of the outskirts of the LMC disc and found that these features can be reproduced in isolation of the MW potential. This entails that the disturbed nature of the MCs is largely due to the LMC-SMC interactions rather than to the effect of the MW. This is supported by high-precision PM measurements (e.g. Kallivayalil et al. 2013) implying that the MCs are most likely on their first passage by the MW. Choi et al. (2018a) detected a ring-like structure in the outskirts of the LMC disc. This stellar overdensity is clearly visible in the distribution of RC stars while it is not visible in young MS stars. This structure was first detected by de Vaucouleurs (1955a) who referred to it as a faint outer loop. It was also found in the distribution of intermediate-age star clusters (Westerlund 1964b) as well as in a map of the number ratio of carbon rich to oxygen rich AGB stars (Cioni & Habing 2003).

2.1.2 SMC morphology

The SMC is an elongated galaxy known for its less pronounced bar and its eastern extension, connecting the SMC to the Bridge, known as the Wing (Shapley 1940). Young and old stellar populations display different spatial distributions. Young stars are concentrated in the central regions of the galaxy as well as in the Wing, following the large-scale irregular and asymmetric structure of the HI distribution (Stanimirović et al. 2004b). Older populations, however, are uniformly distributed and they can be characterised by circular and elliptical structures (e.g. Cioni et al. 2000a; Zaritsky et al. 2000; Harris & Zaritsky 2004a; Haschke et al. 2012; Rubele et al. 2015). Variable stars have been used extensively to provide a thorough study of the 3D structure of the SMC. Able to trace both the young and old populations as well as being distance indicators, these stars are also used to study the depth of the galaxy. RR Lyrae stars indicate that the old population follows an ellipsoidal shape without showing any signs of substructures and/or asymmetries. It was found that the LOS depth can range from 1 to 14 kpc (e.g. Subramanian & Subramaniam 2012; Jacyszyn-Dobrzeniecka et al. 2017; Muraveva et al. 2018). Cepheids trace the younger population. Their age distribution in the SMC is bimodal, younger stars are located closer than older ones (Subramanian & Subramaniam 2015; Jacyszyn-Dobrzeniecka et al. 2016; Ripepi et al. 2017). Scowcroft et al. (2016) found an elongation along the NE-SW axis of up to 20 kpc with the NE closer to us. These results are consistent with other studies (e.g. Haschke et al. 2012; Subramanian & Subramaniam 2012; Subramanian & Subramaniam 2015; Jacyszyn-Dobrzeniecka et al. 2016; Ripepi et al. 2017). The SMC bar is elongated along the LOS (Gardiner & Noguchi 1996); LOS

depth in the eastern part is higher than in western parts and can reach up to 23 kpc in some regions (Nidever et al. 2013). Using RC stars, Subramanian & Subramaniam (2012) found that the SMC is elongated along the NE-SW axis, with a tidal radius between 7 and 12 kpc. Subramanian et al. (2017) found a foreground population highlighted by its distance bi-modality in the distribution of RC stars. This feature can be traced in the direction of the Magellanic Bridge and its origin probably involves material stripped from the SMC.

In this work, we use data from VMC to investigate the spatial distribution of stellar populations of different ages across the MCs and carry out a comprehensive study of their morphological properties. The chapter is organised as follows. Section 2.2 gives a description of the dataset used in our investigation and our criteria for data selection. Section 2.3 focuses on the morphology of the MCs based on various stellar populations, Section 2.4 addresses the comparison of the morphological maps with previous studies followed by a summary and conclusions in Section 2.5. Supporting information is given in the Appendices.

2.2 Observations and Data Selection

The VMC survey (Cioni et al. 2011) is a deep NIR photometric survey of the MCs carried out with the 4.1 m VISTA. It observed $\sim$170 deg^2 until its completion in 2018 October. Covering 68 tiles across the LMC (105 deg^2), 27 across the SMC (42 deg^2), 13 across the Bridge (21 deg^2) and 2 within the Stream (3 deg^2). It provides data in three photometric bands reaching a 5σ limits of Y=21.9, J=22, and $K_{\rm s}$=21.5 mag in the Vega system. The observing strategy involves multi-epoch observations. Each tile covers $\sim$1.77 deg^2 and is observed in at least three epochs in the Y and J bands and in twelve epochs in the $K_{\rm s}$ band. The total exposure time per tile in the Y, J and $K_{\rm s}$ bands are 2400, 2400, and 9000 s, respectively. Each tile is the result of stacking six pawprints in order to cover the gap between the 16 detectors of the VISTA infrared camera (VIRCAM; Sutherland et al. 2015). The observations were acquired under homogeneous sky conditions with a uniform tile coverage in service mode. The median full width at half maximum (FWHM) of the image seeing in each band is Y=1.03″ $\pm$ 0.13″, J=1.00″ $\pm$ 0.10″, and $K_{\rm s}$=0.93″ $\pm$ 0.08″. The main science goals are to determine the spatially resolved SFH of the MCs and derive their 3D structure. This study makes use of all VMC observations obtained until 2017 September 30. The data were extracted from the VISTA Science Archive (VSA[1]; Cross et al. 2012), reduced with the VISTA Data Flow System (VDFS; Irwin et al. 2004) pipeline versions 1.3/1.5, and calibrated according to González-Fernández et al. (2018). Figure 2.1 showcases the MCs observations used in this study. All 27 SMC tiles and 50 LMC tiles have been fully observed, while 18 LMC tiles were partly observed. These tiles are generally located in the outskirts of the LMC where crowding is less significant. Therefore the reduced number of epochs should have little influence on their depth. All VISTA raw data and a fraction of the processed data used in this study are publicly available at the European Southern Observatory (ESO) and VISTA archives, while the VMC data

[1] http://horus.roe.ac.uk/vsa

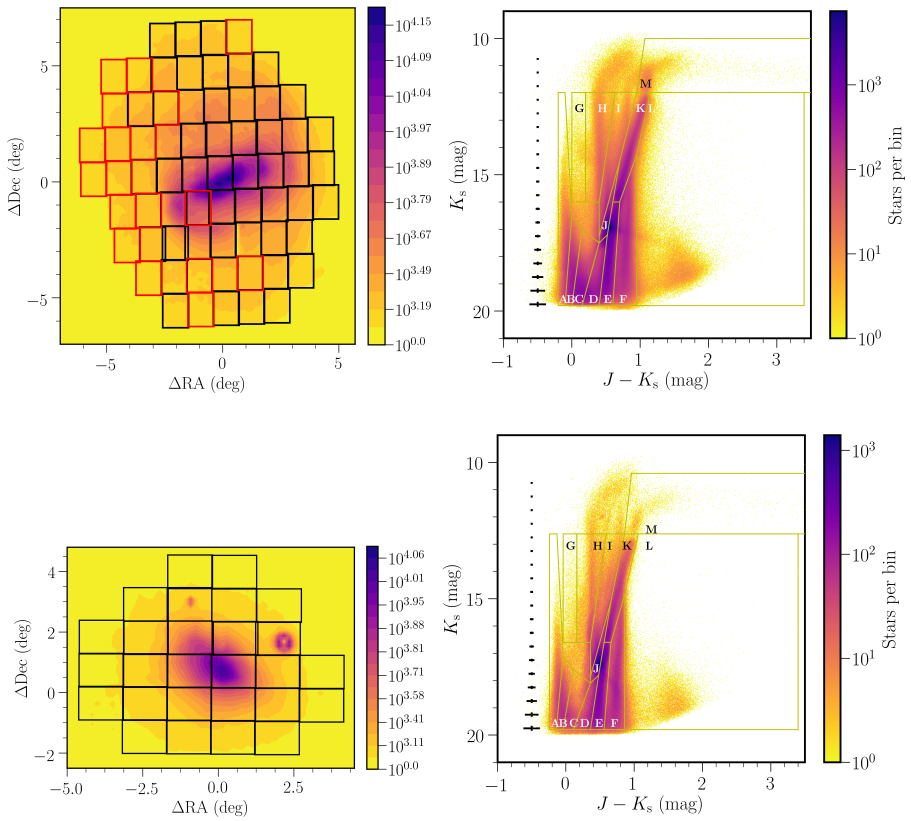

Figure 2.1: (left) Distribution of VMC tiles in the LMC (top left) and SMC (bottom left). Tile boundaries are colour coded by completion of observations as follows: black (fully observed), and red (partly observed). Contours refer to the number density of stars per bin. Bins of 0.15×0.15 deg^2 are used and maps are centred at (RA$_0$, Dec$_0$) = $(81.00°, -69.73°)$ for the LMC and (RA$_0$, Dec$_0$) = $(13.05°, -73.82°)$ for the SMC. We used a zenithal equidistant projection, east is to the left and north to the top. The concentrations of stars west and north of the SMC are due to the MW globular clusters 47 Tuc and NGC 362, respectively. (right) NIR ($J - K_s$, K_s) Hess diagram of the LMC (top right) and SMC (bottom right). The colour scale indicates the stellar density on a logarithmic scale while the yellow boxes, marked by letters, indicate the boundaries of different classes of objects. Region M is limited to $J - K_s$ = 3.5 mag for clarity, but extends to $J - K_s$ = 6.5 mag.

set including the full SMC, Bridge, and Stream is going to be released as part of Data Release #5 (expected in 2019).

2.2.1 Selection of stellar populations

Our aim is to derive the morphology of the MCs using different stellar populations. We used the ($J - K_s$, K_s) CMD in combination with stellar populations models of

the LMC, SMC and the MW to select different classes of objects. These models are produced with the TRILEGAL code (Girardi 2016) in its latest version (Marigo et al. 2017). We selected data from the *vmcsource* table, which contains merged sources from individual VMC source detections. Deprecated data resulting from observations obtained outside the nominal VMC observing requirements were not used. Our selection criteria consisted of objects that were classified as stars with at least a 70 per cent probability (flags `mergedclass`$=-1$ and `mergedclass`$=-2$). We only chose unique (`priOrSec`$\leqslant 0$ or `priOrSec=frameSetID`) objects detected in the J and $K_{\rm s}$ bands, with photometric uncertainties < 0.1 mag in both bands. No selection criteria based on extraction quality flags (flag `ppErrbits`) were applied. We used `aperMag3`, which corresponds to the default point source aperture corrected mag (2.0 arsec aperture diameter). In order to express VISTA magnitudes in the Vega system, we added 0.011 mag to the $K_{\rm s}$ band (González-Fernández et al. 2018) while no adjustment is needed in the J band. Our dataset contains $10,030,967$ and $2,429,550$ sources in the LMC and SMC, respectively, where about 96 per cent of them have a 90 per cent probability or greater being stars.

We used CMD regions defined by Cioni et al. (2014) for the LMC while for the SMC, we shifted these regions to take into account differences in mean distance and metallicity of the stellar populations, as in Cioni et al. (2016). The exact locations of these regions are based on the analysis of the SFH by Rubele et al. (2012). The dimensions of the original regions were mainly conceived for PM studies, based on single-epoch pawprint images (Cioni et al. 2016; Niederhofer et al. 2018a). Here we used stacked multi-epoch tile images and hence we updated those regions as follows. We extended the faint limit of regions A, B, C, D, E, F, and L to $K_{\rm s}$=19.8 mag to maximise the number of stars and the bright limit of regions A, G, H, I, K, and L to $K_{\rm s}$=12.62 mag for the SMC and $K_{\rm s}$=11.98 mag for the LMC coinciding with the location of the tip of the RGB (Cioni et al. 2000b), we also added region M encompassing thermally pulsing AGB stars. Figure 2.1 outlines the regions that disentangle different stellar populations across the LMC and the SMC. Figure 2.2 (top panels) shows the same regions overplotted on CMDs produced from theoretical models (Rubele et al. 2018). These models represent synthetic stellar populations covering a grid of age and metallicity bins shifted to an established distance modulus and extinction, adapted to the conditions of our observations by applying the photometric errors and completeness obtained from artificial star tests as well as to the VISTA system zero points. A model describing the MW foreground is also used to assess the MW contamination of the MCs stellar populations (Girardi 2016). The Rubele et al. (2018) models refer to the SMC while new models of the LMC populations are currently being produced. The distributions of age and metallicity are colour-coded in the diagrams and can be appreciated from the associated panels depicting the age-metallicity relations within each region. The synthetic CMDs include only the stellar populations of the SMC. Tables 2.1 and 2.2 indicate for each region the number of stars, their median age, and the percentage of MW foreground stars using the model and data from the *Gaia* DR2 (Gaia Collaboration et al. 2018a) (see Section 2.2.3) , as well as the type of the dominant stellar population. We omit region L because it is populated mostly by background galaxies.

2.2.2 Completeness

To assess the completeness of the VDFS aperture photometry catalogues, we used the completeness analysis performed on point-spread-function (PSF) photometry catalogues that are available for some tiles (Rubele et al. 2012, 2015). This analysis consists of running large numbers of artificial star tests on tile images in order to trace the distributions of photometric errors and completeness, as a function of position, magnitude, and colour. Figure 2.3 shows the results of the completeness calculations for the J and $K_{\rm s}$ bands, separately. The region boundaries for the selection of stellar populations are influenced by the variation of the completeness across different VMC tiles where the PSF photometry was available. We focus on tile LMC 7_5 as it represents the average quality of our observations. It is located in the inner disc of the LMC where crowding is moderate and comparable to that in the central regions of the SMC. In the external regions of both the LMC and SMC the completeness is higher, while there are tiles in the central regions of the LMC where the completeness is lower, i.e. in the tile containing the 30 Doradus star-forming region. The completeness maps show a rather good recovery of stars even in the crowded central parts of the galaxies. In tile LMC 7_5 the completeness level at the faint end corresponds to 75 per cent while it is only 50 per cent in tile LMC 6_4. Tile LMC 6_4 is located close to the bar of the LMC and it is therefore more crowded than tile LMC 7_5. The completeness of SMC tiles is higher than that of LMC tiles even in crowded regions. At the brightest magnitudes, outside the CMD regions, incompleteness is due to objects close to the saturation limit. Blue objects brighter than $K_{\rm s}$ = 11 mag in the completeness diagram of the $K_{\rm s}$ band reflect saturated sources. These sources are included in region M because they are clearly detected in J and for the morphology study we are only interested in their number.

Completeness established based on PSF photometry may however differ from completeness derived using aperture photometry. In order to test the completeness levels in the aperture photometry, we performed a comparison of the number of stars in the aperture and PSF catalogues (Figure 2.3). No object classification criteria (`mergedclass` flag) was used in our selection, only objects detected in the J and $K_{\rm s}$ bands with photometric uncertainties < 0.1 mag in both bands. The figure shows that both PSF and aperture photometry extract the same number of sources until $K_{\rm s}{\sim}17$ and $J{\sim}17.5$ mag. Fainter than these magnitudes we notice a drop of approximately 10 per cent in both bands. We conclude that the completeness in the aperture-photometry catalogues is the same as that derived from PSF photometry for sources brighter than $K_{\rm s}{\sim}17$ and $J{\sim}17.5$ mag while it is 10 per cent worse for fainter sources in aperture-photometry.

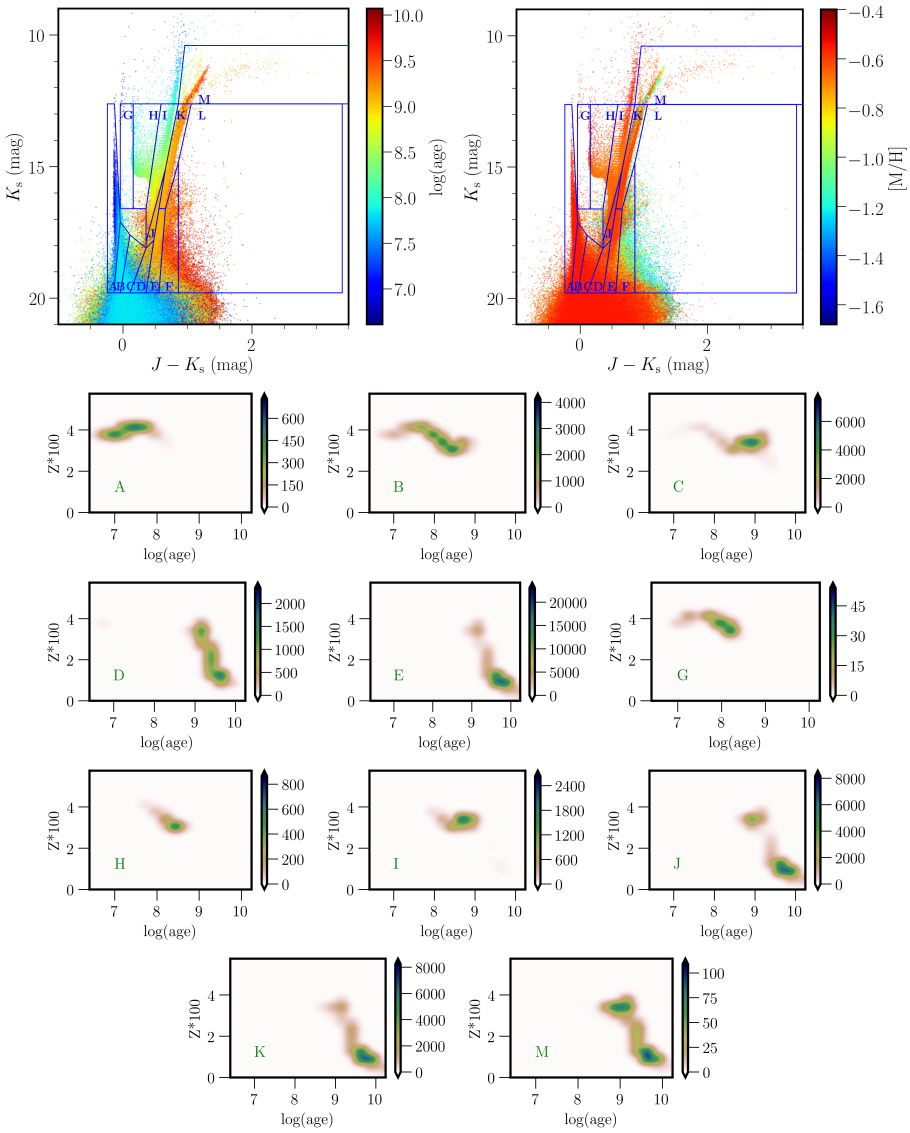

Figure 2.2: (top) Simulated ($J - K_s$, K_s) CMDs illustrating stellar populations in the SMC. The colours correspond to a range of ages (left) and metallicities (right). The boxes refer to the regions used to disentangle different stellar populations. (bottom) Age-metallicity diagrams showing the distribution of ages and metallicities for stars inside each CMD region. The bin size is 0.08 dex^2.

Table 2.1: Stellar populations towards the Large Magellanic Cloud using VMC data.

Region	log(age) (yr)	[M/H] (dex)	N	MW Model (%)	MW *Gaia* (%)[a]	Dominant Stellar Population
A	7.31 ± 0.32	-0.37 ± 0.02	328 034	0	–	Main sequence stars
B	8.29 ± 0.46	-0.39 ± 0.02	547 577	0	–	Main sequence stars
C	8.95 ± 0.36	-0.39 ± 0.05	848 252	0.3	–	Main sequence stars
D	9.39 ± 0.27	-0.60 ± 0.24	1 337 683	1	–	Subgiants & main sequence stars
E	9.57 ± 0.29	-0.96 ± 0.30	973 616	1.4	–	Red giant branch stars
F	9.81 ± 0.19	-0.25 ± 0.47	1 053 240	100	50	MW stars
G	7.91 ± 0.21	-0.43 ± 0.02	11 594	9.5	8.4	Supergiants & giant stars
H	8.23 ± 0.15	-0.39 ± 0.02	145 785	87	78.7	Supergiants & giant stars
I	8.65 ± 0.25	-0.39 ± 0.11	489 333	31	28.3	Supergiants & giant stars
J	9.57 ± 0.40	-0.96 ± 0.34	1 901 035	1.6	–	Red clump stars
K	9.51 ± 0.29	-0.96 ± 0.01	918 552	5.6	6.4	Red giant branch stars
M	9.39 ± 0.28	-0.58 ± 0.23	20 451	1.2	4.6	Asymptotic-giant branch stars

[a] We only provide a lower limit of the Milky Way contamination % up to $K_{\rm s}{\sim}16$ mag (see Section 2.2.3 as well as Figures. 2.8 and 2.9).

Table 2.2: Stellar populations towards the Small Magellanic Cloud using VMC data.

Region	log(age) (yr)	[M/H] (dex)	N	Milky Way Model (%)	Milky Way *Gaia* (%)[b]	Dominant Stellar Population
A	7.31 ± 0.33	-0.55 ± 0.01	69 871	0	–	Main sequence stars
B	8.15 ± 0.46	-0.62 ± 0.05	81 786	0	–	Main sequence stars
C	8.85 ± 0.41	-0.66 ± 0.05	72 681	2	–	Main sequence stars
D	9.41 ± 0.28	-0.84 ± 0.19	187 366	22	–	Subgiants & main sequence stars
E	9.65 ± 0.25	-1.14 ± 0.22	565 019	5.2	–	Red giant branch stars
F	9.81 ± 0.19	-0.35 ± 0.54	354 022	100	90	Milky Way stars
G	8.05 ± 0.31	-0.60 ± 0.03	5830	7.4	3.7	Supergiants & giant stars
H	8.37 ± 0.19	-0.68 ± 0.03	61 529	82	72	Supergiants & giant stars
I	8.71 ± 0.75	-0.66 ± 0.07	209 664	47	31.4	Supergiants & giant stars
J	9.61 ± 0.35	-1.12 ± 0.23	475 076	4	–	Red clump stars
K	9.63 ± 0.27	-1.12 ± 0.22	192 047	16	14.8	Red giant branch stars
M	9.39 ± 0.33	-0.86 ± 0.24	5788	1	3.8	Asymptotic-giant branch stars

[b] As Table 2.1 but for the SMC.

2.2.3 Uncertainties

There are a few factors to consider that influence the position of stars in the CMD and their selection using boxes, such as the presence of dust, photometric uncertainties and distance variations. Additionally, not all stars in the CMD belong to the MCs, but may be part of the MW. In this subsection, we use stellar population models to determine the influence of MW stars. Tables 2.1 and 2.2 showcase the percentage of MW sources. For the LMC, These values were derived using models from an ongoing SFH study by S. Rubele et al. (in preparation) within several LMC tiles, while for the SMC we used stellar population models from Rubele et al. (2018). Regions A, B, C, D, E, J, K and M have negligible fractions of MW sources. Region F has the highest percentage of sources belonging to the MW with 94 per cent, followed by region H with 77 per cent, regions G and I have 13 and 15 per cent of MW stars, respectively. The SMC has similar contamination levels except for regions K, I and D which have percentages up to 24 per cent higher than in similar regions of the LMC. We also used *Gaia* DR2 to test the fraction of MW contamination using a cross-matched *Gaia*-VMC catalogue. In order to obtain this catalogue, accounting for the time at which *Gaia* and VMC observations were obtained was necessary. *Gaia* (J2015) objects were moved to the epoch of the VMC (J2000) survey and therefore only sources with PMs in the *Gaia* catalogue were used. To query the cross-matched catalogue, we used the same selection criteria for the VMC data given in Sect. 2.2.1. Additionally, several *Gaia* selection criteria employed in previous papers were tested. The $\omega/\bar{\omega}$ (parallax / parallax error) ≤ 10 in addition to $G \leq 19$ mag, as in Gaia Collaboration et al. (2018b), only disentangles MW objects up to $K_{\rm s}{\sim}15$ mag and hence was not used in this study. Choosing only objects with $\omega \leq 0.2$ mas is problematic as parallaxes are significantly smaller than the typical measurement error. Therefore only objects with $\omega \leq 0.2$ mas, not consistent with zero at more than 3σ and have an astrometric_excess_noise ≤ 0.2 mas were chosen to be MW objects, as in Vasiliev (2018). Using a simple parallax cut might lead to a greater potential of mistaking MCs stars for MW stars and therefore overestimating the MW contamination percentage (see Figs. 2.8 and 2.9). The limitations of *Gaia* DR2 enables us to estimate the MW contamination only for regions G H, I, K, M and F. We excluded region J because residual RC stars are still present, and provide a lower limit of the percentage of MW stars to $K_{\rm s}{\sim}15$ mag. Apart from region F, which is the one that is mostly influenced by the Gaia sensitivity, the percentages of MW stars between the MW model and the Gaia data are in very good agreement. The spatial distribution of MW objects is expected to be homogeneous across the MCs. Therefore we have not attempted to correct our morphological maps for it. The percentages of MW stars are reported in Tables 2.1 and 2.2. CMDs showing the MW stars towards the MCs are shown in Figs. 2.8 and 2.9.

The dust content towards the MCs is generally quite low. Choi et al. (2018b) found an average LMC reddening corresponding to $E(g-i) = 0.15 \pm 0.05$ mag using RC stars. Using the same stellar population, Haschke et al. (2012) found a mean reddening of the LMC of $E(V-I) = 0.09 \pm 0.07$ mag, while $E(V-I) = 0.04 \pm 0.06$ mag is found for the SMC. The reddening values can be converted using the following equation $E(J-K_{\rm s}) = 0.43 \times E(V-I)$ (Ripepi et al. 2016)

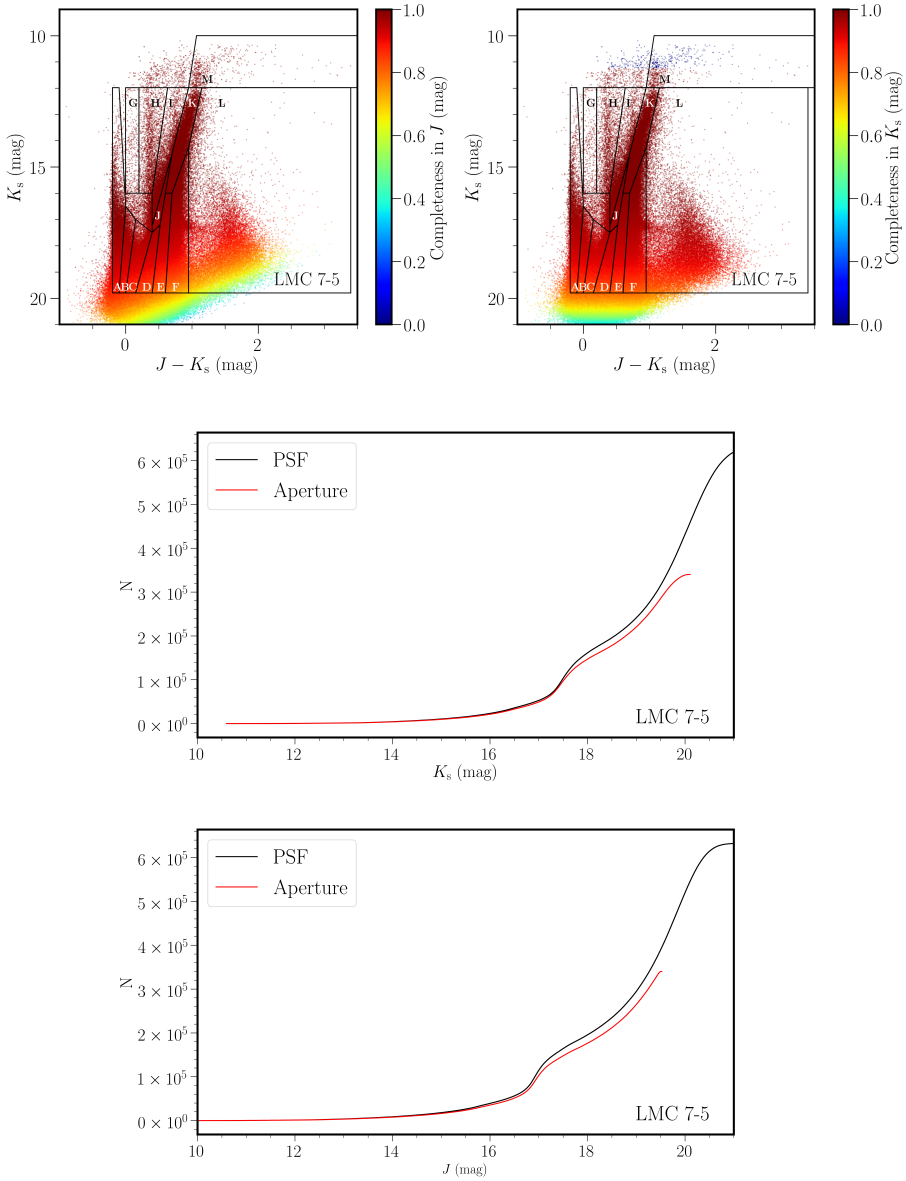

Figure 2.3: (top) Examples of completeness diagrams in the J (right) and K_s (left) bands derived from PSF photometry catalogues on a ($J - K_s$, K_s) CMD for the tile LMC 7_5. (bottom) Comparison between the number of sources extracted with PSF and aperture photometry in the J (left) and K_s (right) bands.

which results in $E(J - K_s) = 0.02 - 0.04$ mag. We have not corrected the VMC data for reddening. It is however important to note that common extinction values of A_V=0.45 mag and A_V=0.35 mag were applied to the theoretical models of the LMC and SMC, respectively. Using the Cardelli et al. (1989) extinction curve for R_V=3.1, A_V can be converted to A_J and A_{K_s} which gives absorption coefficients of A_J=0.1 mag and A_{K_s}=0.04 mag. Since the width of the boxes ranges from 0.1 mag to 0.3 mag, the reddening will have a minor effect on the possible displacement of sources outside the boxes.

Regions F and L represent regions dominated by MW stars and background galaxies, respectively. Their spatial distributions are expected to be homogeneous across the MCs. The remaining overdensities (Figure 2.4) reflect reddened LMC and SMC sources that can be used as indicators of high extinction regions in the MCs, except for that associated with the 47 Tuc cluster.

Photometric uncertainties in the J and K_s bands were limited to < 0.1 mag, which corresponds to uncertainties in $J - K_s$ colours of < 0.14 mag. These uncertainties are well contained within the widths of the boxes at a limiting magnitude of $K_s \sim 17.5$ mag (Figs. 2.1 and 2.12). Displacement of sources from one region to another for sources fainter than these magnitudes is therefore possible, but since our selection criteria were the same for the theoretical models and the data, we expect that the effect is in part accounted for by the age uncertainties (Tables 2.1 and 2.2). Using RC stars, Subramanian & Subramaniam (2009) found that the observed dispersion due to the LOS depth ranges from 0.023 mag to 0.45 mag (a depth from 500 pc to 10.4 kpc) for the LMC and, from 0.025 to 0.34 mag (a depth from 670 pc to 9.53 kpc) for the SMC. Using RR Lyrae stars, the LOS depth is found to be in the range $1-10$ kpc, with an average depth of 4.3 ± 1.0 kpc (Muraveva et al. 2018), while in the LMC, the bar can be traced as a protruding overdensity with a LOS depth of almost 5 kpc (Haschke et al. 2012). Ripepi et al. (2017) found that the SMC is elongated by more than $25 - 30$ kpc in the east/north-east towards south-west direction. The vertical extension of the CMD boxes is larger than the average 0.2 mag variation due to populations at different distances. However, regions that are tilted in colour may suffer from depth effects. A shift of 0.2 mag of the sources in region K, for the LMC, leaves 86 per cent within the box.

2.3 Morphology of the Magellanic Clouds

Figures 2.5 and 2.6 outline morphological maps of stellar population regions for both the LMC and the SMC. They represent two dimensional density maps based on a set of 20 evenly spaced filled contours from the lowest to the highest density. The colour bar depicts star distributions in bins of 0.15×0.15 deg^2. The projection origins for the LMC and SMC are, set at, respectively (RA_0, Dec_0) = ($81.24°$, $-69.73°$) and (RA_0, Dec_0) = ($13.05°$, $-72.83°$), corresponding to the densest point in the LMC bar and the optical centre of the SMC (de Vaucouleurs & Freeman 1972). Coordinates were transformed from angular to Cartesian through a zenithal equidistant projection (van der Marel & Cioni 2001).

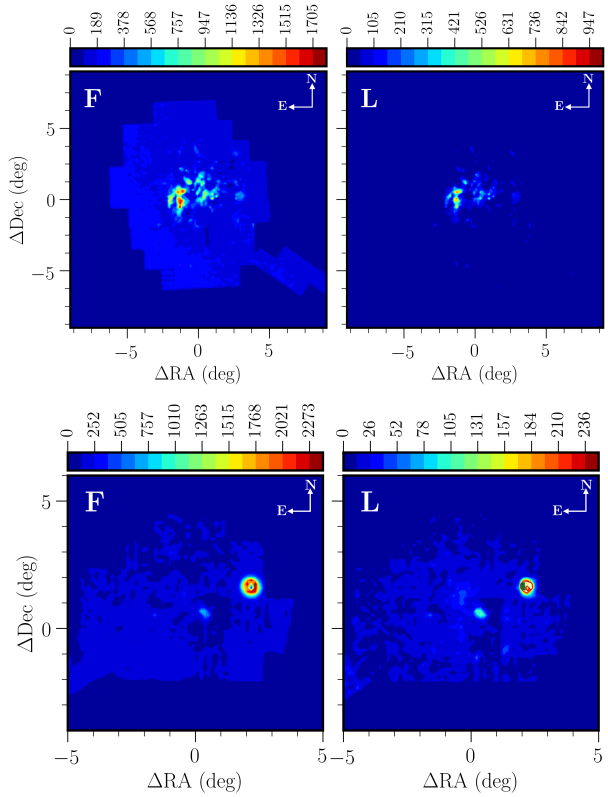

Figure 2.4: Stellar density/contour maps of regions F (dominated by MW stars, but containing reddened MCs giants) and L (dominated by background galaxies, but containing MCs giants and stars of the 47 Tuc star cluster) for the LMC (top) and SMC (bottom). The bin size is 0.03 deg^2. The colour bars show the number of stars per bin.

2.3.1 LMC

In order to investigate the morphological features of the LMC, we selected LMC structures, some of which are well known, based on density contours combined with the age tomography of the various stellar populations. Figure 2.7 gives an overview of the main features we focus on while describing the morphology of the LMC.

Young stellar populations

- **Region A** represents a population of young MS stars with a median age of $\sim$20 Myr ($\pm$ 15 Myr). The overall morphology traced by this population is clumpy and irregular. The bar is thin and spans a length of about $4°$. It has no obvious central overdensity and clumps are distributed along it. Several star forming regions appear as prominent overdensities, Shapley con-

stellation III (ΔRA=$-1°$, ΔDec=$2.5°$), 30 Doradus (ΔRA=$-1°$, ΔDec=$0.5°$), N79 (ΔRA=$2.5°$, ΔDec=$0°$), and N11 (ΔRA=$2.5°$, ΔDec=$2.5°$). We note the presence of spiral arms emerging from the ends of the bar to the south and north of the galaxy. The SE arm is faint and shows an overdensity towards its tip (ΔRA=$-0.5°$, ΔDec=$-2°$) while the SW arm (ΔRA=$2°$, ΔDec=$1°$) is more enhanced with a few overdensities. The NW arm represents the main spiral arm of the galaxy and has a break at (ΔRA=$1°$, ΔDec=$3°$) which divides it in two parts. Harris & Zaritsky (2009) named the vertical part (from ΔDec=$2°$ to ΔDec=$4°$ and ΔRA=$2°$) the blue arm, and the horizontal part, extending to ΔRA=$3.7°$, the NW arm. In the following section, we will refer to the whole structure as the NW arm.

- **Region G** represents a population of blue supergiants and giant stars with a median age of $\sim$81 Myr ($\pm$ 39 Myr). These stars are mainly distributed across a thin bar, similarly to the stars of region A. The SW arm has a clear overdensity at the location of the N79 star forming complex. The star forming region 30 Doradus represents the highest density feature in this map. The vertical and horizontal parts of the NW arm, embedding Shapley constellation III, are clearly visible, but the SE arm is feeble.

- **Region H** represents a population of red supergiants and giant stars with a median age of $\sim$170 Myr ($\pm$ 59 Myr) and contains most of the Cepheids. This region is heavily influenced by the presence of MW stars, which contrary to those in region F are difficult to disentangle using CMD criteria. They are probably responsible for the increase in the number of stars in the outer regions of the galaxy leaning towards the north-east, which is in the direction of the Galactic plane. However, the bar is clearly traced. It has a prominent central density and no obvious gaps. The NW arm is also visible, while the SE and the SW arms are not clear. The low density contours connecting the bar with external clumps encompass the known star forming complexes (30 Doradus, Shapley constellation III, N11, and N79.)

- **Region B** represents a population of MS stars with a median age of $\sim$195 Myr ($\pm$ 206 Myr). The spiral arm features are denser and broader than in Region A. Shapley's Constellation III no longer constitutes the densest area of the map. We note three major overdensities, one at the east and two at the west end of the bar from where the SE and the SW arms originate. The overdensity at (ΔRA=$1.5°$, ΔDec=$0.5°$) connects the bar to the SW arm. The bar has no central overdensity, but is instead traced by a thin ($< 1°$) smooth structure. A protuberance emerging from the SW arm in the direction of the SE arm is also visible. The NW spiral arm is enhanced and it shows an additional faint arm-like feature protruding to the external regions. There is a significant lack of stars between the bar and the NW arm, referred to as the NW void by Harris & Zaritsky (2009), and between the bar and the SW arm. The lack of stars in a linear vertical feature below the bar is due to an observational gap.

- **Region I** represents a population of yellow supergiants and giant stars, similar in median age ($\sim 446 \pm 257$ Myr) to those in region H. We identify the following

features: a prominent bar, a major overdensity near the central region, a weak SE arm, as well as a weak NW arm. The bar appears disconnected from the SE arm.

- **Region C** represents a population of MS stars with a median age of $\sim$891 Myr ($\pm$ 739 Myr). We produced two morphological maps for this region in order to assess completeness variations among tiles. One map contains stars with $K_{\rm s} < 19.8$ mag (Figure 2.10) as was done for the other regions, while the other contains stars with $K_{\rm s} < 19.4$ mag (Figure 2.5). In these figures, the SW arm is connected to the bar and to the SE arm rather than extending south to the outer regions. The bar appears disconnected from the overdensity to the west. The NW arm, although less dense than in the previous maps, clearly shows both the horizontal and vertical parts. The additional northern arm is clearly visible. Furthermore, another external arm-like feature is present in the SW and extends to ΔDec=-5°.

Intermediate-age and old stellar populations

- **Region D** represents a population of MS and/or subgiant stars with a median age of $\sim$2.45 Gyr ($\pm$ 1.53 Gyr). We also produced two morphological maps for this region for the same reasons as stated above (Figs. 2.5 and 2.10). The overall morphology of the galaxy appears more regular than in MS stars with no significant spiral arms, except for the SE inner arm and the SW outer arm. This stellar population has a prominent overdensity at the east end of the bar. The bar itself is inconspicuous. This map complements the previous maps by filling the gaps above and below the bar. The horizontal part of the NW arm is not easily disentangled from its vertical part.

- **Region M** represents the thermally pulsing AGB population with a median age of $\sim$2.45 Gyr ($\pm$ 1.58 Gyr). The AGB phase in the theoretical models is not robust to draw solid conclusions about the properties of the population. Therefore the age of the population should be considered carefully. The bar is well defined and it has a clear central density. The structure is rather regular and smooth, especially compared to that of region D traced by a population with a similar median age. The north-west and SE arms are present but they are faint.

- **Region K** represents the upper RGB stars with a median age of $\sim$3.23 Gyr ($\pm$ 2.16 Gyr). This stellar population is located above the RC and shows that the galaxy has a regular structure with a prominent thick ($\sim 2^{\circ}$) bar. The bar is twice as thick as those outlined by supergiant and MS stars. There is also a major overdensity at its centre, and a gap with respect to the SE arm. The outermost regions of the bar show a flaky distribution that is not found in the other maps and that cannot be explained by the tiling pattern of the VMC survey. The density of stars in the outer disc regions is asymmetric with protuberances that may or may not be associated with spiral features.

- **Region J** is dominated by the intermediate-age RC population, but also includes old horizontal and RGB stars, resulting in a median age of $\sim$3.71 Gyr ($\pm$ 3.42 Gyr), see Figure 2.11. The overall morphology of the stellar population resembles that of stars in region D, but with a denser and larger overdensity encompassing the bar region. The gap between the bar and the SE arm is clearly visible. The NW arm is faint.

- **Region E** represents the lower (below the RC) RGB stars with a median age of $\sim$3.72 Gyr ($\pm$ 2.48 Gyr). The spatial distribution of these stars is leaning towards a radially symmetric structure characterised by inner clumps and irregular contours. The largest overdensity is located west of the centre, but this may be due to a lack of reddened stars that end up instead in region F (cf. Figure 2.7). On the other hand, this overdensity complements the low-density region produced by old MS and subgiant stars. The SW arm is still visible, but this is not the case for the other inner and outer arms highlighted in the previous maps.

In summary, MS stars exhibit coherent structures and the spatial extent of this population grows with age. Several star forming regions are outlined as overdensities (Shapley's constellation III, 30 Doradus, N11, and N79) which grow dimmer as we progress in age. The bar is traced by a relatively thin and clumpy structure without a prominent central feature. Overdensities are present at each end of the bar. They are stronger and appear to detach from the bar itself at older ages. MS stars also trace the distinct multi-arm structure of the LMC. We found a clear connection between the SW spiral arm and the bar which becomes more enhanced with age. Although supergiant stars also represent a young population, they show less substructure than MS stars. Their spatial extent is more or less similar at the different ages, but the bar has a different length. Star forming regions are more evident as overdensities as traced by older supergiants. The spiral arms are not as clearly traced by supergiants as they are by young MS stars. Intermediate-age and old stars are represented by upper and lower RGB stars, RC stars as well as thermally pulsing AGB stars. The oldest stars we detect are over 10 Gyr old, but their number is significantly lower than younger stars populating similar CMD regions. The distribution traced by lower RGB stars exhibits more irregularities in its inner parts, possibly due to the influence of RC stars, and the bar is wider than in the other maps. All four populations show hints of spiral arms, although they are located in the opposite direction compared with those traced by young stars.

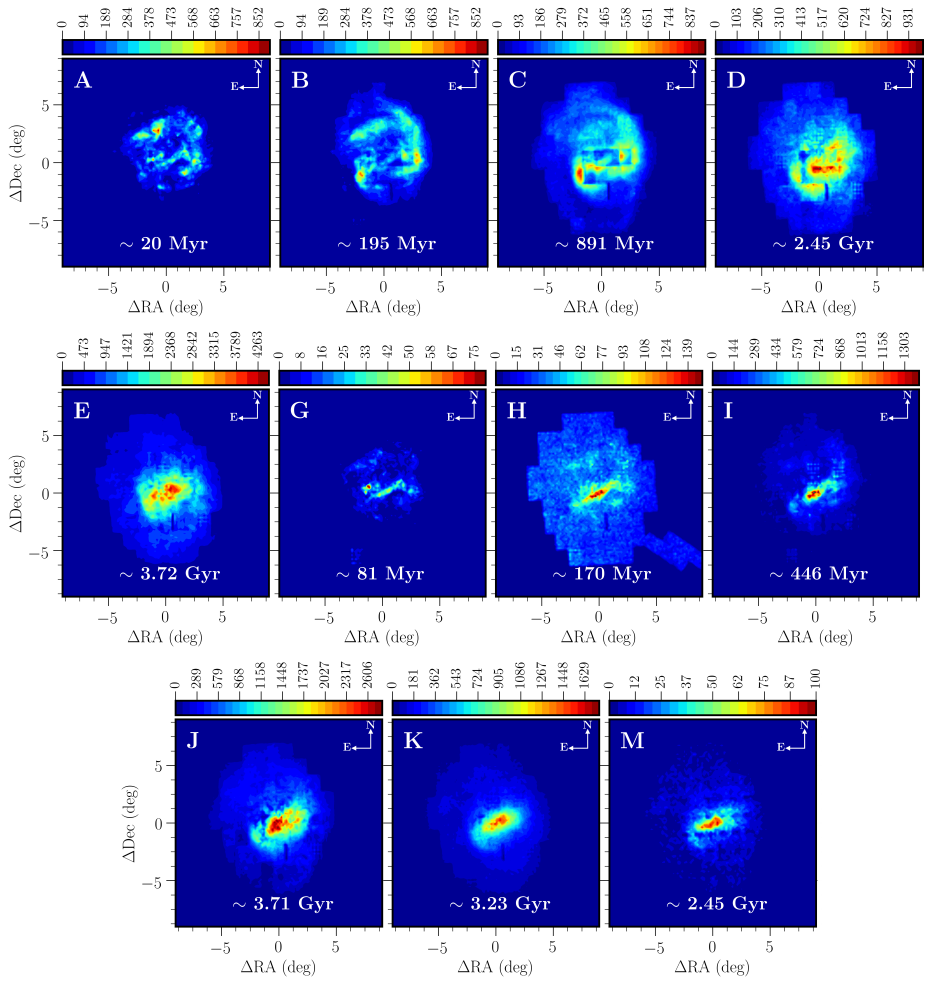

Figure 2.5: Stellar density/contour maps of the LMC's stellar populations extracted from the VMC survey. The bin size is 0.03 deg^2 and the colour bar represents the number of stars per bin. Regions A, B and C refer to MS stars, D to MS/subgiant stars, G, H and I to supergiants and giant stars, J to RC stars, K to upper RGB stars, and M to thermally pulsing AGB stars, More details about the stellar populations can be found in Table 2.1.

2.3.2 SMC

Figure 2.6 reflects the spatial distributions of various stellar populations and highlights the transition of the SMC morphology as function of time, from that of a spherical system to an asymmetric and irregular one. Towards the SMC LOS and within the area surveyed in this study there are two MW star clusters (NGC 362 and 47 Tuc). They appear in the morphology maps as clear overdensities, but they are not discussed in detail. NGC 362 is located to the north of the main body of the galaxy

and 47 Tuc is located to the west. Figure 2.7 gives an overview of the main features we focus on while describing the morphology of the SMC.

Young stellar populations

- **Region A** represents young MS stars with a median age of $\sim$20 Myr ($\pm$ 15 Myr). The presence of the Wing is most evident in this stellar population (ΔRA=-2°, ΔDec=0.5°). The asymmetric appearance of the young population is outlined by a broken bar. The bar density shows a discontinuity at ΔRA=-0.5° after which the bar bends east by $\sim 30^\circ$. The stellar densities within the two parts of the bar are rather homogeneous. Protuberances possibly associated with tidal interaction events are apparent: north of the upper bar (NE extension), south-west of the lower bar (SW extension) and to the Wing. The faint structures around ΔRA=-4° are located towards the direction of the Magellanic Bridge.

- **Region G** represents a population of blue supergiants stars with a median age of $\sim$112 Myr ($\pm$ 80 Myr). The bar is composed of a single density protruding and bending slightly to the north-east. This is a mild effect compared with the broken bar shown in the map from region A. The NE and SW extensions are clearly visible, but the Wing is faint.

- **Region B** represents a population of MS stars with a median age of $\sim$141 Myr ($\pm$ 150 Myr). In this map the bar is not as prominent as in Region A and is composed of only one southern triangular density. North of this structure, instead of the upper bar shown in the previous map of younger MS stars, there is a fuzzy and irregular density distribution of stars. The extension of the Wing is reduced in size and so are the NE and SW extensions.

- **Region H** represents a population of red supergiants stars with a median age of $\sim$234 Myr ($\pm$ 103 Myr) and contains most Cepheids. Its spatial distribution follows the one shown in region G. It has however a lower density and a significantly more irregular structure.

- **Region I** represents a population of yellow supergiants with a median age of $\sim$512 Myr ($\pm$ 886 Myr). The overall spatial distribution of this young population shows the asymmetry of the galaxy. The central region is comprised of a single overdensity that however does not correspond to the $\sim 45^\circ$ inclination of the main body of the galaxy but appears instead rather vertical. The South-West extension and the Wing are inconspicuous. The inner population is more extended to the south and there appears to be a sharp edge north east of the highest density area, but these features are less pronounced than in the maps of other young stellar populations.

- **Region C** represents a population of MS stars with a median age of $\sim$707 Myr ($\pm$ 668 Myr). The body of the galaxy is more extended than in the previous MS stars maps. The outer contours outline a number of protuberances, in particular towards the south-east, the Wing, the north- and south-extensions.

The principal overdensity is located at the same position as in Region B, but the fuzzy distribution of stars has become denser and outlines a somewhat different structure.

Intermediate-age and old stellar populations

- **Region D** represents a population of MS and subgiant stars with a median age of $\sim$2.57 Gyr ($\pm$ 1.65 Gyr). The density distribution is still not completely smooth. Several clumps are visible, but the overall structure appears more regular and symmetric than in young stellar populations. The faint outer contours show protuberances which might be due to tidal effects. The main overdensities are located north, east and south of the highest density areas in the maps of regions B and C. The top overdensity corresponds to the break point of the bar as traced by stars in region A.

- **Region M** represents a population of thermally pulsing AGB stars with a median age of $\sim$2.45 Gyr ($\pm$ 1.86 Gyr). The AGB phase in our theoretical evolutionary models is not reliable enough to draw solid conclusions about the properties of the population, therefore the age of the population should be considered carefully. The overall spatial distribution shows a rather regular structure, but it is not as spatially extended as that shown in regions J and K. There is only one major overdensity region coincident with the southern component in region K. The shape of this high-density area appears tilted with respect to that at the same location in region K. There are several protuberances overall around the central area.

- **Region K** represents a population of upper RGB stars (above the RC) with a median age of $\sim$4.26 Gyr ($\pm$ 2.65 Gyr). The spatial distribution outlined by the outer and intermediate contours is similar to that of other regions, such as regions J and E, dominated by old stars. The features in the central area are similar to those shown in region E, except that here they are more regular and only the two densest regions are evident. Small localised overdensities are not obvious. The southernmost density is denser than its northern counterpart.

- **Region J** is dominated by the intermediate-age RC population, but also includes old horizontal and RGB stars resulting in a median age of $\sim$4.07 Gyr ($\pm$ 3.28 Gyr), see Figure 2.2. The overall morphology of the galaxy is regular and lacks a significant elongation. Unlike red giant and subgiant stars, the central region of the RC population is not comprised of two overdensities but rather of an arc-like overdensity feature. The inner parts of this feature suggest a mild density gradient from east to west. The region enclosed by this arc corresponds to the high density region in the distribution of RGB stars.

- **Region E** represents a population of lower RGB stars (below the RC) with a median age of $\sim$4.46 Gyr ($\pm$ 2.57 Gyr). The outer structure of the galaxy is rounder than that shown above. The central regions are characterised by two main overdensities along the NE to SW axis that complement the overdensities in the distribution of stars from region D. A stripy density pattern, that cannot

be explained by technical and/or observational effects, appears to the south of the galaxy.

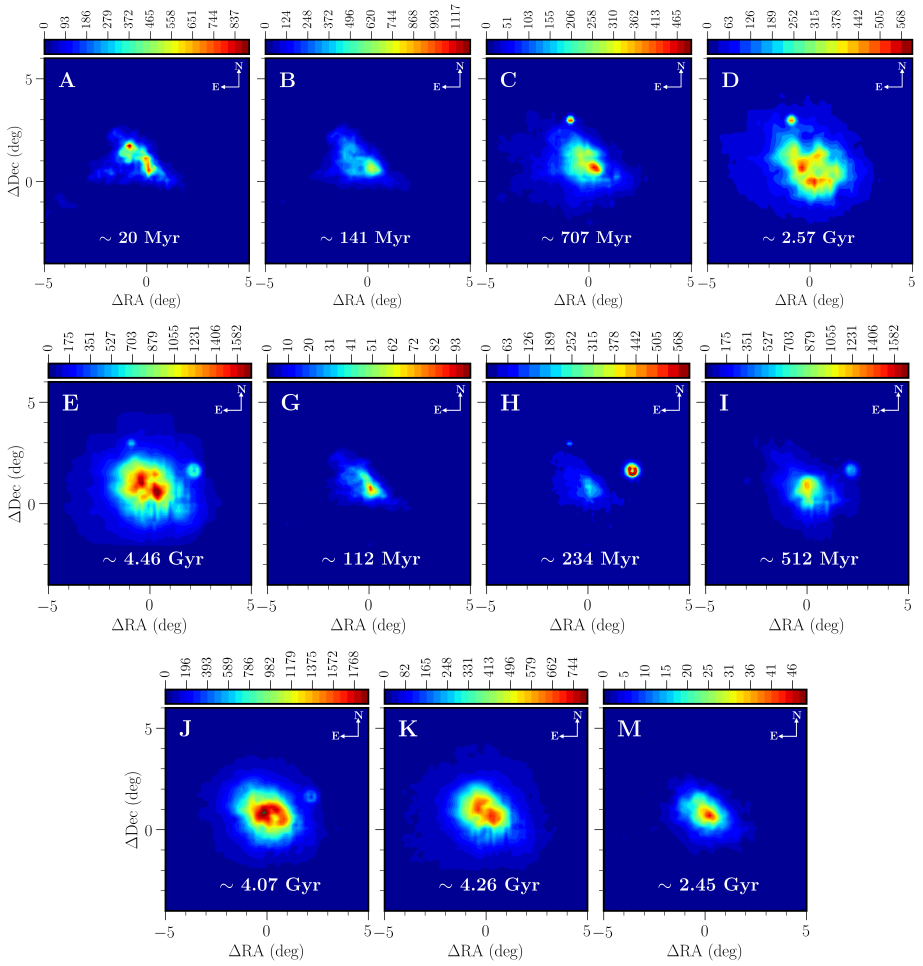

Figure 2.6: As Figure 2.5 but for the SMC.

In summary, the bar traced by the youngest MS stars is denser than the main overdensities in the rest of the young populations including older MS and supergiant stars. The separation between the wing and the bar becomes less evident with age. The contour lines in region C are set in the opposite direction of the PM movement of the galaxy. The inner morphology as traced by RC stars shows an arc-like structure open towards the south, while the distribution of subgiants and MS stars of a similar median age shows several clumps that appear to trace an arc-like structure open towards the west. RGB stars show two central overdensities that

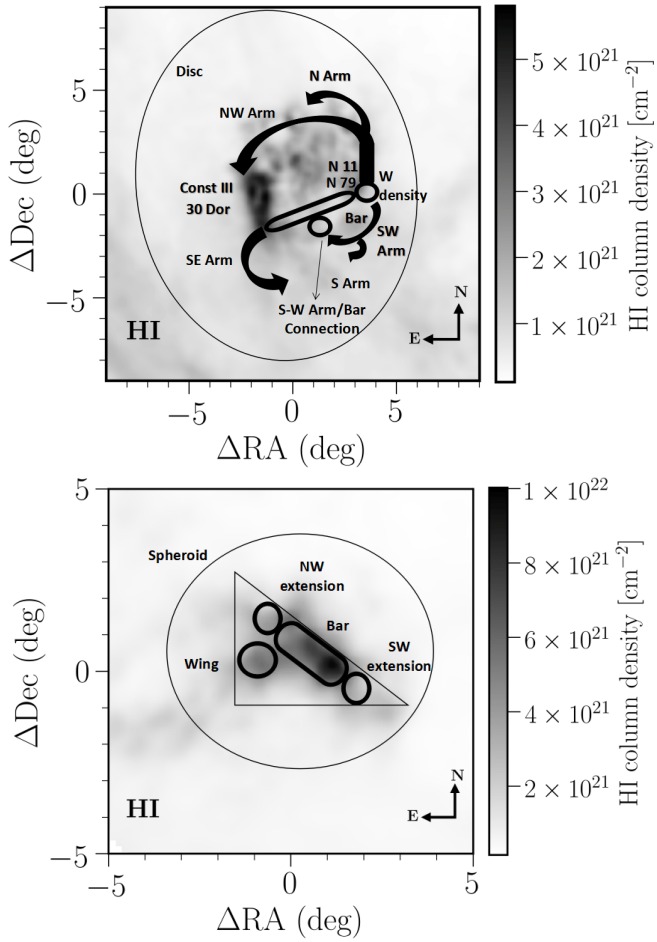

Figure 2.7: Morphological features discussed for the LMC (left) and SMC (right) superimposed on the HI gas column density obtained from HI4PI Collaboration et al. (2016).

seem more populated by lower RGB stars than by the upper RGB stars. Thermally pulsating AGB stars have a central nucleus coincident with the southern density in RGB stars. The external morphology is represented by a circle in intermediate-age and old stars. The oldest stars we detect are over 10 Gyr old, but their number is significantly lower than younger stars populating similar CMD regions.

2.4 Discussion

2.4.1 Morphology and interaction history

Galaxy interactions play an important role in shaping galaxy morphology. Constraining the dynamical history of the MCs is crucial to understand how these interactions have reflected on their morphologies. Our current perception of the orbital history of the MCs indicates that they are either on their first passage of the MW or on an eccentric long period orbit (e.g. Bekki & Chiba 2005; Bekki et al. 2007; Besla et al. 2007; Diaz & Bekki 2012). SFH peaks might correspond to interactions between the LMC and SMC and between the MCs and the MW. These peaks occurred at $100-200$ Myr, $1-3$ Gyr, $4-6$ Gyr, and $7-10$ Gyr (e.g. Harris & Zaritsky 2004a; Noël & Gallart 2007; Harris & Zaritsky 2009; Indu & Subramaniam 2011; Rubele et al. 2012; Cignoni et al. 2013; Rubele et al. 2015). The age uncertainty in CMD regions is quite significant and regions encompass one or more SFH peaks.
Besla et al. (2016) examined the impact of tidal interactions on the periphery of the LMC and found that LMC-SMC interactions in isolation are sufficient for the creation of the asymmetric spiral arms and arcs in the outskirts of the LMC disc similar to those observed. These structures are produced independently of the MW tidal field. After 6.3 Gyr of evolution the SMC has just passed through the disc of the LMC ($b < 10$ kpc). In the LMC, the northern arm feature appears at 100 and 160 Myr in Harris & Zaritsky (2009) SFH maps. In our morphology maps, the northern spiral arm is most prominent in MS stars at $\sim$195 Myr, becomes clearly present at $\sim$891 Myr, which hints of its vertical part are present at $\sim$2.45 Gyr. There is no clear presence of the SW arm before $\sim$195 Myr, this feature is connected to the bar at $\sim$891 Myr, while they are completely combined at $\sim$2.45 Gyr. The SE arm is prominent in RC stars and MS/subgiant stars, but it is also present in RGB and thermally pulsing AGB stars. It agrees well with the star formation bursts since one of the strongest SFH signatures in this substructure peaks at 600 Myr and at 2.5 Gyr. The ages of these populations range from $\sim$1.4 to $\sim$8 Gyr so it is difficult to attribute them to a single interaction event. Furthermore, fine structures such as spiral arms, if formed as a result of LMC-SMC interactions $1-3$ or $6-8$ Gyr cannot be clearly seen using VMC data as they were probably smoothed by the dynamical relaxation of the discs. Therefore most of these features can be attributed to the recent LMC-SMC interaction $\sim$200 Myr ago.

In the SMC, the young populations is limited to the Wing and bar (e.g. Harris & Zaritsky 2004a; Rubele et al. 2015, 2018), in agreement with the highest concentration of stars in our morphology maps for these populations. Compared to the SFH maps of Rubele et al. (2018) the separation between the Wing and the bar is less evident with age and becomes inconspicuous for the oldest MS stars and yellow supergiant distributions. The asymmetric nature of the SMC is apparent until $\sim$707 Myr. It can be attributed to the $1-3$ Gyr interaction. The older populations show signatures of elongations in the SE towards the Magellanic Bridge and the trailing arm, as detected by Belokurov et al. (2017), and extending to large distances from the centre of the galaxy. These elongations have also been detected in RR Lyrae stars (Muraveva et al. 2018) and they can be attributed to the interaction that happened $\sim$200 Myr ago. It is

difficult to discern these elongations in SFH studies, but the general circular structure in the distribution of old stars was found.

2.4.2 Morphology and variable stars

Variable stars have been used extensively to study the morphology as well as the 3D structure of the MCs. Jacyszyn-Dobrzeniecka et al. (2016) used the Optical Gravitational Lensing Experiment (OGLE) survey to study Classical Cepheids in the Magellanic System. This population shows a peak at an age of 100 Myr in the LMC, and can be compared with region A in terms of age and regions A, B, C in terms of spatial distribution. The classical bar of the LMC was redefined to include the western density as both the age and distance tomography show no clear separation between these structures. Our morphological maps shows two distinct overdensities at the western end of the classical bar as well as one in the western density itself in our three MS maps. This break is visible at ΔRA=2°. It is more enhanced in regions B and C. Region C has another distinct break in the bar at ΔRA=1°. Jacyszyn-Dobrzeniecka et al. (2016) also detect the connection of the SW arm to the bar visible in regions B and C, as well as other features visible in our maps. In the SMC, young and intermediate-age Cepheids have a heart-like distribution. Younger Cepheids are concentrated in the north ($10 - 140$ Myr) while older Cepheids are concentrated in the south-west. This is also supported by Ripepi et al. (2017) who found a bimodal age distribution, with two peaks at 120 ± 10 Myr and 220 ± 10 Myr showing a different spatial distribution, which supports the interaction between the MCs $\sim$200 Myr ago. This agrees well with our maps, since stars in region A are concentrated in the north while for the rest of the young populations the main overdensity is located in the south-west.

Furthermore, Jacyszyn-Dobrzeniecka et al. (2017) and Muraveva et al. (2018), the latter using VMC data, studied the structure of the MCs with RR Lyrae stars. RR Lyrae stars generally present a regular smooth structure similar to that of the old and intermediate-age stars in the LMC, although contrary to those populations, no hints of spiral arms are present in RR Lyrae stars. In the SMC, the spatial distribution shows no irregularities or substructures. The central region is composed of a unique nucleus, contrary to other old populations such as RGB and RC stars. These differences might be due to the fact that there is no pure old population among our investigated regions because even though RR Lyrae stars occupy predominantly region C (Cioni et al. 2014), their number is significantly lower than that of the MS stars in the same region. In the models (e.g. Figure 2.2), horizontal branch stars are present in both regions C and J. The eastern part of the SMC is closer than the western part, and a large number of RR Lyrae stars are found in the direction of the SMC's trailing arm (Belokurov et al. 2017).

2.4.3 Multi-wavelength morphology

Galaxy morphology generally appears smoother in the NIR because the dominant stellar population traces the stellar mass distribution and gravitational potential of the galaxy. 2MASS (Skrutskie et al. 2006) was used by Nikolaev & Weinberg (2000)

to provide the most comprehensive morphological maps of the LMC to date. The sensitivity of the survey allowed them to only study stellar populations brighter than the RC. Cioni et al. (2000b) also studied only AGB stars, upper RGB stars and bright young stars, the latter including supergiants and blue loop stars. In the LMC, the young stars from 2MASS (Skrutskie et al. 2006) and the DEep Near Infrared Survey of the Southern Sky (DENIS; Cioni et al. 2000b) have a mean age of $\sim$0.5 Gyr, which can be compared with the young MS and supergiant populations (regions A, G, H and I) in our VMC maps. Similarly, this population shows a clumpy and irregular structure with elongations towards the extremities of the bar indicating the presence of spiral arms. The distribution of AGB stars shows a highly extended population with a broad and faint outer spiral arm in the north-west which in our study is better traced by RC stars. The upper RGB population is comparable to our map from region K, even though we sample a much larger portion of the branch itself. Their SE arm is undetected while it is clearly outlined by our map. The NW arm is very faint but it is emphasised by the dimming of the density in our map.
Gonidakis et al. (2009) investigated the spatial distributions of the SMC stellar component using also 2MASS data, providing isopleth contour maps of four age groups. Their K- and M-type giants show a central concentration, comparable to the morphology of RR Lyrae stars, according to their selection criteria, these stars should be regions H, I and K. Combining these stellar populations a double nucleus is present in our maps. Cioni et al. (2000b) found that the younger population is asymmetric with protuberances that can be due to tidal effects. These proturberances are visible in young MS and supergiant stars distribution, while the older populations show two main concentrations. The western concentration is dominated by RGB stars and the eastern concentration is populated by a significantly younger population. Overall, our maps agree well with theirs but provide a significant improvement in sensitivity and spatial resolution.

HI imaging accounts for spiral structures in galaxies. It traces spiral arms and ring-like features. HI maps can also trace enhanced surface brightness in star forming regions as well as extended gaseous discs compared to their optical and NIR counterparts. Staveley-Smith et al. (2003) provided a new look at the large scale structure of the LMC. The HI morphology of the LMC traces four main spiral arms. Arm 'B' seems to be a tidal arm connecting the LMC to the Magellanic Bridge. The presence of this arm demonstrates the existence of LMC gas in the Bridge and it is composed of two filaments separated by 0.5 deg. Arm 'E' points towards the leading arm while arm 'W' leads to the north. Moreover, the main body of the LMC is bound by arm 'S'. Based on our morphology maps, the spiral structure in the LMC is best traced by MS stars. The gaseous arms 'E' and 'W' have NIR stellar counterparts i.e. the horizontal part of the NW arm and the SE arm, the horizontal part of the SE arm traces arm 'S' although it is not as extended as in the HI map. Furthermore, the main LMC body in HI is also punctuated by holes. These holes show strong correlations with stellar associations, HII regions and supernova remnants. Bozzetto et al. (2017) suggested an association between the spatial distribution of supernova remnants and the environmental density of the LMC, as well as their tendency to be located around supergiant shells. They also found a connection between the highest HII density areas, tracing the spiral structure of HII , and the location of supernova

remnants. Comparing these objects with our MS stars, we find that they are also consistent with their NIR morphology tracing spiral arms not traced by HII such as the SW arm. Overdensities within the spiral arms shown in the map from the youngest MS stars correspond to the location of supershells described by Dawson et al. (2013).
The morphology of the SMC in HII is characterised by the presence of filaments, arcs and shells (Staveley-Smith et al. 1997; Stanimirović et al. 1999). The HII bar is more extended than its stellar counter part, and a bridge seems to connect the bar to the Wing. The smallest overdensity in the Wing, from stars in region A, corresponds to the supershell SMC1 while the larger one corresponds to the HII region N84A. The morphology of the youngest MS stars is closest to that of the HII . McClure-Griffiths et al. (2018) showed that the SMC has an atomic outflow extending to 2 kpc and that these cold outflows may have formed $25 - 60$ Myr ago, which corresponds to the age range of stars in our region A. The spatial distribution of supernova remnants also agrees well with its morphology. Most of the supernova remnants in the SMC are located in the bar (Williams 2009), precisely in the northern and southern regions along the two main overdensities.

The distribution of ionised gas across the MCs, as traced by Hα imaging (Gaustad et al. 2001; Reid & Parker 2012), allows us to isolate star forming regions. In the LMC, Hα evidently traces the spiral structure of the galaxy. Hence a correlation between Hα and the distribution of young stars is expected, although the corresponding overdensities appear much larger and extended in Hα than in our maps since a stellar association can lead to a bright HII region with only a few photoionising stars (Harris & Zaritsky 2009). The same is valid for the SMC where most of the activity is spread over the bar of the galaxy as in the youngest MS stars. Ultraviolet (UV) imaging can also be used to estimate star formation rates and trace the distribution of young stars once dust extinction is estimated. Contrary to the NIR where the correction towards the MCs is small and where different methods yield results that agree within uncertainties, this is not the case for the UV. There is a strong correlation between UV and Hα imaging as the UV is particularly used to trace recent star formation and decouple it from the overall SFH of the galaxy.

In the optical, Choi et al. (2018a) used SMASH (Nidever et al. 2017) and detected a ring like structure in the outskirts of the LMC's disc. They looked at the spatial distribution of MS stars in a range of magnitude bins where the age ranges from 100 Myr to 1.8 Gyr and found that stars <300 Myr old form clumpy structures while MS stars with ages between 300 Myr and 1 Gyr old show conspicuous structures such as the central bar and the NW arm. Zaritsky et al. (2000) compared the distribution of upper MS stars vs. red giant and RC stars using MCPS (Zaritsky et al. 1997) and found that the asymmetric nature of the SMC is mostly made up of young MS stars while the older populations trace an extremely regular distribution. Their study was limited to two morphological maps and their spatial resolution had rendered it hard to characterise central features of the SMC. Furthermore Maragoudaki et al. (2001) used photometric plates in the optical domain to investigate the recent structural evolution of the SMC. Using MS stars, they found that the irregularity of the younger component offers evidence of the encounter with the LMC 0.2 to 0.4 Gyr ago. The recedence of the Wing as the population grows older is noted in their maps as well.

They also detected the overdensities present in this feature as in our map of region A. Our data covers the trailing arm discovered by Belokurov et al. (2017) using *Gaia* DR1 data (Gaia Collaboration et al. 2016a,b). However, we notice an elongation or extension of the contours in several populations. In the upper and lower RGB, it is directed towards the SE, while in subgiant/MS stars (region D) it is directed towards the north-east. The distribution of RC stars does not show any elongations towards the trailing arm.

2.5 Summary and Conclusions

We have presented a morphological study of the MCs using the VMC survey, the most sensitive and higher resolution NIR imaging survey of the Magellanic system to date. We used ($J - K_{\rm s}$, $K_{\rm s}$) CMDs along with stellar population models to select different stellar populations of different median ages. We estimated the influence of MW stars using these models and from the *Gaia* DR2 data. Our main results of the paper are high-resolution maps of the MCs that trace the morphological evolution of the galaxies with age as well as characterisation of the central features for the first time at bin-size resolutions of 0.13 kpc and 0.16 kpc. Below we summarise our main findings:

In the LMC:

- young MS stars exhibit coherent arms and trace the multi-distinct spiral structure of the galaxy. Along with the bar these structures are more enhanced at a median age of $\sim$738 Myr;
- a clear connection between the SW arm and the bar is detected in MS stars, and its density also correlates with age;
- supergiant stars also trace the spiral structure of the galaxy but to a lesser extent. Most of the stars in these populations are concentrated in the bar of the galaxy;
- using MS stars for age tomography, a break in the bar becomes relevant as the population becomes younger;
- lower RGB stars are leaning towards a radially symmetric morphology but still show irregular clumps in the centre;
- unlike RR Lyrae stars, RGB and RC stars still show signatures of tidal arms despite their regular morphology.

In the SMC:

- the bar in the youngest MS stars is more prominent than the central density in the rest of the young populations and its broken appearance may be the result of tidal interactions;

- upper and lower RGB stars show elongations and extensions towards the trailing arm of the SMC;
- intermediate-age populations show irregular central features that are characterised for the first time. These features suggest that tidal interactions influenced the inner SMC.

The VMC survey shows a great capability to trace the morphology of the MCs due to its sensitivity and high spatial resolution, its large area and its reduced sensitivity to dust. In the future, we will explore the outer morphology of the MCs using VHS (McMahon et al. 2013) while upcoming large-scale multi-fibre spectroscopic facilities will be able to characterise substructures with kinematics and chemistry.

Acknowledgements

We thank the Cambridge Astronomy Survey Unit (CASU) and the Wide Field Astronomy Unit (WFAU) in Edinburgh for providing calibrated data products under the support of the Science and Technology Facility Council (STFC). This project has received funding from the European Research Council (ERC) under European Union's Horizon 2020 research and innovation programme (project INTERCLOUDS, grant agreement no. 682115). This study is based on observations obtained with VISTA at the Paranal Observatory under program ID 179.B-2003. SR and LG acknowledge support from the ERC Consolidator Grant funding scheme (project STARKEY, grant agreement no. 615604).

2.6 Appendix - Using Gaia to disentangle the MW population

The CMDs shown in Figure 2.8 refer to the MW stars in the direction of the LMC, distinguished using different selection criteria. These criteria are discussed in Section 2.2.3 and the set adopted here was proposed by Vasiliev (2018).

2.7 Appendix - Additional maps

Maps in Figure 2.10 were made to show the tiling pattern apparent in regions C and D when we probe these populations to $K_{\rm s} < 19.8$ mag. This pattern might be due to the different completeness levels among tiles. It appears to affect only these two CMD regions. In order to take possible incompleteness effects into account, we limited the morphology of the stellar populations within these two regions to $K_{\rm s} \leq 19.4$ mag (Figure 2.5).

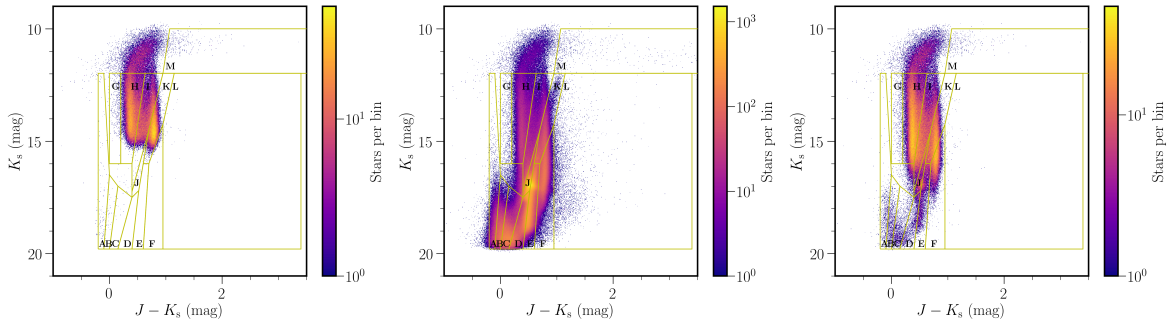

Figure 2.8: NIR ($J - K_s$,K_s) CMDs illustrating the distribution of MW stars across the CMD regions in the LMC using different selection criteria: Gaia Collaboration et al. (2018b) (left), Vasiliev (2018) (centre), ω >0.2 mas (right).

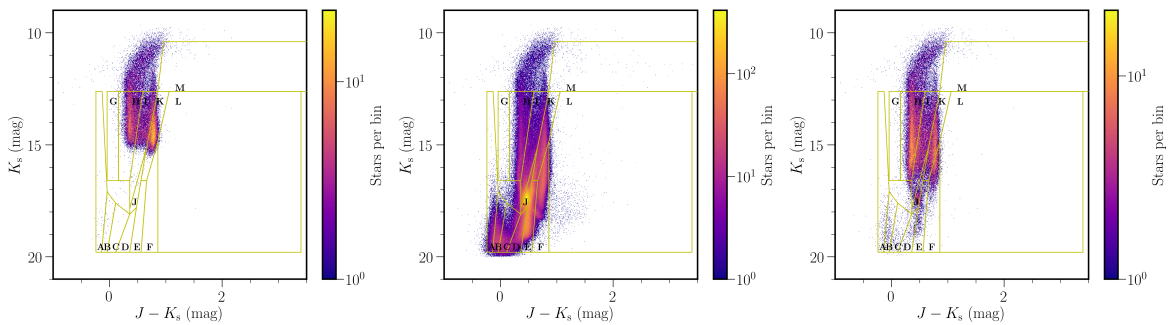

Figure 2.9: As Figure 2.8 but for the SMC.

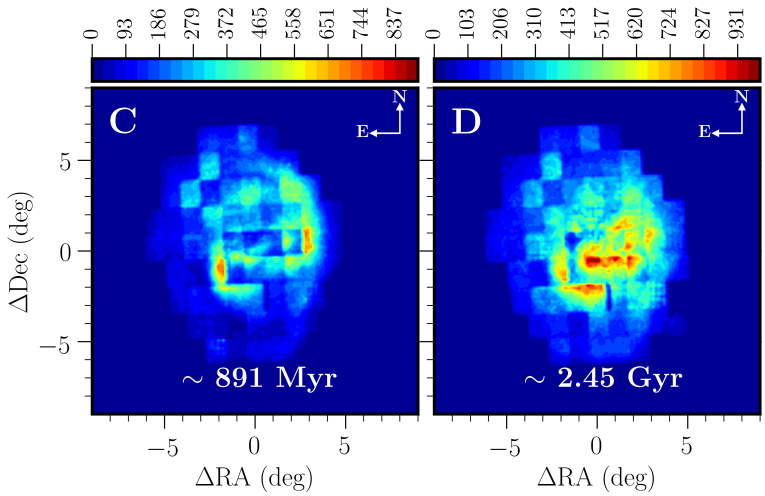

Figure 2.10: Stellar density/contour maps of the LMC's stellar populations within regions C and D obtained from CMD boxes limited to $K_s < 19.8$ mag. The bin size is 0.03 deg^2 and the colour bars represents the number of stars per bin.

2.8 Appendix - Stellar population models of the LMC

Similarly to Figure 2.2, Figure 2.11 shows the theoretical models that have been derived from the analysis of the SFH within several LMC tiles. These models were obtained from an ongoing SFH study by S. Rubele et al. (in preparation) and are used to update region boxes boundaries, stellar population ages as well as the MW percentages published by Cioni et al. (2014).

2.9 Appendix - Photometric errors

The CMDs shown in Figure 2.12 were constructed to show the distribution of σ_{J-K_s} and σ_{K_s} across the stellar population boxes of the LMC and SMC. The boxes widths range from 0.1 to 0.3 mag in colour. We note that we reach half the width of the lower limit at $\sim$18.5 mag.

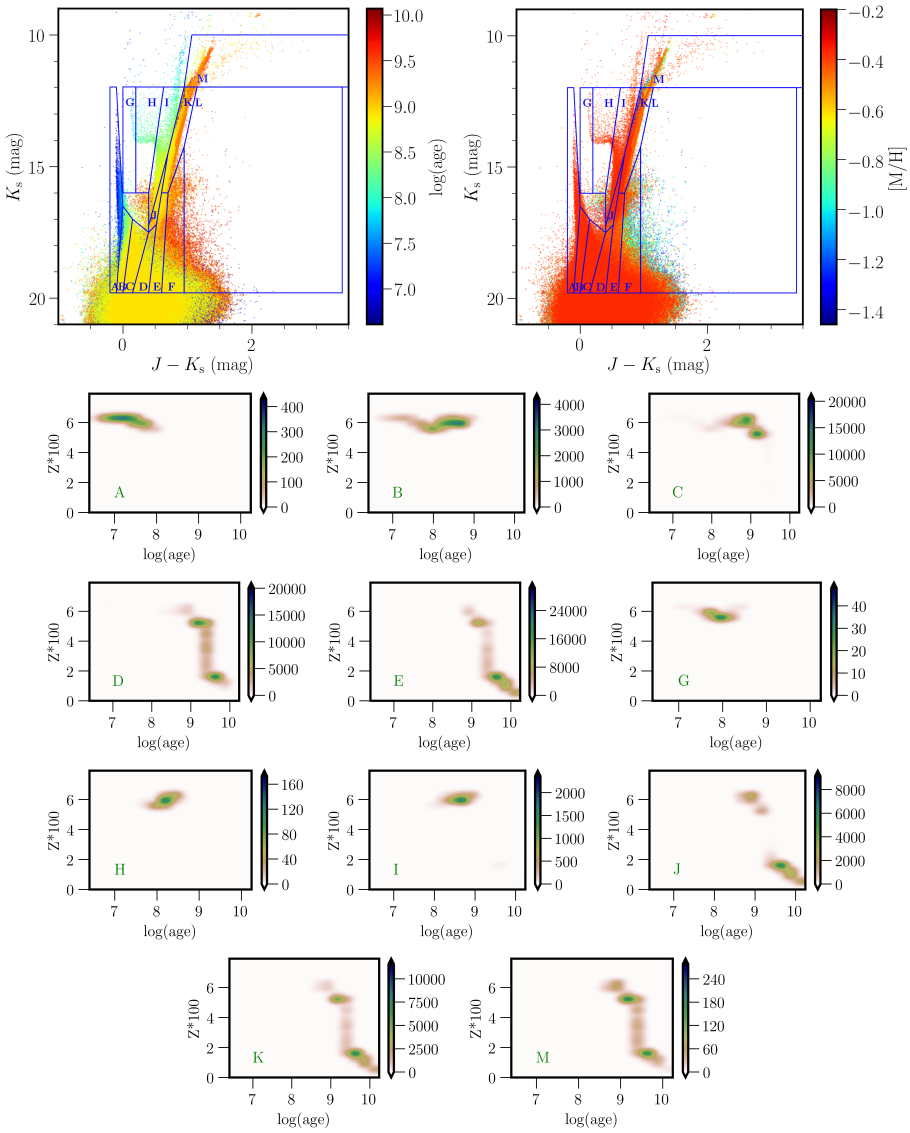

Figure 2.11: (top) Simulated ($J - K_s$,K_s) CMDs illustrating stellar populations of the LMC. The colours correspond to a range of ages (left) and metallicities (right). The boxes refer to the regions used to disentangle different stellar populations. (bottom) Age-metallicity diagrams showing the distribution of ages and metallicities for stars inside each CMD region. The bin size is 0.08 dex^2. The colour bar reflects the number of objects per bin.

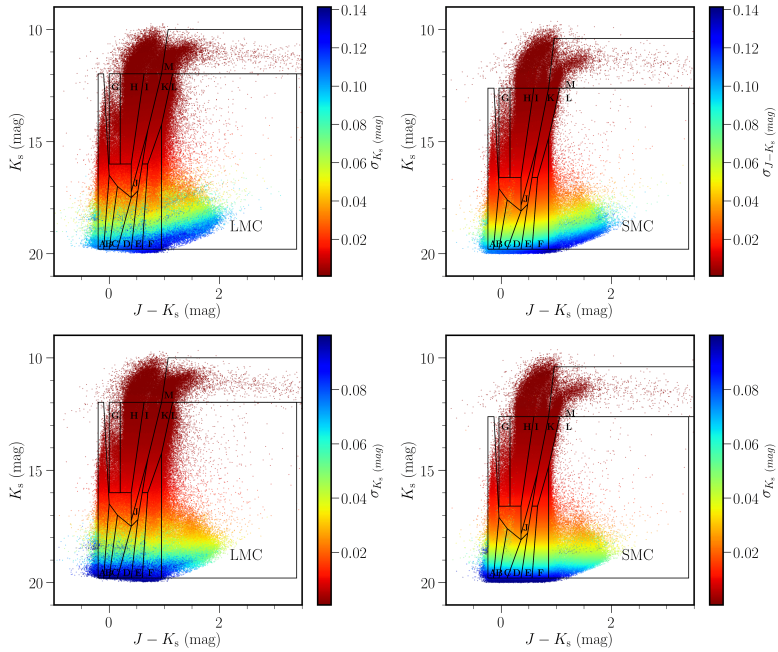

Figure 2.12: CMDs of photometric uncertainties in colour σ_{J-K_s} (top) and magnitude σ_{K_s} (bottom) for LMC (left) and SMC (right) stars. For clarity, we only plotted half the number of stars for the LMC.

3 Stellar substructures in the periphery of the Magellanic Clouds

3.1 Introduction

The LMC and the SMC are the closest pair of interacting dwarf galaxies to the MW. Located at distances of 50 kpc (e.g. de Grijs et al. 2014) and 60 kpc (e.g. de Grijs & Bono 2015), respectively, they represent important testbeds for fundamental astrophysical processes as they provide insights into resolved stellar populations, the cosmological distance scale, the interstellar medium, as well as galaxy interactions and morphology. The LMC is a barred Magellanic spiral galaxy, showing an asymmetric bar (e.g. Zhao & Evans 2000), a few spiral arms (e.g. de Vaucouleurs & Freeman 1972; El Youssoufi et al. 2019) and an inclined disc (e.g. Cioni et al. 2001; van der Marel & Cioni 2001) with a warp (e.g. Olsen & Salyk 2002b; Choi et al. 2018b), while the SMC is an irregular dwarf galaxy characterised by a large LOS depth (e.g. Subramanian & Subramaniam 2012; Jacyszyn-Dobrzeniecka et al. 2017; Scowcroft et al. 2016; Ripepi et al. 2017; Muraveva et al. 2018). It has been found that stellar populations of different ages in the MCs display different morphologies (e.g. Cioni et al. 2000b; Nikolaev & Weinberg 2000; Zaritsky et al. 2000; El Youssoufi et al. 2019). Additionally, the Magellanic system includes the Magellanic Bridge, a feature connecting the two Clouds that is most prominent in HI gas (Hindman et al. 1963) with young (e.g. Shapley 1940; Harris 2007; Skowron et al. 2014; Noël et al. 2015; Mackey et al. 2017) as well as intermediate-age and old stars associated with it (e.g. Bagheri et al. 2013; Carrera et al. 2017; Jacyszyn-Dobrzeniecka et al. 2017). It also includes the Magellanic Stream, a $\sim$200 deg long stream of gas trailing the Clouds in their orbit around the MW (Mathewson et al. 1974) without an identified stellar component as well as the Leading Arm (Putman et al. 1998), a gaseous feature

extending beyond the Galactic plane (Nidever et al. 2010), and across the Galactic disc (McClure-Griffiths et al. 2008).

Dynamical interactions have shaped the evolutionary history of the MCs. The LMC and SMC have been dynamically coupled since at least $\sim$2 Gyr ago and experienced a significant interaction $\sim$150 Myr ago (e.g. Diaz & Bekki 2012; Zivick et al. 2019). Two mechanisms, tidal and ram pressure stripping, have been suggested to account for the creation of the Magellanic Stream and Bridge (e.g. Besla et al. 2007; Diaz & Bekki 2012; Salem et al. 2015). Dynamical interactions can explain many of the diffuse stellar substructures, including arcs, clumps and overdensities, discovered in the periphery of the MCs.

In the outskirts of the SMC (8 deg from its centre), Pieres et al. (2017) found a stellar overdensity, named SMCNOD, using imaging data from the DES (Abbott et al. 2018). Subsequently, imaging data from the MAGellanic SatelLITEs Survey (MagLiteS; Drlica-Wagner et al. 2016) was used to study SMCNOD finding that it lies at the same distance as the SMC and contains mostly intermediate-age stars (6 Gyr old) with a small fraction of young stars (1 Gyr old). SMCNOD was most likely tidally stripped from the SMC. Martínez-Delgado et al. (2019) revisited a shell-like overdensity in the outskirts of the SMC using SMASH (Nidever et al. 2017) data and found that it is solely composed of young stars ($\sim$150 Myr old). There is no evidence of it being of tidal origin and it may have formed in a recent star formation event resulting from an interaction with the LMC or the MW. Massana et al. (2020), also using SMASH data, discovered a new faint feature located at 14 deg from the centre of the SMC, possibly associated with a more distant structure.

In the periphery of the LMC, Mackey et al. (2016, 2018) found numerous substructures in and around the galaxy, including an arc-like structure 13.5 deg north of the centre, of which the stellar populations are indistinguishable from those of the LMC disc. The stars in this feature were most likely stripped from the LMC due to either the tidal force of the MW or to an interaction with the SMC. Belokurov & Erkal (2019) used *Gaia* DR2 (Gaia Collaboration et al. 2018a) to look for low surface brightness features in the periphery of the MCs and found two thin and long stellar streams in the northern and southern regions of the LMC. Numerical simulations indicate that the effect of the MW and SMC on the LMC are both important for the creation of tidal features. Using a combination of *Gaia* DR1 (Gaia Collaboration et al. 2016a) and Galaxy Evolution Explorer (GALEX; Martin et al. 2005) imaging data, Belokurov et al. (2017) demonstrated that the distribution of RR Lyrae stars traces a bridge joining the SMC from its trailing tidal tail to the LMC. However, the nature of this bridge is still under debate as it has not been detected in OGLE (Jacyszyn-Dobrzeniecka et al. 2017, 2020a) nor in *Gaia* DR2 data (Clementini et al. 2019). Deason et al. (2017) found that Mira-like stars trace the LMC as far as 20 deg from its centre.

Established tracers of substructures within and around the MCs are RC stars, low mass stars which have undergone the helium flash to ignite helium burning in their cores (e.g. Girardi 2016 and references therein). Owing to their constrained location in the CMD, they are used as probes of stellar distances allowing the study of the 3D structure and reddening of the MCs (e.g. Subramanian & Subramaniam 2010, 2012, 2013; Tatton et al. 2013; Choi et al. 2018b,a). Nidever et al. (2013) discovered a strong distance bi-modality in the luminosity function of RC stars with one component at

$\sim$67 kpc and a second component at $\sim$55 kpc in three eastern fields located 4 deg from the SMC centre. They suggested that the component found at $\sim$55 kpc is the tidally stripped stellar counterpart of the Magellanic Bridge, in good agreement with dynamical models (e.g. Diaz & Bekki 2012). Using VMC (Cioni et al. 2011), Subramanian et al. (2017) studied the luminosity function of RC stars in the inner 20 deg^2 region of the SMC. A bi-modality in distances to the RC stars was found in the eastern SMC, after having ruled out reddening, RC population effects, and LOS depth effects as potential causes, it was interpreted as a foreground population $\approx$ 11 kpc in front of the main body. This is most likely due to tidal stripping from the SMC during its most recent encounter 100 – 300 Myr ago with the LMC. Tatton (2018) and Tatton et al. (2020) showed how the luminosity function of the RC varies across all VMC tiles belonging to the SMC, while Omkumar et al. (2021) have investigated the RC bi-modality using *Gaia* DR2 data. Additional evidence supporting the tidal stripping of SMC material during the most recent encounter comes in the form of accreted RGB stars belonging to the SMC and discovered in the LMC (Olsen et al. 2011), while Dobbie et al. (2014) found signatures of tidally stripped RGB stars in the outskirts of the SMC.

In this chapter, we present a detailed analysis of the spatial distribution of different stellar populations in the periphery of the MCs using data from VHS (McMahon et al. 2013). VHS enables us to obtain a comprehensive view of the morphology in the outskirts of the MCs over a continuous area, allowing us to confirm the presence of known substructures while also finding new ones. Furthermore, we also investigate the properties of the double RC feature, beyond the main body of the SMC, using a combination of VHS and VMC data. Identifying stellar substructures around the MCs using morphology and luminosity function studies is very important to understand the nature of the interactions between the MCs and will provide inputs for theoretical models. The chapter is organised as follows, Section 3.2 describes the data set used in our study and our selection criteria, Section 3.3 focuses on the outer morphology of the MCs, while Section 3.4 studies the properties of the double RC feature. Finally, Section 3.5 presents a discussion and summary of our results.

3.2 Observations and Data Selection

3.2.1 Data

We used data from VHS, a NIR survey, that covers the whole southern hemisphere when combined with other first–generation VISTA Public Surveys. VHS is carried out by the 4.1 m VISTA (Sutherland et al. 2015) and VIRCAM (Dalton et al. 2006; Emerson et al. 2006). It aims to cover 18,000 deg^2 with observations in at least two photometric bands, J and K_s (central wavelengths: 1.25 μm and 2.15 μm, respectively). Median 5σ point source limits of J = 19.3 mag and K_s = 18.5 mag (in the Vega system) are achieved with a minimum exposure time of 60 s per waveband. VHS includes three programmes: VHS–GPS (Galactic Plane Survey), covering a region of $\approx$8200 deg^2 with exposure times of 60s in the J and K_s bands; VHS–DES, covering a region of $\approx$4500 deg^2 with exposure times of 120s in the JHK_s bands and VHS–ATLAS, covering a region of $\approx$5000 deg^2 evenly divided between the North and South

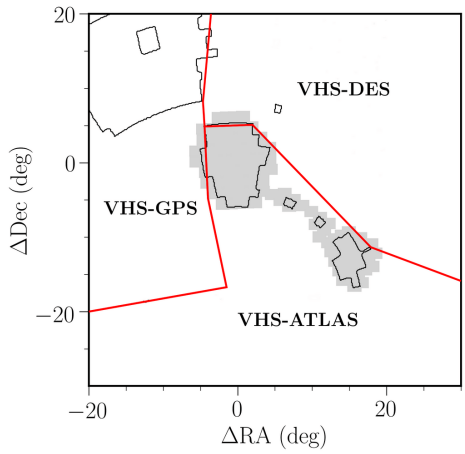

Figure 3.1: Schematic figure showcasing the footprints of the VHS and VMC surveys. The borders of the VHS sub–surveys are indicated in red and those of observational gaps in black, while the area covered by VMC tiles is displayed in light grey. The projection origin for the maps is set at (RA_0, Dec_0) = (81.24 deg, −69.73 deg) corresponding to the densest point in the LMC bar (de Vaucouleurs & Freeman 1972).

Galactic caps with exposure times of 60s in the $YJHK_s$ bands. VHS data from all three programmes border the MCs (Figure 3.1). Our study makes use of all VHS observations obtained until 2017 September 30th. We also use of data from the VMC survey (Cioni et al. 2011), a deep NIR multi–epoch imaging survey of the MCs providing data in three photometric bands reaching 5σ limits of Y = 21.9, J = 22, and K_s = 21.5 mag (in the Vega system). VMC observed the LMC (105 deg^2), SMC (42 deg^2), the Magellanic Bridge (21 deg^2) and the Magellanic Stream (3 deg^2). In this study we make use of observations in the SMC and Bridge components (Figure 3.1). VHS data is combined with VMC data in order to fill observational gaps in the Magellanic Bridge (two small areas within it, see Figure 3.1) and to study the luminosity function of RC stars with continuous coverage within 10 deg from the centre of the SMC. Our selection criteria for VMC sources are the same as those used for VHS sources (see below). Duplicate sources that are present in both surveys (e.g. in the outskirts of the LMC and SMC, as well as the Magellanic Bridge) were eliminated by keeping VMC detections.

VDFS (Irwin et al. 2004) was used for data reduction while the data were extracted from the VSA[1] (Cross et al. 2012). VHS data allow us to explore resolved stellar populations in the periphery of the MCs and to detect sources just below the RC. VHS showcases an improvement in depth over previous NIR surveys such as 2MASS (Skrutskie et al. 2006) and DENIS (Cioni et al. 2000b), which have limiting magnitudes ≈4 mag brighter in K_s. VHS is the deepest NIR survey covering the entire southern hemisphere to date, and although it is by design much shallower than its optical counterparts such as *Gaia* DR2 (Gaia Collaboration et al. 2018a) and the DES

[1] http://horus.roe.ac.uk/vsa

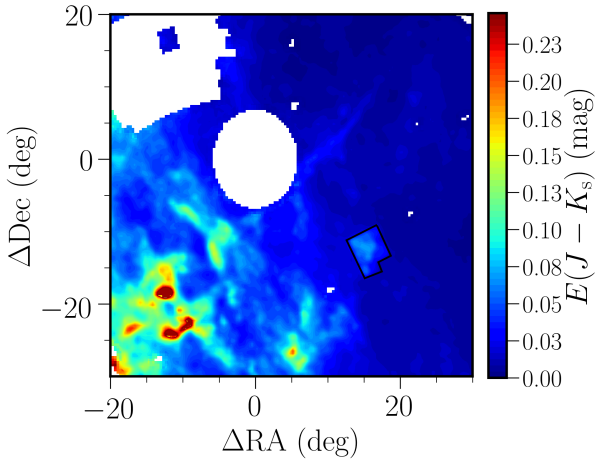

Figure 3.2: Distribution of reddening derived from the Schlegel et al. (1998) dust map as well as from the SFH study of the main body of the SMC (outlined in black) by Rubele et al. (2018) across the footprint analysed in this paper. The map is centred at (RA_0, Dec_0) = (81.24 deg, −69.73 deg) and the colour bar shows the variation of the $E(J - K_s)$ colour excess. White patches refer to the central regions occupied by the LMC and to the incomplete VHS observations towards the NE, as well as to a few tiles in the outskirts of the MCs.

(Abbott et al. 2018), VHS provides an essential contribution to the multi–wavelength view of the periphery of the MCs.

Figure 3.2 shows the LOS Galactic dust reddening derived from the Schlegel et al. (1998) dust maps. In the Bar and Wing regions of the SMC, Schlegel et al. (1998) measurements can be unreliable due to contamination by SMC stars or unresolved temperature structure. We combined the Schlegel et al. (1998) reddening map with reddening derived from the SFH study of the main body of the SMC by Rubele et al. (2018). Rubele et al. (2018) used VMC data across an area of 23.57 deg^2 with a bin size of 0.143 deg^2 and reconstructed the observed CMDs using stellar partial models, recovering the best–fitting extinction A_V as an additional output of the star formation rate. The combination of the Schlegel et al. (1998) and Rubele et al. (2018) maps encompasses the entire area studied in this paper. For the Schlegel et al. (1998) map, $E(B - V)$ values were obtained using the python module SFDMAP[2] and converted to $E(J - K_s)$ values using coefficients from González-Fernández et al. (2018). These coefficients have been calculated assuming R_V = 3.1 and account for the Schlafly & Finkbeiner (2011) recalibration. For the Rubele et al. (2018) map, we converted A_V to $E(B-V)$ values assuming R_V = 3.1 and used the same coefficients to convert them to $E(J - K_s)$ values. Despite the spatial distribution of reddening being generally low in the periphery of the MCs with $E(J - K_s) \approx 0.10$ mag, particularly at the location of the substructures traced in this study, filamentary dust features with high reddening values are present near the Galactic disc. Moreover, the sharp borders (owing to the VISTA field–of–view) suggest that the level of reddening

[2] https://github.com/kbarbary/sfdmap

in the immediate outskirts of the SMC may be underestimated as we only account for the foreground reddening and not the intrinsic reddening of the SMC. In the analysis which follows, we therefore correct for reddening. However, the central regions of the LMC and SMC, including the region covered by the Rubele et al. (2018) reddening map, have been omitted from the morphological maps to enhance the distribution of stars in the outer regions.

3.2.2 Selection of young and old stellar populations

The selection of different stellar populations was based on ($J - K_s$, K_s) CMDs (see Figure 3.3). We selected unique objects (`priOrSec`$\leqslant 0$ `or priOrSec = frameSetID`) from the *vhssource* table detected in both J and K_s bands, classified as stars with at least a 70% probability (`flag mergedclass` $= -1$ `or mergedclass` $= -2$) and with photometric errors less than 0.2 mag. The `AperMag3`, which corresponds to the default point source aperture corrected magnitude (2 arsec aperture diameter), was retrieved for each source in each waveband. No selection criteria based on extraction quality flags (`flag ppErrbits`) were applied. VISTA magnitudes were transformed to the Vega system by adding 0.011 mag to the K_s band while no corrections are required in the J band (González-Fernández et al. 2018).

Stars belonging to the MCs were divided into two regions: region Y occupied by young stars, including tip of the MS and supergiant stars, and region O occupied by old stars, including RGB, AGB, and RC stars. These two regions result from the combination of CMD regions established by El Youssoufi et al. (2019): region Y comprises regions A, B, C, I, G, H and region O includes regions D, E, J, K, M. Region Y has been extended to K_s = 10 mag, instead of K_s = 11.98 mag and to $J - K_s$ = -0.6 mag instead of $J - K_s$ = -0.2 mag, to maximise the number of stars after their cross–correlation with *Gaia* DR2. Both regions Y and O have been limited to K_s = 18.8 mag instead of K_s = 19.8 mag, to reflect the sensitivity of the VHS observations. Due to the small number of stars in the periphery of the MCs, we combined several regions as opposed to using them separately. Studies of MC objects are prone to both foreground and background contamination. Most background galaxies were omitted from our selection by adopting the object classification flag `mergedclass` and avoiding the reddest region of the CMD ($J - K_s > 1$ mag and $K_s > 13$ mag). However, this region may contain reddened MCs sources and a minority of RGB stars scattered from the adjacent region of old stars. To reduce the presence of MW stars in our sample, we combined data from *Gaia* DR2 with VHS and VMC data [3], retaining only sources with a maximum cross–matching distance of 1 arcsec and parallaxes≤ 0.2 mas.

In addition, we applied a PM selection. We examined the stellar density of objects belonging to regions Y and O in PM space and determined two ellipses around the LMC and SMC PM distributions (Figure 3.4). Throughout the paper, we refer to $\mu_{\rm RA}\cos$(Dec) as $\mu_{\rm RA}$. The LMC ellipse is centred at $\mu_{\rm RA}$ = 1.60 mas yr^{-1}, $\mu_{\rm Dec}$ = 0.53 mas yr^{-1}, has a semi-major axis of 1.35 mas yr^{-1}, a semi-minor axis of 0.85 mas yr^{-1}, and is rotated by 15 deg, whereas the SMC ellipse is centred

[3]The catalogues have been cross-matched by G. Matijevič using his own software tools.

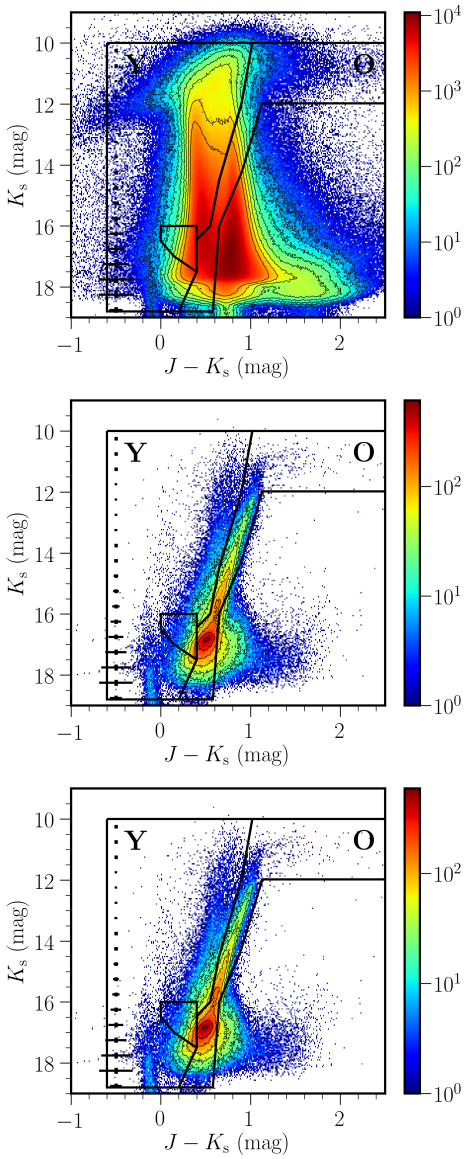

Figure 3.3: NIR ($J - K_s$, K_s) Hess diagrams of the stellar periphery of the MCs before the cross–match with *Gaia* DR2 data (left), after the cross–match using the selection criteria to reduce the presence of MW stars (middle), and after correcting for reddening (right). The colour scale indicates the stellar density on a logarithmic scale whereas horizontal bars show the photometric uncertainties as a function of magnitude. Two different classes of objects are enclosed by black lines, Y referring to young stars and O referring to old stars. Stars belonging to the polygonal area ($16 \leq K_s \leq 17.5$ mag) are not included in our study as they have mixed ages.

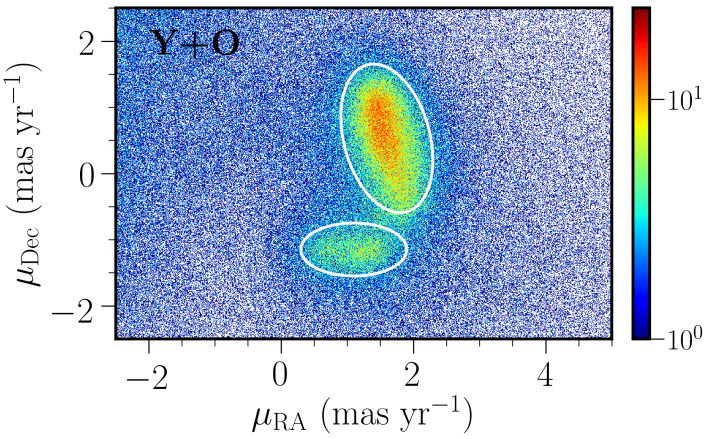

Figure 3.4: Stellar PMs towards the direction of the MCs. Most of the objects with LMC and SMC PMs are enclosed within the large and small ellipse, respectively, whereas many of the objects outside these ellipses belong to the MW.

at $\mu_{\rm RA}$ = 1.10 mas yr^{-1} and $\mu_{\rm Dec}$ = −1.15 mas yr^{-1}, has a semi-major axis of 0.80 mas yr^{-1}, a semi-minor axis of 0.40 mas yr^{-1} and no rotation. Objects belonging to these two ellipses constitute our morphology dataset which contains 312, 748 sources, encompassing an area of 1800 deg^2 around the MCs.

In order to assess the detection limit of the VHS survey, we examined the normalised number of sources in each sub–survey as a function of magnitude compared with the 2MASS and VMC surveys. We used circular areas of 0.5 deg radius with the following (RA, Dec) centres: 2MASS (32.9 deg, −75.0 deg), VMC (32.9 deg, −75.0 deg), VHS–ATLAS (43.5 deg,−77.8 deg), VHS–GPS (111.50 deg,−75.66 deg), and VHS–DES (42.00 deg,−60.97 deg). We found that the VHS programmes ATLAS, GPS, and DES have detection limits in J of 19.84 mag, 19.55 mag and 20.36 mag, respectively, while in $K_{\rm s}$ the detection limits are of 18.08 mag, 17.79 mag and 18.42 mag, respectively. Only sources detected in both J and $K_{\rm s}$ with photometric uncertainties less than 0.2 mag were included. These values show that stellar populations brighter than and including the bulk of the RC are not significantly affected by incompleteness.

3.2.3 Selection of RC stars around the SMC

To study the distribution of RC stars in the outskirts of the SMC we proceeded as follows. We combined VHS with VMC observations of the SMC and Bridge which are within 10 deg from the SMC's optical centre. Due to the smaller number of stars in the periphery of the SMC than in the main body of the galaxy, we divided the SMC into circular annuli of radii 1 deg, 2 deg, 3 deg, 4 deg, 5 deg, 6 deg, 7 deg, and 10 deg from the centre of the galaxy and each annulus into four regions North (N), East (E), South (S) and West (W), see Figure 3.6 (left). In the ($J-K_{\rm s}$, $K_{\rm s}$) CMDs, specific stellar

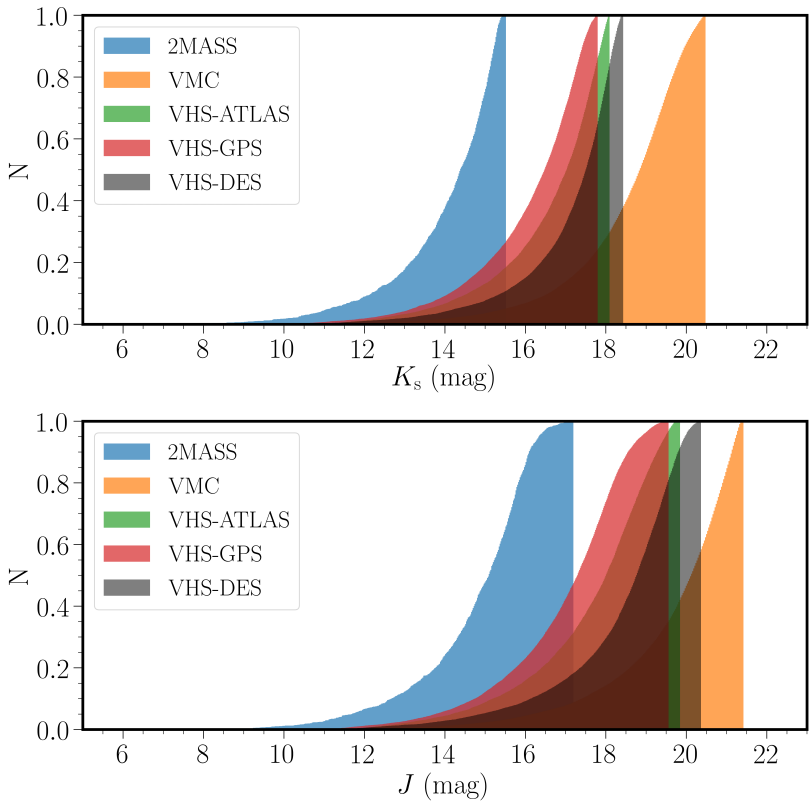

Figure 3.5: Comparison between the detection limits of 2MASS, VMC, VHS-GPS, VHS-DES, and VHS-ATLAS in circular areas of 0.5 deg radius in the J (left) and K_s (right) bands. The number of sources is normalised.

populations are indicated (Figure 3.6 right). Foreground MW stars were removed following a similar procedure as that described above using a combination of parallax and PM cuts. For the PM selection, we examined the stellar density in PM space of sources up to 10 deg from the centre of the SMC and defined an ellipse with the following parameters: centre at $\mu_{\rm RA}$ = 0.76 mas yr^{-1} and $\mu_{\rm Dec}$ = $-$1.12 mas yr^{-1}, semi-major axis at 1.75 mas yr^{-1}s and semi-minor axis at 1.25 mas yr^{-1} (Figure 3.7). This ellipse is larger than the one defined in Section 3.2.2, to distinguish between LMC and SMC stars, in order to include more RC stars in the outer regions of the SMC (not necessarily associated to the SMC itself) and at the same time minimise the influence of the MW. The small difference between the centres of the two PM SMC ellipses reflects the distribution of the type of stellar population dominating the inner and outer regions of the SMC. Zivick et al. (2020) showed that the centre of the PM distribution of red giant stars is clearly offset from where one would place the centre of the distribution of MS stars. The central region of the SMC is masked out in Figure 3.4 but it is included in Figure 3.7. In the ($J - K_s$, K_s) CMDs, we defined a

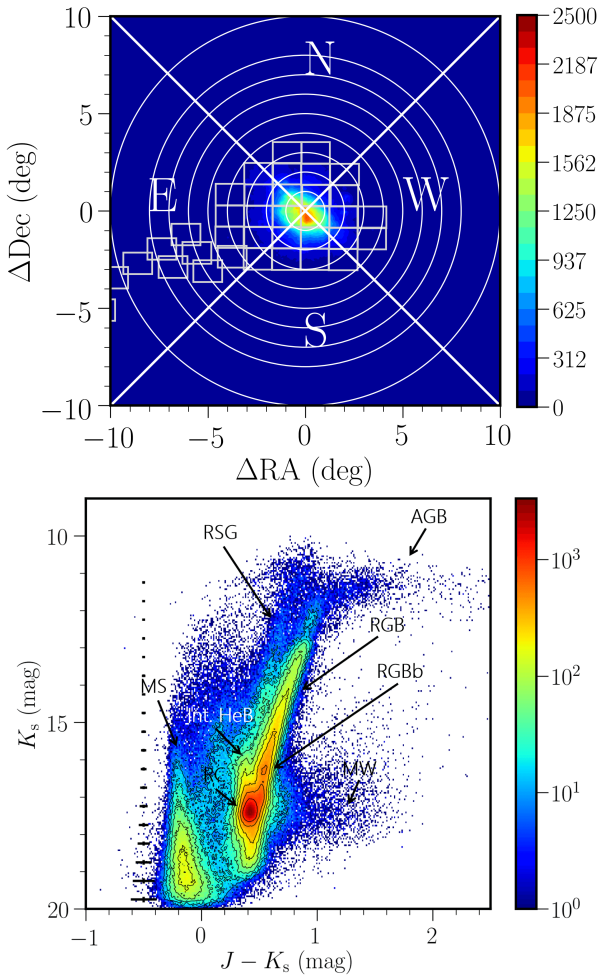

Figure 3.6: (left) Spatial distribution of stars around the SMC and plotted annuli from 0 to 10 deg further divided into 4 regions: N, W, S, and E. VMC tiles are also shown. (right) NIR ($J - K_s$, K_s) Hess diagram (corrected for reddening) of all stars in the region shown in the right panel. Specific stellar populations are indicated as follows: AGB stars, red supergiant (RSG) stars, tip of MS stars, intermediate–age Helium burning (Int. HeB) stars as well as RGB, RC and MW stars while RGBb refers to the RGB bump.

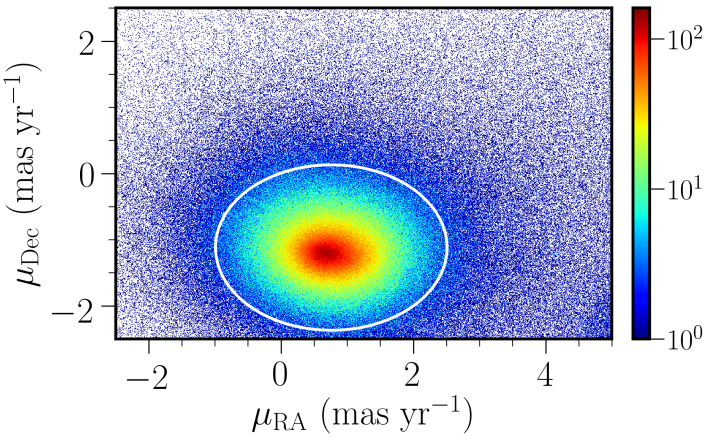

Figure 3.7: Stellar density of objects up to 10 deg from the SMC centre in PM space. The ellipse encloses a region with a reduced number of MW stars.

box to encompass the full extent of RC stars, take into account the influence of RGB stars and minimise contamination from neighbouring stellar populations (Section 3.4 and Figure 3.8). The bright limit ($K_{\rm s}$ = 15 mag) was chosen to include stars beyond the RGB bump for better modelling of the RGB population, while the faint limit ($K_{\rm s}$ = 18.5 mag) represents the 5σ point source limit in the $K_{\rm s}$ band. On the red side, neighbouring populations are RGB and MW stars. Therefore, the red borders of the box are defined as those of K (RGB) and F (MW) from El Youssoufi et al. (2019). On the blue side, the main contaminants are horizontal branch stars, supergiant and subgiant stars. Beyond a radius of 4 deg, photometric uncertainties and metallicity variations elongate the distribution of RC stars, shifting also RGB stars to bluer colours. Therefore, the blue limit for $K_{\rm s} \leq 16.5$ mag is the same as that of region I (red supergiants) from El Youssoufi et al. (2019) to include the full width of the RGB, while for $K_{\rm s} \geq 16.5$ mag, the limit is shifted by $\sigma_{J-K_{\rm s}}$ = 0.13 mag to include RC stars. RR Lyrae stars are generally confined to a compact region below the RC ($0 \leq J - K_{\rm s} \leq 0.5$ mag, $17.7 \leq K_{\rm s} \leq 19.4$ mag). Therefore, they mostly affect the fainter end of the RGB.

3.3 Stellar periphery of the Magellanic Clouds

We used the NIR ($J - K_{\rm s}$, $K_{\rm s}$) CMD to divide the stellar populations into young and old stars. The VHS photometry reaches one magnitude below the RC. Figure 3.9 outlines the morphological features discussed in this work, while Figure 3.10 shows morphology maps of the spatial density of young, old and young+old stars using LMC, SMC and LMC or SMC PM selections (Section 3.2.2). The bin size is 0.12 deg^2. The projection origin for the maps is set at (RA$_0$, Dec$_0$) = (81.24 deg, −69.73 deg) corresponding to the densest point in the LMC bar (de Vaucouleurs & Freeman 1972). The transformation of coordinates from angular to Cartesian was performed through

a zenithal equidistant projection (van der Marel & Cioni 2001). The LMC globular clusters NGC 1841 (ΔRA = 1 deg, ΔDec = -14 deg), Reticulum (ΔRA = 6 deg, ΔDec = 10 deg) and the MW globular cluster NGC 1261 (ΔRA = 17.5 deg, ΔDec = 10 deg) appear as clear overdensities in the morphology maps.

3.3.1 Morphological features

The morphology maps reveal striking substructures in the periphery of the MCs. The Northern Substructure 1 of the LMC detected by Mackey et al. (2016) (ΔRA = 0 deg, ΔDec = 15 deg) is most prominent in the old population extending to $\sim$20 deg from the LMC centre, it is present also in the map of the young population but to a lesser radial extent. The extension of this feature towards the NE is not visible due to incomplete VHS observations. We also detect two substructures on the eastern side of the LMC (Eastern Substructures 1 and 2), revealed at (ΔRA = -15 deg, ΔDec = 1 deg) and (ΔRA = -15 deg, ΔDec = -6 deg), and emerging in the direction of the Galactic disc. We find that these substructures are present despite the strict PM cuts we applied (see Section 3.2.3), suggesting they belong to the LMC rather than to the MW. In the young population and somewhat closer to the LMC disc, Eastern Substructure 1 delineates an approximate circle while Eastern Substructure 2 is similar to a thin stream. There is also a high-density clump between the two substructures at about (ΔRA = -10 deg, ΔDec = 0 deg). These features are less prominent in the old population. de Vaucouleurs (1955a) identified a circular feature in the eastern LMC disc at about (ΔRA = -14 deg, ΔDec = 2 deg) which most likely coincides with Eastern Substructure 1. Eastern Substructure 2 is a new discovery.

South of the LMC we find significant overdensities encompassing the locations of substructures previously identified by Mackey et al. (2018): Southern Substructure 1 at (ΔRA = -2 deg, ΔDec = -12.5 deg) and Southern Substructure 2 at (ΔRA = 6 deg, ΔDec = -10 deg). These substructures are most prominent in the old population. The LMC globular cluster NGC 1841 appears embedded in a low density substructure extending farther south than Substructures 1 and 2. This southernmost extension (Southern Substructure 3; ΔRA = 2 deg, ΔDec = -17.5 deg) probably corresponds to the stream-like feature previously detected by Belokurov & Erkal (2019). In our maps it has a high density in the old populations and its connection to Southern Substructure 1 is unclear. Southern Substructures 1 and 3 characterise the maps obtained from LMC-based PMs, whereas Southern Substructure 2 is also present in SMC-based PM maps, suggesting a possible connection between the LMC and the SMC. This connection, which is supported by an overall extension of the SMC populations towards the east, may be associated with the Old Bridge (Belokurov et al. 2017).

The east of the SMC shows several protuberances that emerge from its more regular elliptical body. We confirm the SMC East substructure (Mackey et al. 2018) at (ΔRA = 18 deg, ΔDec = -14 deg) and the extension of the Wing towards the Magellanic Bridge at (ΔRA = 9.5 deg, ΔDec = -6.5 deg). The SMC East substructure together with the SMCNOD overdensity (Pieres et al. 2017) west of the SMC at (ΔRA = 23 deg, ΔDec = -10 deg) are most obvious in the old population, whereas the extension towards the Magellanic Bridge is better delineated in the young population.

Between the Wing and SMCNOD features there is a clear overdensity extending outwards of the galaxy at (ΔRA = 19.5 deg, ΔDec = -7.5 deg) which is most prominent in the old population. This feature, which we refer to as Northern Substructure 2, appears also in previous studies (e.g. Belokurov & Erkal 2019), but it was not specifically mentioned. All of these SMC features are most prominent in maps created using SMC-based PMs. Combining young and old populations enhances the level of substructure in the outskirts of the MCs with respect to the MW.

3.3.2 Distance and proper motion of morphological features

We determined distances to the morphological features by examining the luminosity function of RC stars within the areas defined in Figure 3.9 and using the CMD box outlined in Section 3.4. We employed a multi–component non–linear least squares fitting technique to characterise the peak of the magnitude distribution produced by RC stars for each feature. Figure (3.11) and Table 3.1 show the histograms and parameters, respectively, obtained for each morphological feature following the same methodology to study the double RC feature across the SMC (Section 3.4). The stellar populations seen in Eastern substructures 1 and 2 features lie at distances similar to that of the LMC ($\sim$50 kpc, e.g. de Grijs et al. 2014). This strengthens the hypotheses that the two substructures are either owing to material being tidally stripped from the disc, or are overdensities in the structure of the disc itself, ruling out that they may be shreds of a dwarf galaxy. We found that Southern Substructures 1 and 2, as well as the SMC East Substructure, are located at distances similar to that of the Magellanic Bridge. If Southern Substructure 2 and SMC East were to be associated with an Old Bridge then this structure would be at the same distance of the Magellanic Bridge. We also found that Southern Substructure 3 is located somewhat closer than the other southern substructures, but this is only marginal in view of the uncertainties involved and the difficult RGB subtraction compared to the other regions. Northern Substructure 1 appears instead further away than the LMC main body suggesting it is made of material tidally stripped from the LMC disc as a result of an interaction with the SMC (Mackey et al. 2016). On the other hand, Northern Substructure 2 appears at the same distance of the SMC main body and it is probably a feature of its ellipsoidal structure. The feature might be undergoing tidal stripping as a consequence of ram pressure effects which dislodged material from the galaxy (e.g. Tatton et al. 2020). Additionally, we find that the SMCNOD substructure is the most distant feature. SMCNOD is located 8 deg away from the SMC centre and its stellar population is similar to that of the SMC main body which, in agreement with Pieres et al. (2017), suggests that it was probably removed from the galaxy.

We have also examined the PMs of the stars enclosed within each morphological feature and compared them with the PM ($\mu_{\rm RA}$, $\mu_{\rm Dec}$) of the LMC (1.871, 0.391) mas yr^{-1} and SMC (0.686, -1.237) mas yr^{-1} obtained using *Gaia* early DR3 (Gaia Collaboration et al. 2020b). These values are consistent with the *Gaia* DR2 values derived by Gaia Collaboration et al. (2018b) up to 6 deg and 4 deg from the LMC and SMC centres, respectively. Table 3.2 shows for each feature the number of stars (Y+O

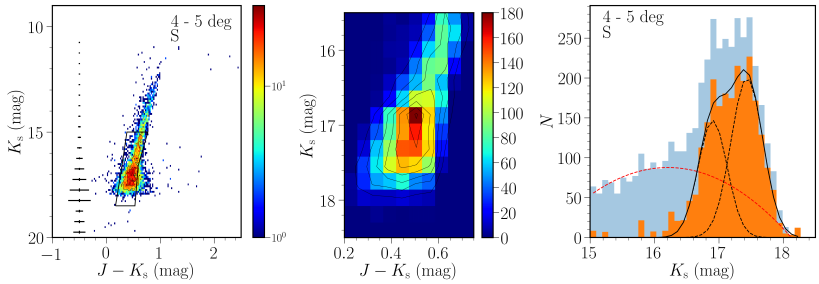

Figure 3.8: (left) Hess diagram (corrected for reddening) for SMC stars within the S sector and a $4 - 5$ deg annulus. (middle) Zoom-in on the selected RC region. (right) Luminosity function of RC stars in the same sector and annulus. The blue histogram shows the distribution of all stars while the orange histogram shows the distribution after the subtraction of the RGB component. The continuous line shows their total fit, while dashed lines represent the separate Gaussian components of the fits (black) and the quadratic polynomial term used to account for RGB stars (red).

according to the CMD selection described in Section 3.2.2), the angular distance from the LMC/SMC centres, and the median PMs with the respective spread.

The features around the LMC are located at angular distances of $11 - 18$ deg from the centre, whereas those around the SMC are at $7 - 8$ deg from the centre. In RA the Southern and Northern substructures have higher PM values than the Easter substructures, all features show however PMs lower than the LMC value. In Dec, Eastern substructures 1 and 2 as well as Southern Substructure 1 show higher PMs than the LMC contrary to the other southern substructures and Northern Substructure 1 which show lower values. Assuming that the substructures belong to the LMC disc then the viewing perspective may account for PM differences of $0.15 - 0.31$ mas yr^{-1} (Kallivayalil et al. 2006b). Except for Eastern Substructure 1 and 2, and for Southern Substructure 2 all other features have both PM components for which the difference with respect to the PM of the LMC can be explained by viewing perspective.

The PMs of the features around the SMC appear higher in RA than in Dec compared to the values attributed to the galaxy. The structure of the SMC is complex and the influence of viewing perspective is difficult to estimate. The PM of the Magellanic Bridge is as expected the most discrepant (in RA) from the SMC because it connects both galaxies. Schmidt et al. (2020) derived ($\mu_{\rm RA}$ = 1.80 ± 0.25, $\mu_{\rm Dec}$ = -0.72 ± 0.13) mas yr^{-1} for the Bridge centre following a procedure that thoroughly removes the influence of MW stars.

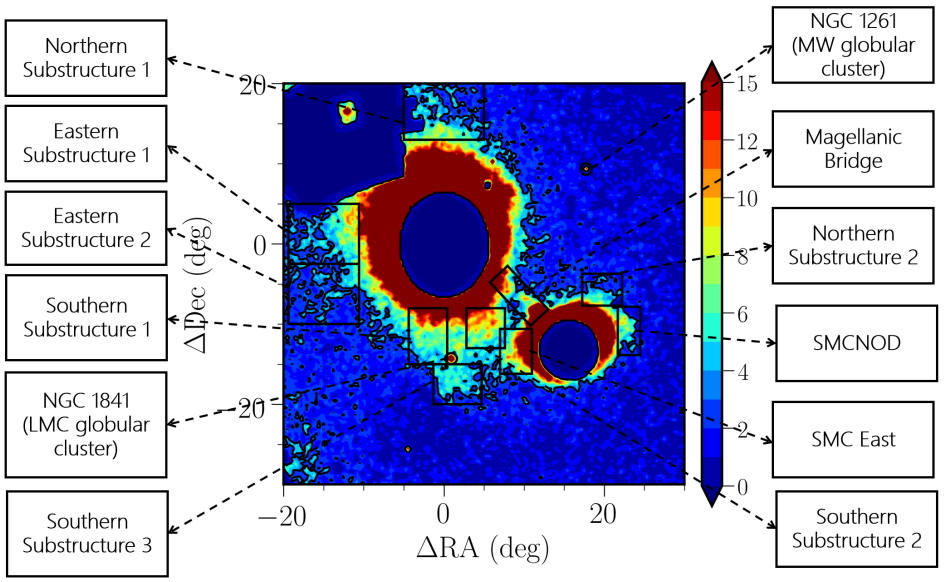

Figure 3.9: Morphological features in the outskirts of the MCs discussed in this paper. The underlying density is that of young and old stars, the bin size is 0.09 deg^2, the colour bar shows the number of stars per bin whereas the map is centred at (RA_0, Dec_0) = (81.24 deg, −69.73 deg). We used elliptical and circular masks of the central region of the LMC and SMC, respectively, to enhance the distribution of stars in the outer regions. Some of these morphological features have already been reported in previous studies: the Eastern Substructure 1 by de Vaucouleurs (1955a), the Northern Substructure 1 by Mackey et al. (2016), SMCNOD by Pieres et al. (2017), the Southern Substructure 3 by Belokurov & Erkal (2019), the Southern Substructures 1 and 2 as well as the SMC East by Mackey et al. (2018), and the Magellanic Bridge by Hindman et al. (1963). The extension of the LMC and SMC outskirts outlined by the SMC East and Southern Substructure 2 embody the Old Bridge of Belokurov et al. (2017), whereas the Eastern Substructure 2 and Northern Substructure 2 have been highlighted for the first time in this work.

Figure 3.10: Morphology maps of young stars (Y; left) dominated by tip of MS and supergiant stars, old stars (O; middle) dominated RGB and RC stars, young and old stars (Y+O; right) surrounding the MCs. The three rows show stars selected based on LMC or SMC PMs (top), LMC PMs (middle) and SMC PMs (bottom). The bin size is 0.12 deg^2 and the maps are centred at (RA$_0$, Dec$_0$) = (81.24 deg, -69.73 deg). The colour bars show the numbers of stars per bin. The central regions of the LMC and SMC have been masked out to enhance the distribution of stars in the outer regions.

Table 3.1: Gaussian parameters, distances and the reduced χ^2 values of the profile fits to the luminosity function of the RC stars in different morphological features.

Feature	μ (mag)	σ (mag)	N (counts)	D (kpc)	$\sigma_{\rm D}$ (kpc)	χ^2
Eastern Substructure 1	16.86 $\pm$ 0.08	0.35	150 $\pm$ 35	47.9 $\pm$1.9	7.72	7.24
Eastern Substructure 2	16.94 $\pm$ 0.04	0.47	95 $\pm$ 8	49.7$\pm$1.0	10.76	4.85
Southern Substructure 1	17.12 $\pm$ 0.01	0.29	395 $\pm$ 19	53.9 $\pm$ 0.4	7.21	2.94
Southern Substructure 2	17.18 $\pm$ 0.01	0.32	227 $\pm$ 10	55.4 $\pm$ 0.5	8.18	1.30
Southern Substructure 3	16.95 $\pm$ 0.06	0.40	531 $\pm$ 10	50.0 $\pm$ 1.3	9.20	5.95
Northern Substructure 1	17.26 $\pm$ 0.03	0.62	123 $\pm$ 6	57.5 $\pm$ 0.9	16.44	2.68
Northern Substructure 2	17.36 $\pm$ 0.02	0.52	92 $\pm$ 5	60.2 $\pm$ 0.7	14.44	1.71
SMCNOD	17.54 $\pm$ 0.03	0.31	51 $\pm$ 5	65.4 $\pm$ 1.1	9.36	1.51
Magellanic Bridge	17.12 $\pm$ 0.01	0.26	411 $\pm$ 23	53.9 $\pm$ 0.5	6.47	2.64
SMC East	17.11$\pm$ 0.03	0.36	255 $\pm$ 23	53.7 $\pm$ 0.8	8.91	7.25

Table 3.2: PMs of morphological features.

Feature	N (counts)	$\rho_{\rm LMC}$ (deg)	$\rho_{\rm SMC}$ (deg)	$\mu_{\rm RA}$ (mas yr^{-1})	$\sigma_{\mu_{\rm RA}}$ (mas yr^{-1})	$\mu_{\rm Dec}$ (mas yr^{-1})	$\sigma_{\mu_{Dec}}$ (mas yr^{-1})
Eastern Substructure 1	4094	16	–	1.33	0.31	0.65	0.60
Eastern Substructure 2	3622	17	–	1.31	0.33	0.49	0.57
Southern Substructure 1	4270	13	–	1.61	0.33	0.59	0.47
Southern Substructure 2	3040	12	–	1.66	0.33	-0.12	0.43
Southern Substructure 3	2286	18	–	1.52	0.34	0.13	0.65
Northern Substructure 1	3460	16	–	1.58	0.31	0.09	0.53
Northern Substructure 2	1720	–	7	1.20	0.27	-1.05	0.20
SMCNOD	1116	–	7	0.93	0.29	-1.13	0.15
Magellanic Bridge	9604	11	8	1.43	0.19	-1.07	0.16
SMC East	5516	–	7	1.31	0.22	-1.12	0.17

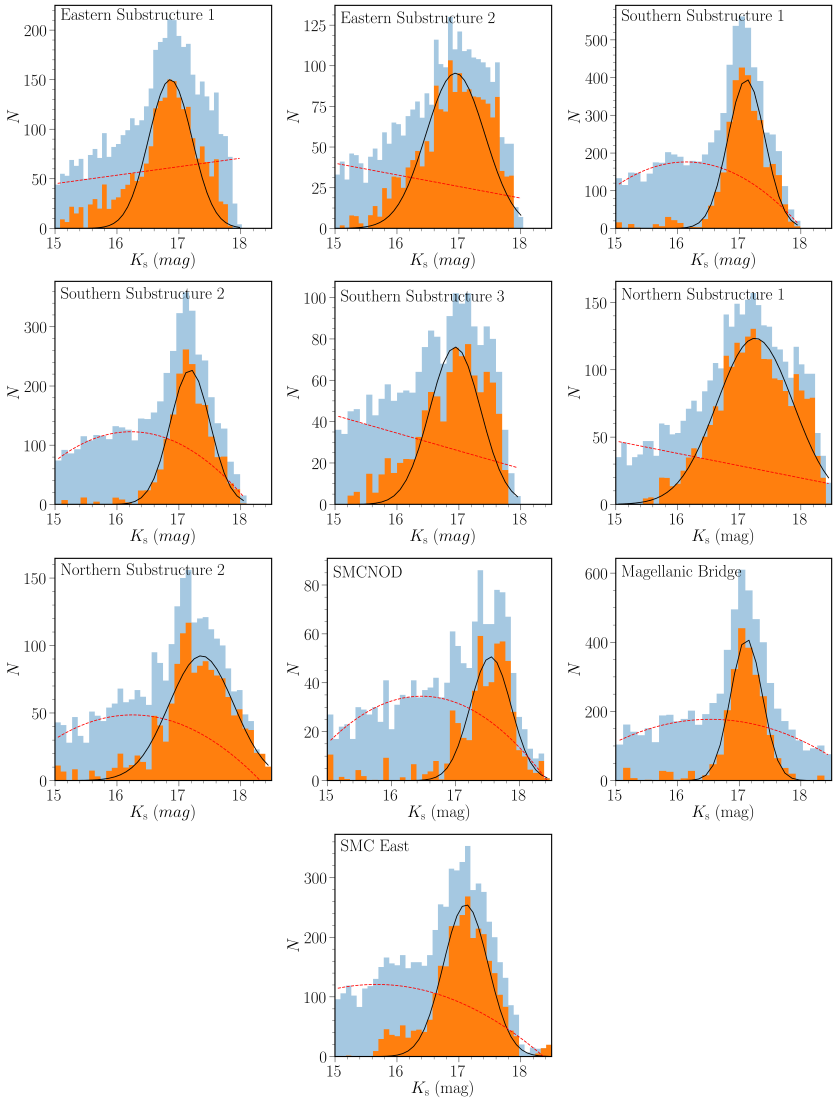

Figure 3.11: Luminosity function of the RC stars of the different morphological features outlined in Figure 3.9. The blue histograms show the observed luminosity functions, whereas orange histograms show the distributions after subtracting the RGB components, the continuous lines show the total fits to the distributions whereas the dashed lines represent the separate components of the fits. The bin size is of 0.09 mag.

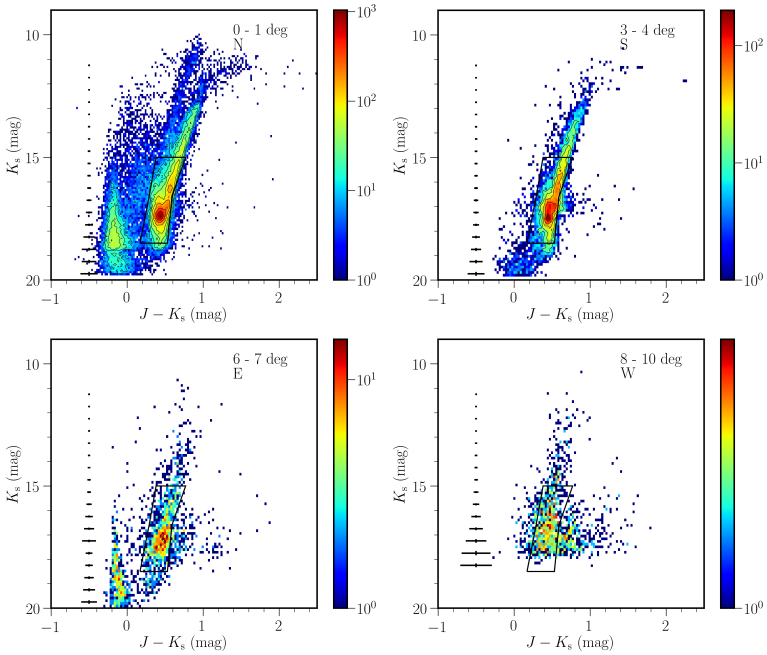

Figure 3.12: NIR ($J - K_s$, K_s) Hess diagrams of a few of the SMC regions discussed in Section 3.4 and presented in full in Appendix 3.6. The colour scale indicates the stellar density on a logarithmic scale per bin. The bin size is 0.027×0.110 deg^2 and the black box limits the region defined to study the distribution of RC stars.

3.4 Double red clump feature in the SMC

Figure 3.6 (left-hand panel) shows the spatial distribution of stars around the SMC, after applying the PM selection criteria (Figure 3.7), in sectors of annuli defined in Section 3.2. The main motivation behind using this cardinal division, is that the tail/Wing as well as the Magellanic Bridge are completely encompassed by the E sector (Figure 3.18). Figure 3.6 (right-hand panel) also shows a Hess diagram of the same stars outlining several stellar populations. A similar Hess diagram for stars within the S sector and the $4 - 5$ deg annulus is shown in Figure 3.8 (with additional examples shown in Figure 3.12), whereas all Hess diagrams corresponding to all sectors in each annulus are shown in Appendix 3.6 (Figure 3.14). These CMDs show that the vertical extent of the RC population is more prominent in the eastern regions out to 10 deg from the centre.

To study the RC stars in more detail, we constructed the luminosity function of the population, see Figure 3.8 (right-hand panel) for stars within the S sector and the $4 - 5$ deg annulus, Figure 3.13 for additional examples at different sectors and annuli, as well as Figure 3.15 for all sectors of each annulus, and obtained distances. Unlike Subramanian et al. (2017) and Tatton et al. (2020), we used the J instead of the Y band to its larger spatial coverage in the VHS survey. We constructed luminosity

functions for RC stars using a bin size of 0.05 mag for regions with radius $R \leq 4$ deg, and 0.1 mag for $R \geq 4$ deg (the bin sizes are on the order of the errors in the $K_{\rm s}$ band). In order to evaluate the luminosity function, we employed a multi–component non–linear least squares fitting method. The CMD box, used to extract RC stars, also includes RGB stars, which we minimised by using a quadratic polynomial term. The main RC component is first modelled with one Gaussian and then, if the reduced χ^2 parameter improves by more than 25 per cent when adding a second Gaussian, the second RC is deemed real. The parameters of the fits to the RC components and the reduced χ^2 values are given in Table 3.3, and the two-dimensional maps of the distances, means, and widths of the RC components are shown in Figure 3.14. Modelling the RGB component proved challenging for some regions ($5-6$ deg S, $6-7$ deg S, $7-8$ deg, $8-10$ deg), where only the brightest RGB component is present. This is owing to VHS observations being limited to just below the RC. In these cases, we modelled the RGB with a linear slope.

$K_{\rm s}$ is an excellent photometric band for absolute RC magnitude determination as it is less affected by reddening and systematic dependence on metallicity than optical bands. Many studies established median RC absolute magnitudes in the $K_{\rm s}$ band, which mostly agree on $M_K = -1.61$ mag. Alves (2000) used K magnitudes from the Caltech Two Micron Sky Survey(Neugebauer & Leighton 1969) of 238 *Hipparcos* RC stars and, under the assumption of no reddening, they found a value of $M_K = -1.61 \pm 0.03$ mag. Using revised *Hipparcos* parallaxes Groenewegen (2008) finds $M_K = -1.54 \pm 0.04$ mag, based on the 2MASS system. The difference in magnitude between the two studies was attributed to a selection bias due to a lack of data for bright nearby RC stars. This was confirmed by Laney et al. (2012) who found $M_K = -1.613 \pm 0.015$ mag from a sample of 226 bright RC stars using accurate K band magnitudes. The drawback of the Alves (2000) study was the quality of the available IR photometry. More recent studies such as Hawkins et al. (2017) and Ruiz-Dern et al. (2018) favour the brighter magnitude of $M_K = -1.61$ mag.

We converted the extinction corrected $K_{\rm s}$ magnitudes of the bright and faint RC components (μ_0 and μ_1) to distance moduli, using the high-precision observations of RC stars in the solar neighbourhood by Laney et al. 2012. Their absolute magnitude in the 2MASS K band corresponds to $M_K = -1.613 \pm 0.015$ mag whereas in the VISTA $K_{\rm s}$ band, it is $M_{K_{\rm s}} = -1.609 \pm 0.015$ mag (González-Fernández et al. 2018). However, since these stars are located in the solar neighbourhood, their absolute magnitude is expected to be different from those of RC stars in the SMC due to differences in metallicity, age and star formation rate. A correction for these population effects is needed and Salaris & Girardi (2002) estimated it to be -0.07 mag in the $K_{\rm s}$ band. They obtained this term by simulating RC stars using stellar population models and including the star formation rate and age–metallicity relation derived from observations and then compared the difference in the absolute magnitudes in the SMC and solar neighbourhood to quantify the corresponding population effects. Once we obtained distance moduli for the different peaks, we calculated distance moduli uncertainties which include both the uncertainty on the absolute magnitude estimate as well as the peak magnitude uncertainty. We converted them to distances and distance uncertainties in kpc, and the values are given in Table 3.3. We followed the same methodology as Subramanian et al. (2017).

Most regions show a bi-modality in their luminosity function distribution, it was first discovered by Nidever et al. (2013) and it can be due to several effects, including distance, LOS depth as well population effects. Reddening has been ruled out as a significant contributor to the spread by Subramanian et al. 2017.

- $0^\circ \leq R \leq 2^\circ$: The bi-modality is less pronounced here than in the outer regions. The difference in magnitude between the bright and faint RC components is on the order of ~ 0.15 mag and is generally less than the width of the bright Gaussian components. The difference between the two peaks is more pronounced in the southern regions. Note that these differences are ten times larger than the error on the peaks, but they are comparable with the width of the RC components. The width of the bright RC component is always larger than that of the faint component. The height of the faint component is always larger than the bright one, except for the northern and eastern regions in the $1^\circ \leq R \leq 2^\circ$ sector.

- $2^\circ \leq R \leq 5^\circ$: A clear separation between the bright and faint RC components becomes obvious in most regions of $2^\circ \leq R \leq 3^\circ$. The difference in magnitude becomes on the order of ~ 0.4 mag. Subramanian et al. (2017) found that this difference is too large to be attributed to any other effect but to different distances in the plane of the sky. The bi-modality has been detected by Nidever et al. (2013) at 4 deg and is likely due to material stripped from the SMC ~ 200 Myr ago. The bi-modality in the western regions was not seen by neither Nidever et al. (2013) or Subramanian et al. (2017).

- $5^\circ \leq R \leq 7^\circ$: A bi-modality is only detected in a few regions. The dominant components are consistent with those in the inner SMC. In region $5-6$ deg W we find a bright component, brighter than previously found, suggesting a foreground structure. In region $6-7$ deg N we find a faint component, fainter than previously found which because of its large distance might belong to the structure known as the Counter Bridge (Diaz & Bekki 2012), whereas a bright component in region $6-7$ deg S might be linked to the Old Bridge (Belokurov et al. 2017). These three features might be influenced by a poor RGB subtraction.

- $7^\circ \leq R \leq 10^\circ$: In the northern regions we detect both a bright and a faint component where the difference in magnitude between the two components is on the order of ~ 0.7. In the region $7-8$ deg S we find a bright component as above, which is possibly linked to the Old Bridge and that at $8-10$ deg appears instead to the east. This demonstrates that the double RC feature is traceable out to 10 deg. A double component in the other regions is less well defined.

The fact that two components are present beyond the E sector at different radii demonstrates that the foreground structure in the form of a distance bi-modality is not solely owing to the Magellanic Bridge and Wing. To further investigate the presence of the double RC feature at these different locations, we explored an alternative cardinal division where we used four sectors (NE, SE, NW, SW) that are

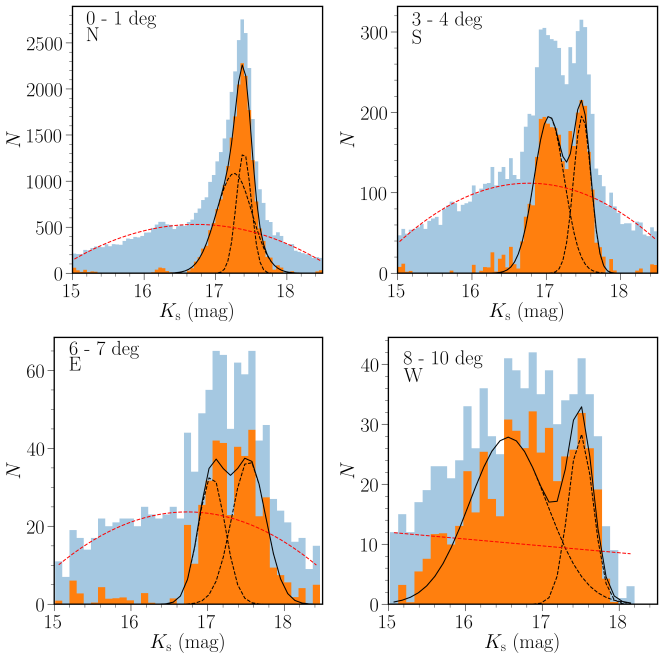

Figure 3.13: Luminosity function of the RC stars in a few different SMC regions discussed in Section 3.4 and presented in full in Appendix 3.6. The blue histograms show the observed luminosity functions, whereas orange histograms show the distributions after subtracting the RGB components and the continuous lines show the total fits to these distributions whereas the dashed lines represent the separate components of the fits.

45 deg offset counter-clockwise from the previous setup (N, E, S, W), see Appendix 3.7. We performed the same analysis for the luminosity functions of the stars within these sectors and found comparable results. This shows also that the faint component detected in the North, which might belong to the Counter Bridge, is present irrespective of the cardinal division scheme chosen. If the bi-modality in the luminosity function of RC stars is interpreted as a distance effect, it will correspond to a difference of $\sim$11 kpc consistent with the findings of Subramanian et al. (2017) and Omkumar et al. (2021). The bright RC component which is detected throughout the N, S, and E sectors out to 10 deg might be owing to a foreground substructure in the periphery of the SMC (including the Magellanic Bridge and the Old Bridge), whereas a faint component detected in the northern outermost regions might belong to the Counter Bridge. Whilst the substructures discussed in Section 3.3 are dominated by single components, the Northern Substructure 2 could also have two, in agreement with the analysis of the RC distribution across the galaxy.

3.5 Conclusions

In this paper, we have presented a study of the outer morphology of the MCs using NIR data from the VHS and ($J - K_s$, K_s) CMDs to distinguish between young (tip of MS and supergiant stars) and old (RGB, AGB and RC stars) stellar populations. We minimise the influence of MW stars by using PM and parallax selection criteria from *Gaia* DR2. Our morphology maps demonstrate that it is possible to trace many of the diffuse stellar substructures present in the periphery of the MCs. Furthermore, we determine distances to these substructures using the luminosity function of RC stars. We confirm the detection of substructures discovered previously such as: the Northern and Southern features in the LMC disc by Mackey et al. (2016, 2018) and Belokurov & Erkal (2019). We also characterise for the first time two new substructures: one on the eastern side of the LMC and one on the northern side of the SMC. A substructure on the east of the LMC was already present in de Vaucouleurs (1955a) and it is possible that both eastern substructures are associated to the disc of the galaxy. The simulations described by Belokurov & Erkal (2019) showed that the tidal influence of the MW and SMC are responsible for creating different substructures in the LMC. The SMC is responsible for creating the northern arm and a more prominent southern arm, while the MW's tidal field can also be responsible for creating, bending and extending the northern arm. The eastern substructures appear consistent with the influence of the MW deflecting the LMC disc. The substructure on the northern side of the SMC is probably associated to the ellipsoidal structure of the galaxy. Overall, we have been able to uncover a wealth of substructures in the periphery of the MCs, showcasing that their outskirts are susceptible to tidal interactions. Mapping these morphological features with fainter stellar populations and comparing their morphology to simulations can provide further constraints on the orbits of past encounters and the mass of the LMC.

We also present a study of the luminosity function of the RC stars from the centre of the SMC to a radius of 10 deg, using NIR data from the VHS and VMC surveys. Previous studies such as Nidever et al. (2013), Subramanian et al. (2017), Tatton (2018) and Tatton et al. (2020) were limited to a radius of 4 deg, therefore only covering the main body of the galaxy. Omkumar et al. (2021) used *Gaia* DR2 data to examine the luminosity function of RC stars up to 10 deg, however, they only detect a double RC feature from 2.5 deg to $5 - 6$ deg in the eastern regions. In this study we find that a bimodal RC feature is present in the eastern, northern and southern regions at different radii suggesting that tidal interactions have affected the entire inner eastern parts of the galaxy and not only its outskirts. In addition, our results reveal that RC stars form a background structure in the north of the SMC which might trace the Counter Bridge (Diaz & Bekki 2012; Wang et al. 2019), and a foreground structure in the south which might trace the Old Bridge (Belokurov et al. 2017). This is consistent with previous studies based on metal-poor red giants (Dobbie et al. 2014), Cepheids and RR Lyrae stars (Ripepi et al. 2017; Jacyszyn-Dobrzeniecka et al. 2020b).

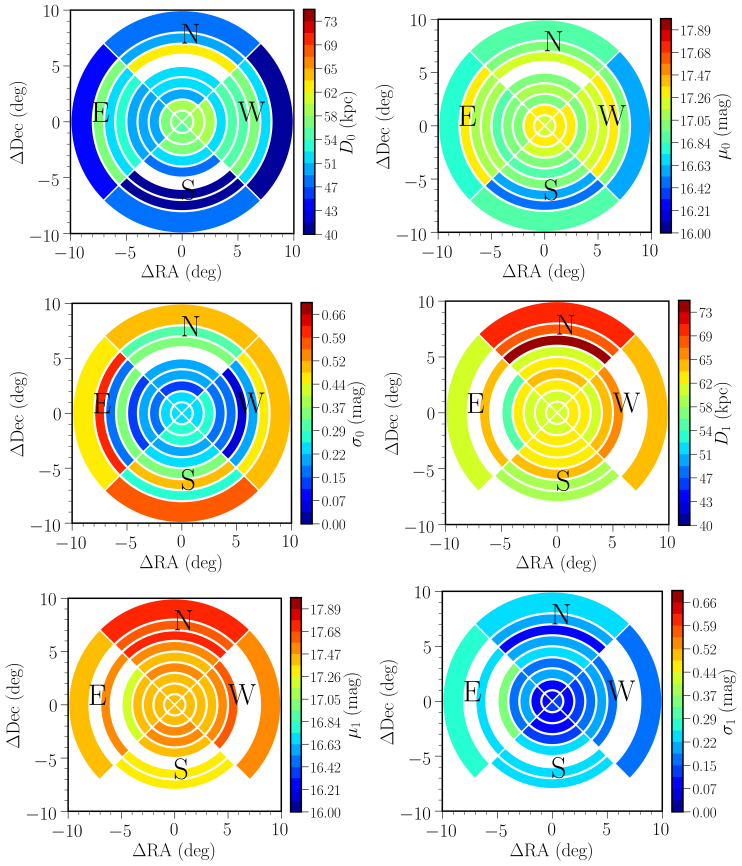

Figure 3.14: Two-dimensional maps of the distance (left), mean brightness (middle) and sigma (right) of the bright (top) and faint RC components (bottom) in all four sectors, N, E, S and W out to 10 deg from the centre of the SMC.

Table 3.3: Gaussian parameters and the reduced χ^2 values of the profile fits to the luminosity function of the RC stars in different areas.

Region	μ_0 (mag)	σ_0 (mag)	N_0 (counts)	D_0 (kpc)	σ_{D0} (kpc)	μ_1 (mag)	σ_1 (mag)	N_1 (counts)	D_1 (kpc)	σ_{D1} (kpc)	χ^2
0–1° N	17.26 ± 0.01	0.25	1083 ± 83	57.5 ± 0.5	6.62	17.40 ± 0.01	0.10	1312 ± 90	61.3 ± 0.4	2.97	2.93
0–1° E	17.27 ± 0.01	0.25	1282 ± 146	57.9 ± 0.6	6.77	17.40 ± 0.01	0.10	1460 ± 155	61.3 ± 0.5	2.97	6.93
0–1° S	17.21 ± 0.03	0.24	947 ± 147	56.3 ± 1.0	6.30	17.40 ± 0.01	0.12	1607 ± 177	61.5 ± 0.5	3.34	6.62
0–1° W	17.25 ± 0.02	0.24	1094 ± 147	57.2 ± 0.7	6.45	17.40 ± 0.01	0.12	1444 ± 155	61.3 ± 0.5	3.34	5.22
1–2° N	17.31 ± 0.01	0.25	1242 ± 86	58.7 ± 0.5	6.89	17.41 ± 0.01	0.10	761 ± 87	61.5 ± 0.5	2.98	2.48
1–2° E	17.26 ± 0.01	0.25	1959 ± 136	57.6 ± 0.5	6.58	17.40 ± 0.01	0.10	1691 ± 132	61.5 ± 0.5	2.89	4.83
1–2° S	17.26 ± 0.01	0.27	1703 ± 92	57.6 ± 0.5	7.16	17.43 ± 0.01	0.10	2448 ± 163	62.1 ± 0.4	2.87	6.51
1–2° W	17.32 ± 0.01	0.24	1658 ± 127	59.2 ± 0.5	6.64	17.44 ± 0.01	0.10	1768 ± 134	62.5 ± 0.4	2.94	4.24
2–3° N	16.98 ± 0.02	0.14	168 ± 20	50.6 ± 0.7	3.19	17.44 ± 0.01	0.21	650 ± 15	62.5 ± 0.5	6.15	1.42
2–3° E	16.95 ± 0.03	0.18	418 ± 64	49.8 ± 0.9	4.08	17.38 ± 0.02	0.22	904 ± 238	60.7 ± 0.7	6.14	1.65
2–3° S	17.26 ± 0.01	0.29	692 ± 29	57.4 ± 0.5	7.66	17.47 ± 0.01	0.11	844 ± 40	63.5 ± 0.4	3.19	1.49
2–3° W	17.35 ± 0.01	0.28	582 ± 54	60.1 ± 0.5	7.88	17.46 ± 0.01	0.11	829 ± 57	63.2 ± 0.5	3.32	2.13
3–4° N	17.08 ± 0.04	0.19	153 ± 14	52.9 ± 1.1	4.72	17.52 ± 0.04	0.18	143 ± 17	64.8 ± 1.3	5.31	1.36
3–4° E	16.99 ± 0.01	0.19	520 ± 17	50.8 ± 0.5	4.44	17.45 ± 0.02	0.16	356 ± 21	62.7 ± 0.6	4.56	1.57
3–4° S	17.04 ± 0.01	0.20	195 ± 8	52.0 ± 0.5	4.88	17.49 ± 0.01	0.12	196 ± 12	63.8 ± 0.5	3.44	1.08
3–4° W	17.01 ± 0.08	0.16	48 ± 12	51.4 ± 2.0	3.78	17.42 ± 0.02	0.17	240 ± 12	62.0 ± 0.7	4.79	1.38
4–5° N	17.02 ± 0.12	0.19	111 ± 73	51.6 ± 2.9	4.46	17.45 ± 0.06	0.24	377 ± 42	62.7 ± 1.7	7.10	1.60
4–5° E	16.94 ± 0.01	0.13	350 ± 37	49.6 ± 0.4	3.08	17.21 ± 0.02	0.35	435 ± 28	56.2 ± 0.7	9.05	1.31
4–5° S	16.90 ± 0.08	0.22	147 ± 29	48.8 ± 1.9	5.05	17.44 ± 0.07	0.25	200 ± 28	62.4 ± 2.0	7.15	2.75
4–5° W	17.16 ± 0.14	0.16	53 ± 42	55.0 ± 3.6	4.12	17.53 ± 0.10	0.20	117 ± 26	65.3 ± 2.9	6.16	1.66

85

Table 3.4: Continued.

Region	μ_0 (mag)	σ_0 (mag)	N_0 (counts)	D_0 (kpc)	σ_{D0} (kpc)	μ_1 (mag)	σ_1 (mag)	N_1 (counts)	D_1 (kpc)	σ_{D1} (kpc)	χ^2
5–6° N	–	–	–	–	–	17.40 ± 0.01	0.32	200 ± 7	61.3 ± 0.5	9.14	0.99
5–6° E	17.15 ± 0.02	0.35	146 ± 7	54.7 ± 0.6	8.88	–	–	–	–	–	1.37
5–6° S	17.02 ± 0.09	0.35	101 ± 9	51.5 ± 2.3	8.22	17.54 ± 0.07	0.19	47 ± 27	65.5 ± 2.1	5.70	1.42
5–6° W	16.83 ± 0.19	0.38	23 ± 5	47.2 ± 4.1	8.27	17.52 ± 0.06	0.16	35 ± 12	64.8 ± 1.5	4.80	4.62
6–7° N	17.47 ± 0.03	0.35	65 ± 5	63.5 ± 0.9	10.13	17.79 ± 0.04	0.10	23 ± 9	73.4 ± 1.4	3.29	0.99
6–7° E	17.05 ± 0.07	0.17	33 ± 8	52.3 ± 1.7	4.19	17.54 ± 0.08	0.22	37 ± 5	65.3 ± 2.4	6.70	0.79
6–7° S	16.54 ± 0.28	0.50	19 ± 3	41.3 ± 5.3	9.43	17.32 ± 0.04	0.26	50 ± 11	59.0 ± 1.2	6.98	1.29
6–7° W	17.30 ± 0.04	0.19	14 ± 3	47.9 ± 1.2	–	–	–	–	–	5.11	1.15
7–8° N	17.00 ± 0.32	0.32	14 ± 5	51.1 ± 7.5	7.64	17.67 ± 0.07	0.22	44 ± 11	69.5 ± 2.4	6.97	2.85
7–8° E	17.27 ± 0.07	0.62	17 ± 2	57.8 ± 1.9	16.53	–	–	–	–	–	1.25
7–8° S	16.52 ± 0.07	0.27	19 ± 3	40.9 ± 1.4	5.16	17.34 ± 0.04	0.23	38 ± 5	59.8 ± 1.1	6.43	1.87
7–8° W	17.03 ± 0.08	0.45	7 ± 1	51.8 ± 2.1	10.77	–	–	–	–	–	1.06
8–10° N	16.92 ± 0.39	0.50	21 ± 5	49.3 ± 8.8	11.47	17.70 ± 0.05	0.22	53 ± 17	70.3 ± 1.8	7.24	3.21
8–10° E	16.74 ± 0.62	0.47	21 ± 11	45.3 ± 13.0	9.74	17.41 ± 0.12	0.27	39 ± 28	61.8 ± 3.1	7.81	1.81
8–10° S	16.91 ± 0.06	0.56	39 ± 4	48.9 ± 1.4	12.71	–	–	–	–	–	2.43
8–10° W	16.56 ± 0.13	0.50	28 ± 5	41.6 ± 2.6	9.65	17.50 ± 0.06	0.16	28 ± 10	64.2 ± 1.8	4.8	4.18

Acknowledgements

We are grateful to the anonymous referee who helped us shape the content and format of the paper with valuable suggestions. We thank the Cambridge Astronomy Survey Unit (CASU) and the Wide Field Astronomy Unit (WFAU) in Edinburgh for providing calibrated data products under the support of the Science and Technology Facility Council (STFC). This project has received funding from the European Research Council (ERC) under European Union's Horizon 2020 research and innovation programme (project INTERCLOUDS, grant agreement no. 682115). We thank Vasiliev Belokurov for the fruitful exchange concerning this work on multiple occasions. This research was supported by the DAAD with funds from the German Federal Ministry of Education and Research within an exchange grant between the Leibniz Institute of Astrophysics Potsdam (AIP, Germany) and the Indian Institute of Astrophysics (IIA, Bangalore). This study is based on observations obtained with VISTA at the Paranal Observatory under programmes 179.B-2003 and 179.A-2010. SS acknowledges support from the Science and Engineering Research Board, India, through a Ramanujan Fellowship. This project has made extensive use of the Tool for OPerations on Catalogues And Tables (TOPCAT) software package (Taylor 2005) as well as the following open-source Python packages: matplotlib (Hunter 2007), NumPy (Oliphant 2015), pandas (McKinney 2010), SciPy (Jones et al. 2001).

3.6 Appendix - Hess diagrams and luminosity functions of RC stars

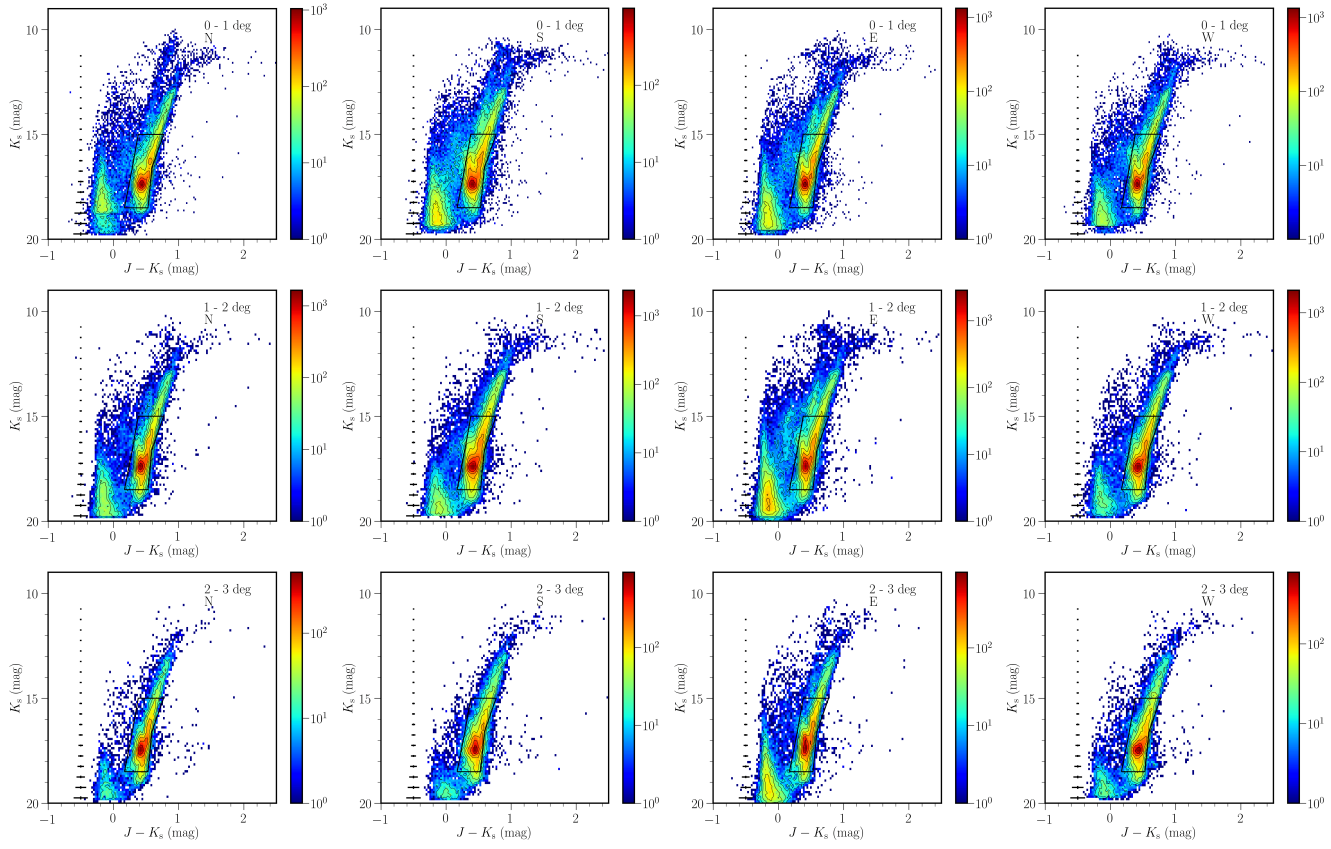

Figure 3.14: NIR ($J - K_s$, K_s) Hess diagrams of different SMC regions. The colour scale indicates the stellar density on a logarithmic scale per bin. The bin size is 0.027×0.110 deg^2 and the black box limits the region defined to study the distribution of RC stars.

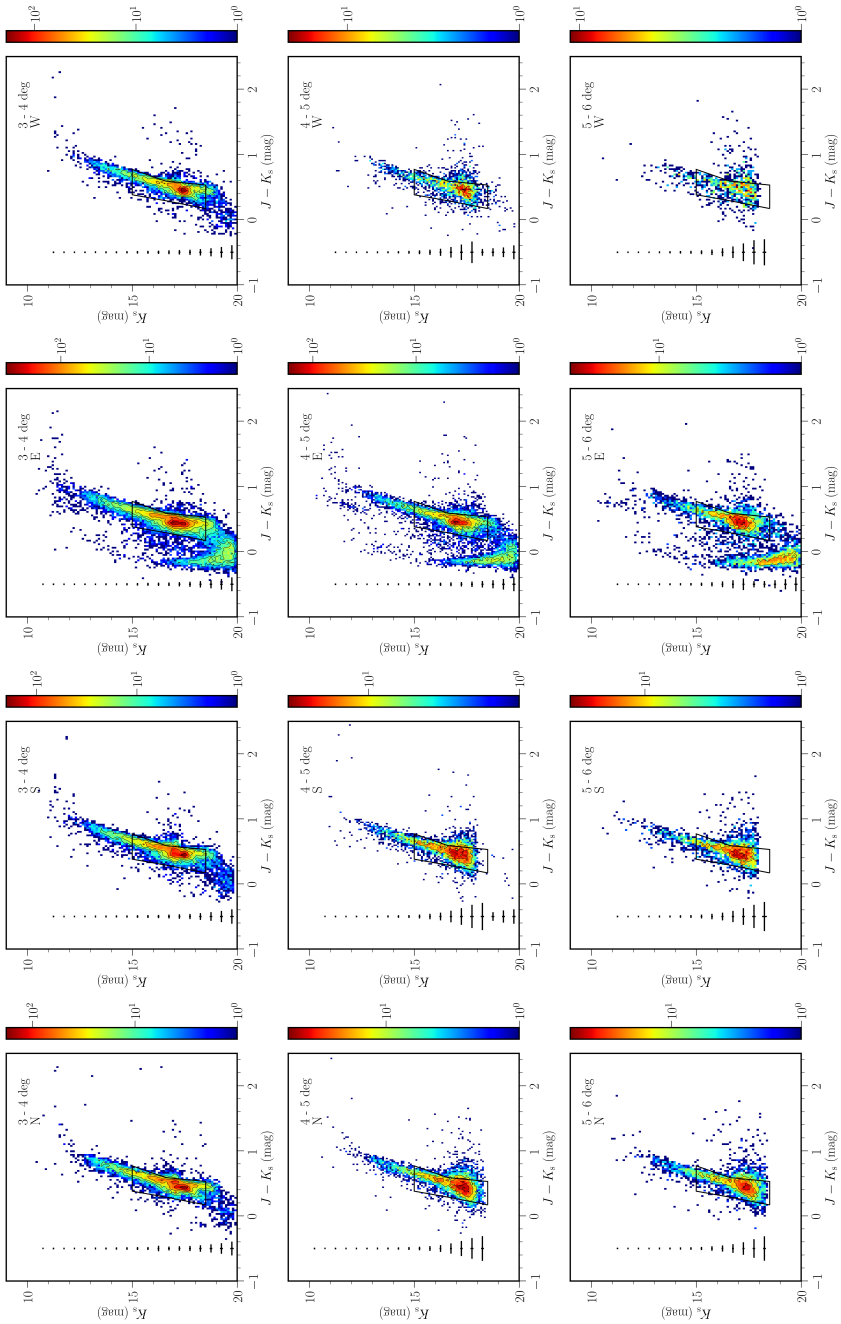

Figure 3.14: (continued)

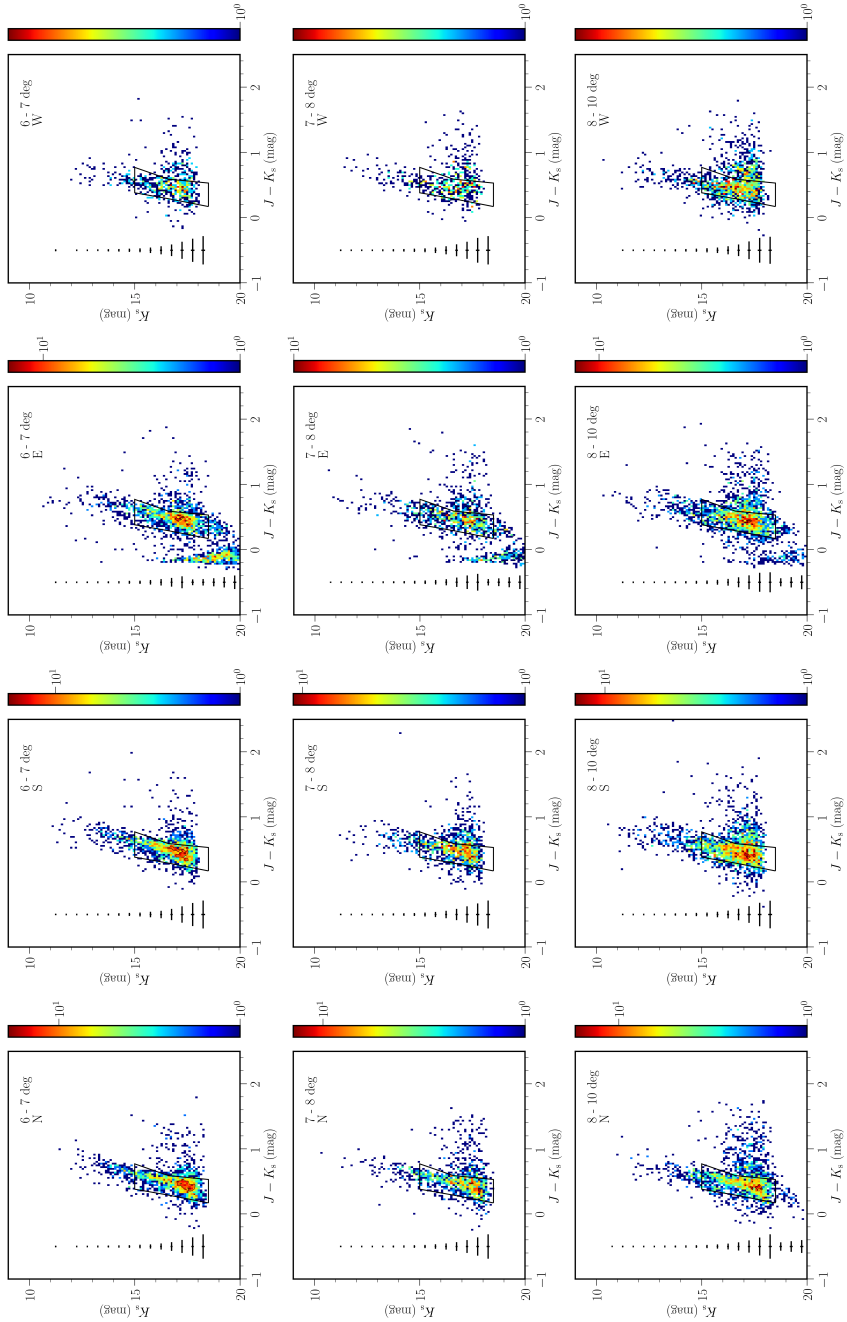

Figure 3.14: (continued)

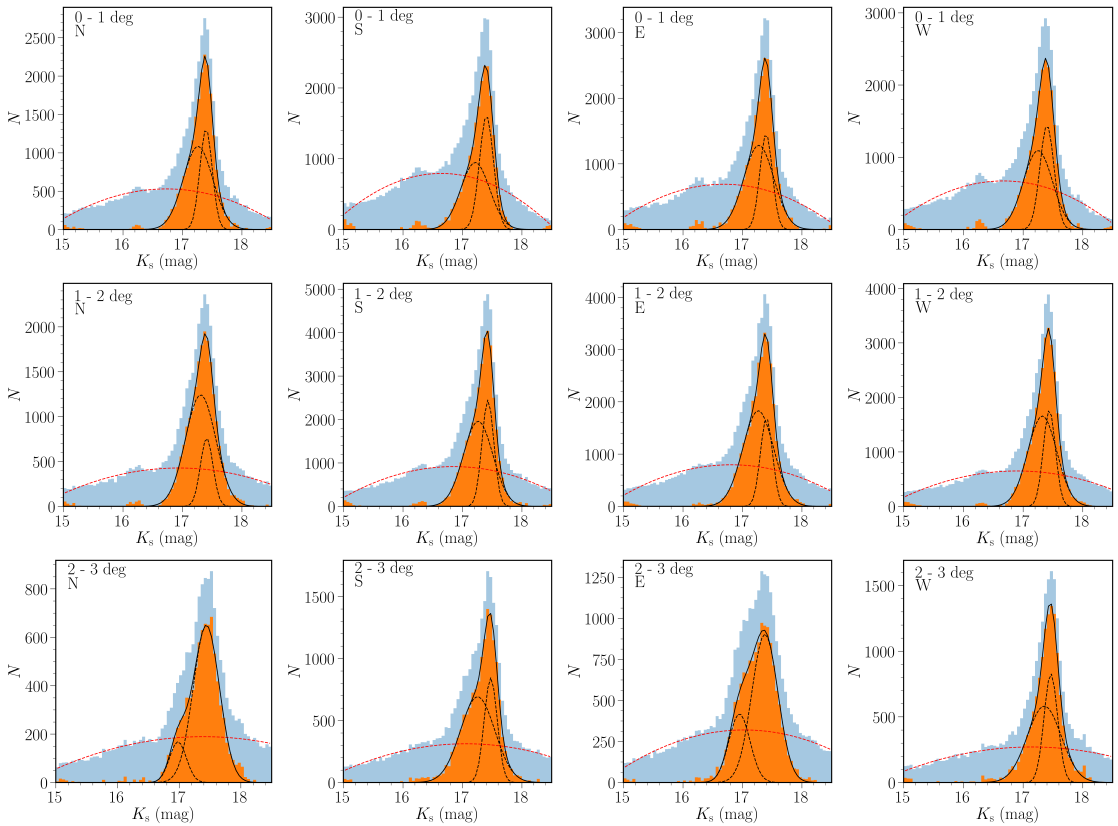

Figure 3.15: Luminosity function of the RC stars in different SMC regions. The blue histograms show the observed luminosity functions, whereas orange histograms show the distributions after subtracting the RGB components and the continuous lines show the total fits to these distributions while the dashed lines represent the separate components of the fits.

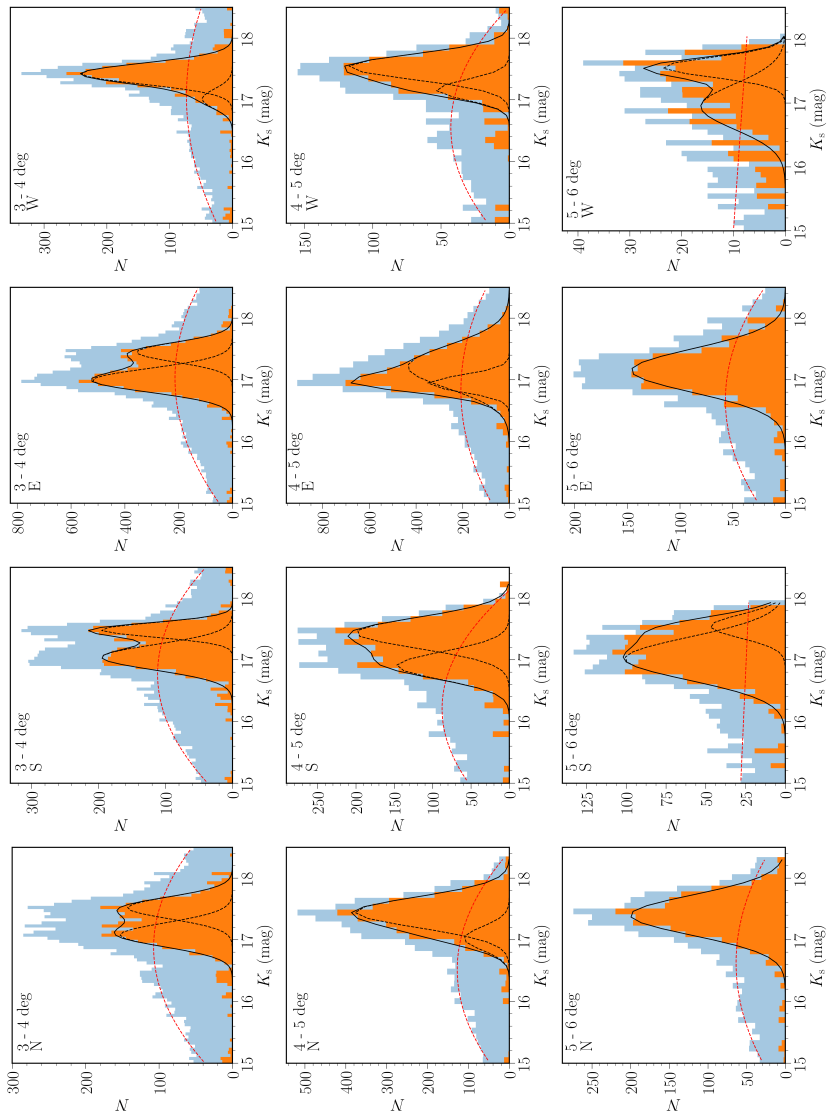

Figure 3.15: (continued)

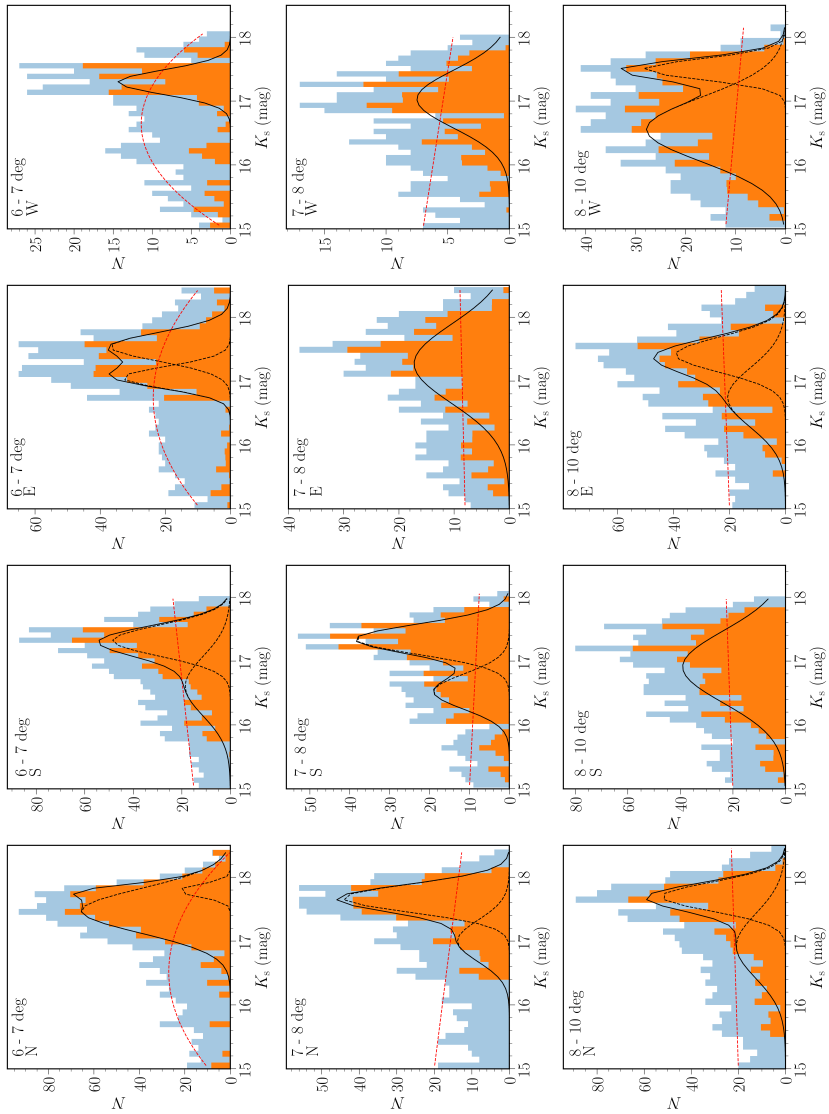

Figure 3.15: (continued)

3.7 Appendix - Alternative cardinal division for RC stars

We explore an alternative cardinal division of the spatial distribution of stars around the SMC. The galaxy is still divided into circular annuli of radii 1 deg, 2 deg, 3 deg, 4 deg, 5 deg, 6 deg, 7 deg, 8 deg and 10° from the centre and each annulus into four sectors: North–East (NE), North–West (NW), South–East (E) and South–West (W), see Figure 3.16. These four regions are 45 deg offset counter-clockwise from the sectors adopted in Section 3.4. As in the previous analysis, we study their NIR ($J - K_s$, K_s) CMD diagrams and RC luminosity functions (Figure 3.17). We only show sectors where a faint component which might be related to the Counter Bridge is detected. Figure 3.18 shows how the cardinal divisions explored in this study map onto the morphological features.

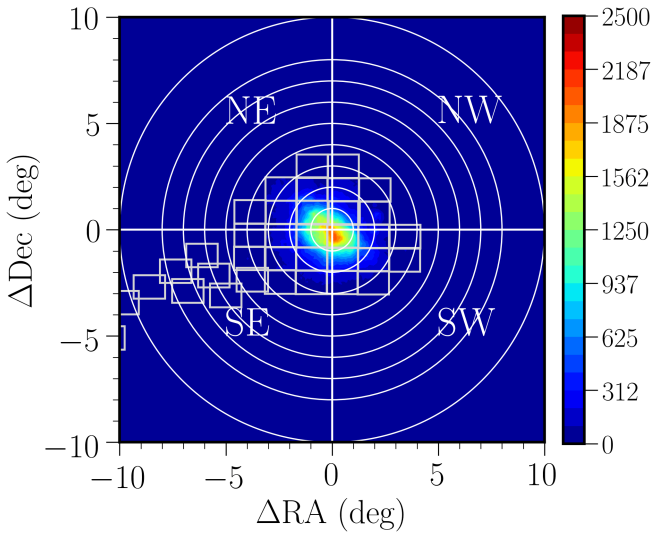

Figure 3.16: Spatial distribution of stars around the SMC and plotted annuli from 0° to 10° further divided into 4 regions: NE, NW, SE and SW. VMC tiles are also shown.

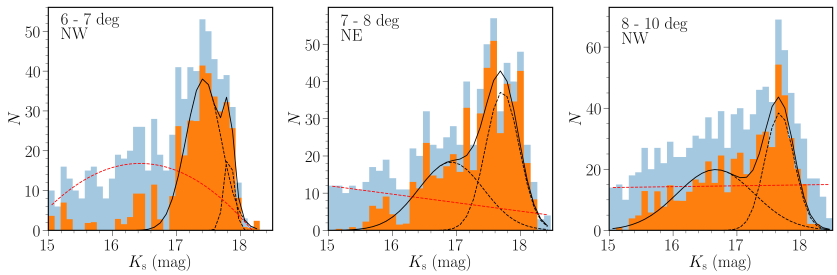

Figure 3.17: Luminosity function of the RC stars in different regions. Each panel shows the luminosity function of the regions discussed in Section 3.4 and Appendix 3.7. The blue histograms show the observed luminosity functions, whereas orange histograms show the distributions after subtracting the RGB components and the continuous lines show the total fits to these distributions whereas the dashed lines represent the separate components of the fits.

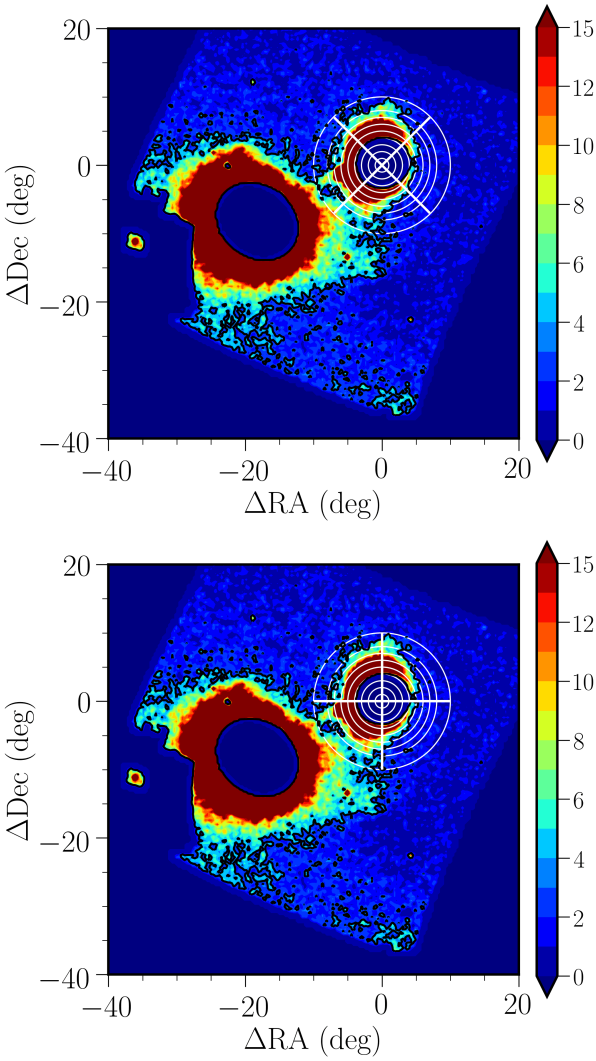

Figure 3.18: Spatial division of the SMC area into sectors and rings as in Figure 3.6 (top) and Figure 3.16 (bottom) superimposed on the density of young and old stars as in Figure 3.9, depicting the morphological features analysed in this study.

4 Kinematics of stellar substructures in the Small Magellanic Cloud

4.1 Introduction

The SMC is a dIrr galaxy, located at ∼60 kpc (de Grijs & Bono 2015) and characterised by a gas rich and low metallicity environment. Together with the LMC, it represents the nearest interacting pair of dwarf galaxies to the MW. The pair has been heavily influenced by dynamical interactions of tidal and/or ram pressure nature and has likely experienced a collision ∼200 Myr ago leading to the formation of the Magellanic Bridge (e.g. Yoshizawa & Noguchi 2003; Diaz & Bekki 2012; Kallivayalil et al. 2013; Zivick et al. 2019; Schmidt et al. 2020) and ∼2 Gyr ago leading to the formation of the Magellanic Stream (e.g. Mathewson et al. 1974; Nidever et al. 2008; D'Onghia & Fox 2016).

The structure of the SMC reflects its complex dynamical H I story where different stellar populations show different features along the line of sight. The galaxy is characterized by an elongated bar-like (bar hereafter) structure along the North East–South West (NE–SW) axis (e.g. de Vaucouleurs & Freeman 1972; Subramanian & Subramaniam 2012; Scowcroft et al. 2016; Jacyszyn-Dobrzeniecka et al. 2016; Ripepi et al. 2017) and an eastern Wing towards the Magellanic Bridge (Shapley 1940). Young stellar populations follow the irregular and asymmetric distribution typical of the H I gas (e.g. Stanimirović et al. 2004a; Di Teodoro et al. 2019) while older stellar populations depict an elliptical/spheroidal distribution (e.g. Cioni et al. 2000b; Zaritsky et al. 2000; Rubele et al. 2015; El Youssoufi et al. 2019).

El Youssoufi et al. (2019, 2021) used photometric data from VMC (Cioni et al. 2011) VHS (McMahon et al. 2013) to obtain a comprehensive morphological view of the MCs and their periphery by tracing stellar populations of different median ages.

El Youssoufi et al. (2019) provided the highest spatial resolution maps of the main bodies of the MCs in the NIR to date. They found that young main sequence stars in the SMC delineate a broken bar while RC as well as RGB stars display signatures of elongations towards the Magellanic Bridge, also detected by Belokurov et al. (2017) and Muraveva et al. (2018), due to a LMC–SMC interaction ∼200 Myr ago. Irregular central features, showing that the inner SMC has been affected by tidal disruption, were also evidenced from the distribution of intermediate-age/old stars (1–7 Gyr old); they include two main overdensities along the NE–SW axis.

Pieres et al. (2017) identified an overdensity (SMCNOD) 8 deg from the centre of the SMC, mainly comprised of intermediate-age (a few Gyr old) stars, which were probably removed from the SMC disc by tidal stripping. El Youssoufi et al. (2021) discovered another substructure in the vicinity of SMCNOD, Northern Substructure 2, lying at a similar distance as the SMC and located seven degrees north-east of the centre; the substructure is probably associated with the ellipsoidal shape of the galaxy and is also comprised of intermediate-age stars. The shell substructure, located at about two degrees from the centre of the SMC in the north-east direction is mainly composed of young ($\sim$150 Myr old) stars suggesting it formed during a recent star formation event as no evidence was found of a tidal origin (Martínez-Delgado et al. 2019).

The outskirts of the SMC appear highly disturbed with tails connected to the Old Bridge, a tail of stars offset from the gaseous Bridge (Belokurov et al. 2017; Mackey et al. 2018; El Youssoufi et al. 2021). The SMC is also characterised by a LOS depth that can reach $\sim$30 kpc depending on the type of stellar tracer (e.g. Subramanian & Subramaniam 2012; Jacyszyn-Dobrzeniecka et al. 2016, 2017; Ripepi et al. 2017; Muraveva et al. 2018). Furthermore, a foreground population manifesting itself as a bi-modality in RC distances has been measured $\sim$11 kpc in front of the SMC's main body (e.g. Nidever et al. 2010; Subramanian et al. 2017; Omkumar et al. 2021; El Youssoufi et al. 2021). This is likely a perturbed population formed at smaller SMC radii and driven outwards (Cullinane et al. 2023). The complex nature of the structure of the SMC is also emphasized by filaments, arcs and shells in the distribution of HI gas (e.g. Stanimirović et al. 2004a; Di Teodoro et al. 2019). Pingel et al. (2022) provided the most sensitive and detailed view of HI emission associated with the SMC, showing details on scales from 10 pc to 5 kpc.

Spectroscopic observations have made significant contributions to the measurement of stellar motions leading to a greater understanding of galaxy kinematics, formation and evolution. Our knowledge of RVs of SMC stars has been limited to modest stellar samples from a few types of tracers such as luminous supergiants (Ardeberg & Maurice 1977, 1979), Cepheids (Mathewson et al. 1988), carbon stars (Hardy et al. 1989; Hatzidimitriou et al. 1997; Kunkel et al. 2000), RC stars (Hatzidimitriou et al. 1993) and RGB stars (Suntzeff et al. 1986). More recently, the kinematics of RC and RGB stars in the periphery of the galaxy have been mapped by MagES (Cullinane et al. 2020).

Harris & Zaritsky (2006) provided the first large spectroscopic survey of RGB stars in the SMC and derived a velocity gradient of 8.3 km s^{-1} deg^{-1}. They also concluded that the SMC is supported by its velocity dispersion rather than by rotation. Evans & Howarth (2008) undertook a large spectroscopic survey of massive stars in the SMC.

They obtained a local velocity dispersion similar to that of RGB stars (σ = 30 km s^{-1}), however unlike Harris & Zaritsky (2006), they found evidence of rotation with a mean velocity gradient of 26.3 ± 1.6 km s^{-1} deg^{-1} at PA = 126.2 ± 3.9 deg. Dobbie et al. (2014) used a large sample of RGB stars to study the kinematics of the SMC, and detected signatures of rotation with an observed rotation curve between $20 - 40$ km s^{-1} at similar PAs ($120 - 130$ deg) to Evans & Howarth (2008). Additionally, Dobbie et al. (2014) found evidence of tidal stripping in the outer SMC. De Leo et al. (2020) used a sample of red giants and found significant tidal disruption in the inner 2 kpc of the SMC using a combination of proper motion and RV measurements, but with no obvious signature of rotation. Stanimirović et al. (2004a) obtained one of the first rotation measurements in HI using RVs with a maximum velocity of 50 km s^{-1}, a mean PA of 40 deg and a velocity dispersion of about 22 km s^{-1}. These results were confirmed by Di Teodoro et al. (2019) using spatially higher resolution observations of HI in the SMC. Differences in velocity dispersion of stars from different stellar populations result also from chemodynamical simulations of the SMC, LMC and the Galaxy (e.g. Bekki 2009). In a first instance, the apparent gradient in RV is of the same order of magnitude as the velocity dispersion and the rotation amplitude which means that bulk motion and rotation cannot be inferred independently from RV data alone.

Until recently, advances made by spectroscopic studies were mostly constrained to one dimensional RVs, highlighting the importance of PMs for a comprehensive understanding of the 3D kinematics and dynamics of the galaxies. The *Hipparcos* satellite provided one of the first PM measurements in the SMC (Kroupa & Bastian 1997), the sample however was limited to eleven massive stars and the uncertainties were of the order of ∼65%. Observations with HST by Kallivayalil et al. (2006b) measured the PM of the SMC to an accuracy of 15% allowing the determination of the PM of the centre of mass of the galaxy and showcasing that the MCs are most likely on their first infall towards the MW or are on a long eccentric orbit. Subsequently, Kallivayalil et al. (2013) reduced the PM uncertainties to 1–2% by increasing the time baseline with additional HST observations, but no conclusion could be reached about the rotation of the galaxy perhaps due to the small number of targeted fields. No evident rotation in the plane of the sky was also found by van der Marel & Sahlmann (2016) using PMs for eight stars from the TGAS Catalog, which contains PMs only for stars in common between *Gaia* DR1 (Gaia Collaboration et al. 2016a) and the *Hipparcos* Tycho–2 Catalog.

Oey et al. (2018) used *Gaia* DR2 PMs in combination with RVs from the Runaways and Isolated O-Type Star Spectroscopic Survey of the SMC (RIOTS4; Lamb et al. 2016) and concluded that the bar and Wing of the SMC are kinematically distinct features, with the Wing having a consistent transverse motion along the Bridge towards the LMC. Results by Murray et al. (2019) showed that the 3D kinematics of a sample of young massive stars (their RV follows that of the HI gas) is inconsistent with disc rotation in the SMC. Niederhofer et al. (2018a) used ground-based VMC observations to present the first stellar resolved PM map of the SMC. This map revealed a non-uniform velocity pattern indicative of a tidal feature behind the main body of the galaxy and a flow of stars along the LOS. Zivick et al. (2019) and Schmidt et al. (2020) studied the kinematics of the Magellanic Bridge and confirmed that old and young

stellar populations are moving away from the SMC towards the LMC. Additionally, Niederhofer et al. (2021) suggested a dynamical stretching of the galaxy with ordered motion of intermediate-age/old stars from the SMC towards the Old Bridge, as well as a stellar motion in the North which might be related to the Counter Bridge (Diaz & Bekki 2012). Grady et al. (2021) found evidence of tidal stripping in the SMC both in PM and metallicity space. The density and velocity flow of stars from the SMC to the LMC along the Bridge is traced by *Gaia* EDR3 data globally and separately for young and evolved stellar populations (Gaia Collaboration et al. 2021b). A best-fit model of the SMC kinematics, based on Gaia DR2, highlights the need to distinguish among the different stellar populations once sufficiently populated and widely distributed RV samples become available (Zivick et al. 2021).

The aim of this paper is to use available spectra from the ESO Science Archive Facility (SAF) to increase the sample of RVs and characterise the kinematics of the morphological features belonging to the SMC and its vicinity. The paper is organised as follows: in Section 4.2 we describe the used data sets and sample selection; we outline the method and steps involved in obtaining RVs in Section 4.3 and we describe our results in Section 4.4, while in Section 4.5 we summarise our main conclusions and future prospects.

4.2 Sample Selection

To select a sample of stars for which to search the ESO SAF for available spectra, we used NIR photometry from the VMC survey and VHS. We distinguished between stars belonging to different stellar populations as in El Youssoufi et al. (2019), using regions in the CMD with different median ages and evolutionary stages. Additionally, we used 2MASS (Skrutskie et al. 2006) photometry for objects that are too bright for the VISTA surveys. The ESO SAF provides access to data acquired with ESO telescopes. Raw, processed and catalogued data can be queried via different web query interfaces. In our work, we used the spectral query form[1] that gives access to reduced spectral ESO phase 3 data products. In the following subsections, we outline our selection criteria for both the photometric and spectroscopic data sets as well as describe the parameters encompassed by the spectroscopic sample.

4.2.1 Photometric data

The VMC survey and VHS are multi-band photometric surveys carried out using VIRCAM (Dalton et al. 2006; Emerson et al. 2006). We used observations in the J and $K_{\rm s}$ bands within a 10 deg radius from the SMC's optical centre, RA=13.05 deg and Dec=$-$72.83 deg at the epoch J2000 (de Vaucouleurs & Freeman 1972). The VMC data were acquired between February 2010 and November 2016 and were released as part of Data Release 5 (DR5) of the VMC survey[2]. VMC observations reach 5σ point source limits of J = 22 mag and $K_{\rm s}$ = 21.5 mag (in the Vega system) across an area

[1] https://Archive.eso.org/wdb/wdb/adp/phase3spectral/form
[2] https://www.eso.org/sci/publications/announcements/sciann17232.html

of $\sim$43 deg^2 on the SMC component of the survey. The median FWHM of point-like sources in the VMC images corresponds to 1 arcsec in J and 0.93 arcsec in K_s. Beyond this area, VHS observations reach 5σ limits of J=19.3 mag and K_s=18.5 mag (also in the Vega system). The median FWHM of point-like sources in the VHS images corresponds to 0.99 arcsec in J and 0.91 arcsec in K_s. VHS observations obtained until 2017 March 30th were released as part of DR5 of the VHS survey[3], whereas for VHS observations obtained until 2017 September 30th only raw images are publicly available. VMC and VHS images were initially processed by CASU using VDFS (Emerson et al. 2006) and further processed by WFAU as well as stored and made available to the community at VSA (Cross et al. 2012). We used the aperture corrected magnitudes calculated within a 2 arcsec diameter (`jAperMag3` and `ksAperMag3`), as these are the most reliable magnitudes for point sources, from the *vmcsource* and *vhssource* tables. These magnitudes were calibrated as outlined by González-Fernández et al. (2018). VMC and VHS observations overlap in the area of the Magellanic Bridge and around the SMC. We eliminated duplicate sources by keeping the VMC sources because VMC data are deeper than the VHS data. Our initial selection criteria refer to detections in both J and K_s bands for objects that have at least a 70 per cent probability of being stars (`flag mergedClass` = -1 `or` -2), as well as with photometric uncertainties better than 0.1 mag in both bands. Furthermore, we only selected sources with minor quality issues (`flag ksppErrBits` $\leq$ 256 `and jppErrBits` $\leq$ 256). Applying these criteria, we obtained 3 407 966 sources.

2MASS data across the SMC were obtained from a dedicated 1.3 metre telescope at the Cerro Tololo Inter-American Observatory. They correspond to a sensitivity of J=15.8 mag and K_s=14.3 mag (in the Vega system) at a signal-to-noise ratio (SNR) of 10. The median FWHM of the 2MASS images corresponds to 2.9 arcsec in both J and K_s. However, multiple dithered observations improved the spatial resolution of the images. 2MASS observations were acquired between 1997 June and 2001 February. The data were downloaded from the Gaia@AIP portal[4]. We required that the objects were detected in both bands, with photometric uncertainties smaller than 0.05 mag, and quality flags applied to the J, H and K_s bands (we included the H band to obtain a more reliable sample), as follows: photometric quality flag (`flag ph_qual` = AAA, reflecting detections where valid measurements were made with a SNR>10 and photometric errors below 0.1 mag, Read flag (`flag rd_flg` = 222 indicating that the default magnitude is derived from a profile-fitting measurement made on six individual 1.3 s exposures covering the sources, blend flag (`flag rd_flg` = 111, indicating that one component was fit when estimating the brightness of the source, contamination and confusion flag (`flag cc_flg` = 000, where only sources unaffected by known artifacts are kept.In total, 27 716 sources were selected, excluding sources in common with the VISTA sample. We note that the difference between the filter systems (e.g. Cioni et al. 2011; González-Fernández et al. 2018) does not influence our study.

[3] https://www.eso.org/sci/publications/announcements/sciann17290.html
[4] https://gaia.aip.de/

We combined data from *Gaia* EDR3 (Gaia Collaboration et al. 2021a) with the NIR samples because the astrometric solution (RA and Dec – position on the sky, ω – parallax, $\mu_{\rm RA}$ and $\mu_{\rm Dec}$ – PM) allowed us to reduce the number of MW foreground stars. *Gaia* EDR3 data are based on observations collected during the first 34 months of the mission which started in 2013 December. They include objects with a limiting magnitude of G= 21 mag (in the Vega system). We performed the cross-correlation between *Gaia* EDR3, VMC and VHS data to retain sources within a distance of 1 arcsec. The cross-match of *Gaia* EDR3 and 2MASS is provided by the *Gaia* Data Processing and Analysis Consortium. The selection criteria we applied to maximise the number of SMC stars are the following: $\omega \geq 0.2$ mas, $-4 \leq \mu_{\rm Dec} \leq 2$ mas yr^{-1} and $-2.5 \leq \mu_{\rm RA} \leq 4.5$ mas yr^{-1}. The parallax criterion is the same as in El Youssoufi et al. (2021) whereas the PM criteria encompass also the diffuse component around the galaxy. These criteria remove bright MS and giant stars of the MW (e.g. Vasiliev 2018), but due to the uncertainties of parallax and PM at the distance of the SMC do not allow us to distinguish MW stars among the faint sources. In total, $1\,931\,462$ sources were removed from our sample based on these criteria.

Furthermore, we used OGLE III (Soszyński et al. 2011) and IV (Soszyński et al. 2015, 2016) data to exclude Cepheids, RR Lyrae stars and Long Period Variables from our sample because their corresponding ESO SAF spectra will also include a variation due to the intrinsic stellar pulsation velocity which is difficult to disentangle with single-epoch spectra. The exclusion of variable stars was performed using TOPCAT[5] and a maximum cross-matching distance of 1 arcsec. In total, $30\,668$ variable sources were removed from our sample.

The resulting photometric data set contained $1\,504\,220$ sources. Their CMD and spatial distribution are displayed in Figure 4.1.

4.2.2 Spectroscopic data

We initially selected from the ESO SAF all objects with 1D spectra within a 10 deg radius from the SMC optical centre. The query form offers access to various parameters and the most relevant to us are outlined in Table 4.1. The ARCFILE (column 1) represents the name under which the data product is stored in the ESO SAF where the timestamp (ADP.timestamp) specifies the time of the data archival. The coordinates RA and Dec (columns 2 and 3) are given in the FK5 J2000 coordinate system which are equivalent to equatorial coordinates and coordinates in the International Celestial Reference System (ICRS); the instrument and spectral grating used for the observations (columns 4 and 5) are also indicated. Column 6 represents the wavelength coverage λ, column 7 the resolving power R ($\lambda/\Delta\lambda$) and column 8 the median SNR of the spectra. Columns 9 and 10 show the Programme ID associated with the spectra and the observing date on which the spectra were obtained, respectively. Column 11 contains the product version. For single observing blocks where more than just one exposure is available, the individual spectra are stacked and are referred to as product version 2. However this is only available for science spectra with identical instrument set ups belonging to the same observing block. Otherwise, single spectra are referred to as product version 1.

[5]http://www.star.bris.ac.uk/ mbt/topcat/

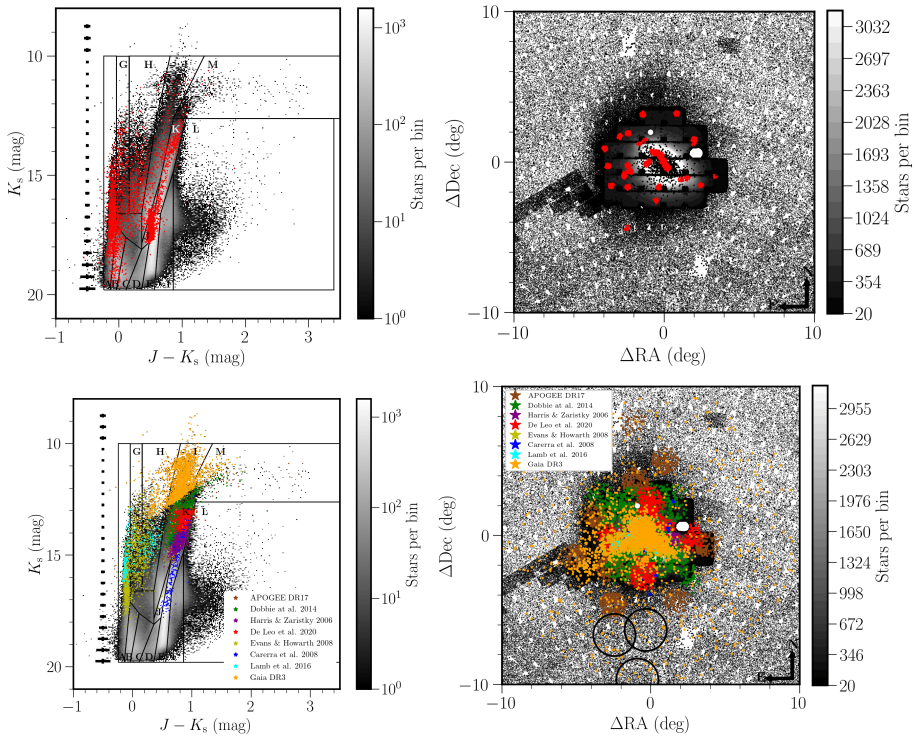

Figure 4.1: (top-left) NIR ($J - K_s$, K_s) Hess diagrams of the SMC stars after the cross-match with *Gaia* EDR3 data. The grey scale indicates the stellar density on a logarithmic scale whereas horizontal bars show the photometric uncertainties as a function of magnitude. VMC, VHS and 2MASS photometry is used. Points in red refer to stars with available spectra in the ESO archive, after applying the selection criteria discussed in Section4.2. Boxes outline the stellar population regions as in El Youssoufi et al. (2019). (top-right) Spatial distribution of SMC stars. The stellar clusters 47 Tuc and NGC 362, at (ΔRA, ΔDec) of (2.1 deg, 0.6 deg) and (−0.9 deg, 1.96 deg) respectively, have been excluded using circular masks. Rectangular regions of high stellar density represent the location of VMC tiles. The overdensity at (ΔRA, ΔDec) of (5 deg, 8 deg) corresponds to a tile in the Magellanic Stream component of the VMC survey. The gaps at the bottom of each VISTA tile refer to the excluded detector #16. The grey scale indicates the stellar density per deg^2, with (red) and without available spectra in the ESO archive. (bottom-left and -right) As figures in the upper panels but with points in colour referring to stars with available spectra in different literature studies. Circles to the extreme outskirts encompass the regions studied using data from the Magellanic Edges Survey (Cullinane et al. 2023).

In order to find photometric counterparts for the selected spectra, we used TOPCAT and a maximum cross-matching distance of 1 arcsec (Figure 4.2). The cross-match was done using ICRS coordinates at the J2000 epoch. For each row in the spectroscopic catalogue only the best (nearest) match from the photometric catalogue will appear as a result, but rows from the photometric catalogue may appear multiple times. This allowed us to group data by their source identifier (source ID) and identify objects with more than one spectrum. Not every object of the spectroscopic catalogue had a match in the photometric catalogue because MW stars and variable stars were excluded from our photometric catalogue using the selection criteria described in Section 4.2.1. We found a photometric counterpart for $24\,609$ spectra.

As stars can have multiple observations, we decided to use only the best spectrum of each star in terms of R and SNR. The first step was to group data by source ID and identify sources with more than one spectrum. We then proceeded to select spectra from each data group with the highest value of R; at this stage there can still be multiple spectra as more than one spectrum can have the same R. From this list of high resolution spectra, we proceeded to select spectra with the highest value of SNR, which can also result in multiple spectra. We found that only 22 sources still have multiple spectra and we proceeded to pick a random spectrum from among those available. Furthermore, we applied one last positional cut to discard spectra belonging to the MW globular clusters 47 Tuc and NGC 362. We masked two areas centred at (ΔRA= 2.1 deg, ΔDec= 0.6 deg) and (ΔRA=-0.9 deg, ΔDec = 1.96 deg) with radii of 0.22 deg and 0.17 deg, respectively. Finally, we selected only spectra with SNR ≥ 10. After applying these selection criteria we obtain a sample comprised of 3814 spectra, of which about 97 per cent (3700) refer to observations with the GIRAFFE spectrograph of FLAMES. We decided to focus only on this sample because the remaining 114 spectra were obtained with other instruments and are insufficient to quantify possible systematic uncertainties. The GIRAFFE spectra in our sample have not been associated with journal publications as is visible in the ESO SAF. However, during the revision of our work an analysis of 206 RGB stars members of the SMC appeared in Mucciarelli et al. (2023). The distribution of the 3700 sources on the CMD and across the SMC is shown in Figure 4.1.

FLAMES is a multi-object spectrograph mounted on the Unit Telescope 2 (UT2; Kueyen) of the Very Large Telescope (VLT) facility at the ESO Paranal Observatory. It gives access to targets across a field-of-view of 25 arcmin in diameter and feeds two spectrographs, GIRAFFE and UVES. GIRAFFE covers the visible range, $370-950$ nm, with three types of feeding fibre systems: MEDUSA, IFU, ARGUS. We limited our study to the MEDUSA mode as we are interested in 1D spectra of individual stars. In this mode, GIRAFFE provides intermediate to high resolving power (R from ~ 5000 to $38\,100$) spectra and can observe up to 132 targets (including sky fibres) at a given time. Each fibre has an aperture of 1.2 arcsec on the sky. The spectra obtained by GIRAFFE are cleaned from cosmic rays as a pre-processing step and consecutively have most of their instrument signature removed; they have been de-biased, flat fielded, extracted, and wavelength calibrated. Their wavelength scale has been corrected to the heliocentric reference system using barycentric, heliocentric and geocentric corrections. However they are neither flux calibrated, nor sky subtracted.

Additional information about the spectra is available in the ESO Phase 3 Data Release Description document[6].

Figure 4.2 shows the parameter ranges of the spectra used in our study. The spectra have R from 6500 to $38\,000$, with 68 per cent having $R{\leq}10\,000$ and the SNR ranges from 10 to 200, with 75 per cent of the spectra having a SNR $\leq$50. Most of the spectra were obtained during the years 2003, 2010 and 2019. The distance between photometric and spectroscopic counterparts ranges from 0 to 1 arcsec with 61 percent of the sources having a distance $\leq$0.02 arcsec. Figure 4.3 shows the distribution of the sources in PM space. Most of the sources with available spectra in the ESO SAF (black points) are within the main stellar locus of the SMC, which is outlined by a white ellipse. The photometric properties of the 3700 sources such as the NIR survey of provenance, their NIR magnitudes in the J and $K_{\rm s}$ bands, their optical magnitudes in the G, $G_{\rm BP}$ and $G_{\rm RP}$ bands, as well as the respective photometric uncertainties are given in Table 4.2.

[6] https://www.eso.org/rm/api/v1/public/releaseDescriptions/73

Table 4.1: Parameters of the spectra used in this study. The table is published in its entirety as supporting material with the electronic version of the article.

ARCFILE	RA (deg)	Dec (deg)	Instrument (nm)	Grating	λ	R	SNR	Program ID	Product version
ADP.2015-04-13T10:11:06.923	13.713166	-72.637166	GIRAFFE	LR3	450−508	7500	15.8	386.D-0541	1
ADP.2015-04-13T10:11:07.283	13.797333	-72.285638	GIRAFFE	LR3	450−508	7500	60.6	386.D-0541	1
ADP.2015-04-13T10:11:13.337	14.055874	-72.652472	GIRAFFE	LR3	450−508	7500	42.2	386.D-0541	1
ADP.2015-04-13T10:11:16.837	14.412333	-72.511472	GIRAFFE	LR3	450−508	7500	12.9	386.D-0541	1
ADP.2015-04-13T10:11:26.400	13.348958	-72.481388	GIRAFFE	LR3	450−508	7500	29.7	386.D-0541	1
ADP.2015-04-13T10:11:53.937	13.948374	-72.658611	GIRAFFE	LR3	450−508	7500	138.0	386.D-0541	1
ADP.2015-04-13T10:12:02.720	13.237999	-72.484055	GIRAFFE	LR3	450−508	7500	74.8	386.D-0541	1
ADP.2015-04-13T10:12:15.860	14.158791	-72.609666	GIRAFFE	LR3	450−508	7500	112.0	386.D-0541	1
ADP.2015-04-13T10:12:19.657	13.607041	-72.393305	GIRAFFE	LR3	450−508	7500	110.4	386.D-0541	1

Table 4.2: Photometric characteristics of the spectra. The table is published in its entirety as supporting material with the electronic version of the article.

NIR source ID	NIR survey	*Gaia* EDR3 source ID	G (mag)	σ_G [a] (mag)	$G_{\rm BP}$ (mag)	$\sigma_{G_{\rm BP}}$ [a] (mag)	$G_{\rm RP}$ (mag)	$\sigma_{G_{\rm RP}}$ [a] (mag)	J (mag)	σ_J (mag)	$K_{\rm s}$ (mag)	$\sigma_{K_{\rm s}}$ (mag)
558358499858	VMC	4688987114793104384	18.665	0.003	18.477	0.015	18.640	0.036	18.775	0.038	18.799	0.072
558370021706	VMC	4689011166567250944	15.344	0.003	15.283	0.006	15.429	0.006	15.408	0.004	15.145	0.007
558358869977	VMC	4685986066534948864	15.755	0.003	15.661	0.004	15.883	0.005	16.099	0.006	16.297	0.012
558370088420	VMC	4688995498568136704	19.036	0.004	18.696	0.039	18.715	0.051	18.675	0.027	18.466	0.082
558369977606	VMC	4689004986121150464	17.156	0.005	16.922	0.006	17.106	0.008	17.274	0.011	17.369	0.034
558358846869	VMC	4685985933366169600	13.271	0.003	13.289	0.003	13.207	0.004	13.158	0.001	13.108	0.003
558369967505	VMC	4689005054840926208	14.645	0.004	14.648	0.021	14.602	0.028	14.615	0.003	14.561	0.006
558358892671	VMC	4685986483121884160	13.567	0.003	13.511	0.003	13.661	0.004	13.828	0.002	13.865	0.004
558370002756	VMC	4689007322583053312	13.844	0.003	13.794	0.003	13.883	0.005	13.988	0.002	13.956	0.004

[a] The standard error of G, $G_{\rm BP}$, and $G_{\rm RP}$ mean magnitudes were computed as a simple error propagation on the fluxes, according to the formula: $\sigma_G = \sqrt{(-2.5/\ln(10) * \sigma_{F_G}/F_G)^2 + \sigma_{G_0}^2}$, where F_G is the mean flux in the G, $G_{\rm BP}$, or $G_{\rm RP}$ bands respectively, σ_{F_G} is the error on the mean flux, while σ_{G_0} is the zero point uncertainty.

107

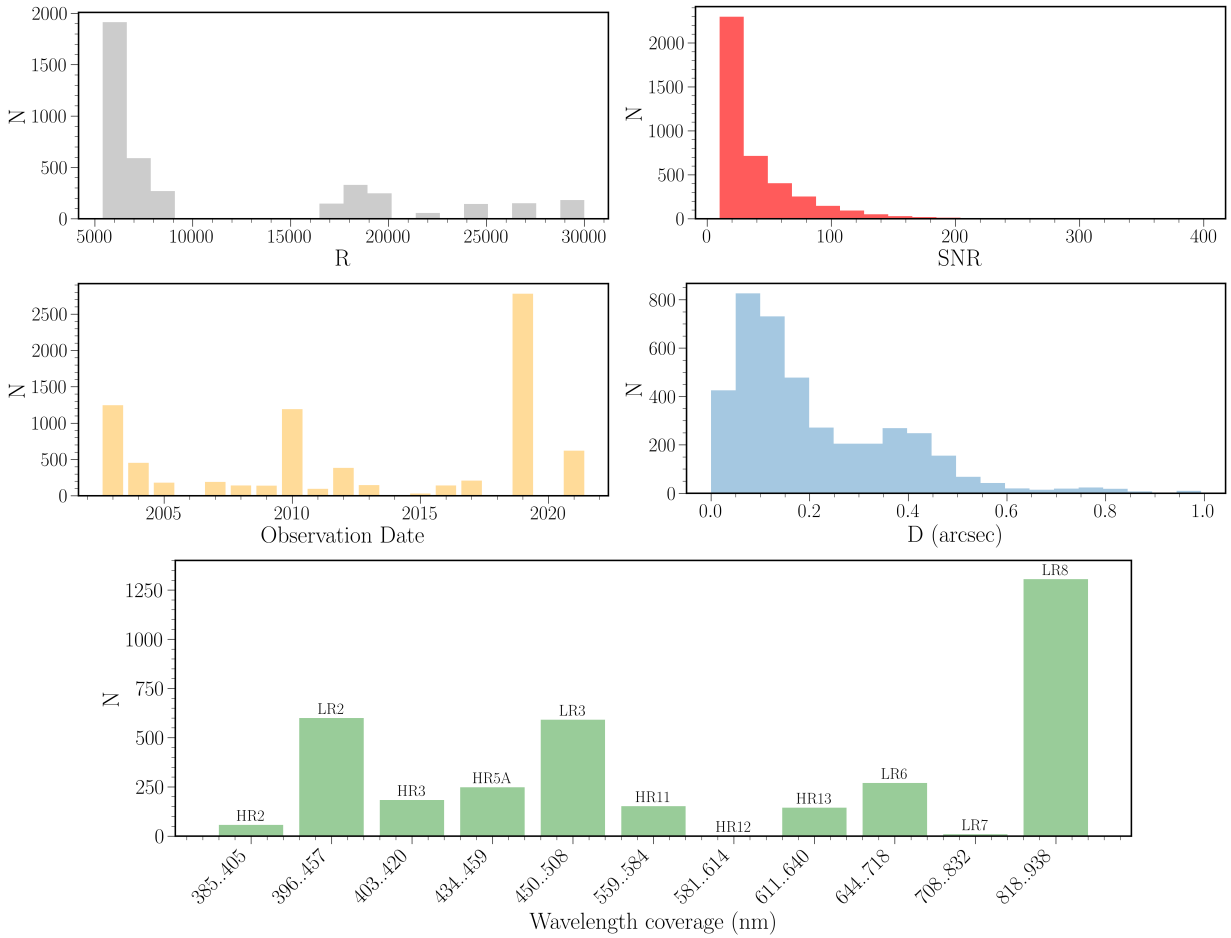

Figure 4.2: Histograms showing the parameter range of the spectra used in this study in terms of resolving power R (top-left), signal-to-noise ratio SNR (top-right), year of observation (middle-left), the separation between the coordinates of the photometric and spectroscopic data (middle-right), and the wavelength coverage (bottom).

4.3 Analysis

After applying the selection criteria outlined in the previous section and obtaining a final sample of 3700 sources, we proceed to analyse the spectra by initially performing the sky subtraction followed by full spectrum fitting to obtain LOS velocities.

4.3.1 Sky subtraction

The ESO pipeline recipes for GIRAFFE do not perform any sky subtraction, therefore reduced GIRAFFE spectra obtained as ESO phase 3 data products still have their sky signatures. However when available, all fibres with a sky signal (as defined by the observer) are collected in the associated MOSSKY ancillary product files, allowing for optimal sky subtraction. Usually 10 to 20 sky fibres are assigned by the observer to obtain sky spectra. We proceed to obtain a median sky spectrum for each observing block, comprising the observation of many targets within a given plate configuration, by median combining the sky spectra available at the MOSSKY ancillary product files. Since the object spectra are already shifted to the heliocentric RV system, while the sky spectra are not, we correct the median sky spectra to the heliocentric rest frame that has been applied to the science spectra by using the header keyword HELICORR. The corrected wavelength is defined by $\lambda_{\rm cor} = (1 + v_{\rm helio}/c) \times \lambda_{\rm uncor}$ with c being the speed of light and $v_{\rm helio}$ the projected heliocentric velocity shift that was calculated from the ESO pipeline for each science spectrum. We follow a similar methodology for the sky subtraction as in Koch et al. (2007), where the sky spectrum is modelled as a second-order Legendre polynomial plus the median sky. Additionally, we allow a small velocity shift in the sky spectrum so it is wavelength calibrated to our science spectra. We employed a Markov Chain Monte Carlo (MCMC) approach to determine the three parameters of the second order Legendre polynomial and the small additional velocity correction using the logarithmic likelihood function given as:

$$\log \mathcal{L} = \sum_{i=1}^{N} [\log \left(\frac{1}{\sqrt{2\pi}\sigma} \right) - \frac{(F_{\rm obj} - F_{{\rm sky},i})^2}{2\sigma^2}] \tag{4.1}$$

N is the number of tracers, $F_{\rm obj}$ is the flux of the object spectrum and $F_{{\rm sky},i}$ is the modelled sky spectrum defined as the median sky in addition to the second order polynomial:

$$F_{{\rm sky},i} = a\lambda^2 + b\lambda + c + F_{\rm median\ sky} \tag{4.2}$$

where a, b and c are the parameters to be determined. The uncertainty σ results from the uncertainties on the flux of the object and sky spectra as:

$$\sigma^2 = \sigma^2_{\rm obj} + \sigma^2_{\rm median\ sky,i}. \tag{4.3}$$

4.3.2 pPXF method

In order to determine LOS velocities, we are performing a full spectrum fitting using the penalised pixel fitting routine (pPXF; Cappellari & Emsellem 2004; Cappellari

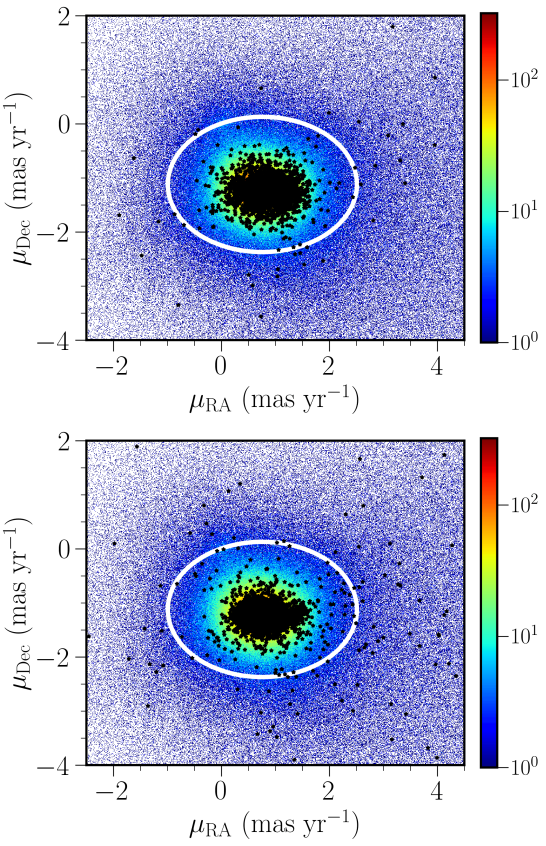

Figure 4.3: Stellar density of objects up to 10 deg from the SMC centre in PM space. The ellipse encloses a region dominated by SMC stars. The black points show objects with available spectra in our sample (top) and in the literature sample (bottom).

2017). pPXF fits an observed spectrum with a best-fitting linear combination of differently weighted stellar templates in pixel space. It recovers the LOS velocity distribution through moments of a Gauss–Hermite series and the parameters of the distribution are optimised by a χ^2 minimisation by direct comparison with the observed spectrum. The main advantage of pPXF is that it makes optimal usage of the entire spectrum, rather than focusing on a few spectral lines. pPXF has been extensively used to study kinematics of galaxies (e.g. Boardman et al. 2017), however its implementation is independent of the system in question. The main improvement introduced in Cappellari (2017) resulted in accurate velocities regardless of the velocity dispersion σ, which in our case is simply the instrumental broadening of the spectra. The pPXF method approximates the observed spectrum using the following parameterisation:

$$G_{\rm mod}(x) = \sum_{n=1}^{N} w_n \left\{ [T_n(x) * \mathcal{R}_n(cx)] \sum_{k=1}^{K} a_k \mathcal{P}_k(x) \right\} + \sum_{l=0}^{L} b_l \mathcal{P}_l(x),$$

where $\mathcal{R}_n$ are the LOS velocity distributions, $T_n(x)$ represent the templates, $\mathcal{P}_k(x)$ and $\mathcal{P}_l(x)$ are multiplicative and additive orthogonal polynomials of degrees k and l respectively, while w_n, a_k and b_i are weights to be solved for. The implementation of pPXF requires several inputs including a set of spectral templates. The noise spectrum of the observations and the starting value for the velocity and line broadening are also required. The input and noise spectra of the object to be measured are normalized and logarithmically rebinned while conserving the flux, using the `log_rebin` routine from pPXF.

Even after performing the sky subtraction, some of our spectra still suffer from contamination of sky emission lines and residual bad pixels, which can affect the fit severely. In order to further clean our spectra we use the following methodology. We median smooth the log re-binned spectrum by 7 pixels and then subtract the smoothed spectrum from the not-smoothed spectrum. Using this residual-subtracted spectrum, we proceed to use an iterative sigma clipping that selects all pixels that deviate from the mean by more than 3σ; the clipping is iterative until convergence is achieved (i.e., until no pixels are removed). We then expand the binning mask by ± 2 pixels, we obtain the indices of the good pixels and feed them to pPXF by using the `goodpixels` keyword; only these spectral pixels are included in the fit.

The pPXF method combines the set of input template spectra to best fit the observed spectrum. These templates can either be synthetic or empirical. Considering the resolving power and wavelength range of our spectra (Figure 4.2), we chose the X-shooter Spectral Library (XSL; Arentsen et al. 2019; Gonneau et al. 2020). This library contains empirical spectra with a resolving power close to $R = 10\,000$ for stars across a large range of spectral types and chemical compositions, which account for the different stellar populations we have in our sample. The spectra cover the following ranges of stellar parameters: $2\,600 \leq T_{\rm eff} \leq 38\,000$ K, $0.0 \leq \log(g) \leq 5.7$, and $-2.5 \leq$ [Fe/H] $\leq +1.0$ dex. They are corrected for RV and provided in the rest frame (with wavelength in air), logarithmically sampled in wavelength and normalised.

The full spectrum fit is conducted using fourth-order additive and multiplicative Legendre polynomials in order to account and correct for any potential low frequency differences in shape between the target's and the template's spectra continuum shape. Since pPXF uses a local minimisation algorithm, reasonably close starting values ($V_{\rm start}$) of the velocity and line broadening are required in order to avoid the algorithm to converge prematurely and hence being stuck in a local minimum. For $V_{\rm start}$ values ranging from 0 to 200 km s^{-1} with a step of 25 km s^{-1} are used; as to the line broadening, since we are dealing with stellar spectra, we set the starting value as the quadratic difference between the stellar spectra and templates' instrumental resolutions. We re-sample the stellar spectra and their associated uncertainties onto the arbitrary wavelength grid of the templates, while preserving the integrated flux. In order to evaluate whether the results represent a good fit, a reduced χ^2 as close

Table 4.3: Number of sources observed in different GIRAFFE gratings.

	HR2	LR2	HR3	HR5A	LR3	HR11	HR13	LR6
HR2	66	0	66	64	0	0	0	0
LR2	0	600	0	27	100	0	0	83
HR3	66	0	183	69	0	0	0	0
HR5A	64	27	69	248	17	0	0	0
LR3	0	100	0	17	591	0	0	83
HR11	0	0	0	0	0	152	11	0
HR13	0	0	0	0	0	11	144	0
LR6	0	83	0	0	83	0	0	270

as possible to 1 should be returned; furthermore we visually inspect the fit. We assess any potential template mismatch by analysing the residual of the fit where the standard deviation of the residuals should be similar to their mean, for a good template match. Note that pPXF assigns a linear combination of templates to each source (usually between 6 and 10) so there is no single template star corresponding to each source. In addition, our templates are not set on a regular grid and since we did not apply regularisation of the fits they are not expected to cluster around specific parameter values. In the Appendix we show two examples. This work is focused on determining LOS velocities whereas stellar parameters (temperature, surface gravity and metallicity) will be explored in a subsequent study.

4.3.3 Systematic uncertainties

To evaluate the systematic uncertainties that might arise from the use of different GIRAFFE gratings, we obtain RVs for objects that have an available spectrum in at least two gratings. We found that these spectra always belong to the same Programme ID. Table 4.3 outlines the number of objects in common between these gratings. As it appears in the table, this is only available for eight combinations of gratings. These spectra have undergone the same analysis discussed in Sections 4.3.1 and 4.3.2. Figure 4.4 shows the comparison between the RV estimates where the mean difference in terms of velocity and the respective standard deviation is indicated. We find mean differences in velocities of 1.77 ± 0.22 km s^{-1}. The dispersion within each grating is about 1 km s^{-1}. These differences might be related to the non-uniform fibre illumination, the template mismatch in the cross-correlation procedure, as well as the resolution and SNR of the spectra. As they could not be estimated for enough combinations of gratings to homogenise the sample, we refrain from applying a correction for the systematic uncertainties.

Table 4.4: RVs of sources from the 3700 sources in our sample. The table is published in its entirety as supporting material with the electronic version of the article.

ARCFILE	V km s^{-1}	$V_{\rm corr.}$ km s^{-1}	corr. km s^{-1}	$V_{\rm error}$ km s^{-1}	χ^2	$V_{\rm error} \times \chi^2$ km s^{-1}
ADP.2015-04-13T10:11:06.923	185.1	185.6	0.5	5.8	0.5	2.9
ADP.2015-04-13T10:11:07.283	139.5	142.0	−2.5	0.9	0.8	0.7
ADP.2015-04-13T10:11:13.337	183.7	183.8	−0.1	3.8	0.3	1.1
ADP.2015-04-13T10:11:16.837	164.8	165.3	−0.5	8.7	0.4	3.5
ADP.2015-04-13T10:11:26.400	98.6	100.4	−1.8	4.0	0.4	1.6
ADP.2015-04-13T10:11:53.937	152.5	152.6	−0.1	0.7	5.5	3.8
ADP.2015-04-13T10:12:02.720	173.0	174.9	−1.9	1.2	0.4	0.5
ADP.2015-04-13T10:12:15.860	165.3	165.5	−0.2	0.7	0.8	0.6
ADP.2015-04-13T10:12:19.657	181.8	183.9	−1.2	0.8	0.8	0.6

4.4 Results

4.4.1 Radial velocities

Figure 4.5 displays the distribution of RVs derived for the 3700 sources in the ESO SAF sample. It shows two distinct peaks with a small peak around 18 ± 2 km s^{-1} representing the MW foreground stars in the direction of the SMC and a large peak around 159 ± 2 km s^{-1} representing stars belonging to the SMC. The latter corresponds to a velocity dispersion (σ_V) of 33 ± 2 km s^{-1} which is the best-fit sigma of the Gaussian without taking into account the velocity errors. The limits to the tails of the RV distribution representing SMC stars are set at 60 km s^{-1} and 258 km s^{-1} which is $\pm 3\,\sigma_V$ of the distribution. The measured velocities and their corresponding uncertainties are summarised in Table 4.4. In this table we indicate also the velocities corrected for the projected bulk PM, the values of the correction, the initial velocity used by the pPXF routine ($V_{\rm start}$), the reduced χ^2, the formal velocity error ($V_{\rm error}$) and the corrected velocity error ($V_{\rm error} \times \chi^2$). Formal uncertainties provided directly by pPXF are based on the covariance matrix of the fitted parameters under the assumptions that the χ^2 space is smooth, unimodal and close to unity. These errors only serve as an estimate of the order of magnitude unless $\chi^2 \sim 1$. We find that 92 and 99 per cent of our sample has a $V_{\rm error} \leq 5$ km s^{-1} and $V_{\rm error} \leq 10$ km s^{-1}, respectively. Our mean RV is $\sim$10 km s^{-1} higher compared to other studies such as De Leo et al. (2020) and Dobbie et al. (2014) where the mean of their distributions was found to be around 149 km s^{-1}. This difference is due to combining different type stellar populations. De Leo et al. (2020) and Dobbie et al. (2014) observed giant stars while the mean in our study also includes MS and supergiant stars. The overall distribution of RVs derived in literature studies is also shown in Figure 4.5 and discussed in Section 4.4.2. The RV of the different stellar populations in this work is further explored in Section 4.4.3.

4.4.2 Radial velocities from the literature

Several spectroscopic studies have targeted the SMC using different stellar populations to characterise its internal kinematics. In our analysis, we consider data from the following literature studies and construct a comprehensive homogenised catalogue to complement the spectroscopic sample obtained in Section 4.2.2.

- Carrera et al. (2008) presented the chemical enrichment of the SMC by providing stellar metallicities as well as RVs for 350 RGB stars distributed across the inner 4 deg of the galaxy. The observations were carried out using the visual and near-ultraviolet FOcal Reducer and low dispersion Spectrograph 2 (FORS2) at the VLT in 13 fields of about 7×7 arcmin^2 each in size. The Spectroscopic Mask (MXU) mode was used to obtain multi-object spectra in the wavelength range $773 - 948$ nm with $R = 2560$. This study outlined the first spectroscopic metallicity gradient in the SMC and RVs were also used to reject non SMC members from the sample. Their RV uncertainty was ~ 4 km s^{-1}.

- Evans & Howarth (2008) traced the dynamics of the young stellar population of the SMC by obtaining RVs of 2045 OBA-type stars. They observed with the Two Degree Field Facility (2dF) at the Anglo-Australian Telescope (AAT) and obtained spectra that cover the wavelength range $390 - 480$ nm. The resolving power of $R = 1600$ resulted in an accuracy of $\sim$11 km s^{-1} on the RV of individual stars distributed across an area of 2×12.5 deg^2. The authors found a velocity gradient across the SMC bar of 26.3 ± 1.6 km s^{-1} deg^{-1} at PA = 126 deg. They also noted a difference in RV between the Wing and bar as well as a $\sim$20 km s^{-1} red-shift of their young stars compared to older stellar populations.

- Harris & Zaritsky (2006) observed 2046 red giant stars in the central 4×2 kpc^2 of the galaxy using the Inamori-Magellan Areal Camera and Spectrograph (IMACS) at the Magellan Baade Telescope. The spectra spanned a wavelength range from $560 - 1000$ nm with a resolving power $R \sim 5000$ resulting in a RV uncertainty of ≈ 10 km s^{-1}. The authors found a global velocity distribution centred at 146 km s^{-1} with a dispersion of 28 km s^{-1} as well as evidence of a velocity gradient across the SMC.

- Dobbie et al. (2014) provided RVs of 4172 red giant stars and 352 carbon stars across an area of 37.5 deg^2 with an accuracy better than 5 km s^{-1}. The spectra were acquired using the AAOmega spectrograph at the AAT. The blue and red arms of the instrument were configured with the 1500V ($R \sim 4000$) and 1700D ($R \sim 10\,000$) gratings with a wavelength coverage ranging from $425 - 600$ nm and $845 - 900$ nm, respectively. The authors found that a rotating disc model best represents the rest frame velocity of the youngest red giants in their sample. Beyond ≥ 4 deg they found signatures of tidal stripping. Their global velocity distribution is centred at 147.8 ± 0.5 km s^{-1}.

- Lamb et al. (2016) observed 374 stars as part of the RIOTS4 Survey, a uniformly selected survey of young stars in the SMC. They found that the SMC has a

systemic velocity of $\sim$150 km s^{-1} and kinematics like those of other massive stars surveys (e.g. Evans & Howarth 2008). Their spectral coverage for each star varied. However every spectrum includes the wavelength range from $400 - 470$ nm. A majority of their targets (328) were observed using IMACS at the Magellan Baade telescope with a spectral resolving power of $R = 2600$–3700. The other targets were observed with IMACS at a resolving power of $R = 1000$–1300 or with the Magellan Inamori Kyocera Echelle (MIKE) Spectrograph on the Magellan Clay telescope with a resolving power of $R \sim 28\,000$. The uncertainties on their RV measurements are $\sim$5 km s^{-1} for MIKE observations and 10–25 km s^{-1} for IMACS observations.

- De Leo et al. (2020) targeted 2573 red giant stars within $\sim$4 kpc from the SMC's centre using the AAOmega spectrograph at the AAT. Observations used the grating 1700D spanning a wavelength coverage of $845 - 900$ nm and providing a resolving power of $R \sim$8500. They achieved a velocity uncertainty better than 5 km s^{-1} and their velocity distribution is centred at $\sim$ 150 km s^{-1}. They found an outward stellar motion in the direction towards the LMC supporting that the SMC is undergoing tidal disruption.

- Nidever et al. (2020) studied 3800 objects in the MCs using data from SDSS DR16 (Ahumada et al. 2020). Observations were obtained from the APOGEE 2 South (APOGEE-2S; Majewski et al. 2017; Wilson et al. 2019) on the du Pont telescope at Las Campanas Observatory (LCO) in the near-infrared ($1.51 - 1.70$ μm) with a resolving power of $R\sim$20 000. Nidever et al. (2020) mostly focused on the RGB population, but observations included also AGB stars, MS stars, and supergiants distributed within 10 deg of the LMC and 6 deg of the SMC centres. They obtained a mean radial velocity of 135 km s^{-1} and RV uncertainties of $\sim 0.1 - 0.2$ km s^{-1}. In our study we use the current DR17 (Abdurro'uf et al. 2022) which contains observations for 3600 objects in the SMC.

- *Gaia* DR3 (Gaia Collaboration et al. 2022) contains median RVs for 33 812 183 stars brighter than G = 14 mag and distributed throughout the entire celestial sphere. The median formal precision of the RVs is of 1.3 km s^{-1} at G = 12 and 6.4 km s^{-1} at G = 14 mag (Katz et al. 2022). The spectra are taken with the Radial Velocity Spectrograph and have a resolving power of $R = 11\,500$ across a wavelength range of $845 - 872$ nm.

We proceed to cross-match the targets of the literature studies with our photometric sample outlined in Section 4.2.1 to obtain their NIR photometry and *Gaia* EDR3 astrometric solution. The cross-matching facility of TOPCAT were used adopting a maximum cross-matching distance of 1 arcsec. Figure 4.1 shows the NIR CMD of the sources in the literature sample and their location across the different stellar population regions outlined in El Youssoufi et al. (2019) as well as their spatial distribution, which displays the coverage of the main body of the galaxy and of some fields in the outskirts. The location of the fields studied by Cullinane et al. (2023) using data from MagES is also indicated. Figure 4.3 shows the distribution of the

sources across the PM space highlighting that most of them are enclosed within a region containing a reduced number of MW stars due to the astrometric selection criteria discussed in Section 4.2.1.

We then cross-match the targets among the literature studies to find common sources. Their numbers are summarised in Table 4.5. As a consequence of combining data from different spectroscopic literature studies, we need to assess if there are any systematic offsets present in the RVs and to take them into account to produce a homogenised sample. We decided to anchor the RVs on APOGEE DR17. This catalogue has data with the highest resolving power, which span different stellar populations, and has sources in common with almost all of the other studies. Table 4.6 summarises the number of objects each study has in common with APOGEE DR17 and provides the median differences between the RVs ($\langle \Delta V \rangle$) of APOGEE DR17 and the other studies as well as the standard deviation of the differences ($\sigma_{\Delta V}$). We eliminate duplicates by retaining sources with the most precise RVs and obtain a homogeneous sample by adding the median RV differences to each study respectively (for example, $V = V_{\rm Dobbie\ et\ al.} + \langle \Delta V \rangle$). We discard the Carrera et al. (2008) sample because it does not have enough sources in common with APOGEE DR17 or other studies. Our final homogenised sample of RVs from the literature studies contains 9110 sources. Figure 4.5 displays the distribution of RVs derived for the literature sample. It shows a single peak at 150.8 ± 0.4 km s^{-1} representing stars belonging to the SMC, with $\sigma_V = 29.3 \pm 0.4$ km s^{-1}. The tails of the RV distribution representing SMC stars are set at 63 km s^{-1} and 239 km s^{-1} which is $\pm\, 3\, \sigma_V$ of the distribution. We find that the velocity dispersion between the ESO SAF and literature samples agree within their dispersions. However the mean velocities differ by ~ 8 km s^{-1}. A one-to-one comparison of the velocities for the sources in common is shown in Figure 4.6. The distribution appears flat because the data spread is similar within both ranges of RVs. The distribution of residuals, except for the few sources at the lowest and highest velocities, does not show any obvious trends overall and for any of the samples. We find a mean star by star offset of $V_{\rm ESO} - V_{\rm Lit} = -6.5$ km s^{-1} for targets in common and a velocity dispersion of 38.8 km s^{-1}, which is larger than the errors on individual sources.

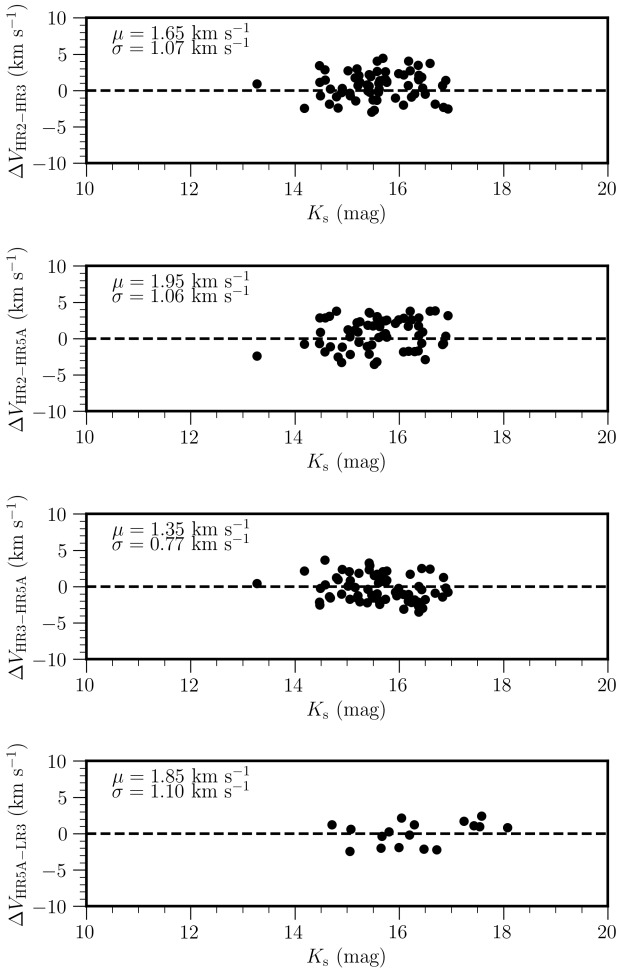

Figure 4.4: Comparison between the RV estimated from spectra obtained with different GIRAFFE gratings as a function of magnitude. Means and corresponding standard deviations are indicated within each panel. The uncertainty on individual points corresponds to 2 km s^{-1}.

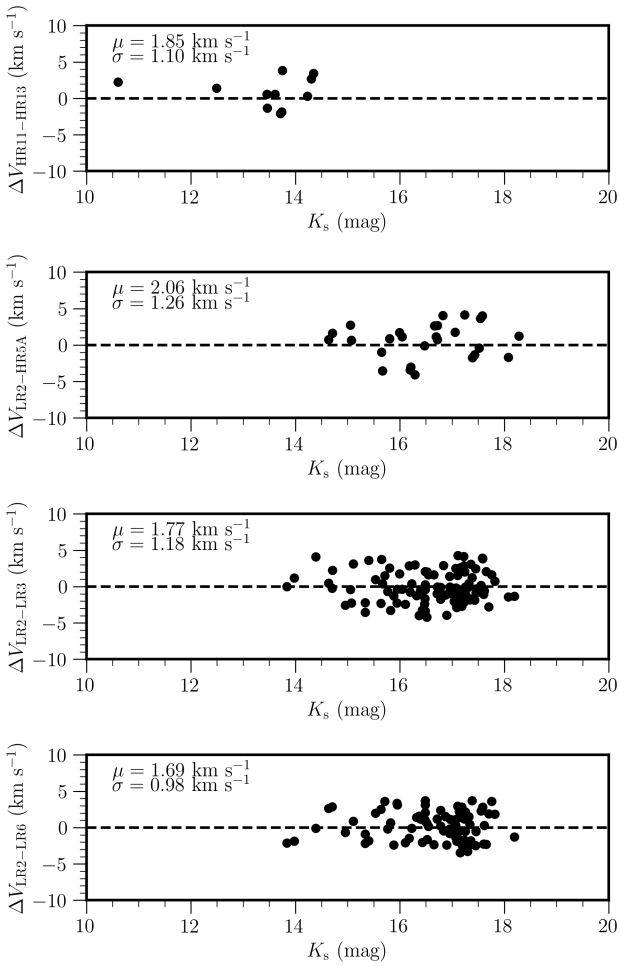

Figure 4.4: (Continued)

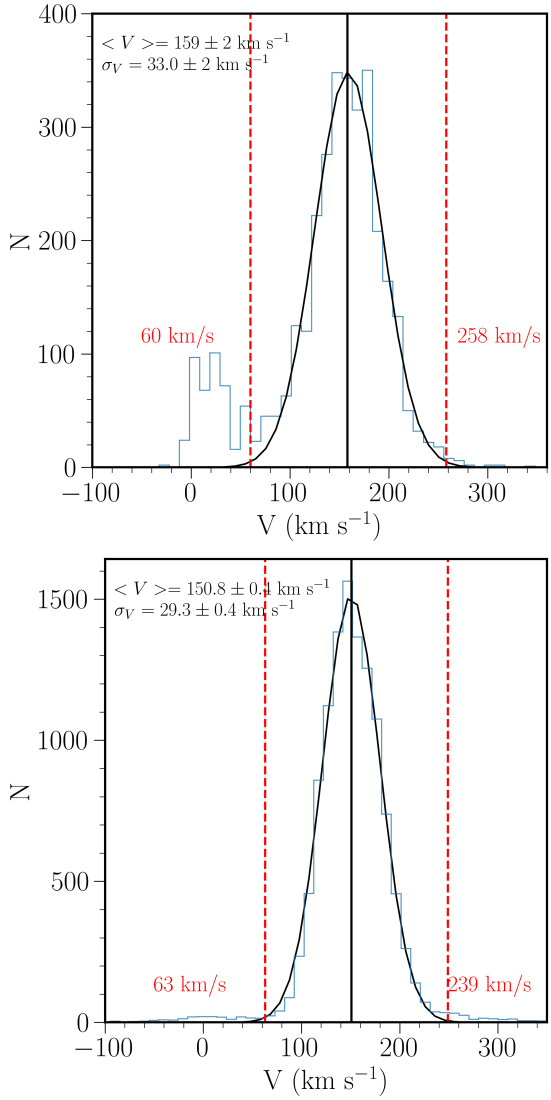

Figure 4.5: Distribution of RVs from our sample (top) and the homogenised literature (bottom). Black continuous lines represent the Gaussian fit of the distribution for SMC stars and the corresponding mean. The latter and its dispersion are indicated at the top left. The bin size is 10 km s^{-1}. Red vertical dashed lines mark the velocity cuts applied to reduce the influence of MW stars. These are also indicated on each side of the lines.

Table 4.5: Number of sources found in our NIR photometric sample and in common among the RV literature studies.

	$N_{\text{APOGEE DR17}}$	$N_{\text{Dobbie et al.}}$	$N_{\text{De Leo et al.}}$	$N_{\text{Harris \& Zaritsky}}$	$N_{\text{Evans \& Howarth}}$	$N_{\text{Carrera et al.}}$
$N_{\text{APOGEE DR17}}$	1913	103	97	0	9	0
$N_{\text{Dobbie et al.}}$	103	2743	103	93	1	2
$N_{\text{De Leo et al.}}$	97	103	1005	4	0	2
$N_{\text{Harris \& Zaritsky}}$	0	93	4	1581	0	1
$N_{\text{Evans \& Howarth}}$	9	1	0	0	1303	0
$N_{\text{Carrera et al.}}$	0	2	2	1	0	215
$N_{\text{Lamb et al.}}$	2	0	0	0	35	0
$N_{\text{Gaia DR3}}$	115	180	0	0	18	0

	$N_{\text{Lamb et al.}}$	$N_{\text{Gaia DR3}}$
$N_{\text{APOGEE DR17}}$	2	115
$N_{\text{Dobbie et al.}}$	0	180
$N_{\text{De Leo et al.}}$	0	0
$N_{\text{Harris \& Zaritsky}}$	0	0
$N_{\text{Evans \& Howarth}}$	35	18
$N_{\text{Carrera et al.}}$	0	0
$N_{\text{Lamb et al.}}$	196	0
$N_{\text{Gaia DR3}}$	0	2833

Table 4.6: RV differences between APOGEE DR17 and literature studies.

	N	$\langle \Delta V \rangle$ km s^{-1}	$\sigma_{\Delta V}$ km s^{-1}
APOGEE DR17 – Dobbie et al.	103	0.51	3.51
APOGEE DR17 – De Leo et al.	96	−0.07	3.03
APOGEE DR17 – Evans & Howarth	9	−8.86	67.77
APOGEE DR17 – Carrera et al.	0	–	–
APOGEE DR17 – Lamb et al.	2	7.14	99.41
APOGEE DR17 – Gaia DR3	115	0.03	3.93
APOGEE DR17 – Harris & Zaritsky	0	1.53[a]	18.72[a]
Dobbie et al. – Harris & Zaritsky	93	1.10	16.10
Evans & Howarth – Lamb et al.	35	16.00	31.64

[a] This value was calculated from the combination of the results from APOGEE DR17 – Dobbie et al. and Dobbie et al. – Harris & Zaritsky samples.

4.4.3 Stellar kinematics of the SMC

Kinematics of stellar populations

Figure 4.7 compares the RV distributions of different CMD regions (El Youssoufi et al. 2019) between our sample and the literature sample. The majority of the stars in our sample populate region A (MS stars) and J (RC stars). There are also many stars (about 200 or more) in regions B (MS stars), E (faint RGB stars), G, H and I (supergiant stars), and K (bright RGB stars). Very few stars are found in region M (AGB stars). In particular, our sample provides RVs for stars in regions B, E and J which are poorly sampled in the literature studies. It is noticeable that regions E, I and J are those mostly contaminated by MW stars which have small RVs. In the following, we consider stars with $60 < V < 258$ km s^{-1} to belong to the SMC and we compute mean RVs within each region by fitting a Gaussian to their RV distributions using a non-linear least-squares minimisation technique. The number of sources in both our sample and the literature sample, the respective values of RVs and dispersions, as well as the corresponding median ages and age intervals of the stars within each CMD region are reported in Table 4.7. This shows that there are two groups differing by 20 km s^{-1}: one formed by stars in regions A, B, G, H, and M with a RV of $\sim$170 km s^{-1} and another one formed by stars in regions E, I, J, and K with a RV of $\sim$150 km s^{-1}. The velocity dispersion of each region is comparable and corresponds to $\sim$30 km s^{-1}. The same dichotomy is found for stars in the literature sample with the exception of those in region M which have instead a mean RV of $\sim$150 km s^{-1}. However, in our sample regions B, J and M contain only a few stars and it may not be appropriate to compare their mean values with those from regions that are instead well populated. Figure 4.8 shows the spatial distribution of the RVs across the SMC for stars in the two samples whereas Figure 4.10 shows similar distributions but for each CMD region. The literature sample, which encompasses a rather homogeneous wide area of the galaxy, shows larger RVs to the SE of the SMC centre and lower RVs in the other area along and west of the bar. A large RV to the SE is also present in our

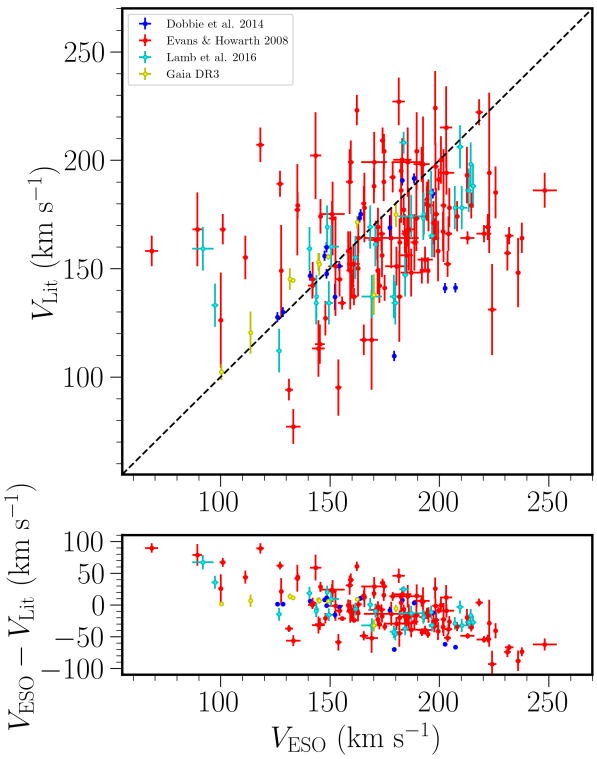

Figure 4.6: (top) Comparison between the RVs from our sample obtained in this study versus those derived in literature studies. The dotted line shows the one-to-one relation. (bottom) Distribution of residuals with a mean velocity of -6.5 km s^{-1} and a velocity dispersion of 38.8 km s^{-1}.

sample, but it is more difficult to discern an overall RV trend because our sample is concentrated on the bar with only sparse fields located around it. We computed the perspective correction to the RVs from the projected bulk PM of the galaxy (Figure 4.9). We used the coordinates for the centre ($\alpha = 13.05$ deg, $\delta = -72.03$ deg) as given in Section 4.2, the PMs ($\mu_\alpha$cosδ=0.686 mas yr^{-1}, μ_δ=$-$1.237 mas yr^{-1}) from Gaia Collaboration et al. (2021b) and the distance modulus $(m - M) = 18.88$ mag from Muraveva et al. (2018). Figure 4.9 shows that the correction on the eastern side of the galaxy is larger than on its western side suggestive of a rotation pattern, but it is constant along the bar region.

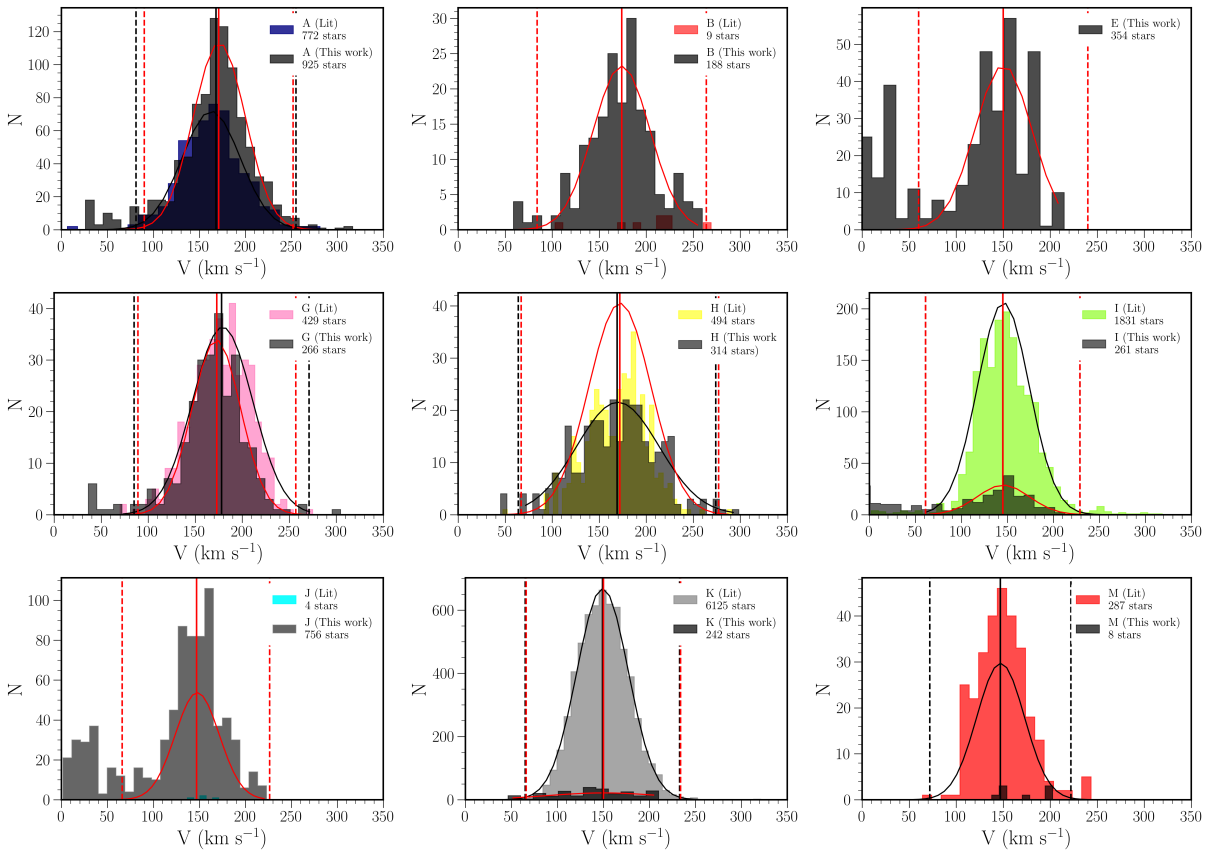

Figure 4.7: Distributions of RVs in the different CMD regions outlined in Figure 4.1 and adapted from El Youssoufi et al. (2019), for the literature sample (coloured histograms) and our sample (dark grey histograms). The distribution of SMC stars within each panel is fitted with a Gaussian. The vertical axes represent the number counts within bins of 12 km s^{-1} in size. Regions C and D are not included due to the low number of sources.

123

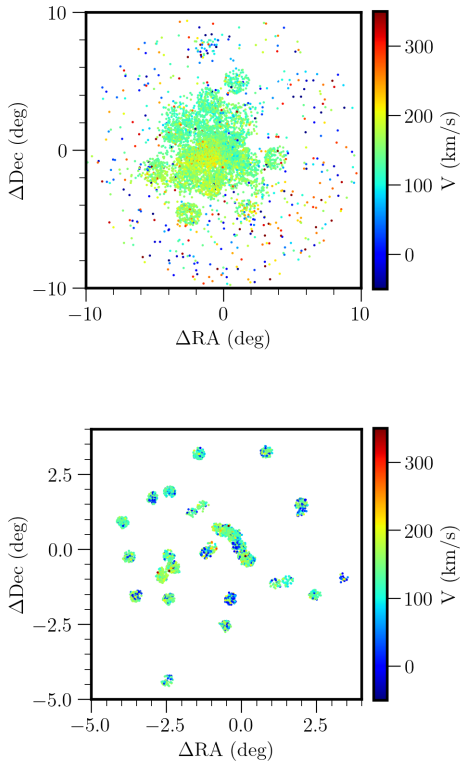

Figure 4.8: Distribution of RVs obtained from the literature sample (top) and our sample (bottom).

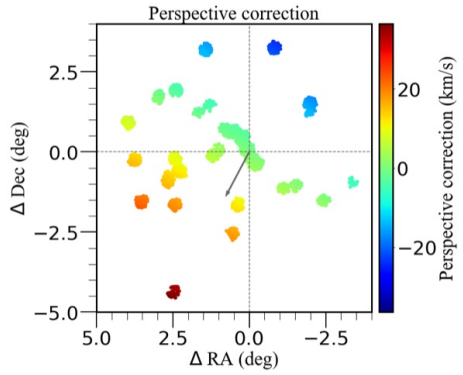

Figure 4.9: Distribution of the perspective correction derived from the projected bulk PM of the galaxy, which is indicated with an arrow departing from the centre.

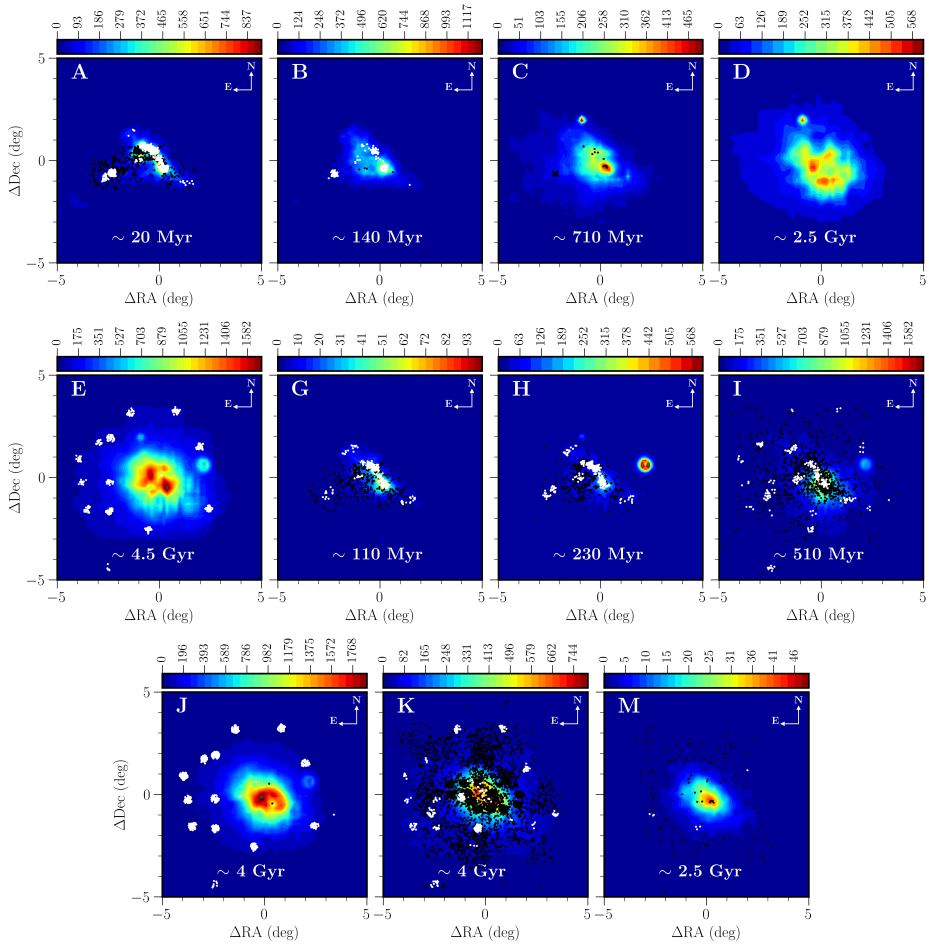

Figure 4.10: Distribution of RVs from our sample (white points) and the literature sample (black points) superimposed onto morphological maps of stellar populations in the SMC from El Youssoufi et al. (2019). The bin size is 0.03 deg^2 and the colour bar represents the number of stars per bin. Regions A, B and C refer to MS stars, D to MS/subgiant stars, E to faint RGB stars, G, H and I to supergiant and giant stars, J to RC stars, K to bright RGB stars, and M to thermally pulsing AGB stars. Median ages for each stellar population, as derived by El Youssoufi et al. (2019), are indicated in the panels.

Table 4.7: Mean radial velocity for each CMD region.

CMD Region	ESO SAF sample			Literature sample			Median age[a]	Age range[a]
	N	$\langle V \rangle$ km s^{-1}	σ_V km s^{-1}	N	$\langle V \rangle$ km s^{-1}	σ_V km s^{-1}	Myr	Myr
A	925	171	28	772	168	30	20	10–50
B	188	174	30	9	201	38	150	50–410
C	28	32	8	–	–	–	700	250–2000
D	–	–	–	–	–	–	2500	1500–5000
E	354	150	30	–	–	–	4500	2500–8000
G	266	173	28	429	179	31	110	50–230
H	314	169	36	494	172	33	230	150–360
I	261	145	28	1831	146	28	510	90–3000
J	756	148	27	4	152	12	4000	2000–9000
K	242	151	28	6125	149	28	4000	2000–8000
M	8	170	25	287	147	25	2500	1000–5000

[a] Ages are from El Youssoufi et al. (2019).

Regions A and B represent both MS populations and their morphology delineates the asymmetric nature of the galaxy (El Youssoufi et al. 2019). In these regions, both samples are of a comparable size and populate the bar and the Wing. The literature sample is also present between the two structures, but only for stars $10-50$ Myr old, and our sample provides stars $50-410$ Myr old (El Youssoufi et al. 2019). Regions G and H represent supergiant populations of $30-200$ Myr old and $130-340$ Myr old, respectively and the two samples show similar distributions to those in regions A and B despite having about twice as many sources in the literature sample than in our sample. In contrast in region I, which is also populated by supergiant stars with a median age of $\sim$510 Myr (El Youssoufi et al. 2019), we find that both samples probe the extended body of the galaxy. Region I includes fainter stars than those in regions G and H. The literature sample has also a large concentration of stars in the SW part of the bar compared to the part in the NE. Regions E and K represent the faint and bright RGB populations, respectively with an approximate range of $2-8$ Gyr (El Youssoufi et al. 2019). Our sample in region E occupies sparse fields in the outskirts of the galaxy with more fields being present in the east than in the west. There are no stars in the literature sample from this region. Our sample in region K has a similar spatial distribution as that of region E. Region K encompasses the largest number of stars in the literature sample and the widest coverage of the galaxy. The comparison between region K and regions populated by younger stars highlights that the NE of the bar is on average younger than its SW as well as other regions around it. The RVs of the old populations are on average lower than those of the young populations. This is perhaps due to the young stars having formed out of gas already influenced by tidal stripping. Region J represents the RC population with an age in the range from $2-9$ Gyr (El Youssoufi et al. 2019) for which the spatial distribution and average RV from our sample is similar to that of regions E and K; no stars in the literature sample populate this region. Region M represents the AGB population with an approximate age of $1-5$ Gyr (El Youssoufi et al. 2019). The literature sample is sparsely distributed mostly across the outer region of the galaxy. Our sample only has 8 stars in this region. In addition, regions I and M show a small overdensity in the RV histograms around 250 km s^{-1}. However, these stars are sparsely distributed across the galaxy and do not trace a particular substructure. Due to their low number they could be fluctuations of the histogram distributions, as it appears in other CMD regions, or perhaps members of a stellar stream.

We conclude that the RVs obtained from our sample and the literature sample for stellar populations within each CMD region are in good agreement within the uncertainties. Existing differences for regions B and M can be attributed to the small size of the literature sample. We chose to proceed continuing to keep both samples separated, in order to avoid introducing systematic effects and uncertainties that may be relevant at the level of fewer sources and their spatial distribution compared to the mean values.

Kinematics of the bar and Wing

The distribution of sources with available RV estimates from the ESO SAF and literature samples encompasses different morphological features of the SMC. In

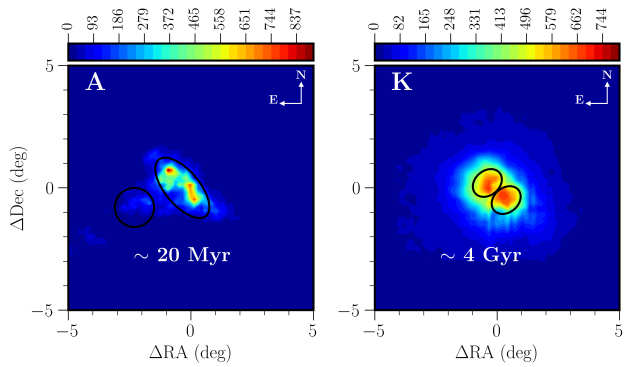

Figure 4.11: (Left) Morphological map of young MS stars (region A) with superimposed circular and elliptical masks encompassing the Wing and bar of the SMC, respectively. (Right) Morphological map of bright RGB stars (region K) with elliptical masks encompassing two apparent overdensities. The bin size is 0.03 deg^2 and the colour bars represent the number of stars per bin. Median ages are as in Figure 4.10.

the following, we examine the kinematics of the bar and Wing regions which are prominent features in our sample. To study the kinematics of these two regions, we define two masks to enclose them – see Figure 4.11.

The SMC bar spans $\sim$2.5 deg in length (El Youssoufi et al. 2019) and is also known to be elongated across the line of sight reaching up to 23 kpc (Gardiner & Noguchi 1996; Haschke et al. 2012; Subramanian & Subramaniam 2012; Nidever et al. 2013; Jacyszyn-Dobrzeniecka et al. 2017; Muraveva et al. 2018). The elliptical mask defined to enclose the bar is centred at (ΔRA=-0.35 deg, ΔDec=0 deg), has a semi-minor axis of 3 deg, a semi-major axis of 1.4 deg, and a PA of 40 deg in the NE direction. We find that in the bar region, the mean RV estimates decrease by about 20 km s^{-1} with increasing stellar population age, from young MS stars ($\sim$170 km s^{-1}) to old supergiant stars ($\sim$150 km s^{-1}) corresponding to an age difference of about 100 Myr. Differences in kinematics between the NE (ΔDec$>$0 deg) and SW (ΔDec$<$0 deg) bar correspond to 10 km s^{-1} in the youngest MS stars, with the NE bar having the highest velocity (177 km s^{-1}). In supergiants, there is a similar velocity difference (8 km s^{-1}), but only for stars in region H (yellow supergiants) and it is the SW bar that instead has the highest velocity (172 km s^{-1}). Uncertainties on the RV measurements are $\sim$1 km s^{-1}.

At intermediate-ages, traced by bright RGB stars in region K, the inner SMC is also dominated by two overdensities which are located along the bar, but that differ in shape compared to those traced by younger stars (Figure 4.11). Data for these substructures are only available in the literature sample. We calculate the mean RV of these overdensities using two masks defined as follows. The elliptical mask defined to encompass the overdensity in the NE is centred at (ΔRA=-0.4 deg, ΔDec=0.2 deg), has a semi-minor axis of 1 deg, a semi-major axis of 1.3 deg, and a PA of 40 deg whereas the elliptical mask defined to encompass the overdensity in the SW is centred at (ΔRA=0.37 deg, ΔDec=-0.50 deg), has a semi-minor axis of 1.0 deg,

a semi-major axis of 1.3 deg, and a PA of 40 deg. Using only RVs from bright RGB stars we obtain that the SW overdensity has a mean RV of 152 ± 1 km s^{-1} whereas the NE overdensity has a mean RV of 144 ± 1 km s^{-1}. These velocities are similar to the velocity of old supergiant stars.

The Wing is a morphological substructure discovered by Shapley (1940), located at the SE of the SMC, connecting the galaxy to the Magellanic Bridge. The circular mask defined to cover the Wing is centred at (ΔRA=-2.30 deg, ΔDec=-0.80 deg) and has a radius of 0.80 deg. We find that both the youngest MS stars and supergiant stars show the same mean RV of $\sim$180 km s^{-1} which is on average larger than the RV derived for stellar populations within the bar, but for young MS stars in the NE.

4.5 Conclusions

In El Youssoufi et al. (2019) we provided an updated view of the morphology of the SMC through a comprehensive age tomography. In this study, we complement their work through a homogeneous and extensive kinematic study of the different resolved stellar populations. The SMC is known to have a complicated interaction history, a complex 3D structure and an eventful star formation history; all of these factors can have an impact on the kinematics of stellar populations within the galaxy. To this end we proceed as follows:

(i) We search the ESO SAF for the best available spectra of objects belonging to the SMC, making use of near-infrared photometry from the VMC, VHS, 2MASS and OGLE IV projects. Parallaxes and PMs from *Gaia* EDR3 are used to reduce the influence of MW foreground stars. The selected stars form a sample of 3700 sources. The spectra used in this study are taken with the FLAMES/GIRAFFE instrument, have a SNR ≥ 10 and a resolving power from 6500 to $38\,000$. The spectra are sky subtracted and a full spectrum fitting method is used to obtain RVs; the stellar spectra and their associated uncertainties were re-sampled onto the arbitrary wavelength grid of the templates which were taken from the X-shooter spectral library. Systematic uncertainties among the FLAMES gratings were found to be $\sim$2 km s^{-1}, but were not applied to correct the spectra due to not having enough combinations of gratings to homogenise the sample.

(ii) We obtain a RV distribution which shows two distinct peaks: a small peak around 18 ± 2 km s^{-1} representing the MW foreground stars in the direction of the SMC and a large peak around 159 ± 2 km s^{-1} representing stars belonging to the SMC and corresponding to a velocity dispersion (σ_V) of 33 ± 2 km s^{-1}. Furthermore, we compare these values to those obtained from a homogenised RV sample of several spectroscopic studies that have previously observed SMC stars and that we anchor to the APOGEE DR17 spectra.

(iii) We find that stars occupying regions of the CMD, as defined by El Youssoufi et al. (2019), that have been poorly sampled by spectroscopic studies in the literature such as regions B (MS stars $50 - 410$ Myr old), E (faint RGB stars $2.5 - 8$ Gyr old) and J (RC stars $2 - 9$ Gyr old) have RVs resembling those of stellar populations of similar median ages: regions G (supergiant stars $50 - 230$ Myr old) and K (bright RGB stars $2 - 8$ Gyr old). On average, the RV of stellar populations younger than

500 Myr is $\sim$ 20 km s^{-1} larger than that of stellar populations older than 2 Gyr. A similar RV dichotomy has recently been found by Mucciarelli et al. (2023) from an independent analysis of 206 RGB stars, which are also included in our sample, located on the eastern side of the galaxy around the globular cluster NGC 419. The authors characterised a metal-rich component with a large RV ([Fe/H]~-0.9 dex and RV$\sim$172 km s^{-1}) and a metal-poor component with a low RV ([Fe/H]~-1.1 dex and RV$\sim$154 km s^{-1}), suggesting that they could result from separate bursts of star formation (Massana et al. 2020).

(iv) We measure a RV difference between the Wing and bar, dominating the morphology of the SMC as traced by our sample, confirming that these two substructures are kinematically distinct. This RV difference was already noticed by Evans & Howarth (2008) from their analysis of the kinematics of OBA type stars. PM studies corroborate this result, with the Wing kinematics following the transverse motion along the Magellanic Bridge towards the LMC (e.g. Zivick et al. 2019; Schmidt et al. 2020; Niederhofer et al. 2021). Consequently, the increased star formation rate in the Wing region following the interaction between the LMC and the SMC about 200 Myr ago (Harris & Zaritsky 2004b; Rubele et al. 2015) imprinted a large RV on the newly formed stars compared to those in the bar. The Wing substructure is found to lie at a distance closer to us than the main body of the SMC, further contributing to these discrepancies (Tatton et al. 2021). The differences in kinematics between the bar and Wing are more pronounced in supergiants ($150-360$ Myr old; $\sim$30 km s^{-1}) than in young MS stars ($10-50$ Myr old; $\sim$10 km s^{-1}) where the RV of stars in the bar is smaller in the former than in the latter population. Moreover, the RVs of stars in the bar are found to be larger in young MS stars than in red supergiants; we attribute this to the peak of star formation in the SMC bar at $\sim$40 Myr (Rubele et al. 2015) from gas already influenced by tidal stripping. This is consistent with a cold gas outflow, which is stronger in the Northern bar, that originated $33-56$ Myr ago (McClure-Griffiths et al. 2018). SMC debris with large RVs has been found at the extreme southern disc of the galaxy ($6-9$ deg from the centre beyond the Wing) using data from MagES (Cullinane et al. 2023).

(v) We measure different RVs between the NE and SW portions of the bar. These differences are $\sim$10 km s^{-1} and are found to be present in young populations such as MS stars ($10-50$ Myr old) and yellow supergiants ($150-360$ Myr old) as well as in old populations like bright RGB stars ($2-8$ Gyr old). This also shows consistency between our (MS and supergiant stars) and literature (bright RGB stars) studies. The NE bar region has a larger RV in young MS stars than the SW region; the reverse is true for the supergiants and RGB populations. These gradients are not influenced by the projected bulk PM. However, we confirm a previously found rotation pattern (Dobbie et al. 2014; Di Teodoro et al. 2019; De Leo et al. 2020; Abdurro'uf et al. 2022). A prominent episode of star formation $\sim$25 Myr ago is evident at the NE extremity of the bar according to Rubele et al. (2015, 2018) which coincides with the NE bar structure. In this region there is also a predominance of young ($<$140 Myr old) Cepheids in front of the main body of the SMC (Ripepi et al. 2017). The larger RV of stars in this region corroborates their formation subsequent to the gas stripping resulting from the dynamical interaction with the LMC. The largest outflow gas velocities are also found in this region (McClure-Griffiths et al.

2018). Furthermore, numerical simulations including interstellar gas dynamics and star formation processes showed that the observed structural, kinematic and stellar properties of the SMC are predominantly of tidal origin (Yoshizawa & Noguchi 2003).

(vi) Soszyński et al. (2010) and Haschke et al. (2012) noticed that RR Lyrae stars, which are distributed fairly homogeneously over the whole body of the SMC, trace two overdensities at the centre similar to those we detect from bright and faint RGB stars. Jacyszyn-Dobrzeniecka et al. (2017) found similar features in the on-sky projection of the OGLE-IV data. However the two overdensities are not present in the 3D Cartesian density maps, deducing that they might be due to a projection effect. The RR Lyrae distribution does not show any substructure or asymmetry along the LOS. Furthermore, no discrepancies in the LOS depth are found between the locations of the two overdensities from the analysis of RC stars (Tatton et al. 2021). In the plane of the sky, several studies based on PMs (De Leo et al. 2020; Niederhofer et al. 2018a; Zivick et al. 2019) found that stars follow a non-uniform velocity structure at the location of the SW-bar overdensity which might indicate a stretching or tidal stripping of the SMC.

In our future work, we plan to carry out a similar investigation of the stellar populations of the LMC. The upcoming large-scale spectroscopic facilities and their planned survey projects: the One Thousand and One Magellanic Fields survey (1001MC; Cioni et al. 2019) using the 4-metre Multi-Object Spectroscopic Telescope (4MOST; de Jong et al. 2019) facility at VISTA and the Survey of the Milky Way and its Satellites (Gonzalez et al. 2020) using the Multi-Object Optical and Near-infrared spectrograph (MOONS; Cirasuolo et al. 2020) facility at the VLT will significantly enlarge spectroscopic stellar sample sizes, cover large areas encompassing also the halo of the MCs, and increase the sensitivity to enable us to investigate substructures with kinematics, metallicity and chemistry in great detail.

4.6 Appendix - Examples of spectral fits

Figure 4.12 shows the spectra of two randomly-selected sources, their spectral fit obtained using pPXF, and the residuals. Each fit is the combination of a number of templates at the same radial velocity of which the first five, with their associated parameters, are listed in Table 4.8 in order of weight. The sum of the weights of the templates participating to a fit is about 1.0, which means that the individual weights can be interpreted as percentage contributions to the spectrum. However, the range of stellar parameters should not be over-interpreted because first, they are not set on a regular grid and second because we have not applied regularisation of the template weights, which is necessary to attach a physical interpretation to the results. Nevertheless, the 1.2 arcsec aperture of the MEDUSA fibres would, in dense stellar regions like the MCs, collect the flux from more than just one source. This might be captured by the pPXF method similarly to what happens in the observation of nearby galaxies with integral field spectrographs for which the pPXF method was originally designed.

Source ADP.2019-02-01T01_00_32.982 is represented by a hot stellar spectrum. It is located in CMD region B and it is most likely a MS star. The resulting RV is

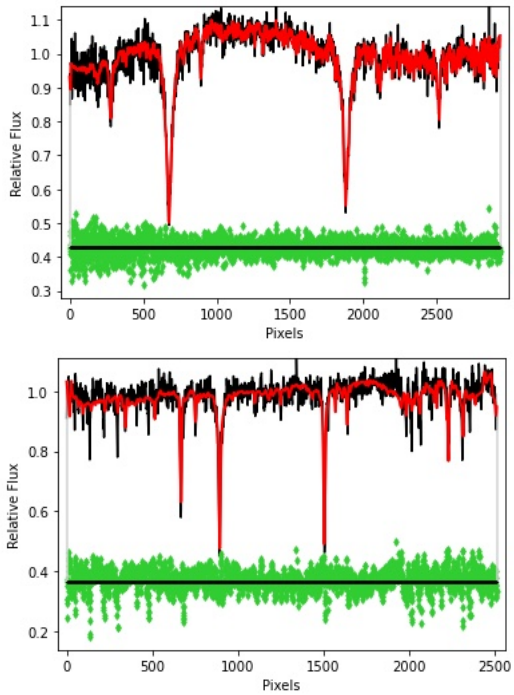

Figure 4.12: Spectra, spectral fits and residuals for sources ADP.2019-02-01T01_00_32.982 (top) and ADP.2019-10-23T14_43_58.789 (bottom).

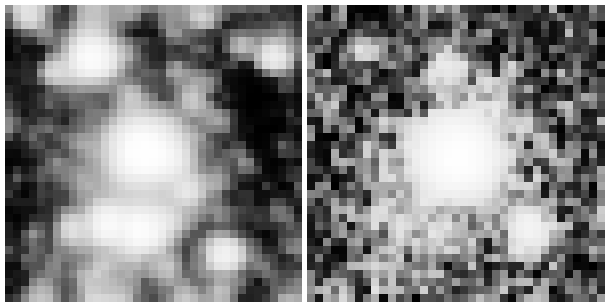

Figure 4.13: Post-stamp 0.2×0.2 arcmin^2 K_s-band images of sources ADP.2019-02-01T01_00_32.982 (left) and ADP.2019-10-23T14_43_58.789 (right).

of 112.9 km s^{-1}. Source ADP.2019-10-23T14_43_58.789 is represented by a rather heterogeneous set of template spectra. It is located in CMD region E and it is most likely a red giant branch star. The resulting RV is of 146.6 km s^{-1}. Figure 4.13 shows that both sources have neighbouring sources and/or nebulous emission suggesting a possible contamination of their spectra.

Table 4.8: Spectral templates and their parameters contributing to the pPXF-based fits of two sources.

Template	$T_{\rm eff}$ K	log(g) cm s^{-2}	[Fe/H] dex	weight
Source ADP.2019-02-01T01_00_32.982:				
HD 38856 (X0817)	15659	4.18	-0.04	0.23
HD 149382 (X0692)	34165	5.54	-1.16	0.20
HD 176301 (X0676)	14552	3.77	0.26	0.11
HD 170783 (X0470)	15500	3.63	0.29	0.10
HD 43286 (X0539)	16006	4.16	-0.11	0.06
Source ADP.2019-10-23T14_43_58.789:				
HE 1201-1512 (X0622)	5729	3.59	-2.61	0.40
HD 4359 (X0448)	17340	4.86	-0.04	0.39
NGC 1904 223 (X0523)	4226	0.69	-1.42	0.25
HE 1207-3108 (X0630)	5435	3.24	-2.65	0.23
HD 4539 (X0463)	17303	4.84	-0.04	0.18

Acknowledgements

This project received funding from the European Research Council (ERC), under the European Union's Horizon 2020 research and innovation programme (grant agreement no. 682115), and was supported in part by the Australian Research Council Centre of Excellence for All Sky Astrophysics in 3 Dimensions (ASTRO 3D), through project number CE170100013. We thank the Cambridge Astronomy Survey Unit (CASU) and the Wide Field Astronomy Unit (WFAU) in Edinburgh for providing the necessary data products under the support of the Science and Technology Facility Council (STFC) in the UK. This study is based on observations obtained with VISTA at the Paranal Observatory under programmes 179.B-2003 and 179.A-2010. This work has made use of data products from the Two Micron All Sky Survey, which is a joint project of the University of Massachusetts and the Infrared Processing and Analysis Center/California Institute of Technology, funded by the National Aeronautics and Space Administration and the National Science Foundation. This work has made use of data from the European Space Agency (ESA) mission *Gaia* (http://www.cosmos.esa.int/gaia), processed by the *Gaia* Data Processing and Analysis Consortium (DPAC; http://www.cosmos.esa.int/web/gaia/dpac/consortium). Funding for the DPAC has been provided by national institutions, in particular the institutions participating in the *Gaia* Multilateral Agreement. This project has made extensive use of the Tool for OPerations on Catalogues And Tables (TOPCAT) software package (Taylor 2005) as well as the following open-source Python packages: matplotlib (Hunter 2007), NumPy (Oliphant 2015), pandas (McKinney 2010), SciPy (Jones et al. 2001). We thank Marica Valentini and Salvatore Taibi for the fruitful discussions concerning the sky subtraction.

Data Availability

The data underlying this study are available in the ESO Archive (http://archive.eso.org). This concerns both catalogues to select the stellar sample and spectra to obtain the radial velocities. The Gaia data to establish the memberships to the SMC are also publicly available. All other data resulting from our study are made available with the publication.

5 Conclusions & Future Outlook

"Begin at the beginning," the King said, very gravely,
"and go on till you come to the end: then stop."
— Lewis Carroll, Alice in Wonderland

5.1 Conclusions

In a ΛCDM universe, one of the main modes of galaxy formation is hierarchical merging, structures form bottom-up and galaxies grow through continuous interactions and mergers with other galaxies. These gravitational perturbations can result in substantial disruptions to their stellar distributions and kinematics, therefore their properties (such as morphology, luminosity, structure parameters and star-formation rate) have a strong dependence on the local environment in which they reside. At a distance of 50 and 60 kpc, the MCs represent the nearest interacting pair of galaxies to the MW, rendering them an important test bed for galaxy morphology and kinematics in the context of galaxy interactions. Their proximity enables us to resolve their light into its individual constituent stars and allows us to employ resolved stellar populations to study their properties.

In this concluding chapter, I provide a concise summary of my key findings, explore a range of possible directions for future work and offer insights into the future prospects of photometric and spectroscopic surveys concerning the MCs. Chapter 2, along with certain sections of Chapter 3, presents morphological maps of the MCs' with unparalleled resolution. These maps are constructed through a comprehensive age tomography approach, utilising NIR photometry obtained from the VMC survey. Additionally, the investigation extends to exploring the outer regions of these galaxies and identifying new substructures associated with their intricate history of interactions, facilitated by the VHS. A detailed examination of the kinematics of select substructures is presented in portions of Chapter 3 and

Chapter 4. This analysis leverages PM data from the *Gaia* mission and RVs extracted from spectroscopic observations taken with FLAMES, offering valuable insights into the origins of the identified substructures are obtained.

A substantial amount of telescope time has been dedicated to multi–wavelength photometric observations and imaging surveys of the MCs. NIR observations have become increasingly important for studies of galaxies and their evolution over cosmic time, due to the reduced sensitivity of the NIR observations to dust and to the increased sensitivity to age or metallicity spread of the underlying stellar population, particularly in combination with the optical or UV. Studies analysing the morphology of the MCs in the NIR date back more than twenty years ago, great strides have been made since then, not only in terms of sensitivity and spatial resolution of photometric surveys but also in regard to stellar evolutionary models used to characterise these stellar populations, highlighting a pressing need for an updated view of the morphology of the MCs. In Chapter 2, I employed VMC to derive the highest-resolution morphological maps of the main bodies of the MCs in the NIR to date. To this end, I utilised a combination of NIR CMDs and theoretical evolutionary models to segregate different stellar populations for which median ages were estimated, allowing to derive the morphology of the MCs through a comprehensive age tomography. The morphology maps revealed detailed features in the central regions that are characterised for the first time at spatial resolutions of 0.13 kpc (LMC) and 0.16 kpc (SMC) showcasing evidence that the tidal interaction between the MCs affected their inner regions and not just their outskirts. In the LMC, MS stars showed coherent structures that grow more enhanced with age and trace the multiple spiral arms of the galaxy. Most of the fine structures such as spiral arms, can be attributed to the recent LMC-SMC interaction $\sim$200 Myr ago, if formed as a result of LMC-SMC interactions $1-3$ or $6-8$ Gyr ago, they would have been most likely smoothed by the dynamical relaxation of the discs. Intermediate-age and old stars, despite tracing a regular and symmetrical morphology, showed central clumps and hints of spiral arms outlining the turbulent history of the galaxy. The asymmetric nature of young populations in the SMC can be attributed to the $1-3$ Gyr ago interaction as it is still prominent in stellar populations $\sim$700 Myr old. Intermediate-age populations showed irregular central features suggesting that tidal interactions also influenced the inner SMC, unlike older populations where the distribution is regular and is characterised by a central over-density. These intermediate–age populations also showed elongations and extensions towards the trailing arm, they have been detected in older populations (RR Lyrae stars) and they can be attributed to the interaction that happened $\sim$200 Myr ago.

Knowledge of the distribution and population characteristics in outlying regions of the MCs is essential for understanding the early history of these galaxies and their place in ΛCDM hierarchy. The outskirts of the MCs lie in a shallower gravitational potential well and are therefore less bound than their main bodies, making them more prone to be disturbed by the interactions between the two galaxies with each other and with the MW. I extend the morphological study to the periphery of the MCs in Chapter 3 and use the NIR photometry from the VHS in combination with multi–dimensional phase–space information from the space astrometry mission *Gaia*. The morphology maps revealed many of the diffuse stellar substructures present in the

periphery of the MCs, some of which were newly discovered such as the Eastern Substructure 2 and Northern Substructure 2. Eastern Substructure 2 resides east of the LMC and is most prominent in the young population. Resembling a young stream, it was found to be lying at a similar distance to the LMC disc suggesting that it belongs to the disc and is unlikely not a residue of a dwarf galaxy. The feature has similar kinematics as the LMC disc when taking into account viewing perspectives. Numerical simulations showed that the substructure is consistent with the MW's tidal field deflecting the LMC disc. The Northern Substructure 2 lies between the SMC's wing and SMCNOD feature and is found to be at a similar distance as the SMC's main body and is mainly made of intermediate–age populations. We also evaluated the luminosity function of RC stars in the SMC and confirmed the presence of a bi-modal distance distribution detectable in the eastern regions of the galaxy out to a 10 deg distance from its centre. This foreground substructure is attributed to the LMC–SMC interaction ~ 200 Myr ago. Additionally, a background structure was detected in the North between 7 deg and 10 deg from the centre which might belong to the Counter Bridge, and a foreground structure is detected in the South between 6 deg and 8 deg from the centre which might be linked to the Old Bridge.

The measurement of motions using LOS velocities in combination with precision astrometry is a necessary component to further the advances made in understanding the MCs using wide photometric surveys and resolved stellar population studies. In Chapter 4, I present a kinematic analysis of the SMC using 3700 spectra extracted from the ESO archive. Data from *Gaia* and near-infrared photometry from VMC to select stellar populations and discard Galactic foreground stars. The sample includes MS, RGB and RC stars, observed with FLAMES. The spectra have a resolving power $\lambda/\Delta\lambda$ from 6500 to $38\,000$. I derived RVs by employing a full spectrum fitting method using a penalised pixel fitting routine. A mean RV for the galaxy of 159 ± 2 km s^{-1}, with avelocity dispersion of 33 ± 2 km s^{-1} was obtained. The calculated velocities agree with literature estimates for similar (young or old) stellar populations. The RV of stars in the Wing and bar-like structures differ as a consequence of the dynamical interaction with the LMC. The higher RV of young MS stars in the bar compared to that of supergiants can be attributed to star formation around 40 Myr ago from gas already influenced by tidal stripping. Similarly, young MS stars in the northern part of the bar, resulting from a prominent star-forming episode 25 Myr ago, have a higher RV than stars in the southern part. RV differences between the northern and southern bar overdensities are also traced by giant stars. They are corroborated by studies of the cold gas and PM indicating stretching/tidal stripping of the galaxy.

5.2 Future outlook

5.2.1 Fainter stellar populations

The MCs have been the subject of extensive multi-wavelength photometric imaging surveys aimed at understanding their morphology. In this thesis, I utilised NIR photometry from VMC and VHS to obtain a comprehensive view of the morphology of these galaxies. However, it is worth noting that there are past, ongoing, and future

photometric surveys that specifically target fainter stellar populations, surpassing the detection capabilities of VMC and VHS. These surveys offer promising opportunities to probe the morphology of faint stellar populations, as well as to unveil new substructures within the MCs and their surroundings. In the subsequent sections, we provide a concise overview of selected surveys and discuss their significance in exploring the morphology of faint stellar populations and identifying previously undiscovered features within the MCs and their periphery.

- **Survey of the Magellanic Stellar History (SMASH):**

The SMASH survey (Nidever et al. 2017) is a deep photometric NOAO community survey with the DECam on the Blanco 4 m telescope at Cerro Tololo Inter-American Observatory, it performs deep photometric imaging in $ugriz$ over a total area of 480 deg^2 (distributed over $\sim$2400 deg^2 with a filling factor of 20 per cent in the outskirts) of the main bodies of the MCs and their periphery. The median 5 σ point-source depths in the $ugriz$ bands are $(23.9, 24.8, 24.5, 24.2, 23.5)$ mag. The second SMASH data release has been circulated in December 2020 and contains all 197 fully-calibrated DECam fields. SMASH is respectively $\sim$2 mag deeper than SDSS, $\sim$1.4 mag than Pan-STARRS1 and $\sim$1.8 mag than VMC. The depth and coverage of the survey have substantial potential for tracing and measuring extended stellar populations of the MCs and searching for low surface–brightness substructure in the periphery of the MCs (e.g. Choi et al. 2018a,b; Nidever et al. 2020; Massana et al. 2020).

- **DECam Local Volume Exploration (DELVE):**

The legacy of the SMASH survey is continued as part of the DECam Local Volume Exploration (DELVE) survey (Drlica-Wagner et al. 2021), another survey program on the 4-m Blanco telescope targeting the entire high–Galactic–Latitude ($\mid$ b $\mid \geq 10$) southern sky seeking to understand dwarf galaxies throughout the Local Volume over a wide range of luminosities. The DELVE survey has three components:

DELVE–WIDE a high Galactic Wide area survey in g, r, i, z aiming to complete DECam coverage of $\sim$ 15000 deg^2 to a depth of $g\sim$23.5 mag, seeking to provide a census of resolved stellar structures including ultra-faint dwarf galaxies around the MW and stellar streams constraining the recent accretion history of the Galaxy as well as the formation and evolution of its halo.

DELVE–MC, providing deep continuous coverage of 2200 deg^2 in g, r, i around the LMC and the SMC to a depth of $g\sim$24.5 mag, extending beyond the faintest MS turn off stars. These observations will enable us to trace faint stellar substructures in the MCs, stellar tidal features around them as well as unearthing spatially resolved star formation histories at unprecedented details owing to deep colour-magnitude diagrams. Additionally DELVE–MC will help detect new satellite galaxies found around the MCs.

DELVE–DEEP providing deep imaging of 135 deg^2 in g, i around four Magellanic analogues in the local volume to a depth of $g\sim$25 mag targeting resolved stars 1.5 mag below the tip of RGB and allowing to detect ultra–faint galaxies with $M_V \leq -7$. The search for satellites around isolated MC analogues without a massive host will enable us to understand the role of environmental effects on MC mass hosts on their satellite populations, further more DELVE–DEEP will allow a detailed study of the targets including quantifying their stellar density profile to extended radii low

surface brightness.
The DELVE survey has revealed the existence of ultra-faint systems: Centaurus I, DELVE 1 (Mau et al. 2020), DELVE2 (Cerny et al. 2021a) and Eridanus IV (Cerny et al. 2021b) as well as the characterisation of the Jet stream (Ferguson et al. 2022). These findings reinforce the prediction of numerical simulations that $\sim$100 MW satellites are remaining to be discovered (Nadler et al. 2020) and strengthen the necessity of resolved stellar population studies with ongoing and future deep and wide-area photometric surveys.

-**Rubin Observatory Legacy Survey of Space and Time (LSST)**:
The DELVE survey provides a significant precursor legacy to future photometric facilities such as the Vera C. Rubin Observatory, an optical 8.4 m telescope located at Cerro Pachón in Chile that will see light in 2024. The facility aims to monitor the entire southern hemisphere sky continuously over a ten year period as part of the Rubin Observatory Legacy Survey of Space and Time (Ivezić et al. 2019; LSST). Its exceedingly large field of view ($\sim$3.2 deg) will allow wide–field deep imaging of the sky, combined with its high spatial resolution, high cadence, and high sensitivity, LSST will contribute significantly to our understanding of the MCs. The proposed footprint covering the MCs and their periphery has three components: A modified Wide-Deep-Fast survey covering an area of 72.25 deg $\leq$ Dec $\leq$ 12.4 deg and the Galactic latitude range |b| $\geq$ 15 deg and achieving depths of ($ugriz$) = $(26.4, 27.6, 27.2, 26.6, 25.7)$ mag, a mini-survey of the South Celestial Pole covering an area of 950 deg^2 with Dec $\leq$75, and a Deep Drilling-style survey covering the main bodies of the MCs with 3 fields in the SMC and 9 in the LMC.
LSST will improve our understanding of resolved stellar populations in the MCs significantly by providing deep, homogeneous photometry for an unprecedented amount of stars. Reaching depths as faint as $r\sim$27 mag, LSST will reach beyond the faintest MS turn-off stars allowing us to trace stellar substructures resulting from their interactions as well as detect, map and characterise their extended discs and stellar halos with substantial potential for discovering new MC satellite galaxies. MS turn-off stars have proved to be useful for characterising the low surface brightness periphery of the MCs, however the depth limit of this population will not be dictated by the photometric detection limit of the survey but rather by the factor of galaxy-star separation. The ability to differentiate between stars and unresolved backgrounds galaxies worsens significantly towards fainter magnitudes. Furthermore, MS turn-off stars can be used to map the photometric metallicity distribution of the MCs as u–band data exhibits the strongest metallicity dependence of the LSST filters, enabling us to trace out population gradients in the MCs and uncover the origin of their very extended stellar peripheries. Owing to high cadence observations, LSST will enable us to fully characterise the variable stars content of the MCs over timescales ranging from 15 sec to 10 years by studying trends in their period distributions as well as possible variations in absolute magnitude with period, age, and metallicity. Furthermore, distances obtained from RR Lyrae and δ Scuti stars will shed light on the 3D structure of the MCs. *Gaia* will provide PMs of resolved stellar populations down to a magnitude of $\sim$ 20 mag. LSST will be complementary to *Gaia* and provide PM measurements for magnitudes ranging from 20 to 24 mag including MS turn-off stars with a precision reaching $0.3 - 0.4$ mas yr^{-1} for r $\sim$ 23 mag. Coupled with

LOS velocities from future spectroscopic surveys, a comprehensive view of the 3D kinematics of the MCs will be reached.

5.2.2 Future *Gaia* data releases

Gaia is the space astrometry mission of the European Space Agency (Gaia Collaboration et al. 2016b), its main aim is to measure the 3D spatial and the 3D velocity distribution of stars and to determine their astrophysical properties, such as surface gravity and effective temperature, to map and understand the formation, structure, and past and future evolution of the MW as well as its satellites. *Gaia* eDR3 became available towards the end of 2020 (Gaia Collaboration et al. 2021a), it consisted of photometry and astrometry for 1.8 billion sources brighter than $G{\sim}20.7$ mag in addition to an updated list of RVs from *Gaia* DR2, cleaned from spurious sources. *Gaia* DR3 was released in 2022 June and included *Gaia* eDR3 products complemented with new data including mean RVs for 33 millions objects with $G{\leq}14$ mag, astrophysical parameters for about 500 millions objects, BP/RP spectra for at least 100 millions sources with G$\leq$17.6 mag and RVS spectra for 1 million well-behaved objects. *Gaia* DR4 will be the final data release of the nominal mission based on 66 months of data, it is not expected to be released before the end of 2025. The overall gain in precision in photometry, astrometry and RVs compared to DR2 is foreseen to be a factor of 1.7, while PMs are expected to improve by a factor of 4.5. A *Gaia* DR5 is anticipated to contain all collected data. *Gaia* will continue to revolutionise our understanding of the formation and evolution of the MCs, and is impacting many other areas of astrophysics ranging from solar system science to quasars.

5.2.3 Future spectroscopic facilities

Future spectroscopic facilities targeting the MCs play a critical role in the near–IR and optical spectroscopic follow–up for the *Gaia* mission and for other ground based imaging surveys (VISTA, Pan-STARRS, DES, LSST, SMASH) as well as following up on objects observed at other wavelengths (e.g ALMA, Herschel, eRosita, LOFAR, WISE, ASKAP, and MeerKAT).

One of these facilities is MOONS, the new Multi-Object Optical and Near-infrared Spectrograph currently under construction for the VLT at ESO (Cirasuolo et al. 2020). It offers both medium ($R = 4000$ and $R = 6000$) and high-resolution ($R = 8000$ and $R = 20000$) spectroscopy in the NIR ($0.8 - 1.8\ \mu m$) with a baseline design consisting of ∼1000 fibres, deployed across 500 arcmin^2. MOONS will target the central regions of both the LMC and SMC by observing a 5×5 and 3×3 mosaics, respectively. It will also include about 17 fields located along the major axis of the bar and in the LMC disc as well as 4 additional fields around the LMC centre. In the SMC, MOONS will observe about 13 fields along the SMC northeast extension. The culmination of these fields will result in observing ∼35000 stars in the LMC and ∼18000 in the SMC down to I_{AB} = 18 mag ($H_{AB} \leq 17.6$ mag), allowing to study the chemical composition and kinematics of the densest regions and accurately identify the position of their dynamical centres.

Another spectroscopic facility that will advance our understanding of the MCs is 4MOST, a new high-multiplex, wide-field spectroscopic facility to be installed at VISTA (de Jong et al. 2019), it will replace VIRCAM, the instrument that observed both VMC and VHS, which a good proportion of this thesis was based on. 4MOST will provide a field–of–view of 4.2 deg^2 with 1624 fibres feeding two low-resolution spectrographs (R$\sim$6500, λ=$3700 - 9500$ Å), and 812 fibres transferring light to the high-resolution spectrograph (R$\sim$20000, λ=$3926 - 4355, 5160 - 5730, 6100 - 6790$ Å). Among the 4MOST consortium surveys is the 1001MC survey (Cioni et al. 2019), its aim is to obtain kinematics and element abundances for many stellar populations representing the formation and evolution of the MCs. The survey will observe $\sim$ 1 million spectra with G ≤ 20 mag (Vega) across an area of $\sim$1000 deg^2.

5.2.4 Kinematics and Chemistry

Origins of the non-axisymmetric substructures of the LMC:
The presence of non-axisymmetric characteristics, such as spiral arms, alters the velocity distribution within a rotating disc. Differentiating between types of spiral arms, such as density waves, tidally induced arms, transient co-rotating arms, or bar-induced arms, can be achieved by analysing their distinct signatures in the velocity field (Roca-Fàbrega et al. 2013, 2014). However, the origin of the LMC's asymmetric nature and the specific source of its spiral arms, as opposed to more massive spiral galaxies, remains uncertain. Consequently, it is essential to conduct a thorough examination of detailed kinematic profiles and maps to supplement the investigation of these substructures.

Chemodynamical study of the foreground RC substructure in the SMC:
The origin of the RC foreground structure found in the SMC (Nidever et al. 2010; Subramanian et al. 2017; Omkumar et al. 2021; El Youssoufi et al. 2021) is still ambiguous. RR Lyrae stars do not exhibit such a bi-modality, Tatton et al. (2020) suggests that tidal stripping would have affected all stellar populations similarly and that the nearer RC component resulted from ram-pressure stripping of gas a few Gyr ago which led to subsequent formation of stars including what are now RC stars. To understand the origin of the substructure. RVs and chemical abundances from spectroscopic observations in combination with PMs of the foreground RC and field RC stars in combination with *Gaia* EDR3 data is crucial to comprehensive characterisation in 6D space is necessary.

Accreted stars in the MCs:
The identification of accreted stars in the MCs can be achieved through a multi-faceted approach, combining kinematics, chemical information, and advanced data analysis techniques such as t-SNE (t-Distributed Stochastic Neighbor Embedding) and PCA (Principal Component Analysis). PMs and LOS velocities provide crucial kinematic data, allowing us to trace the apparent motion of stars and detect potential outliers. By comparing the kinematics of individual stars with the local bulk motion in the MCs, significant deviations can be identified, potentially indicating stars that have migrated between the MCs. Chemical information, such as abundances

of different elements, provides valuable insights into the formation and evolution environments of stars. By employing chemical tagging techniques, which group stars based on their positions in chemical abundance space, we can identify stars with similar chemical compositions, potentially revealing populations of stars that were accreted from one Cloud to another. This approach was first proposed by Freeman & Bland-Hawthorn (2002) and has since been applied successfully in various studies. To further enhance the search for accreted stars, dimensionality reduction techniques such as t-SNE and PCA can be applied. t-SNE can reveal non-linear relationships and hidden structures in the data by mapping high-dimensional chemical and kinematic information onto a lower-dimensional space. This can help identify clusters or subgroups of stars with similar properties, potentially representing accreted populations. Similarly, PCA can uncover the dominant patterns of variation in chemical abundances, RVs, and PMs. By analyzing the principal components, which capture the major sources of variation in the data, it is possible to identify outliers or distinct subgroups that deviate from the majority population. These outliers may correspond to accreted stars with unique chemical compositions or kinematic behaviour. By combining PMs, chemical information, and dimensionality reduction techniques like t-SNE and PCA, it is possible to enhance our ability to detect and characterize accreted stars in the MCs. These approaches provide complementary insights into the migration histories and formation origins of stars, contributing to our understanding of the complex interactions between the MCs.

Bibliography

1997, ESA Special Publication, Vol. 1200, The HIPPARCOS and TYCHO catalogues. Astrometric and photometric star catalogues derived from the ESA HIPPARCOS Space Astrometry Mission

Abbott, T. M. C., Abdalla, F. B., Allam, S., et al. 2018, The Astrophysical Journal Supplement Series, 239, 18

Abdurro'uf, Accetta, K., Aerts, C., et al. 2022, ApJS, 259, 35

Ahumada, R., Prieto, C. A., Almeida, A., et al. 2020, ApJS, 249, 3

Alves, D. R. 2000, ApJ, 539, 732

Alves, D. R. & Nelson, C. A. 2000, ApJ, 542, 789

Ardeberg, A. & Maurice, E. 1977, A&AS, 30, 261

Ardeberg, A. & Maurice, E. 1979, A&A, 77, 277

Arentsen, A., Prugniel, P., Gonneau, A., et al. 2019, A&A, 627, A138

Avner, E. S. & King, I. R. 1967, AJ, 72, 650

Bagheri, G., Cioni, M. R. L., & Napiwotzki, R. 2013, A&A, 551, A78

Balbinot, E., Santiago, B. X., Girardi, L., et al. 2015, MNRAS, 449, 1129

Battaglia, G., Taibi, S., Thomas, G. F., & Fritz, T. K. 2022, A&A, 657, A54

Bechtol, K., Drlica-Wagner, A., Balbinot, E., et al. 2015, ApJ, 807, 50

Behroozi, P. S., Wechsler, R. H., & Conroy, C. 2013, ApJ, 770, 57

Bekki, K. 2009, MNRAS, 399, 2221

Bekki, K. & Chiba, M. 2005, MNRAS, 356, 680

Bekki, K. & Stanimirović, S. 2009, MNRAS, 395, 342

Bekki, K., Yahagi, H., Nagashima, M., & Forbes, D. A. 2007, MNRAS, 382, L87

Belcheva, M. K., Livanou, E., Kontizas, M., Nikolov, G. B., & Kontizas, E. 2011, A&A, 527, A31

Belokurov, V., Erkal, D., Deason, A. J., et al. 2017, MNRAS, 466, 4711

Belokurov, V. & Koposov, S. E. 2016, MNRAS, 456, 602

Belokurov, V. A. & Erkal, D. 2019, MNRAS, 482, L9

Bertelli, G., Mateo, M., Chiosi, C., & Bressan, A. 1992, ApJ, 388, 400

Besla, G., Kallivayalil, N., Hernquist, L., et al. 2007, ApJ, 668, 949

Besla, G., Kallivayalil, N., Hernquist, L., et al. 2010, ApJ, 721, L97

Besla, G., Kallivayalil, N., Hernquist, L., et al. 2012, MNRAS, 421, 2109

Besla, G., Martínez-Delgado, D., van der Marel, R. P., et al. 2016, ApJ, 825, 20

Bica, E., Bonatto, C., Dutra, C. M., & Santos, J. F. C. 2008, MNRAS, 389, 678

Boardman, N. F., Weijmans, A.-M., van den Bosch, R., et al. 2017, MNRAS, 471, 4005

Boubert, D., Erkal, D., & Gualandris, A. 2020, MNRAS, 497, 2930

Boylan-Kolchin, M., Springel, V., White, S. D. M., & Jenkins, A. 2010, MNRAS, 406, 896

Bozzetto, L. M., Filipović, M. D., Vukotić, B., et al. 2017, ApJS, 230, 2

Brown, A. G. A. 2021, ARA&A, 59, 59

Bullock, J. S. & Johnston, K. V. 2005, ApJ, 635, 931

Burkert, A. 1995, ApJ, 447, L25

Busha, M. T., Wechsler, R. H., Behroozi, P. S., et al. 2011, ApJ, 743, 117

Cappellari, M. 2017, MNRAS, 466, 798

Cappellari, M. & Emsellem, E. 2004, PASP, 116, 138

Cardelli, J. A., Clayton, G. C., & Mathis, J. S. 1989, ApJ, 345, 245

Carrera, R., Conn, B. C., Noël, N. E. D., Read, J. I., & López Sánchez, Á. R. 2017, MNRAS, 471, 4571

Carrera, R., Gallart, C., Aparicio, A., et al. 2008, AJ, 136, 1039

Cerny, W., Pace, A. B., Drlica-Wagner, A., et al. 2021a, ApJ, 910, 18

Cerny, W., Pace, A. B., Drlica-Wagner, A., et al. 2021b, ApJ, 920, L44

Chambers, K. C., Magnier, E. A., Metcalfe, N., et al. 2016, arXiv e-prints, arXiv:1612.05560

Cheng, X., Choi, Y., Olsen, K., et al. 2022, ApJ, 928, 95

Choi, Y., Nidever, D. L., Olsen, K., et al. 2018a, ApJ, 869, 125

Choi, Y., Nidever, D. L., Olsen, K., et al. 2018b, ApJ, 866, 90

Choi, Y., Olsen, K. A. G., Besla, G., et al. 2022, ApJ, 927, 153

Cignoni, M., Cole, A. A., Tosi, M., et al. 2013, ApJ, 775, 83

Cioni, M. . R. L., Storm, J., Bell, C. P. M., et al. 2019, The Messenger, 175, 54

Cioni, M.-R. L., Bekki, K., Girardi, L., et al. 2016, A&A, 586, A77

Cioni, M.-R. L., Clementini, G., Girardi, L., et al. 2011, A&A, 527, A116

Cioni, M.-R. L., Girardi, L., Moretti, M. I., et al. 2014, A&A, 562, A32

Cioni, M.-R. L. & Habing, H. J. 2003, A&A, 402, 133

Cioni, M.-R. L., Habing, H. J., & Israel, F. P. 2000a, A&A, 358, L9

Cioni, M.-R. L., Marquette, J.-B., Loup, C., et al. 2001, A&A, 377, 945

Cioni, M.-R. L., van der Marel, R. P., Loup, C., & Habing, H. J. 2000b, A&A, 359, 601

Cirasuolo, M., Fairley, A., Rees, P., et al. 2020, The Messenger, 180, 10

Clementini, G., Ripepi, V., Molinaro, R., et al. 2019, A&A, 622, A60

Cole, A. A., Tolstoy, E., Gallagher, John S., I., & Smecker-Hane, T. A. 2005, AJ, 129, 1465

Correa Magnus, L. & Vasiliev, E. 2022, MNRAS, 511, 2610

Cross, N. J. G., Collins, R. S., Mann, R. G., et al. 2012, A&A, 548, A119

Cullinane, L. R., Mackey, A. D., Da Costa, G. S., et al. 2022a, MNRAS, 510, 445

Cullinane, L. R., Mackey, A. D., Da Costa, G. S., et al. 2022b, MNRAS, 512, 4798

Cullinane, L. R., Mackey, A. D., Da Costa, G. S., et al. 2020, MNRAS, 497, 3055

Cullinane, L. R., Mackey, A. D., Da Costa, G. S., Koposov, S. E., & Erkal, D. 2023, MNRAS, 518, L25

Dalton, G. B., Caldwell, M., Ward, A. K., et al. 2006, in Ground-based and Airborne Instrumentation for Astronomy, ed. I. S. McLean & M. Iye, Vol. 6269, International Society for Optics and Photonics (SPIE), 314 – 323

Dawson, J. R., McClure-Griffiths, N. M., Wong, T., et al. 2013, ApJ, 763, 56

de Grijs, R. & Bono, G. 2015, AJ, 149, 179

de Grijs, R., Wicker, J. E., & Bono, G. 2014, AJ, 147, 122

de Jong, R. S., Agertz, O., Berbel, A. A., et al. 2019, The Messenger, 175, 3

De Leo, M., Carrera, R., Noël, N. E. D., et al. 2020, MNRAS, 495, 98

de Vaucouleurs, G. 1954a, The Observatory, 74, 23

de Vaucouleurs, G. 1954b, The Observatory, 74, 158

de Vaucouleurs, G. 1955a, AJ, 60, 126

de Vaucouleurs, G. 1955b, AJ, 60, 219

de Vaucouleurs, G. 1955c, PASP, 67, 350

de Vaucouleurs, G. 1957, AJ, 62, 69

de Vaucouleurs, G. & Freeman, K. C. 1972, Vistas in Astronomy, 14, 163

Deason, A. J., Belokurov, V., Erkal, D., Koposov, S. E., & Mackey, D. 2017, MNRAS, 467, 2636

Deason, A. J., Wetzel, A. R., Garrison-Kimmel, S., & Belokurov, V. 2015, MNRAS, 453, 3568

Dennefeld, M. 2020, The Messenger, 181, 37

Di Teodoro, E. M., McClure-Griffiths, N. M., Jameson, K. E., et al. 2019, MNRAS, 483, 392

Diaz, J. D. & Bekki, K. 2012, ApJ, 750, 36

Dobbie, P. D., Cole, A. A., Subramaniam, A., & Keller, S. 2014, MNRAS, 442, 1663

D'Onghia, E. & Fox, A. J. 2016, ARA&A, 54, 363

D'Onghia, E. & Lake, G. 2008, ApJ, 686, L61

Dooley, G. A., Peter, A. H. G., Carlin, J. L., et al. 2017a, MNRAS, 472, 1060

Dooley, G. A., Peter, A. H. G., Yang, T., et al. 2017b, MNRAS, 471, 4894

Drlica-Wagner, A., Bechtol, K., Allam, S., et al. 2016, ApJ, 833, L5

Drlica-Wagner, A., Bechtol, K., Rykoff, E. S., et al. 2015, ApJ, 813, 109

Drlica-Wagner, A., Carlin, J. L., Nidever, D. L., et al. 2021, ApJS, 256, 2

Dutra, C. M., Bica, E., Claria, J. J., & Piatti, A. E. 1999, MNRAS, 305, 373

El Youssoufi, D., Cioni, M.-R. L., Bell, C. P. M., et al. 2021, MNRAS, 505, 2020

El Youssoufi, D., Cioni, M.-R. L., Bell, C. P. M., et al. 2019, MNRAS, 490, 1076

El Youssoufi, D., Cioni, M.-R. L., Kacharov, N., et al. 2023, MNRAS, 523, 347

Emerson, J., McPherson, A., & Sutherland, W. 2006, The Messenger, 126, 41

Erkal, D., Belokurov, V., Laporte, C. F. P., et al. 2019, MNRAS, 487, 2685

Erkal, D. & Belokurov, V. A. 2020, MNRAS, 495, 2554

Evans, C. J. & Howarth, I. D. 2008, MNRAS, 386, 826
Feitzinger, J. V., Isserstedt, J., & Schmidt-Kaler, T. 1977, A&A, 57, 265
Ferguson, P. S., Shipp, N., Drlica-Wagner, A., et al. 2022, AJ, 163, 18
Fox, A. J., Richter, P., Wakker, B. P., et al. 2013, ApJ, 772, 110
Fox, A. J., Wakker, B. P., Barger, K. A., et al. 2014, ApJ, 787, 147
Freedman, W. L., Madore, B. F., Gibson, B. K., et al. 2001, ApJ, 553, 47
Freeman, K. & Bland-Hawthorn, J. 2002, ARA&A, 40, 487
Freeman, K. C., Illingworth, G., & Oemler, A., J. 1983, ApJ, 272, 488
Fritz, T. K., Battaglia, G., Pawlowski, M. S., et al. 2018, A&A, 619, A103
Gaia Collaboration, Brown, A. G. A., Vallenari, A., et al. 2018a, A&A, 616, A1
Gaia Collaboration, Brown, A. G. A., Vallenari, A., et al. 2020a, arXiv e-prints, arXiv:2012.01533
Gaia Collaboration, Brown, A. G. A., Vallenari, A., et al. 2021a, A&A, 649, A1
Gaia Collaboration, Brown, A. G. A., Vallenari, A., et al. 2016a, A&A, 595, A2
Gaia Collaboration, Helmi, A., van Leeuwen, F., et al. 2018b, A&A, 616, A12
Gaia Collaboration, Luri, X., Chemin, L., et al. 2020b, arXiv e-prints, arXiv:2012.01771
Gaia Collaboration, Luri, X., Chemin, L., et al. 2021b, A&A, 649, A7
Gaia Collaboration, Prusti, T., de Bruijne, J. H. J., et al. 2016b, A&A, 595, A1
Gaia Collaboration, Vallenari, A., Brown, A. G. A., et al. 2022, arXiv e-prints, arXiv:2208.00211
Garavito-Camargo, N., Besla, G., Laporte, C. F. P., et al. 2019, ApJ, 884, 51
Gardiner, L. T. & Hatzidimitriou, D. 1992, MNRAS, 257, 195
Gardiner, L. T. & Noguchi, M. 1996, MNRAS, 278, 191
Gatto, M., Ripepi, V., Bellazzini, M., et al. 2020, MNRAS, 499, 4114
Gatto, M., Ripepi, V., Bellazzini, M., et al. 2022, arXiv e-prints, arXiv:2207.09478
Gaustad, J. E., McCullough, P. R., Rosing, W., & Van Buren, D. 2001, PASP, 113, 1326
Girardi, L. 2016, Astron. Nachr., 337, 871
Gómez, F. A., Besla, G., Carpintero, D. D., et al. 2015, ApJ, 802, 128
Gonidakis, I., Livanou, E., Kontizas, E., et al. 2009, A&A, 496, 375
Gonneau, A., Lyubenova, M., Lançon, A., et al. 2020, A&A, 634, A133
Gonzalez, O. A., Mucciarelli, A., Origlia, L., et al. 2020, The Messenger, 180, 18
González, R. E., Kravtsov, A. V., & Gnedin, N. Y. 2013, ApJ, 770, 96
González-Fernández, C., Hodgkin, S. T., Irwin, M. J., et al. 2018, MNRAS, 474, 5459
Grady, J., Belokurov, V., & Evans, N. W. 2021, ApJ, 909, 150
Grocholski, A. J., Cole, A. A., Sarajedini, A., Geisler, D., & Smith, V. V. 2006, AJ, 132, 1630
Groenewegen, M. A. T. 2008, A&A, 488, 935
Hagen, L. M. Z., Siegel, M. H., Hoversten, E. A., et al. 2017, MNRAS, 466, 4540
Hammer, F., Yang, Y. B., Flores, H., Puech, M., & Fouquet, S. 2015, ApJ, 813, 110
Hardy, E., Suntzeff, N. B., & Azzopardi, M. 1989, ApJ, 344, 210

Harris, J. 2007, ApJ, 658, 345

Harris, J. & Zaritsky, D. 2004a, AJ, 127, 1531

Harris, J. & Zaritsky, D. 2004b, AJ, 127, 1531

Harris, J. & Zaritsky, D. 2006, AJ, 131, 2514

Harris, J. & Zaritsky, D. 2009, AJ, 138, 1243

Haschke, R., Grebel, E. K., & Duffau, S. 2012, AJ, 144, 106

Hatzidimitriou, D., Cannon, R. D., & Hawkins, M. R. S. 1993, MNRAS, 261, 873

Hatzidimitriou, D., Croke, B. F., Morgan, D. H., & Cannon, R. D. 1997, A&AS, 122, 507

Hawkins, K., Leistedt, B., Bovy, J., & Hogg, D. W. 2017, MNRAS, 471, 722

Herschel, John Frederick William, S. 1847, Results of astronomical observations made during the years 1834, 5, 6, 7, 8, at the Cape of Good Hope; being the completion of a telescopic survey of the whole surface of the visible heavens, commenced in 1825

HI4PI Collaboration, Ben Bekhti, N., Flöer, L., et al. 2016, A&A, 594, A116

Hindman, J. V., Kerr, F. J., & McGee, R. X. 1963, Australian Journal of Physics, 16, 570

Hodge, P. 1985, PASP, 97, 530

Høg, E., Fabricius, C., Makarov, V. V., et al. 2000, A&A, 355, L27

Homma, D., Chiba, M., Okamoto, S., et al. 2018, PASJ, 70, S18

Hotan, A. W., Bunton, J. D., Chippendale, A. P., et al. 2021, , 38, e009

Hunter, C. & Toomre, A. 1969, ApJ, 155, 747

Hunter, J. D. 2007, Computing in Science and Engineering, 9, 90

Indu, G. & Subramaniam, A. 2011, A&A, 535, A115

Inno, L., Bono, G., Matsunaga, N., et al. 2016, ApJ, 832, 176

Irwin, M. J. 1991, in The Magellanic Clouds, ed. R. Haynes & D. Milne, Vol. 148, 453

Irwin, M. J., Demers, S., & Kunkel, W. E. 1990, AJ, 99, 191

Irwin, M. J., Lewis, J., Hodgkin, S., et al. 2004, in Proc. SPIE, Vol. 5493, Optimizing Scientific Return for Astronomy through Information Technologies, ed. P. J. Quinn & A. Bridger, 411–422

Ivezić, Ž., Kahn, S. M., Tyson, J. A., et al. 2019, ApJ, 873, 111

Jacyszyn-Dobrzeniecka, A. M., Mróz, P., Kruszyńska, K., et al. 2020a, ApJ, 889, 26

Jacyszyn-Dobrzeniecka, A. M., Skowron, D. M., Mróz, P., et al. 2016, AcA, 66, 149

Jacyszyn-Dobrzeniecka, A. M., Skowron, D. M., Mróz, P., et al. 2017, AcA, 67, 1

Jacyszyn-Dobrzeniecka, A. M., Soszyński, I., Udalski, A., et al. 2020b, ApJ, 889, 25

Jahn, E. D., Sales, L. V., Wetzel, A., et al. 2019, MNRAS, 489, 5348

James, D., Subramanian, S., Omkumar, A. O., et al. 2021, MNRAS, 508, 5854

Jethwa, P., Erkal, D., & Belokurov, V. 2016, MNRAS, 461, 2212

Jones, B. F., Klemola, A. R., & Lin, D. N. C. 1994, AJ, 107, 1333

Jones, E., Oliphant, T. E., Peterson, P., et al. 2001, SciPy: Open source scientific tools for Python

Kahn, F. D. & Woltjer, L. 1959, ApJ, 130, 705
Kallivayalil, N., Sales, L. V., Zivick, P., et al. 2018, ApJ, 867, 19
Kallivayalil, N., van der Marel, R. P., & Alcock, C. 2006a, ApJ, 652, 1213
Kallivayalil, N., van der Marel, R. P., Alcock, C., et al. 2006b, ApJ, 638, 772
Kallivayalil, N., van der Marel, R. P., Besla, G., Anderson, J., & Alcock, C. 2013, ApJ, 764, 161
Katz, D., Sartoretti, P., Guerrier, A., et al. 2022, arXiv e-prints, arXiv:2206.05902
Kim, D. & Jerjen, H. 2015, ApJ, 808, L39
Kim, D., Jerjen, H., Mackey, D., Da Costa, G. S., & Milone, A. P. 2015, ApJ, 804, L44
Kim, S., Staveley-Smith, L., Dopita, M. A., et al. 2003, ApJS, 148, 473
Koch, A., Wilkinson, M. I., Kleyna, J. T., et al. 2007, ApJ, 657, 241
Koposov, S. E., Belokurov, V., Li, T. S., et al. 2019, MNRAS, 485, 4726
Koposov, S. E., Belokurov, V., Torrealba, G., & Evans, N. W. 2015, ApJ, 805, 130
Koposov, S. E., Walker, M. G., Belokurov, V., et al. 2018, MNRAS, 479, 5343
Kroupa, P. & Bastian, U. 1997, New Astron., 2, 77
Kroupa, P., Röser, S., & Bastian, U. 1994, MNRAS, 266, 412
Kunkel, W. E., Demers, S., & Irwin, M. J. 2000, AJ, 119, 2789
Laevens, B. P. M., Martin, N. F., Bernard, E. J., et al. 2015, ApJ, 813, 44
Lamb, J. B., Oey, M. S., Segura-Cox, D. M., et al. 2016, ApJ, 817, 113
Laney, C. D., Joner, M. D., & Pietrzyński, G. 2012, MNRAS, 419, 1637
Laporte, C. F. P., Gómez, F. A., Besla, G., Johnston, K. V., & Garavito-Camargo, N. 2018, MNRAS, 473, 1218
Leavitt, H. S. 1908, Annals of Harvard College Observatory, 60, 87
Leavitt, H. S. & Pickering, E. C. 1912, Harvard College Observatory Circular, 173, 1
Lin, D. N. C. & Lynden-Bell, D. 1982, MNRAS, 198, 707
Lindegren, L., Lammers, U., Bastian, U., et al. 2016, A&A, 595, A4
Liu, L., Gerke, B. F., Wechsler, R. H., Behroozi, P. S., & Busha, M. T. 2011, ApJ, 733, 62
Lucchini, S., D'Onghia, E., & Fox, A. J. 2021, ApJ, 921, L36
Lucchini, S., D'Onghia, E., Fox, A. J., et al. 2020, Nature, 585, 203
Lundmark, K. 1924, The Observatory, 47, 276
Luque, E., Queiroz, A., Santiago, B., et al. 2016, MNRAS, 458, 603
Lynden-Bell, D. 1976, MNRAS, 174, 695
Lynden-Bell, D. 1981, The Observatory, 101, 111
Lynden-Bell, D. 1982, The Observatory, 102, 202
Mackey, A. D., Koposov, S. E., Da Costa, G. S., et al. 2017, MNRAS, 472, 2975
Mackey, A. D., Koposov, S. E., Erkal, D., et al. 2016, MNRAS, 459, 239
Mackey, D., Koposov, S., Da Costa, G., et al. 2018, ApJ, 858, L21
Majewski, S. R., Nidever, D. L., Muñoz, R. R., et al. 2009, in The Magellanic System: Stars, Gas, and Galaxies, ed. J. T. Van Loon & J. M. Oliveira, Vol. 256, 51–56

Majewski, S. R., Schiavon, R. P., Frinchaboy, P. M., et al. 2017, AJ, 154, 94
Maragoudaki, F., Kontizas, M., Morgan, D. H., et al. 2001, A&A, 379, 864
Marigo, P., Girardi, L., Bressan, A., et al. 2017, ApJ, 835, 77
Martin, D. C., Fanson, J., Schiminovich, D., et al. 2005, ApJ, 619, L1
Martin, N. F., Nidever, D. L., Besla, G., et al. 2015, ApJ, 804, L5
Martínez-Delgado, D., Katherina Vivas, A., Grebel, E. K., et al. 2019, A&A, 631, A98
Massana, P., Noël, N. E. D., Nidever, D. L., et al. 2020, MNRAS, 498, 1034
Massana, P., Ruiz-Lara, T., Noël, N. E. D., et al. 2022, MNRAS, 513, L40
Massari, D. & Helmi, A. 2018, A&A, 620, A155
Mateo, M., Hodge, P., & Schommer, R. A. 1986, ApJ, 311, 113
Mathewson, D. S., Cleary, M. N., & Murray, J. D. 1974, ApJ, 190, 291
Mathewson, D. S., Ford, V. L., & Visvanathan, N. 1988, ApJ, 333, 617
Mau, S., Cerny, W., Pace, A. B., et al. 2020, ApJ, 890, 136
Mazzi, A., Girardi, L., Zaggia, S., et al. 2021, MNRAS, 508, 245
McClure-Griffiths, N. M., Dénes, H., Dickey, J. M., et al. 2018, Nat. Astron., 2, 901
McClure-Griffiths, N. M., Staveley-Smith, L., Lockman, F. J., et al. 2008, ApJ, 673, L143
McConnachie, A. W. & Venn, K. A. 2020, AJ, 160, 124
McKinney, W. 2010, in Proceedings of the 9th Python in Science Conference, ed. S. van der Walt & J. Millman, 51
McMahon, R. G., Banerji, M., Gonzalez, E., et al. 2013, The Messenger, 154, 35
Meatheringham, S. J., Dopita, M. A., Ford, H. C., & Webster, B. L. 1988, ApJ, 327, 651
Minniti, D., Borissova, J., Rejkuba, M., et al. 2003, Science, 301, 1508
Moretti, M. I., Clementini, G., Muraveva, T., et al. 2014, MNRAS, 437, 2702
Moster, B. P., Naab, T., & White, S. D. M. 2013, MNRAS, 428, 3121
Muñoz, R. R., Majewski, S. R., Zaggia, S., et al. 2006, ApJ, 649, 201
Mucciarelli, A., Minelli, A., Bellazzini, M., et al. 2023, arXiv e-prints, arXiv:2301.08758
Murali, C. 2000, ApJ, 529, L81
Muraveva, T., Subramanian, S., Clementini, G., et al. 2018, MNRAS, 473, 3131
Murray, C. E., Peek, J. E. G., Di Teodoro, E. M., et al. 2019, ApJ, 887, 267
Nadler, E. O., Wechsler, R. H., Bechtol, K., et al. 2020, ApJ, 893, 48
Navarrete, C., Aguado, D. S., Belokurov, V., et al. 2023, arXiv e-prints, arXiv:2302.04579
Navarrete, C., Belokurov, V., Catelan, M., et al. 2019, MNRAS, 483, 4160
Navarro, J. F., Frenk, C. S., & White, S. D. M. 1997, ApJ, 490, 493
Neugebauer, G. & Leighton, R. B. 1969, Two-micron sky survey. A preliminary catalogue
Nichols, M. & Bland-Hawthorn, J. 2011, ApJ, 732, 17
Nidever, D. L., Hasselquist, S., Hayes, C. R., et al. 2020, ApJ, 895, 88
Nidever, D. L., Majewski, S. R., & Butler Burton, W. 2008, ApJ, 679, 432

Nidever, D. L., Majewski, S. R., Butler Burton, W., & Nigra, L. 2010, ApJ, 723, 1618
Nidever, D. L., Monachesi, A., Bell, E. F., et al. 2013, ApJ, 779, 145
Nidever, D. L., Olsen, K., Walker, A. R., et al. 2017, AJ, 154, 199
Niederhofer, F., Cioni, M.-R. L., Rubele, S., et al. 2018a, A&A, 613, L8
Niederhofer, F., Cioni, M. R. L., Rubele, S., et al. 2018b, A&A, 613, L8
Niederhofer, F., Cioni, M.-R. L., Rubele, S., et al. 2021, MNRAS, 502, 2859
Niederhofer, F., Cioni, M.-R. L., Schmidt, T., et al. 2022, MNRAS, 512, 5423
Nikolaev, S., Drake, A. J., Keller, S. C., et al. 2004, ApJ, 601, 260
Nikolaev, S. & Weinberg, M. D. 2000, ApJ, 542, 804
Noël, N. E. D., Aparicio, A., Gallart, C., et al. 2009, ApJ, 705, 1260
Noël, N. E. D., Conn, B. C., Read, J. I., et al. 2015, MNRAS, 452, 4222
Noël, N. E. D. & Gallart, C. 2007, ApJ, 665, L23
Oey, M. S., Dorigo Jones, J., Castro, N., et al. 2018, ApJ, 867, L8
Oliphant, T. E. 2015, Guide to NumPy (CreateSpace Independent Publishing Platform, 2nd ed.)
Olsen, K. A. G., Hodge, P. W., Mateo, M., et al. 1998, MNRAS, 300, 665
Olsen, K. A. G. & Massey, P. 2007, ApJ, 656, L61
Olsen, K. A. G. & Salyk, C. 2002a, AJ, 124, 2045
Olsen, K. A. G. & Salyk, C. 2002b, AJ, 124, 2045
Olsen, K. A. G., Zaritsky, D., Blum, R. D., Boyer, M. L., & Gordon, K. D. 2011, ApJ, 737, 29
Olszewski, E. W., Schommer, R. A., Suntzeff, N. B., & Harris, H. C. 1991, AJ, 101, 515
Omkumar, A. O., Subramanian, S., Niederhofer, F., et al. 2021, MNRAS, 500, 2757
Pace, A. B., Erkal, D., & Li, T. S. 2022, ApJ, 940, 136
Pardy, S. A., D'Onghia, E., Athanassoula, E., Wilcots, E. M., & Sheth, K. 2016, ApJ, 827, 149
Pardy, S. A., D'Onghia, E., Navarro, J. F., et al. 2020, MNRAS, 492, 1543
Partridge, C., Lahav, O., & Hoffman, Y. 2013, MNRAS, 436, L45
Pasquini, L., Avila, G., Blecha, A., et al. 2002, The Messenger, 110, 1
Patel, E., Kallivayalil, N., Garavito-Camargo, N., et al. 2020, ApJ, 893, 121
Paudel, S. & Sengupta, C. 2017, ApJ, 849, L28
Peñarrubia, J., Gómez, F. A., Besla, G., Erkal, D., & Ma, Y.-Z. 2016, MNRAS, 456, L54
Phookun, B., Mundy, L. G., Teuben, P. J., & Wainscoat, R. J. 1992, ApJ, 400, 516
Piatek, S., Pryor, C., & Olszewski, E. W. 2008, AJ, 135, 1024
Piatti, A. E. 2022, MNRAS, 511, L72
Pieres, A., Santiago, B. X., Drlica-Wagner, A., et al. 2017, MNRAS, 468, 1349
Pierre, M., Viton, M., Sivan, J. P., & Courtes, G. 1986, A&A, 154, 249
Pingel, N. M., Dempsey, J., McClure-Griffiths, N. M., et al. 2022, , 39, e005
Putman, M. E., Gibson, B. K., Staveley-Smith, L., et al. 1998, Nature, 394, 752
Reid, W. A. & Parker, Q. A. 2012, MNRAS, 425, 355

Richter, P., Fox, A. J., Wakker, B. P., et al. 2013, ApJ, 772, 111

Ripepi, V., Cioni, M.-R. L., Moretti, M. I., et al. 2017, MNRAS, 472, 808

Ripepi, V., Marconi, M., Moretti, M. I., et al. 2016, ApJS, 224, 21

Roca-Fàbrega, S., Figueras, F., Valenzuela, O., et al. 2014, in EAS Publications Series, Vol. 67-68, EAS Publications Series, 393–394

Roca-Fàbrega, S., Valenzuela, O., Figueras, F., et al. 2013, MNRAS, 432, 2878

Rodríguez-Puebla, A., Avila-Reese, V., & Drory, N. 2013, ApJ, 773, 172

Röser, S. & Bastian, U. 1993, Bulletin d'Information du Centre de Donnees Stellaires, 42, 11

Rubele, S., Girardi, L., Kerber, L., et al. 2015, MNRAS, 449, 639

Rubele, S., Kerber, L., Girardi, L., et al. 2012, A&A, 537, A106

Rubele, S., Pastorelli, G., Girardi, L., et al. 2018, MNRAS, 478, 5017

Ruiz-Dern, L., Babusiaux, C., Arenou, F., Turon, C., & Lallement, R. 2018, A&A, 609, A116

Ruiz-Lara, T., Gallart, C., Monelli, M., et al. 2020, A&A, 639, L3

Saha, A., Olszewski, E. W., Brondel, B., et al. 2010, AJ, 140, 1719

Salaris, M. & Girardi, L. 2002, MNRAS, 337, 332

Salem, M., Besla, G., Bryan, G., et al. 2015, ApJ, 815, 77

Sandage, A. & Tammann, G. A. 1968, ApJ, 151, 531

Saroon, S. & Subramanian, S. 2022, A&A, 666, A103

Schlafly, E. F. & Finkbeiner, D. P. 2011, ApJ, 737, 103

Schlegel, D. J., Finkbeiner, D. P., & Davis, M. 1998, ApJ, 500, 525

Schmidt, T., Cioni, M.-R. L., Niederhofer, F., et al. 2020, A&A, 641, A134

Schmidt, T., Cioni, M.-R. L., Niederhofer, F., et al. 2022, A&A, 663, A107

Schommer, R. A., Suntzeff, N. B., Olszewski, E. W., & Harris, H. C. 1992, AJ, 103, 447

Scowcroft, V., Freedman, W. L., Madore, B. F., et al. 2016, ApJ, 816, 49

Shao, S., Cautun, M., Deason, A. J., Frenk, C. S., & Theuns, T. 2018, MNRAS, 479, 284

Shapley, H. 1924, Harvard College Observatory Circular, 268, 1

Shapley, H. 1940, Harvard Coll. Obs. Bull., 914, 8

Shipp, N., Li, T. S., Pace, A. B., et al. 2019, ApJ, 885, 3

Simon, J. D. 2018, ApJ, 863, 89

Skowron, D. M., Jacyszyn, A. M., Udalski, A., et al. 2014, ApJ, 795, 108

Skrutskie, M. F., Cutri, R. M., Stiening, R., et al. 2006, AJ, 131, 1163

Soszyński, I., Udalski, A., Szymański, M. K., et al. 2010, AcA, 60, 165

Soszyński, I., Udalski, A., Szymański, M. K., et al. 2011, AcA, 61, 217

Soszyński, I., Udalski, A., Szymański, M. K., et al. 2015, AcA, 65, 297

Soszyński, I., Udalski, A., Szymański, M. K., et al. 2016, AcA, 66, 131

Stanimirović, S., Staveley-Smith, L., Dickey, J. M., Sault, R. J., & Snowden, S. L. 1999, MNRAS, 302, 417

Stanimirović, S., Staveley-Smith, L., & Jones, P. A. 2004a, ApJ, 604, 176

Stanimirović, S., Staveley-Smith, L., & Jones, P. A. 2004b, ApJ, 604, 176

Staveley-Smith, L., Kim, S., Calabretta, M. R., Haynes, R. F., & Kesteven, M. J. 2003, MNRAS, 339, 87

Staveley-Smith, L., Sault, R. J., Hatzidimitriou, D., Kesteven, M. J., & McConnell, D. 1997, MNRAS, 289, 225

Subramaniam, A. 2003, ApJ, 598, L19

Subramaniam, A. & Subramanian, S. 2009, ApJ, 703, L37

Subramanian, S., Rubele, S., Sun, N.-C., et al. 2017, MNRAS, 467, 2980

Subramanian, S. & Subramaniam, A. 2009, A&A, 496, 399

Subramanian, S. & Subramaniam, A. 2010, A&A, 520, A24

Subramanian, S. & Subramaniam, A. 2012, ApJ, 744, 128

Subramanian, S. & Subramaniam, A. 2013, A&A, 552, A144

Subramanian, S. & Subramaniam, A. 2015, A&A, 573, A135

Suntzeff, N. B., Friel, E., Klemola, A., Kraft, R. P., & Graham, J. A. 1986, AJ, 91, 275

Suntzeff, N. B., Schommer, R. A., Olszewski, E. W., & Walker, A. R. 1992, AJ, 104, 1743

Sutherland, W., Emerson, J., Dalton, G., et al. 2015, A&A, 575, A25

Tatton, B. 2018, PhD thesis, Keele University

Tatton, B. L., van Loon, J. T., Cioni, M. R., et al. 2013, A&A, 554, A33

Tatton, B. L., van Loon, J. T., Cioni, M. R. L., et al. 2020, arXiv e-prints, arXiv:2012.12288

Tatton, B. L., van Loon, J. T., Cioni, M. R. L., et al. 2021, MNRAS, 504, 2983

Taylor, M. B. 2005, in Astronomical Society of the Pacific Conference Series, Vol. 347, Astronomical Data Analysis Software and Systems XIV, ed. P. Shopbell, M. Britton, & R. Ebert, 29

Thackeray, A. D. & Wesselink, A. J. 1953, Nature, 171, 693

Thackeray, A. D. & Wesselink, A. J. 1955, The Observatory, 75, 33

The Dark Energy Survey Collaboration. 2005, arXiv e-prints, astro

Torrealba, G., Belokurov, V., Koposov, S. E., et al. 2018, MNRAS, 475, 5085

van der Marel, R. P. 2001, AJ, 122, 1827

van der Marel, R. P., Alves, D. R., Hardy, E., & Suntzeff, N. B. 2002, AJ, 124, 2639

van der Marel, R. P. & Cioni, M.-R. L. 2001, AJ, 122, 1807

van der Marel, R. P. & Kallivayalil, N. 2014, ApJ, 781, 121

van der Marel, R. P. & Sahlmann, J. 2016, ApJ, 832, L23

Van der Swaelmen, M., Hill, V., Primas, F., & Cole, A. A. 2013, A&A, 560, A44

Vasiliev, E. 2018, MNRAS, 481, L100

Vasiliev, E., Belokurov, V., & Erkal, D. 2021, MNRAS, 501, 2279

Wan, Z., Guglielmo, M., Lewis, G. F., Mackey, D., & Ibata, R. A. 2020, MNRAS, 492, 782

Wang, J., Hammer, F., Yang, Y., et al. 2019, MNRAS, 486, 5907

Weisz, D. R., Dolphin, A. E., Skillman, E. D., et al. 2013, MNRAS, 431, 364

Westerlund, B. E. 1964a, MNRAS, 127, 429

Westerlund, B. E. 1964b, in IAU Symp., Vol. 20, The Galaxy and the Magellanic Clouds, ed. F. J. Kerr, 239

Westerlund, B. E. & Glaspey, J. 1971, A&A, 10, 1

Wetzel, A. R., Deason, A. J., & Garrison-Kimmel, S. 2015, ApJ, 807, 49

White, S. D. M. & Frenk, C. S. 1991, ApJ, 379, 52

Wilcots, E. M. & Prescott, M. K. M. 2004, AJ, 127, 1900

Williams, R. N. M. 2009, in IAU Symposium, Vol. 256, The Magellanic System: Stars, Gas, and Galaxies, ed. J. T. Van Loon & J. M. Oliveira, 443–453

Wilson, J. C., Hearty, F. R., Skrutskie, M. F., et al. 2019, PASP, 131, 055001

Wilson, R. E. 1924, AJ, 35, 183

Wolf, C., Onken, C. A., Luvaul, L. C., et al. 2018, , 35, e010

York, D. G., Adelman, J., Anderson, John E., J., et al. 2000, AJ, 120, 1579

Yoshizawa, A. M. & Noguchi, M. 2003, MNRAS, 339, 1135

Yozin, C. & Bekki, K. 2014, MNRAS, 439, 1948

Zaritsky, D. 2004, ApJ, 614, L37

Zaritsky, D., Harris, J., Grebel, E. K., & Thompson, I. B. 2000, ApJ, 534, L53

Zaritsky, D., Harris, J., & Thompson, I. 1997, AJ, 114, 1002

Zaritsky, D., Salo, H., Laurikainen, E., et al. 2013, ApJ, 772, 135

Zhao, H. & Evans, N. W. 2000, ApJ, 545, L35

Zhao, H., Ibata, R. A., Lewis, G. F., & Irwin, M. J. 2003, MNRAS, 339, 701

Zivick, P., Kallivayalil, N., Besla, G., et al. 2019, ApJ, 874, 78

Zivick, P., Kallivayalil, N., & van der Marel, R. P. 2020, arXiv e-prints, arXiv:2011.02525

Zivick, P., Kallivayalil, N., & van der Marel, R. P. 2021, ApJ, 910, 36

Zivick, P., Kallivayalil, N., van der Marel, R. P., et al. 2018, ApJ, 864, 55

Publications

The Ph.D candidate has contributed to the following list of publications during her doctoral studies.

Journal Articles

1. The Kinematics of stellar substructures in the Small Magellanic Cloud
   El Youssoufi, Dalal ; Cioni, Maria-Rosa L. ; Kacharov, Nikolay ; Bell, Cameron P. M. ; Matjević, Gal ; Bekki, Kenji ; de Grijs, Richard ; Ivanov, Valentin D. ; van Loon, Jacco; MNRAS, Accepted, May 2023.

2. The VMC survey. XLV. Proper motion of the outer LMC and the impact of the SMC
   Schmidt, Thomas ; Cioni, Maria-Rosa L. s; Niederhofer, Florian ; Bekki, Kenji ; Bell, Cameron P. M. ; de Grijs, Richard ; **El Youssoufi, Dalal** ; Ivanov, Valentin D. ; Oliveira, Joana M. ; Ripepi, Vincenzo ; van Loon, Jacco Th.; **A&A**, Volume 663, id.A107, 21 pp., July 2022.

3. The VMC survey - XLVIII. Classical cepheids unveil the 3D geometry of the LMC
   Ripepi, Vincenzo; Chemin, Laurent; Molinaro, Roberto; Cioni, Maria-Rosa L.; Bekki, Kenji; Clementini, Gisella; de Grijs, Richard; De Somma, Giulia; **El Youssoufi, Dalal**; Girardi, Léo; Groenewegen, Martin A. T.; Ivanov, Valentin; Marconi, Marcella; McMillan, Paul J.; van Loon, Jacco Th; MNRAS, Volume 512, Issue 1, pp.563-582, May 2022.

4. Presence of red giant population in the foreground stellar substructure of the Small Magellanic Cloud
   James, Dizna; Subramanian, Smitha; Omkumar, Abinaya O.; Mary, Adhya; Bekki, Kenji; Cioni, Maria-Rosa L.; de Grijs, Richard; **El Youssoufi, Dalal**; Kartha, Sreeja S.; Niederhofer, Florian; van Loon, Jacco Th; MNRAS, Volume 508, Issue 4, pp.5854-5863, December 2021.

5. Stellar substructures in the periphery of the Magellanic Clouds with the VISTA hemisphere survey from the red clump and other tracers
   El Youssoufi, Dalal; Cioni, Maria-Rosa L.; Bell, Cameron P. M.; de Grijs, Richard ; Groenewegen, Martin A. T. ; Ivanov, Valentin D.; Matijevĭc, Gal; Niederhofer, Florian; Oliveira, Joana M.; Ripepi, Vincenzo; Schmidt, Thomas;

Subramanian, Smitha; Sun, Ning-Chen; van Loon, Jacco Th.; MNRAS, Volume 505, Issue 2, pp.2020-2038, August 2021.

6. The VMC survey - XLI. Stellar proper motions within the Small Magellanic Cloud
Niederhofer, Florian; Cioni, Maria-Rosa L.; Rubele, Stefano; Schmidt, Thomas; Diaz, Jonathan D.; Matijevĭc, Gal; Bekki, Kenji; Bell, Cameron P. M.; de Grijs, Richard; **El Youssoufi, Dalal**; Ivanov, Valentin; Oliveira, Joana M.; Ripepi, Vincenzo; Subramanian, Smitha; Sun, Ning-Chen; van Loon, Jacco Th; MNRAS, Volume 502, Issue 2, pp.2859-2878, April 2021.

7. Gaia view of a stellar sub-structure in front of the Small Magellanic Cloud
Omkumar, Abinaya O.; Subramanian, Smitha; Niederhofer, Florian; Diaz, Jonathan; Cioni, Maria-Rosa L.; **El Youssoufi, Dalal**; Bekki, Kenji; de Grijs, Richard; van Loon, Jacco Th; MNRAS, Volume 500, Issue 3, pp.2757-2776, January 2021.

8. The VMC survey. XXXVIII. Proper motion of the Magellanic Bridge
Schmidt, Thomas; Cioni, Maria-Rosa L.; Niederhofer, Florian ; Bekki, Kenji ; Bell, Cameron P. M.; de Grijs, Richard; Diaz, Jonathan; **El Youssoufi, Dalal**; Emerson, Jim; Groenewegen, Martin A. T.; Ivanov, Valentin D.; Matijevic, Gal; Oliveira, Joana M.; Petr-Gotzens, Monika G.; Queiroz, Anna B. A.; Ripepi, Vincenzo ; van Loon, Jacco Th.; A&A, Volume 641, id.A134, 17 pp., September 2020.

9. The VMC survey - XXXIV. Morphology of stellar populations in the Magellanic Clouds
El Youssoufi, Dalal; Cioni, Maria-Rosa L.; Bell, Cameron P. M.; Rubele, Stefano; Bekki, Kenji; de Grijs, Richard; Girardi, Léo; Ivanov, Valentin D.; Matijevic, Gal; Niederhofer, Florian; Oliveira, Joana M.; Ripepi, Vincenzo; Subramanian, Smitha; van Loon, Jacco Th; MNRAS, Volume 490, Issue 1, p.1076-1093, November 2019.

Conference Proceedings

1. A comprehensive view of the morphology of the Magellanic Clouds in the near-infrared
El Youssoufi, Dalal, AAS meeting 236, id. 109.01. Bulletin of the American Astronomical Society, Vol. 52, No. 3, June 2020.

2. A near-infrared view of the morphology of the Magellanic Clouds using the VMC and VHS surveys
El Youssoufi, Dalal; A Synoptic View of the Magellanic Clouds: VMC, Gaia

and Beyond, Proceedings of the conference held 9-13 September, 2019 in Garching, Germany.

3. Morphology of stellar populations in the Magellanic Clouds using the VMC survey
El Youssoufi, Dalal; Cioni, Maria-Rosa L.; Bell, Cameron P. M.; Rubele, Stefano; Niederhofer, Florian; Matijevic, Gal; IAU Symposium 344, Dwarf Galaxies: from the Deep Universe to the Present, (Eds) S. Stierwalt & K. McQuinn.

4. Behavior of the Doubling of Metal Lines as Function of the Blazhko Phase in the Spectra of RR Lyr
Sefyani, Fouad L.; Benhida, Abdelmajid; Benkhaldoun, Zouhair; De France, Thibaut; Gillet, Dennis; Mathias, Phillip; Daassou, Ahmed; **El Youssoufi, Dalal**; El Jariri, Youssef ; Chafouai, Khadija; The RR Lyrae 2017 Conference. Revival of the Classical Pulsators: from Galactic Structure to Stellar Interior Diagnostics. Proceedings of the meeting held 17-21 September, 2017 in Niepołomice, Poland. Proceedings of the Polish Astronomical Society, Vol. 6. Edited by R. Smolec, K. Kinemuchi, and R.I. Anderson

5. RR Lyr Spectrophotometric Campaign from Oukaimeden Observatory
Benhida, Abdelmajid; Sefyani, Fouad L.; Benkhaldoun, Zouhair; **El Youssoufi, Dalal**; De France, Thibaut; Gillet, Denis; Mathias, Phillipe; Chafouai, Khadija; El Jariri, Youssef; Daassou, Ahmed; The RR Lyrae 2017 Conference. Revival of the Classical Pulsators: from Galactic Structure to Stellar Interior Diagnostics. Proceedings of the meeting held 17-21 September, 2017 in Niepołomice, Poland. Proceedings of the Polish Astronomical Society, Vol. 6. Edited by R. Smolec, K. Kinemuchi, and R.I. Anderson, ISBN 978-83-938279-9-2, pp.279-28

Other

1. Being a doctoral researcher in the Leibniz Association: 2019 Leibniz PhD Network survey report
Beadle, Brian ; Do, Stefanie; **El Youssoufi, Dalal**; Felder, Daniel; Gorenflos López,Jacob; Jahn, Anja; Pérez-Bosch Quesada, Emilio; Rottleb, Tim; Rüter, Fabian; Schanze, Jan-Lucas Schanze; Stroppe, Anne-Kathrin; Thater, Sabine; Verrière, Antoine; Weltin, Meike

2. 4MOST Consortium Survey 9: One Thousand and One Magellanic Fields (1001MC)
Cioni, Maria-Rosa L. ; Storm, Jesper; Bell, Cameron P. M.; Lemasle, Bertrand; Niederhofer, Florian; Bestenlehner, Joachim M.; **El Youssoufi, Dalal**; Feltzing, Sofia; González-Fernández, Carlos; Grebel, Eva K.; Hobbs, David; Irwin, Mike; Jablonka, Pascale; Koch, Andreas ; Schnurr, Oliver; Schmidt, Thomas; Steinmetz, Matthias; The Messenger, vol. 175, p. 54-57, March 2019.

3. 4MOST: Project overview and information for the First Call for Proposals

de Jong, R. S.; Agertz, O.; Berbel, A. A.; Aird, J.; Alexander, D. A.; Amarsi, A.; Anders, F.; Andrae, R.; Ansarinejad, B.; Ansorge, W.; Antilogus, P.; Anwand-Heerwart, H. and ... **El Youssoufi, D.**; ... et al; The Messenger, 175:3–11, March 2019.

Acknowledgements

فإذا كنت أغني للفرح
فلأن العاصفة، وعدتني بنبيذ، و بأنخاب جديدة، و بأقواس قزح

محمود درويش، وعود من العاصفة

Firstly, I would like to express my sincere gratitude to my supervisor Maria-Rosa L. Cioni for offering me the chance to pursue my PhD at the AIP, for her guidance and input throughout the years. I want to extend my thanks to the members of my thesis committee, Matthias Steinmetz and Jesper Storm, for their time, support and for stimulating discussions during my Ph.D. committee meetings, I would also like to thank Andrew Cole for agreeing to referee my thesis and the entire examination committee for their careful reading of this manuscript.

To the VMC team, it has been a pleasure being part of the collaboration for the past few years, thank you for the valuable insights and constant feedback. Particular thanks go to my collaborators Cameron P. M. Bell, Kenji Bekki, Maria-Rosa L. Cioni, Richard de Grijs, Léo Girardi, Martin A T Groenewegen, Valentin D. Ivanov, Florian Niederhofer, Joana M Oliveira, Abinaya O. Omkumar, Vincenzo Ripepi, Stefano Rubele, Thomas Schmidt, Smitha Subramanian, Ning-Chen Sun and Jacco Th. van Loon. Our consortium meeting used to be one of my favourite scientific events of the year and I am thrilled about all the engaging science that is yet to come from VMC.

To members of the Milky Way and the Local Volume as well as Dwarf Galaxies and the Galactic Halo sections, thank you for providing a wonderful and friendly environment to work in.

To Smitha Subramanian and Anapurni Subramaniam, thank you for warmly welcoming me to your institute for an extended research visit. To Sneha, Chayan, Prasanta, Sindhu and Vikrant thank you for your hospitality and generosity, I have the fondest

memories from my visit to India and I'll always cherish the time I spent with all of you.

To Cameron, I fondly recall you fetching me from the reception on my first day at the AIP and showing me around, thank you for being the best office mate one can hope for, for always providing calm and kind support, advice, and feedback, no matter what problems or questions I had. I dearly miss our random tea and cookie breaks and sharing an office with you.

To Anna, your unwavering support and encouragement throughout this PhD has been invaluable. Your kindness, empathy, and willingness to lend a listening ear have been a source of comfort and kept me going during challenging times. I am grateful for your friendship and the memories we have shared over the years.

To Kris, here's to those countless after-work drinks, the engaging conversations during our long commutes, and showing me all that Berlin has to offer. Your presence and infectious energy are dearly missed.

To Guillaume, your presence at the institute brought a sense of homeliness and familiarity, and I will forever hold dear the shared picnics, dinners, and delightful raclette gatherings we enjoyed throughout the years. Thank you for being a dear friend.

To Amy, I cherish the bond we formed through shared experiences and hold dear the time you spent in Potsdam, thank you for your friendship, you are dearly missed and I am looking forward to your return.

To Florian, thank you for patiently answering all my many questions over the last few years, and for being kind and generous with your time whenever I needed help.

To Petra, thank you for your immense help, support, and for going above and beyond to make sure I was safe during that tough first year in Potsdam. I will always be grateful for our friendship.

To the IT-section of the AIP, particularly Karl-Heinz Boing and Ronny Nigel, thank you for always welcoming me to your offices with a warm smile and reassurance. Further thanks go to the Welcome Centre of the University of Potsdam and particularly Frau Frauke Stobbe for all the help and kind advice they provided me with in terms of bureaucracy during my move from Morocco to Germany.

There are many more people I met at the AIP I would like to thank, Sanja, Gal, Andrea, Matteo, Eduardo, Anke, Else, Cristina, Ivan, Eloy, In-Sung, Thomas, Samir, Viswajith, Nikolay, Eloy, Sam, Marica, Elena, Erasmo, Marcel.

To Jordan, what a couple of years it has been. Here's to the memories we've created and the growth we've experienced. To many more years of treasured friendship and

shared adventures.

To Gabriele, thank you for always taking an interest in my work, we became flatmates 2 months before the first COVID lockdown, and I will always cherish your reassurance and company during those difficult times and all the creative ways you came up with to keep us entertained, I miss your food and our Kitchen Karaoke nights.

To Beatrice and Greg, thank you for your generosity and for offering me a home when I most needed one, for going above and beyond to make sure I am happy and comfortable, I will always be grateful.

To Tolga, thank you for all that you've done. Your unwavering support and the countless late-night talks we shared have not only rekindled my love for astronomy but have also enriched my life in immeasurable ways. Your passion for science is contagious.

To Jordan, Enzo, Amelie, Jonas, Ben, Max, and Steffen, your dedication and unwavering commitment to creating positive change in our communities has been a constant source of inspiration and support. I am deeply grateful for your friendship and relentless dedication to making the world a better place.

To the Leibniz PhD Network, thank you for providing a platform for exchange and networking among doctoral researchers within the Leibniz Association. Your efforts towards promoting common standards of working conditions and transparency in academic careers are greatly appreciated. I would like to thank the steering committee, working groups, and all members of the network for their contributions and support during my doctoral research.

I extend my deepest appreciation and gratitude to my mentors throughout my time at the Univerity Cadi Ayyad, particularly Zouhair Benkhaldoun, Mohammed Chabab, Abdelmjid Benhida, and Fouad Sefyani whose guidance and unwavering support have been indispensable in shaping my academic career. Your perseverance and dedication to the development of Astronomy and High Energy Physics in Morocco are nothing short of inspiring.

To Igor, I will never find a neighbour as kind as you, thank you for introducing me to Marin, Kristijan, Maja and Doris, I love all of you.

To Thiago, Tolga, Sanja, Ahmed, Jens, Arjun, Lindsay, Medea, Shea, Alex, Maissam, Sara and Carlos, thank you for your support, encouragement, and advice during my transition out of astronomy. Your guidance and mentorship have been invaluable in helping me navigate the transition and find a career path that aligns with my values and interests.

To my new colleagues, Michael, Thiago, Tobias, Dominic, Julia, Stella, and Johanna I am deeply grateful for your immense support, flexibility, and understanding. Thank you for introducing me to the fascinating world of provenance research.

My profound gratitude goes to my family, whose unwavering love and support have been a constant source of strength and inspiration. To my parents, Nezha and Hamid, and my brother Ali, thank you for instilling in me a love of learning, thank you for your encouragement and unwavering belief in my abilities. To the entire El Youssoufi family, this achievement is as much yours as it is mine. No words can convey how lucky I am to have all of you. To the loving memory of my grandparents, the sense of unity and love that you instilled in our family continues to this day and is a testament to the enduring impact you have had on all of us. Your legacy lives on through the strong bonds that tie us together, and we will always be grateful for the example you set and the values you instilled in all of us.

In closing, I recognise that this is not an exhaustive list and that many others have contributed in countless ways to my academic and personal growth. To each of you, whether named here or not, I offer my heartfelt thanks and appreciation. It is through your support and encouragement that I have been able to complete this work, and I am grateful and humbled to have had you by my side throughout this journey.

When I heard the learn'd astronomer,
When the proofs, the figures, were ranged in columns before me,
When I was shown the charts and diagrams, to add, divide, and measure them,
When I sitting heard the astronomer where he lectured with much applause in the lecture-room,
How soon unaccountable I became tired and sick,
Till rising and gliding out I wander'd off by myself,
In the mystical moist night-air, and from time to time,
Look'd up in perfect silence at the stars.

– Walt Whitman

إلى خيابت دابا تزيان.